

**Efficient Digitizing Interface Circuits for Various
Resistive Sensor Configurations with Considerations on
Wide-span and Remote Measurements**

A thesis submitted
in partial fulfillment for the award of the degree of

Doctor of Philosophy

by

ELANGO VAN K



Department of Avionics

Indian Institute of Space Science and Technology

Thiruvananthapuram, India

October 2022

Certificate

This is to certify that the thesis titled *Efficient Digitizing Interface Circuits for Various Resistive Sensor Configurations with Considerations on Wide-span and Remote Measurements* submitted by Elangovan K, to the Indian Institute of Space Science and Technology, Thiruvananthapuram, in partial fulfillment for the award of the degree of Doctor of Philosophy is a bonafide record of the original work carried out by him under my supervision. The contents of this thesis, in full or in parts, have not been submitted to any other Institute or University for the award of any degree or diploma.

Dr. Anoop C. S.
(Ph.D. Advisor)
Associate Professor
Department of Avionics
IIST

Prof. Deepak Mishra
Professor & Head
Department of Avionics
IIST

Place: Thiruvananthapuram

Date: October 2022

Declaration

I declare that this thesis titled *Efficient Digitizing Interface Circuits for Various Resistive Sensor Configurations with Considerations on Wide-span and Remote Measurements* submitted in partial fulfillment for the award of the degree of Doctor of Philosophy is a record of the original work carried out by me under the supervision of Dr. Anoop C. S., and has not formed the basis for the award of any degree, diploma, associateship, fellowship, or other titles in this or any other Institution or University of higher learning. In keeping with the ethical practice in reporting scientific information, due acknowledgments have been made wherever the findings of others have been cited.

Place: Thiruvananthapuram

Date: October 2022

Elangovan K

(SC18D002)

Dedication

This thesis is dedicated to my Amma, Brother, Grandfather, Supervisor, and the people who have supported me throughout my research journey. Thanks for making me this adventure through to the end.

Acknowledgments

First and foremost, praises and thanks to God, the Almighty, for their showers of blessings throughout my research journey to complete the research successfully.

Next, I express my sincere thanks to my Ph.D. supervisor Dr. Anoop C. S., Associate Professor, Department of Avionics, Indian Institute of Space Science and Technology (IIST), for taking me as his Ph.D. student. He is the person who discussed with me and introduced the scientific research world. His experience and patience and friendly approach to exploring and resolving problems helped me to realize my Ph.D. work. His kind approach to me provided sufficient freedom to participate in all other activities. I thank him specifically for supporting me in my good as well as worst times. He is the motivator, supporter, and friend throughout my research journey. Without him, I cannot complete this journey smoothly.

I am so grateful to the members of my Doctoral Committee, Dr. Deepak Mishra, Professor & Head, Department of Avionics, IIST, Dr. N. Selvaganesan, Professor, Department of Avionics, IIST, Dr. Rajeevan P. P., Associate Professor, Department of Avionics, IIST, Dr. Sourin Mukhopadhyay, Assistant Professor, Department of Physics, IIST, for reviewing my work and providing feedback and suggestions throughout the Ph.D. work. I extend my gratitude to Dr. Sudharshan Kaarthik, Associate Professor, Department of Avionics, IIST, for his voluntary involvement and care in my research works. Thanks to Dr. Vineeth B. S. for the support in my research career. Sincere thanks to Dr. V. Govindaraj, Assistant Professor, National Institute of Technology, Puducherry, for his immersive advice and care taken on me during my Ph.D. degree. Thanks to my co-authors British Ashok Sonetakke, Dr. Kishor Bhaskarrao Nandapukar, Assistant Professor, Indian Institute of Technology, Dhanbad, Ashikhi Antony, Sagnik Dutta, Sawan Kumar Ambedkar, and Subham Saha for their extraordinary help during my research activities. Thanks to Ms. Anjali Devi, Ms. Rinu Preethi, Ms. Husnara Parveen, and Mr. Jishnu for their support in my research. My research-related work was not fulfilled without the presence of

Mrs. Smitha S, who is the lab staff of Instrumentation and Measurement Lab. She played the most important role in intending, purchasing, and making the hardware components available on time during my research work. My sincere thanks to Prakash R. S., technical staff in the aerospace department who helped me in the development of the characterization model. I extend my thanks to Mr. Sreehari B Nair, Ph.D. student, IIST, who worked with me in the earlier days, and helped in many of my up and down situations as a co-researcher, friend, and beloved brother.

I extend my respect and gratitude to the technical staffs, Mrs. Smitha S, Mrs. Divya R. S., Mrs. Preeti Yadav A. G., Mrs. Ananthalakshmi S., Mrs. Dhanya G. D. Nair, Mrs. Archana K. P., Mrs. Rinta Raj K. R., Mrs. Lekshmi Devan A., Mr. Abhilash S., Mr. Nidheesh Ravi, Mr. Satish Kumar. V, and Mr. M. Narasimha Murthy for providing me a homely atmosphere in my institute. Special thanks to my lab mates Mr. Thomaskutty Mathew, Safeer S S, and Ms. Rudrakshi Garg for their support during my research.

Last but not least, I thank every one of my friends in IIST and outside of IIST to give their valuable support for my balancing life in academic and non-academic activities.

Elangovan K

Abstract

Resistive sensors are widely employed for several applications in automobile, aerospace, chemical, and other process industries. They are routinely used for the measurement of physical variables such as temperature, displacement, magnetic field, and force. The properties (such as simplicity in construction, durability, good dynamic range, and low cost) of resistive sensors make them an excellent choice for the above measurement scenarios. There are different variants and configurations (e. g., single element, differential sensor, and bridge-based versions) of resistive sensors. Several other measurement challenges (including remote measurements, wide-operational span, non-linear transfer characteristics, and presence of secondary sensing elements) are associated with industrial resistive sensors.

Efficient interfacing electronics are required to process the resistive sensors and realize automated instrumentation systems. This thesis proposes the design and development of simple and efficient digitizing interface circuits for broad classes of resistive sensors. Initially, this thesis focuses on the design and development of a dual-slope-based digitizer suited for different resistive sensor configurations. This digitizer enables constant current excitation and can be used to control self-heating errors. Moreover, the circuit uses only a single reference voltage. Next, an alternate technique based on the relaxation oscillator principle is proposed. This scheme provides many meritorious features such as simple architecture, low output error, adaptability with various resistive sensor configurations, independence from many circuit nonidealities, etc. Further, this scheme is enhanced to adapt with wide-span sensors. This scheme implements a novel multiregiming technique, based on geometric series principles, and provides low conversion time for the entire measurement range.

Further, digitizing schemes for remotely-located resistive sensors are also proposed. The proposed digitizers with inbuilt wire resistance compensation show excellent immunity against the connecting leads. These circuits are suitable for a broad class of resistive sensors including bridge configurations. The proposed universal

digitizer for bridge-based sensors shows independence from the mismatch of wire resistances and parasitic elements of sensors.

The thesis later focuses on the design of a simple microcontroller-based scheme for remotely-located resistive sensors. This scheme can be easily modified to adapt with the various class of resistive sensors. This technique has the advantage of independence from microcontroller threshold voltages, low power consumption, wide range measurement, etc. Later, this technique has been enhanced for the interface of RC impedance sensors. Here, this enhanced method is useful to measure the resistance as well as the capacitance of RC sensors. Finally, a digitizing circuit for another special type of resistive sensor (e. g., thermistor) is also proposed. This method proposes a novel linearization approach to linearize the output of the thermistor. In addition, this technique is independent of connecting wire resistances.

The methodology of the proposed digitizers was mathematically brought out and their performance was verified using simulation studies. Detailed error analysis was carried out to determine the influence of various parameters on the digitizers' output. Hardware prototypes of the digitizing interfaces were built and tested with various commercial resistive sensors. Details of the developed methodologies, simulation and error analysis performed, hardware setup, and evaluation results achieved are presented in this thesis.

Contents

List of Figures	xv
List of Tables	xxv
Abbreviations	xxvii
Nomenclature	xxix
1 Introduction	1
1.1. Measurements and Sensors	1
1.2. Resistive Sensors and Their Applications	3
1.3. Classifications of Resistive Sensors	3
1.4. Measurement Challenges Associated with Resistive Sensors	12
1.5. Interface Circuits for Resistive Sensors	16
1.6. Motivation	19
1.7. Objectives and Scope	20
1.8. Organization of the Thesis	21
2 Dual-slope-based Digitizing Circuit for a Broad Class of Current Excited Resistive Sensors	25
2.1. Introduction	25
2.2. Detailed Discussion on Digitizing Interface for Resistive Sensors	25
2.3. Digitizing Circuit for Resistive Sensors	28
2.4. Error Analysis of DCR	33
2.5. Simulation Studies of DCR	35
2.6. Emulation Studies	38
2.7. Performance Verification with Actual Sensors	40
2.8. Temperature-Stability Studies	45

2.9.	Summary	47
3	Relaxation Oscillator-based Digital Techniques for Resistive Sensors	49
3.1.	Introduction	49
3.2.	Relaxation oscillator-based Digitizer for Resistive sensors (RDR)	50
3.3.	Relaxation oscillator-based Digitizer for Resistive sensors with Wide-span (RDR _w)	55
3.4.	Error Analysis	61
3.5.	Performance Verification of RDR Circuits	65
3.6.	Performance Evaluation of RDR and RDR* with GMR Sensors	70
3.7.	Performance Verification of RDR _w Circuit	73
3.8.	Summary	79
4	Design of Digitizing Circuits for Remotely Connected Resistive Sensors	81
4.1.	Introduction	81
4.2.	Interfaces for Remotely Connected Resistive Sensors	83
4.3.	Digitizer for Remotely Connected Resistive Sensors	84
4.4.	Error Analysis	94
4.5.	Performance Verification of DRR-1 Circuit	96
4.6.	Performance Verification of DRR-2 Circuit	99
4.7.	Performance Verification of DRR-3 Circuit	104
4.8.	Comparison Studies	109
4.9.	Summary	111
5	Improved Microcontroller-Based Digitizing Interface Circuits for Resistive Sensors in Different Configurations	113
5.1.	Introduction	113
5.2.	Digitizing Interface for Resistive Sensors	113
5.3.	Error Analysis	120

5.4.	Performance Verification of the DIR Circuits	122
5.5.	Experimental Studies of the DIR Circuits	127
5.6.	Summary	132
6	Simple and Accurate Digitizer Circuit for Parallel RC Impedance Sensors	133
6.1.	Introduction	133
6.2.	RC Sensors and Interfacing Techniques	133
6.3.	Front-end for Interfacing Parallel RC Impedance Transducer	136
6.4.	Sources of Errors and Their Effects	140
6.5.	Simulation Studies of the DFRC Circuits	143
6.6.	Experimentation of DFRC	146
6.7.	Summary	152
7	Linearizing Circuit for Thermistor-Based Temperature Measurement System	153
7.1.	Introduction	153
7.2.	Existing Measurement Systems for Thermistors	153
7.3.	Linearized Thermistor-Based Digital Measurement System	156
7.4.	Effect of Error Sources	164
7.5.	Performance Verification of the Th-LDM Circuits	166
7.6.	Experimental Studies of Complete Th-LDM System	170
7.7.	Summary	177
8	Conclusions and Future Works	179
8.1.	Future Works	181
	Bibliography	183
	List of Publications	199

Appendices	201
A. Expressions Used for the Calculation of Various Performance Parameters	201
B.1. Measurement Results Related to DCR Circuit (During Experimentation with DS-type Sensor)	203
B.2. Experimental Results Related to RDR _w Circuit (During Experimentation with SE-type Sensor)	204
B.3. Data Related to DRR-3 Interface with the AA004 GMR Sensor	205
B.4. Measurement Data Related to DIR Circuit During Interface with SE type Sensor	206
B.5. Emulation Results of the DFRC Circuit During the Measurement of Capacitance	207
B.6. Experimental Results of Th-LDM With Thermistor (T-2) Sensor	208
Biodata	209
Doctoral Committee Members	211

List of Figures

1.1	Photograph of common resistive sensors. (a) RTD [39], (b) non-contact potentiometer [40], (c) strain gauge [41], (d) thermistor [42], (e) LDR [43], and (f) GMR [37].	5
1.2	Expected requirement of autonomous vehicles globally, from 2021 to 2030 [44].	6
1.3	Input-output relationship of thermistor.	8
1.4	Pictorial representation of GMR principle, (a) high resistance and (b) low resistance.	10
1.5	Electrical equivalent model of (a) SE, (b) DS, (c) QB, (d) HB, and (e) FB is shown here.	11
1.6	Wiring infrastructure of resistive sensors. R_X denote the resistive sensor. (a) Two-wire, (b) Three-wire, and (c) Four-wire connection.	14
1.7	Electrical equivalent model of RC impedance sensor.	15
2.1	Proposed circuit diagram of the DCR, based on an improved dual-slope technique.	29
2.2	Output waveforms, observed at the nodes v_{A2} and v_{A3} are figured here. The control signal V_C given by TLU is also plotted.	30
2.3	Error sources of the proposed DCR are added to Fig. 2.1 and presented here, whenever the switch is located at position-1. I_P and I_N represents the bias currents of the Op-amps and V_{os} is the offset voltage. Resistances, R_N and R_F are the on and off-resistance of the switch, S_W .	33
2.4	Simulation results of the proposed DCR is shown here for SE/HB sensor interface, ((i) RTD-Pt100, (ii) RTD-Pt1000, and (iii) GMR-AA004).	36

2.5	Simulation results of the proposed DCR with DS, ((i) DS-1 (Potentiometric sensor – P11S [83]), (ii) DS-2 ([47]), (iii) DS-3 (Rectilinear displacement transducer-LT-150 [84])).	36
2.6	Emulation results of the proposed DCR with SE/HB sensor, ((i) RTD-Pt100, (ii) RTD-Pt1000, and (iii) GMR-AA004).	38
2.7	Emulation results of the proposed DCR is shown here for DS interface, ((i) DS-1 (Potentiometric sensor – P11S [83]), (ii) DS-2 ([47]), (iii) DS-3 (Rectilinear displacement transducer-LT-150 [84])).	39
2.8	Screenshot of waveforms observed using oscilloscope at different nodes of DCR at R_X and $R_S = 5 \text{ k}\Omega$.	39
2.9	Characterization setup of RTD-Pt100 sensor.	41
2.10	Characterization of RTD-Pt100 sensor is shown here. The measured e_{NL} is also plotted in this graph.	41
2.11	RTD-DCR interface results are figured here. The measured e_{NL} is also shown.	41
2.12	Characterization of GMR sensor is shown here. The measured e_{NL} and mismatch between GMR elements are also plotted in this graph.	43
2.13	Experimental setup used for GMR sensor interface with DCR is shown here.	43
2.14	GMR-DCR interface results are shown here. The measured e_{NL} is also depicted for each step of magnetic field.	44
2.15	Characterization setup for rectilinear displacement transducer-LT-150	44
2.16	DCR interface results with rectilinear displacement transducer-LT-150 is plotted here.	45
2.17	Simulation and the experimentation results of the DCR at different temperatures (except sensor elements) are plotted.	46
2.18	Measured error of the GMR sensor alone (theoretical), and with DCR (simulation) is plotted.	46

3.1	Circuit diagram of the proposed relaxation-oscillator-based digitizer, RDR.	50
3.2	Important node (v_{OA} and v_O) voltages of RDR and the control signal V_{CON} is shown here.	51
3.3	Circuit diagram of the proposed relaxation-oscillator-based digitizer (i. e., RDR*).	53
3.4	Circuit diagram of relaxation oscillator-based digitizer for resistive sensors with wide-span (RDR _w).	56
3.5	Node (v_1 and v_2) voltage waveforms of RDR _w .	56
3.6	Internal structure of the PGA that could be used along with RDR _w . This circuit is suited for the triple operation of RDR _w ($N_R = 3$). It could be suitably extended or reduced for $N_R \neq 3$.	60
3.7	Results obtained from simulation studies for RDR.	66
3.8	Results obtained from simulation studies for RDR*.	66
3.9	Simulation results showing the immunity of the proposed schemes to power-supply drifts.	67
3.10	Linear transfer characteristics of RDR obtained on emulation studies.	67
3.11	Emulation results of RDR*. Measured e_{NL} is also plotted.	68
3.12	Screenshot of the waveforms at important nodes of RDR. These waveforms are closely matched with the expected nature (see Fig. 3.2).	69
3.13	Oscilloscope waveforms at important nodes of RDR*. Waveforms are matched with the expected results and shows relaxation oscillator behavior.	69
3.14	Results obtained from characterization of AA005 GMR sensor IC.	70
3.15	Photograph of the developed RDR circuit being tested with a commercially available GMR sensor.	71
3.16	Output of RDR observed when interfaced with GMR sensors.	71
3.17	Output versus magnetic field characteristics of GMR-RDR* instrumentation system.	72

3.18	Sequence of steps followed by TLU to compute R_b in RDR _w .	73
3.19	Input-output characteristics of the developed RDR _w during hardware-based tests with SE-type sensor.	74
3.20	Cardinal waveforms observed at different nodes of the proposed RDR _w are presented here. The waveforms in (a) and (b) are captured respectively, in region-1 and region-2 of RDR _w operation.	75
3.21	Test results obtained on interfacing RDR _w with DS-type. e_{NL} of RDR _w on interfacing with DS is also plotted.	76
3.22	Experimental results of the developed RDR _w when it is interfaced with the RTD-Pt 1000 temperature sensor. The inherent e_{NL} of the sensor is also plotted here.	76
4.1	Circuit diagram of the digitizer (DRR-1) for remote resistive sensors.	85
4.2	Important waveforms of DRR-1. Control signals, V_{CON1} and V_{CON2} are also depicted.	86
4.3	Circuit schematic of the Digitizer for Remote Resistive sensors (DRR-2).	88
4.4	Typical waveforms at the nodes v_1 and v_2 of DRR-2. Control signal, V_s is also depicted.	88
4.5	Proposed DRR-3 circuit for bridge-connected resistive sensors	90
4.6	Typical waveforms at the nodes v_I and v_C and the control signal, v_{C1} of DRR-3.	91
4.7	Comparison study between the DRR-1 and DRR-2. Relative error is computed with respect to the ideal condition (i. e., $\Delta V_\gamma = 0$ or $\Delta R_w = 0$, as the case may be).	94
4.8	Simulation results of input-output characteristics of DRR-1. Measured e_{NL} is also plotted.	97
4.9	Simulation plot showing the effect of wire-resistance on RDR, RDR*, and the compensated DRR-1.	97
4.10	Transfer characteristic of DRR-1 using emulation studies.	98

4.11	Effect of wire-resistance on RDR, RDR*, and the compensated DRR-1 are shown here while interfacing with emulated RTD-Pt1000 temperature sensor.	98
4.12	Linear transfer characteristics obtained using simulation of DRR-2 with a remotely-located SE sensor.	100
4.13	Simulation test results depicted the immunity of the DRR-2 on the effect of the wire resistances.	101
4.14	Linear transfer characteristics obtained when a hardware prototype of DRR-2 is tested with a remotely-located SE sensor.	102
4.15	Emulation test results depicted the immunity of the DRR-2 on the effect of the wire resistances.	102
4.16	Transfer characteristics and e_{NL} of DRR-2 + RTD system (remote case, $R_w = 100 \Omega$). Measured e_{NL} in remote and non-remote cases is also plotted.	103
4.17	Simulation results of interfacing RTD and GMR sensor with DRR-3. Measured e_{NL} is also plotted.	104
4.18	Simulation results of DRR-3 with AMR sensor characteristics. Measured e_{NL} at each step of x is shown and the maximum e_{NL} is 0.03 %.	105
4.19	Simulation study of effect of the wire impedance on the performance of DRR-3. Wire resistances were varied from 0 to 100 Ω and the maximum e_{REL} is 0.03 %.	105
4.20	Emulation results of interfacing RTD and GMR sensor with DRR-3.	106
4.21	Experimental tests of DRR-3 with AMR sensor characteristics.	107
4.22	Effect of the wire impedance on the performance of DRR-3.	107
4.23	Experimental setup of DRR-3 + GMR system with oscillogram in inset.	108
4.24	Experimental interface results of DRR-3 with the AA004 GMR sensor.	108

5.1	Proposed digitizing interface (DIR-SE) for remotely connected three wire single element resistive sensor.	114
5.2	Various node voltages (v_O and v_X) and control signal (v_{C1}) waveforms of DIR-SE.	115
5.3	Circuit diagram of the proposed digitizing interface (DIR-DS) for three wire remote differential sensor.	117
5.4	Digitizing interface (DIR-B) for bridge-type resistive sensors.	119
5.5	Emulation results of the proposed DIR-SE with RTD-Pt100 sensor and RTD-Pt1000 sensor-based SE sensors.	122
5.6	Results depict the low dependence of wire resistances on the performance of DIR circuits.	124
5.7	Emulation results of the proposed DIR-DS with two types of commercial differential sensors.	125
5.8	Results of the proposed DIR-B are plotted when interfaced with magneto-resistance-based bridge sensors.	126
5.9	Photograph of the experimental setup used for RTD sensor interface with DIR-SE.	127
5.10	Experimental results of the developed DIR-SE with RTD-Pt100 sensor.	127
5.11	Oscilloscope waveforms of RTD + DIR-SE circuit at $\theta = 55^\circ\text{C}$. Here T_C is fixed as 5 ms and the x-axis is 5ms/division.	128
5.12	Photograph of the experimental setup used for RTD sensor with DIR-DS.	128
5.13	Experimental results of the developed DIR-DS with displacement sensor.	129
5.14	Photograph of the experimental setup used for the interface of GMR sensor with DIR-B.	129
5.15	Experimental results of the developed DIR-B with GMR sensor.	130
5.16	Comparison results of the simulation and emulation studies for SE, DS, and bridge-type sensors.	131

6.1	Circuit diagram of the proposed DFRC for parallel RC sensor.	137
6.2	Expected voltage waveforms (v_c and v_x) of the DFRC is shown in (a). Control signals, v_{c1} , v_{c2} , and v_{c3} are shown in (b) for the measurement of R_x and C_x of the RC sensor (H and L indicates the High and Low level of control signals).	137
6.3	Parasitic capacitances of DFRC are modeled and shown here. The parasitics of S_1 are represented as C_{1S} , C_{1D} , C_{1DS} . Similarly, the switches S_2 and S_3 have parasitics of C_{2S} , C_{2D} , C_{2DS} , and C_{3S} , C_{3D} , C_{3DS} , respectively. Method of active shielding is also illustrated.	141
6.4	Relationship between measured resistance and the sensor resistance of the DFRC when $C_x = 200$ pF. The measured nonlinearity and relative error at each step of the sensor resistance are also plotted.	144
6.5	Simulation results depicting the immunity against the variation in the capacitance, C_x during the measurement of R_x ($= 100$ k Ω).	144
6.6	Simulation results of the DFRC in capacitance measurement mode ($R_x = 100$ k Ω). Measured e_{NL} and e_{REL} are also plotted.	145
6.7	Simulation results of DFRC, when R_x is varied from 100 k Ω to 300 k Ω and C_x is kept as 200 pF.	145
6.8	Developed experimental setup for the resistance and capacitance measurement using DFRC circuit (C_x - mode). Note: Photograph was taken at $R_x = 100$ k Ω and $C_x = 100$ pF.	147
6.9	Experimental results of the DFRC (R_x - mode) are plotted.	147
6.10	Oscilloscope waveforms of the DFRC when the sensor resistance is 100 k Ω . Zoomed view of an important portion is also clearly shown at the bottom of the image.	148
6.11	Experimental results of DFRC (R_x - mode), when C_x is varied from 0 to 200 pF. Here R_x is kept as 100 k Ω .	148
6.12	Results of the DFRC used for the capacitance measurement.	150

6.13	Oscilloscope waveforms are observed from the important nodes of DFRC.	150
6.14	Effect of changes in sensor resistance during the capacitance measurement of 200 pF ($= C_x$), observed on DFRC experimentation.	150
7.1	A graphical summary of the proposed Th-LDM and its technical features.	155
7.2	Detailed schematic of Th-LDM for thermistor (R_X) linked with connecting wires (modeled as R_{w1} , R_{w2} , and R_{w3}).	157
7.3	Important node voltage (v_{INT} and v_{COM}) waveforms of Th-LDM. Control signals, v_{CON1} and v_{CON2} , are also depicted.	157
7.4	Reduced model of Th-LDM for non-remote temperature measurement using thermistors.	160
7.5	(a) Variation of e_{NL} of Th-LDM with respect to the number of linearization terms (say, n) and number of calibration points (say, P). It can be seen that higher value of n ($= 3$) gives good output linearity, almost regardless of P . (b) Variation of e_{NL} in third-order polynomial equation with respect to P .	163
7.6	Emulation results of the Th-LDM. Graph indicates the relation between the applied resistance (1 k Ω to 100 k Ω) and measured output resistance. Measured e_{NL} and e_{REL} are also shown.	167
7.7	Comparison results between emulation, simulation, and theoretical results are depicted.	167
7.8	Results showing the negligible influence of the wire impedances on the Th-LDM.	168
7.9	Plot of 400 repeated measurements of Th-LDM taken when $R_X = 10$ k Ω .	169
7.10	Experimental results of Th-LDM when tested with synthesized characteristics of T-1. Linearized transfer characteristics of Th-LDM can be observed, with maximum e_{NL} less than 0.44 %.	171

7.11	Experimental results of Th-LDM tested with characteristics of T-2. Linearized transfer characteristics of Th-LDM can be observed, with maximum e_{NL} less than 0.4 %.	172
7.12	Simulation and emulation results using T-2. Temperature is varied in sub-degrees from 0 to 4 °C and 101 °C to 105 °C.	172
7.13	Experimental setup used for evaluating Th-LDM hardware prototype with commercial sensors. Top view of the calibration-tank, incorporated with thermistor and reference sensor, is shown as inset.	173
7.14	Performance evaluation of Th-LDM with commercial sensor (T-1). Five input-output characteristics points obtained from calibration are plotted in a dashed line. Linearized transfer characteristics (bold line) of the Th-LDM are also plotted, along with experimentally obtained e_{NL} values.	174
7.15	Performance evaluation of Th-LDM with commercial sensor, T-2. Thermistor characteristics and linearized transfer characteristics (bold line) of the Th-LDM are also plotted, along with experimentally obtained e_{NL} values.	175
7.16	Oscilloscope waveforms were observed during simulation and experimental studies at three different θ (\approx 40 °C, 60 °C, and 80 °C). (a), (b), and (c) denotes the simulation graphs while (d), (e), and (f) depicts the experimental graphs.	176

List of Tables

1.1	Some of the Resistive Sensors and Their Industrial Applications	2
1.2	Some of the Resistive Sensors and Their Specifications	4
1.3	GMR Sensors and Their Properties	9
1.4	Wide Range Resistive Sensors and Their Specifications	13
2.1	Results obtained from Simulation and Emulation Studies	37
3.1	Details and Results of Simulation and Emulation Studies of RDRw	74
3.2	Estimated Values of Statistical Performance Parameters	77
3.3	Comparison Study of Proposed Techniques with Existing Interface Circuits	78
4.1	Literature Map of Various Digitization Schemes for Remote Resistance Measurements	82
4.2	Modes of Operation of DRR-1	86
4.3	Adaptable Bridge Configurations of DRR-3	92
4.4	Details and Results of Simulation and Emulation Studies of DRR-2	100
4.5	Estimated Values of Statistical Performance Parameters	104
4.6	Comparison Study between Developed DRR Circuits	110
5.1	Switch Positions Based on the Different Modes of DIR-SE	116
5.2	Switch Positions Based on the Different Modes of DIR-B	119
5.3	Results of the Static Parameters Estimation	131
6.1	Literature Map and Comparison Study Between the Existing Readouts for Impedance Sensors with DFRC	134

6.2	Results of the Estimation of Performance Parameters	151
7.1	Literature-Map of Linearized Thermistor-based Measurement System and Comparison Study	154
7.2	Switch Positions During the Th-LDM Operation	159
7.3	Precision Related Parameters	170
7.4	Linearization Constants values Associated with Th-LDM Interfaces with Different Thermistors	171
B.1	Output and Error Characteristics of DCR Circuit when Tested with a Differential Resistive Sensor	203
B.2	Dataset Reflecting Experimental Results of RDRw Circuit	204
B.3	Experimental Results of DRR-3 when Interfaced with GMR Sensor	205
B.4	Output Characteristics Obtained on Testing DIR with a SE-Type Sensor	206
B.5	Output Datasets Related to DFRC Circuit (Capacitance Mode)	207
B.6	Measurement Results of Th-LDM System	208

Abbreviations

ADC	Analog-to-Digital Converter
AMR	Anisotropic Magneto-Resistive
CTU	Control and Timing Unit
DCR	Digitizing Circuit for Resistive sensors
DFRC	Digital Front-end for parallel RC sensors
DIR	Digitizing Interface Resistive sensors
DM	Direct Microcontroller
DRR	Digitizer for Remote Resistive sensors
DS	Differential Sensor
ENOB	Effective Number Of Bits
FB	Full Bridge
GMR	Giant Magneto-Resistance
IDS	Inverse Differential Sensor
IFB	Inverse Full Bridge
HB	Half Bridge
LDR	Light Dependent Resistor
MR	Magneto-Resistance
MSOP	Mini Small-Outline Package
PGA	Programmable Gain Amplifier
PWC	Pulse Width Conversion
QB	Quarter Bridge
RDR	Relaxation oscillator-based Digitizer for Resistive sensors
RDR _w	Relaxation oscillator-based Digitizer for Resistive sensors with Wide-span
RO	Relaxation Oscillator
RTD	Resistance Temperature Detector
SE	Single Element

SHHE	SteinHart and Hart Equation
SNR	Signal-to-Noise Ratio
SOIC	Small-Outline Integrated Circuit
SPST	Single Pole Single Throw
SPDT	Single Pole Double Throw
TCE	Thermally Conductive Enclosure
Th-LDM	Thermistor Linearizing Digital Measurement system
TLU	Timing and Logic Unit
VLSI	Very Large Scale Integration

Nomenclature

x	Fractional resistance change
e_{FSE}	Full-scale error
θ	Temperature
e_{NL}	Nonlinearity error
e_{REL}	Relative error
$\lceil \rceil$	Ceil function
B_{EXT}	External magnetic field
σ	Standard deviation
R_E	Repeatability error
e_{TWO}	Error in two-wire scheme
e_{THR}	Error in three-wire scheme
T_{ON}	ON time duration
T_{OFF}	OFF time duration
T_{cmax}	Maximum conversion time
N_R	Number of regions
R_{eq}	Equivalent resistance
μC	Microcontroller
α	Temperature coefficient of resistance
β	Characteristic temperature of the material
R_0	Nominal resistance
I_B	Bias current
V_{OS}	Offset voltage
R_{SW}	Switch resistance
R_W	Wire resistance
R_X	Sensor resistance

Chapter 1

Introduction

1.1. Measurements and Sensors

Measurements play a key role in day-to-day life ranging from simple measurement of human temperature using a thermometer to aircraft attitude estimation in aerospace applications [1], and thermal-/vibration-induced strains [2] in the automotive sector. Measurements are important in various industries such as pharmaceutical, power, automotive, maritime/oil, aerospace, chemical, and other process industries [3]. For the smooth functioning of the above industries, different physical variables such as temperature, force, liquid level, magnetic field, displacement, strain, acceleration, velocity, pressure, flow, etc. need to be measured. Technically, measurement is defined as the numerical estimation of the properties of an object or event, which can be used to compare with other objects or events [3]. The importance of precision measurement can be evidenced by the famous quote of Lord Kelvin ‘*There is nothing new to be discovered in physics now. All that remains is more and more precise measurement*’.

Sensors serve as the foundation block for modern measurement systems. A sensor measures and converts the physical quantity to an equivalent electrical signal [4], [5]. A good sensor should have adequate values for parameters such as linearity, sensitivity, resolution, and power consumption. Sensors can be broadly classified, according to their output type (e. g., resistive, inductive, capacitive, voltage, and current). Among these sensor models, resistive sensors are preferred for many of the above-discussed applications, due to their simplicity of construction, durability, good dynamic range, and low cost. Efficient interface electronic circuits are required to process these sensors and condition their outputs. Such interface circuits should comply with modern industry demands, including digital instrumentation, and address a variety of measurement challenges present in industrial scenarios.

In this thesis, new and efficient digitizing interface circuits for resistive sensors are proffered and evaluated for performance. The proposed digitizers are designed to cater to a number of industrial measurement scenarios involving resistive sensors. These scenarios include remote and wide-span measurements, linearization of nonlinear response, compensation and detection of secondary sensing elements, etc. Furthermore, the proposed digitizers are designed to be suited for all resistive sensor configurations and hence, can be interfaced with a wide gamut of resistive sensors, ranging from a standard Resistance Temperature Detector (RTD) to modern Magneto-

Table 1.1

Some of the Resistive Sensors and Their Industrial Applications

Sensors	Applications		
	Aerospace industry	Automotive industry	Biomedical industry
RTD	Air conditioning/management, flight control [14]	Temperature measurement of engine, intake air, etc. [15]	Breathing analysis and monitoring [16]
Potentiometric sensor	Used for fuel and engine control in unmanned aerial vehicle [17]	Used in clutch master cylinders [18]	pH sensing [19]
Strain gauge	Aircraft load-bearing structure [20]	Used in wheel force measurement system [21]	Physiotherapy equipment, kidney dialysis machines [22]
Thermistor	Temperature measurement of magnetometers [23]	Temperature measurement of coolant, intake air, cylinder head, etc. [24]	Temperature measurement in anesthesia apparatus, infusion pumps [25]
GMR	In-orbit magnetic field measurement [26]	Estimation of wheel speed, position [27]	Biomedical signal acquisition, magneto-plethysmograph [28], [29]
AMR	Magnetic-based attitude control system [26]	Speed, vehicle detection, position, etc. [30]	Biomedical diagnosis, environmental monitoring [31]

RTD – Resistance Temperature Detector, GMR – Giant Magneto-Resistance, AMR – Anisotropic Magneto-Resistive

Resistance (MR)-based transducers. The next section of the thesis discusses resistive sensors and their typical applications.

1.2. Resistive Sensors and Their Applications

As mentioned in the previous section, resistive sensors have many merits over inductive and capacitive counterparts. Various types of resistive sensors are routinely used for the measurement of temperature, pressure, force, displacement, and magnetic field [2], [4]-[10] in automobile, aerospace, chemical, and other process industries. For instance, RTDs are used in fryer basket applications, grill and griddle cooking units, and commercial ovens. Similarly, the advancement of sensor technology has tended to the development of state-of-the-art resistive sensors [e. g., Giant Magneto-Resistance (GMR) sensor]. GMR sensor is now used for vehicle speed sensing, non-destructive material testing, and biomedical signal acquisition [11]-[13].

A brief account of applications of some of the important resistive sensors is tabulated in Table 1.1. These sensors are used in various industries and some of the industrial applications are given in Table 1.1. Strain gauge sensors are used to find the structure of load-bearing in an aircraft [20]. These sensors are used in kidney dialysis instruments and syringe pumps to monitor fluid flow rates [22]. Likewise, Anisotropic Magneto-Resistive (AMR) sensors have been used in the aerospace sector to find the attitude of satellites [26]. In addition, AMR sensors are useful to find speed, position, vehicle detection, food safety, and environmental monitoring [30], [31]. The usage of other sensors in various industries can be inferred from Table 1.1. Resistive sensors employed in these vast ranges of applications differ in many aspects, such as measurand being sensed, configuration being used, etc. The next section discusses the classifications and common examples of resistive sensors.

1.3. Classifications of Resistive Sensors

Resistive sensors can be classified according to physical quantities such as temperature, displacement, strain, magnetic field, etc. [4]. Resistive sensors can also

Table 1.2
Some of the Resistive Sensors and Their Specifications

Physical quantity	Sensor	Typical model	Available configuration	Nature of output	Nominal resistance (Ω)	Typical range	Cost (\approx \$)
Temperature	RTD	HSRTD-3-100-A-40-E [32]	SE	Linear	100	120 Ω	74
Disp.	Potentiometer	LT-150 [33]	DS		5000	2 k Ω	134
Strain/stress	Strain gauge	MMF402183 [34]	SE, FB		350	$\pm 1.5^*$	30
Temperature	Thermistor	NTCM-100K-B3950 [35]	SE	Nonlinear	100 k	101 k Ω	0.5
Luminous intensity	LDR	NORP12RS 651-507 [36]			-	9 k Ω	2
Magnetic field	GMR	AA004 [37]			HB	5 k	500 Ω
Gas concentration	Gas sensor	MICS-VZ-89TE [38]	RC model	Linear	-	1600 ppm	12.5

Note: Features and price mentioned correspond to the given models. Disp. – Displacement, SE – Single Element, DS – Differential Sensor, FB – Full-Bridge, HB – Half-Bridge, * – Represented in %.

be categorized based on their configurations. The specifications and details of some of the important resistance-based sensors are tabulated and given in Table 1.2. For instance, a potentiometric sensor (e. g., LT-150) can be used to measure the displacement [33]. This sensor is configured as a Differential Sensor (DS) and provides a linear output with respect to the measurand. Similarly, the AA004 GMR sensor [37] has a half-bridge configuration with a nominal resistance of 5 k Ω . A detailed description of these typical sensors is explained in the upcoming subsections.

1.3.1. Common Resistive Sensors

1.3.1.1. Resistance temperature detector (RTD)

An RTD is a temperature sensor which works based on the variation in electrical resistance. The common metal for this sensor is Platinum. Fig. 1.1(a) shows a commercial platinum-based RTD sensor [39]. Generally, RTD sensors have a positive temperature coefficient. As temperature increases, atoms in metal will vibrate more and collide with free electrons. Thus, the path length of the electron motion increases, which results in increased resistance. The resistance of the RTD sensor (say, R_{RTD}) can be written as $R_{RTD} = R_0 [1 + \alpha_1 (T - T_0) + \alpha_2 (T - T_0)^2 + \dots + \alpha_n (T - T_0)^n]$ with the temperature, T . Here, R_0 is the resistance at the nominal temperature (T_0), and $\alpha_1, \alpha_2, \dots, \alpha_n$ are the temperature coefficients of resistance. The above expression can be approximated, in its linear region [4], as given in (1.1).

$$R_{RTD} = R_0 [1 + \alpha_1 (T - T_0)] \quad (1.1)$$

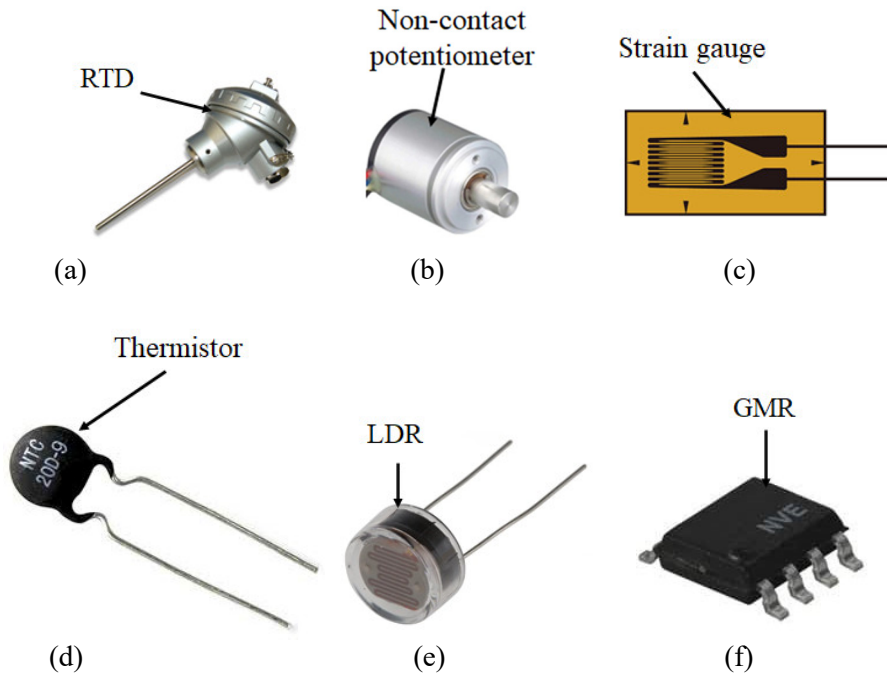


Fig. 1.1. Photograph of common resistive sensors. (a) RTD [39], (b) non-contact potentiometer [40], (c) strain gauge [41], (d) thermistor [42], (e) LDR [43], and (f) GMR [37].



Fig. 1.2. Expected requirement of autonomous vehicles globally, from 2021 to 2030 [44].

Temperature measurement using RTD has some challenges involved, such as minimizing the effects of self-heating as well as connecting leads. The self-heating errors can be reduced using preset current excitation to the sensor. Likewise, the wire effects can be minimized using multi-wire configurations of the RTD sensor.

As discussed in the previous section, the RTD sensor is used in the automotive sector to measure the temperature of the intake air, oil, gas, etc. (see Table 1.1). The requirement of autonomous vehicles in the automotive industry will be expected to be high in the upcoming years. This can be inferred from Fig. 1.2 [44]. Therefore, we can infer that the usage of RTD will also follow an increasing trend in the coming years.

1.3.1.2. Potentiometric sensor

The potentiometric principle can be used as a (linear or rotary) displacement sensor. This sensor basically consists of fixed resistance winding and sliding contact, which is connected to the target. The resistances (R_{P1} and R_{P2}) of the contact with respect to two ends of the windings can be written as in (1.2), where k depends on resistivity and cross-section of the windings and y is the displacement.

$$R_{P1} = ky; R_{P2} = k(1 - y) \quad (1.2)$$

In conventional potentiometers, wear and tear effects can occur. In addition, errors can be introduced in the output due to the jitter present in the contact resistance.

To overcome these problems, non-contact potentiometric sensors [see Fig. 1.1(b)] are introduced in recent years [45]. Noncontact sensors are used in automobiles, robotics, and manufacturing plants [46]-[48]. Electronic interfaces for these types of potentiometric sensors are also required.

1.3.1.3. Strain gauge

A strain gauge is a transducer whose resistance varies with input force. It converts measurements such as pressure, tension, and weight to a change in electrical resistance. Strain gauges are classified as semiconductor and metallic, based on the material used. Semiconductor strain gauges work based on the piezoresistive effect in semiconductors (e. g., silicon and germanium) to obtain greater sensitivity and a high degree of output. In metallic strain gauges, the change in resistance is small. Hence, an efficient interface circuit is needed to measure this small change in resistance. The photograph of a strain gauge is given in Fig. 1.1(c) [41]. The variation in resistance of the strain gauge (say, ΔR) can be found using (1.3), where R_0 is the nominal resistance, ΔL is the change in length, L is the actual length, and GF is the gauge factor.

$$\Delta R = R_0 \times GF \times (\Delta L / L) \quad (1.3)$$

These strain gauge sensors can be configured in the form of bridge circuits. More details of various bridge configurations will be discussed in Section 1.3.2.

1.3.1.4. Thermistors

Thermistors can be termed temperature-sensitive resistors. The resistance of a Negative Temperature Coefficient (NTC) thermistor decreases with temperature. The input-output characteristics of the thermistor are given in Fig. 1.3. Thermistors with Positive Temperature Coefficient (PTC) are also available. PTC thermistors are mostly used in switching applications, liquid level detection, stabilization, etc. [4]. A photograph of the NTC thermistor is shown in Fig. 1.1 (d) [42]. This sensor is fabricated using semiconductor material. NTC behavior is due to the increased

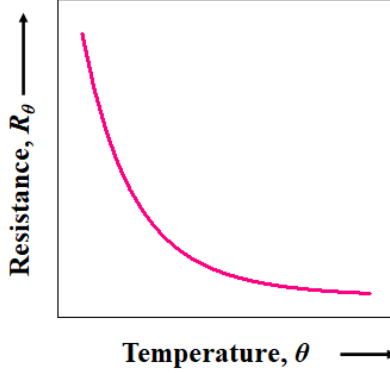


Fig. 1.3. Input-output relationship of thermistor.

transition of the valence band to the conduction band of the conductors with the increase in temperature.

From Fig. 1.3, it can be observed that the thermistors follow a nonlinear relationship with temperature. Many researchers have tried out to model the thermistor characteristics [4], [49]. One of the accurate expressions for the relationship between temperature and resistance of thermistor (say, R_{THERM}) is given in (1.4) where β is the characteristic temperature of the material [4].

$$R_{THERM} = R_0 e^{\beta(1/T - 1/T_0)} \quad (1.4)$$

Here R_0 is the thermistor resistance at room temperature, T_0 , and T is the temperature, and it is expressed in kelvins. Similarly, Steinhart and Hart equation (SHHE) can also be used to model the thermistor characteristics, given in (1.5) [49], [50].

$$\frac{1}{T} = A + B \ln(R_{THERM}) + C [\ln(R_{THERM})]^3 \quad (1.5)$$

Here, A , B , and C are the SHHE coefficients. It should be noted that the self-heating issues also cause an error in the output of a thermistor (as in RTDs). Based on the above discussions, it can be deduced that special linearizing circuits are needed for interfacing the thermistors and providing an accurate and linear indication of temperature.

1.3.1.5. Light-dependent resistors (LDR)

The LDR works based on the principle of photoconductivity. The photograph of LDR is given in Fig. 1.1(e) [43]. When the light falls on the LDR, the electrons in

the valence band of the material will try to move to the conduction band. However, this transition will be successful when the photons in the incident light must have energy superior to the bandgap of the material. These sensors are used in the automotive industry as automatic headlight dimmers and light control [51]. It is also used as a product separator [52]. However, the input-output characteristic of LDR decreases in a nonlinear fashion with light. Therefore, the LDR requires an interface circuit to linearize its output.

1.3.1.6. GMR sensor

GMR-based sensors are low-power-consuming magnetometers that have high sensitivity to magnetic fields. It can measure a wide range of constant as well as alternating magnetic fields [53]. GMR sensors are also available as gradiometers [37]. Some of the properties of commercial GMR sensors are given in Table 1.3 [37]. From Table 1.3, it can be observed that the GMR sensors are available in small-sized packages. The photograph of a commercial GMR IC is given in Fig. 1.1(f). The typical resistance (i. e., nominal resistance) of the sensor can also vary from one model to another. In addition, the sensitivity of the GMR sensor is also good. Thus, the GMR sensor is a good choice for the measurement of physical and electrical quantities (like displacement, angle, current, and speed) in many application fields [54], [55].

The internal structure of a GMR element is shown in Fig. 1.4. A GMR element consists of two ferromagnetic layers (marked as B, in Fig. 1.4) and a nonmagnetic layer (A). Layer A can be seen to be sandwiched between layer B. When no magnetic field is present, the magnetization direction of ferromagnetic layers is antiparallel. This

Table 1.3

GMR Sensors and Their Properties

GMR sensor part number	Linear range (mT)		Sensitivity (mV/V/mT)		Maximum nonlinearity (%)	Typical resistance (Ω)	Package
	Min.	Max.	Min.	Max.			
AA002-02	0.15	1.05	30	42	2	5 k	SOIC8
AA004-02	0.5	3.5	9	13	2	5 k	SOIC8
AA006-00	0.5	3.5	9	13	2	30 k	MSOP8
AAH004-00	0.15	0.75	32	48	4	2 k	MSOP8
Min. – Minimum, Max. – Maximum.							

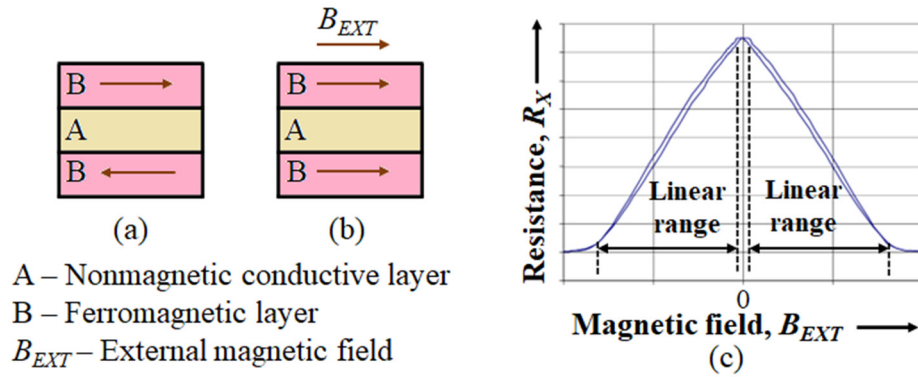


Fig. 1.4. Pictorial representation of GMR principle, (a) high resistance and (b) low resistance.

opposes the movement of electrons in the conduction layer, resulting in high resistance. The pictorial representation of this event is shown in Fig. 1.4(a). In the presence of an input magnetic field (B_{EXT}), the antiparallel configuration gets disturbed, leading to a decrease in the resistance [vide Fig. 1.4(b)] of the GMR elements. The decrease in GMR resistance is linear [see Fig. 1.4(c)] till the input field reaches a saturation value. Summarizing, GMR elements possess linear transfer relations in a range of magnetic fields. The equation for the resistance of the GMR element can be written as in (1.6) where K_G is the transformation constant of the GMR element.

$$R_{X1} = R_0(1 - K_G B_{EXT}) \quad (1.6)$$

The GMR sensors are packaged as a half-bridge model. More details about the bridge configurations will be in the next section.

It should be pointed out that few representative (classical as well as recent) examples were discussed till now. There are number of other resistive sensors such as hygrometers, humidity sensors, gas sensors, and liquid conductivity sensors that works based on the resistive principle. An in-depth explanation for these sensor types can be found in [4]. The resistive sensors are available in different electrical configurations. A concise discussion on the typical resistive sensor configuration is given next.

1.3.2. Configurations of Resistive Sensors

Resistive sensors are available in various configurations. A diagrammatic representation of different configurations is given in Fig. 1.5. Fig. 1.5(a) shows a Single Element (SE) configuration. Here, a resistive sensor (shown as R_X), available as a SE, will vary with respect to the measurand. Common examples for SE types of sensors include RTD, strain gauge, LDR, and thermistor. Some of the sensors [e. g., potentiometric-displacement sensor) can be modeled as in Fig. 1.5(b). In this case, the elements of the sensors will vary in a push-pull manner. As in Fig. 1.5(b), the sensor can be represented as two resistive elements (R_{X1} and R_{X2}), varying in a differential manner. This type of sensor is termed as DS. The electrical model of the DS is shown in Fig. 1.5(b). The equation for R_{X1} and R_{X2} can be written as in (1.7), where R_0 is the nominal resistance and x is the change in fractional resistance.

$$\begin{aligned} R_{X1} &= R_0(1+x) \\ R_{X2} &= R_0(1-x) \end{aligned} \quad (1.7)$$

Wheatstone bridge arrangement is very commonly used for resistive sensors. This arrangement can provide offset-free accurate output, with independence from

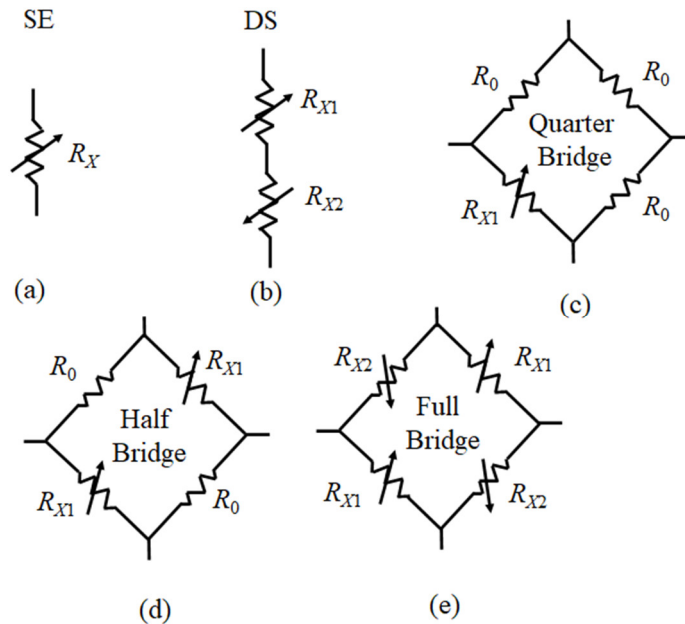


Fig. 1.5. Electrical equivalent model of (a) SE, (b) DS, (c) QB, (d) HB, and (e) FB is shown here.

some undesired parameters (e. g., environmental temperature, cross-axis sensing, etc.). The typical bridge arrangements are shown in Fig. 1.5(c) to (e). The Quarter Bridge (QB), in Fig. 1.5(c), consists of one resistive sensor element (e. g., RTD, strain gauge) and three discrete resistors. Half Bridges (HB) are used with two resistive elements (shown as R_{X1}) which are located in opposite arms, which will vary with respect to the input quantity and R_{X1} can be written as $R_0 (1 \pm x)$. At the same time, the other two elements (R_0) will be constant [refer Fig. 1.5(d)]. GMR sensor, discussed in Section 1.3.1.6, is a good example of an HB-type sensor.

The structure of a Full Bridge (FB) resistive sensor is shown in Fig. 1.5(e). Here, two elements [$R_{X1} = R_0 (1 + x)$] will increase with x . The other two elements will vary as $R_0 (1 - x)$. The properties of these configurations can vary from each other. For example, QB and HB types possess nonlinear output characteristics with respect to the measurand, while FB output has linear transfer characteristics. The parameters such as sensitivity, and range can also vary depending on the sensor elements used. It is very important to develop interfacing electronics that are suited for the above various resistive sensor configurations and address the related measurement problems.

1.4. Measurement Challenges Associated with Resistive Sensors

Several research challenges are associated with the measurement of resistive sensors. Some of the important challenges are explained next.

1.4.1. Digitizing Interfaces for Resistive Sensors

Resistive sensors require good-quality signal conditioners to perform operations such as linearization, amplification, compensation against nonidealities, etc. Digital instrumentation stages are preferred in modern systems. They offer many merits (such as high accuracy, less power consumption, high resolution, and greater noise margin [56]) over their analog counterparts. Therefore, it is also beneficial to design and develop direct-digitizing interfaces for the conditioning of resistive sensors. This

Table 1.4

Wide Range Resistive Sensors and Their Specifications

Sensor Model	Lower limit	Upper limit	Dynamic span (dB)
NTCM-100K-B3950 [35]	5.382 k Ω	3227 k Ω	55.56*
NTCLE413E2103H400A [57]	0.6 k Ω	335 k Ω	\approx 55*
TGS822 [58]	0.08 (R_s/R_0)	3	31.5 [#]
WO ₃ based gas sensor [59]	1 (R_{NO_2}/R_{air})	4.5	13.6
* - Temperature range of -40 °C to 105 °C, # - Acetone concentration of 50 ppm to 5000 ppm, R_s - Change in resistance, R_0 - Nominal resistance at 300 ppm, WO ₃ - Tri-Tungsten (VI) Oxide Complex, NO ₂ concentration of 0 to 250 ppb, R_{NO_2} - Resistance related to NO ₂ concentration and R_{air} - Resistance at air, Dynamic span (dB) = $20\log(\text{upper limit/lower limit})$.			

avoids the requirement of a separate Analog-to-Digital Converter (ADC) for each sensor and minimizes the error due to cascading of signal conditioning blocks in conventional instrumentation systems. Such digitizers should also be versatile and adaptable for all resistive sensor configurations.

1.4.2. Wide-range Resistive Sensors

Some of the resistive sensors have a wide operating span. Examples of such sensors include thermistors and gas sensors (e. g., metal-oxide gas sensors). The properties (upper measurement limit, lower limit, and dynamic range) of some of these sensors are tabulated and given in Table 1.4. This table clearly shows that the sensors can have considerable spans. Interfacing circuits capable of handling wide-range sensors will be useful in many applications.

1.4.3. Distantly connected Resistive Sensors

In some industrial scenarios, the remotely-available resistive sensors need to be connected to the measurement system using long connecting wires. For example, an RTD sensor can be placed in a thermal power plant. Electronics cannot be integrated in such locations. Hence, the RTD sensor is connected, using long wires to the electronic unit, which may be at a considerable distance from the plant. Improved two-wire, three-wire, and four-wire measurement techniques are commonly used with the above class of resistive sensors [4], [5], [60]-[65] for wire resistance compensation.

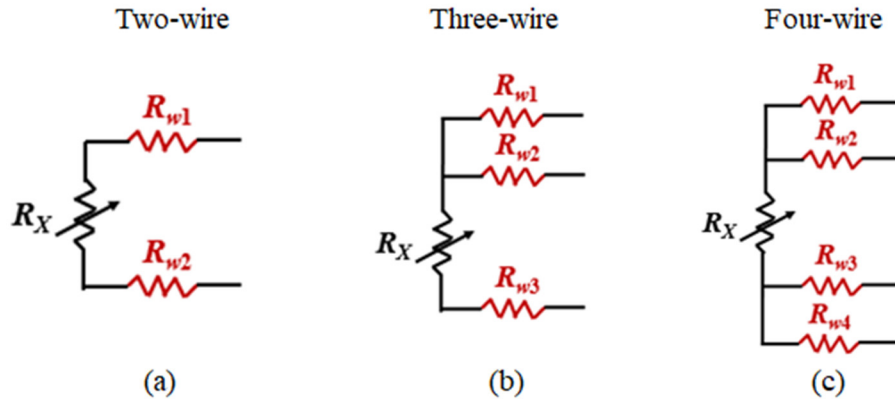


Fig. 1.6. Wiring infrastructure of resistive sensors. R_X denote the resistive sensor. (a) Two-wire, (b) Three-wire, and (c) Four-wire connection.

The digitizers, equipped with such compensation techniques, would be quite useful in practical applications. The basic compensation methods are presented next.

1.4.3.1. Two-wire scheme

In this scheme, two wires are used to interconnect the sensor and the electronics. The pictorial representation of this scheme is illustrated in Fig. 1.6(a). The resistances, R_{w1} and R_{w2} are the resistances of the connecting wires. This two-terminal resistive sensing is not suitable for distantly located sensors and low resistance measurements. In these cases, the wire resistances play a major role in the output. In addition, the wire resistances will vary with respect to the gauge length and temperature. Thus, the resistance of the connecting wires will get added to the sensor resistance (i. e., $R_X + R_{w1} + R_{w2}$), and lead to a considerable error in the output. Improved two-wire-based arrangements with lead-wire compensation are recently being reported [60]-[63], [65]. These schemes will be explained in Chapter 4.

1.4.3.2. Three-wire scheme

In three wire technique, the sensor resistance, R_X is connected to the measurement unit using three connecting wires [64], [65]. The wires are represented to have the resistances of R_{w1} , R_{w2} , and R_{w3} . The schematic representation of the connection is shown in Fig. 1.6(b). This scheme is used to nullify the error generated

in the two-wire technique [60]-[63], [65]. However, any mismatch in the wire resistances (R_{w1} , R_{w2} , and R_{w3}) can lead to an output error in SE and DS cases.

1.4.3.3. Four-wire technique

Four-wire-based sensing is another effective choice for distant sensors. The wiring infrastructure of the four-wire scheme is shown in Fig. 1.6(c). Here, the resistance of the connecting wires is represented using R_{w1} , R_{w2} , R_{w3} , and R_{w4} . This method can be used to nullify the effect of wire resistances as well as the mismatch in the wire resistances [114].

1.4.4. Presence of Secondary Sensing Element

Some of the real-world resistive sensors can have associated secondary elements. Such secondary elements may provide additional information about the measurand or could be parasitic in nature. This type of sensor is seen in industrial scenarios such as humidity sensing, air-quality monitoring, chemical sensing, and fruit quality estimation. In the above cases, the sensors can be modeled as a parallel network (as shown in Fig. 1.7) of a resistor and a capacitor [66]-[68]. In some cases, the resistance, R_x , and capacitance, C_x indicate the varying quantity with respect to the measurand. In other cases, the sensor resistance will vary with respect to the measurand, and the capacitor acts as a parasitic element. For example, titanium dioxide-based chemical sensors [68] show a resistive behavior (range: $\approx 1 \text{ k}\Omega$ to $100 \text{ M}\Omega$) coupled with a parasitic capacitance element. Latter can be the significant cross-sectional area of the chemical sensor needs to be increased, to improve the sensitivity and speed of response [69], [70]. On the other hand, lossy capacitive sensors can be affected by parasitic resistance [71], [72]. This type of sensor is used in the

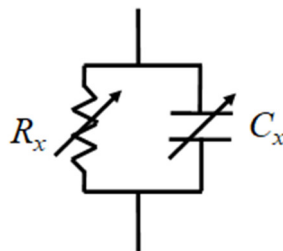


Fig. 1.7. Electrical equivalent model of RC impedance sensor.

measurement of proximity [73], humidity [74]-[76], and two-phase liquid concentration [77]. In addition, this parasitic resistance is not constant, and it varies with parameters such as temperature, pollution, and condensation [72]. Thus, it is essential to develop interface electronics that can measure both R_x and C_x of the RC impedance sensors.

1.4.5. Nonlinear Response

As discussed in Section 1.3, the sensors such as thermistors, LDRs, and GMR-bridges possess a nonlinear output. It is easy to calibrate and minimizes the uncertainty in the sensor output if the sensor output is more linear (i. e., low nonlinearity). Thus, the sensors which have nonlinear output in nature require special electronic circuitry to perform linearization.

1.5. Interface Circuits for Resistive Sensors

The previous sections discussed the importance, application, and types of resistive sensors and, further, pointed out some of the related measurement issues. It can be deduced that efficient electronic stages would be needed to address the different types of resistive sensors. Such interfaces should be capable of handling measurement scenarios given in Section 1.4. Several research works have been illustrated in the field of signal conditioning of resistive sensors. A brief account of the literature is reported in this section.

Analog interfaces for resistive sensors have been demonstrated in [4], [5], [78]. These interfaces are designed with some of specific features (such as good accuracy, linearization, and remote resistance measurement). Analog interface circuits require a dedicated ADC. In addition, these circuits possess an output-error due to the cascade stages of the interface circuit and an ADC. Direct-digital interfaces have been reported to resolve these issues. A number of digital techniques, like pulse-width conversion, dual-slope, direct microcontroller interfacing, sigma-delta, and relaxation-oscillator are prevalent for resistive sensors. Each of the above interfacing techniques

possesses some desirable features and a few significant issues. An account of the digital interfaces for resistive sensors is given below.

A dual resistance-to-frequency converter based on pulse-width conversion is proposed in [79]. Similarly, dual-slope-based circuits have been present in [59], [80]-[82], [84]-[87], [89] for various types of resistive sensors. In general, the dual-slope scheme requires bipolar reference voltage, and its output depends on the resistance of the switches. Simple microcontroller-based schemes are reported in [90]-[94]. This scheme is quite simpler than the Op-amp-based technique [59], [79]-[89]. However, this method has drawbacks of dependency on the microcontroller threshold voltages and higher conversion time. Similarly, sigma-delta and relaxation oscillator-based techniques are also illustrated for resistive sensors. Some of the schemes, discussed in [59], [79]-[109], are not suitable for a wide range of resistance measurements. It is mainly due to the factors, such as high conversion time (during the estimation of high resistance), gain and offset error of the direct microcontroller approach [90]-[94], and saturation-related effects in the Op-amp-based circuits [104], [105]. Techniques involved in [102], [110], and [111] use the relaxation oscillator method to measure a wide range of resistances. The schemes in [102], and [110] require a bipolar voltage source and high conversion time. Methodology to reduce the conversion time is also attended in [111]-[113]. However, the complexity of the circuit is high [111]. Most of the aforementioned schemes are designed for non-remote resistive sensors.

Interface circuits for remotely-connected resistive sensors are proposed in [60]-[65], [85], [86], [114], and [115]. These techniques can be classified as two-wire, three-wire, and more than three-wire. Basically, the two-wire technique [60]-[63] uses a dual-diode configuration in the sensor side. This dual-diode arrangement eliminates the effect of connecting wire resistance. However, this technique requires matched diodes. With the inclusion of one more connecting wire, the error present in the circuit can be reduced. This three-wire technique [64], [65] does not need dual-diode arrangements. Schemes employing more than three connecting wires are also present in [85], [86], [114], and [115]. All these techniques are mostly useful for SE and bridge-connected resistive sensors. It should be pointed out that an increase in the number of

connecting wires increases the cost and complexity of the system. The resistive sensor digitizers should be enhanced with adequate compensation techniques. Then, the overall solution will provide a direct indication of the measurand sensed in a remote location.

Many of the existing digitizers [78]-[115] consider the availability of purely resistive sensor elements. As discussed in Section 1.4.4, some sensors can be modeled as a parallel resistor-capacitor (RC) network. Interface circuits for RC impedance sensors are discussed in [71], [72], [88], [116]-[122]. These RC sensors can be placed either floating [71], [72], [88] or grounded model [123], [124]. Some of the interface circuits are suitable only for the measurement of either resistance or capacitance [120]-[122]. The need for the measurement of resistance and capacitance is essential in some applications [117], [119], and [124]. In such cases, the interface circuit is needed to measure both resistance and capacitance as well.

Linearization of the non-linear behavior of sensors has also been attempted in some research works. For example, linearization of the thermistor's output is attempted in [50], [87], [125]-[132]. Here, these schemes are works based on the techniques which use an astable multivibrator, field programmable gate array, artificial neural network, and Op-amp-based model [87], [131], and [132]. Many of these techniques require a large number of thermistor data points to linearize their output. In addition, some of the techniques discussed in [50], [87], [125]-[132] are useful only for a short range of temperature measurements. Further, these schemes have higher nonlinearity errors in the output. Some of the circuits need a complex architecture for the linearization operation and are not suitable for remote-located thermistors.

These digitizers can be designed using discrete components and used with different commercial sensors. Such enhanced digitizing architectures can also be miniaturized for realizing an ultra-compact instrumentation system using Very Large-Scale Integration (VLSI) technology [133].

1.6. Motivation

As brought forth in previous sections, there are a number of research challenges related to the measurement of resistive sensors. The properties and configuration of sensors are also different. Some of the resistive sensors have special requirements, such as minimization of self-heating errors and other circuit nonidealities. Though several digitizing interfaces have been reported for resistive sensors, significant issues are still present. For example, one of the most common digitizing techniques (dual-slope) provides a linear and accurate indication of the sensing variable. However, most of the dual-slope implementations are based on voltage-excitation for sensors. Excitation of sensors using a preset current is helpful to reduce self-heating errors. In addition, the circuit output is dependent on nonideal parameters, including switch resistances. This call for the design and development of constant-current excitation-based dual-slope architecture which is robust against circuit nonidealities. Such a circuit will be quite beneficial for many sensors, including RTD.

The literature survey (Section 1.5) revealed the possibility of employing a relaxation oscillator-based technique, as a simple and effective method for conditioning resistive sensors. However, the inherent problems (e. g., dependency on the power supply and capacitor drifts) of this technique need to be nullified. It would be useful if accurate relaxation oscillator interfaces can be developed for resistive sensors. As discussed in Section 1.4.2, industrial resistive sensors can have a wide operational span. Therefore, simple digitizing interfaces capable of handling such sensors need to be investigated and proposed. These interfaces should comply with typical demands such as low conversion time, simplicity of architecture, etc.

The widespread presence of remotely-connected sensors has been pointed out in Section 1.4.3. There have been various researches, reporting compensation techniques for wire resistance, observed in the above scenario. Most of the reported circuits are analog in nature. Digital implementations of wire-resistance compensations for resistive sensors are either complex or need many connecting leads or high error due to other circuit nonidealities, etc. Keeping this in mind, it will be good if digitizers

are proposed in this thesis. Thesis can be extended and enabled with adequate wire compensation techniques while ensuring a reduced number of connecting leads and universal interfacing nature.

The technique of direct microcontroller-based interfacing has been briefly discussed in Section 1.5. The inherent method of charging and discharging of a capacitor, through different resistive sensor paths, has scopes for improvement, in terms of increased precision, lead resistance compensation, etc. Improved microcontroller-based digitizer interfacing devoid of the above issues would be quite useful for the research and industrial community.

It is also equally important to cater to some of the other measurement challenges related to resistive sensors. For example, an interface circuit capable of simultaneous and mutually-independent measurement of resistance and capacitance of an impedance sensor has a significant number of applications. Similarly, some of the sensors (e. g., thermistors) exhibit nonlinear behaviour. Linearizing digital interfaces for such sensors will lead to the development of much-sought linear instrumentation systems. However, care should be taken to design a simple interface that minimizes the calibration requirements of the sensor and connecting lead effects.

The thesis presents innovative and improved digitizing interfacing solutions for the aforementioned sensor requirements. These circuits are based on the new and enhanced version of principles, such as dual-slope, relaxation oscillator, and direct microcontroller. Each implementation addresses one or more of the measurement challenges discussed and provides a linear direct-digital indication of the measurand.

1.7. Objectives and Scope

This thesis addresses the problems by focussing on the following objectives and scope:

- (1) Design and development of digitizers suitable for various types of resistive sensors with linear output using single/no reference voltage. These circuits are targeted to have the features of simple architecture, high accuracy, low-cost

design, etc.

- (2) Design and development of wide-span digitizing interface circuits for processing various types of resistive sensors. The desirable features of these circuits are simplicity in design, low conversion time, usage of a single reference voltage, low error due to circuit nonidealities, etc.
- (3) Design and performance evaluation of digitizing interface circuit for remotely connected resistive sensors, considering the requirements of wide-span, universal interfacing nature, negligible effect due to the imbalance in wire resistance, and mismatch in sensor elements.
- (4) Design, analysis, and implementation of simplified microcontroller-based digitizing interface circuit for various types of remotely connected resistive sensors with wide span and minimal dependence due to the microcontroller threshold voltages and pin resistances.
- (5) Design and development of digitizing interface circuits for a special type of resistive sensors. This objective considers the estimation of a common type of impedance sensor and the linearization of nonlinear sensors. The expected features of these circuits are a mutually independent measurement of sensing elements, low error due to circuit nonidealities, simple architecture, low conversion time, limited calibration requirements, etc.

1.8. Organization of the Thesis

This thesis is organized as follows.

Chapter 1: This chapter introduces the importance of measurement and resistive sensors. It presents the details of some of the important resistive sensors and their applications. Further, this chapter discusses the measurement challenges associated with resistive sensors and a literature survey of the existing interface circuits for resistive sensors.

Chapter 2: This chapter focuses on the design and implementation of the enhanced dual-slope-based digitizing interface circuit for various types of resistive sensors. The methodology and the error analysis of the circuit are detailed in this chapter. Elaborate performance studies of the developed circuit are also reported in this chapter.

Chapter 3: This chapter details an alternate method, based on the relaxation oscillator principle, for resistive sensors. Further, this chapter discusses the methodology to reduce the conversion time for wide-range sensors. Extensive error analysis, performance verifications, and comparison of the proposed techniques with the prior art are given in this chapter.

Chapter 4: This chapter discusses the design and implementation of the interface circuits for remotely-connected resistive sensors. First, the chapter discusses the digitizer using a dual-diode approach for SE-type. Then, a digitizer equipped with a three-wire technique for SE and DS is discussed. Later, a dual-slope-based universal interface for remote resistive bridges is proposed. The efficacy analysis and tests of these schemes are also given in this chapter.

Chapter 5: This chapter brings forth simple charge-discharge-based digitizing circuits for remote resistive sensors. The adaptability of the circuit towards SE, DS, and bridge configurations is detailed and their positive features are also verified and reported in this chapter.

Chapter 6: This chapter discusses an enhanced charge-discharge scheme to measure both the resistance and the capacitance associated with an RC impedance sensor. In addition, a calibration method to nullify the effects of offset capacitance is also derived and reported. The performance studies and related discussions form the final part of this chapter.

Chapter 7: This chapter focuses on the design and development of a novel linearized measurement system for thermistors. The methodology of the measurement system is established and further verified using a number of tests, in this chapter.

Chapter 8: This chapter summarizes the major conclusions derived from this thesis. In addition, this chapter discusses the future scope of research related to this thesis.

Chapter 2

Dual-slope-based Digitizing Circuit for a Broad Class of Current Excited Resistive Sensors

2.1. Introduction

In this chapter, an efficient direct digitizer for resistive sensors is proposed. This would prevent the need of separate ADC for each sensor, and also reduce the errors in the instrumentation system and processing requirements. The digitizer is based on an improved dual-slope-based principle, which is specifically suited for current-excited resistive sensors. A discussion about prior art is given first in this chapter, followed by an elaborate description of the circuit methodology and its efficacy analysis.

2.2. Detailed Discussion on Digitizing Interface for Resistive Sensors

As mentioned in Section 1.5, a number of digitizing interfaces have been developed for resistive sensors. Most of these interfaces are based on techniques such as resistance-to-frequency conversion, dual-slope method, direct microcontroller, relaxation oscillator technique, etc. An elaborate discussion of the prior art on these interfaces is given here.

Resistance-to-frequency/time converters are reported in [79], [98], [102]-[105], [110], [134]. A digitizer employing a dual resistance-to-frequency converter has been proposed for resistive sensors [79]. This scheme, though complex, works well for a wide range of sensor resistances. Similar resistance to pulse-width conversion

This chapter is partially adapted from the post-print version of Elangovan K, S. Dutta, A. Antony, and Anoop C. S., "Performance Verification of a Digital Interface Suitable for a Broad Class of Resistive Sensors," in *IEEE Sensors Journal*, vol. 20, no. 23, pp. 13901-13909, 1 Dec.1, 2020.

approach has been reported in [98]. Work in [98] generates an output pulse-width dependent on sensor resistance. This high-resolution output is created using complex architecture comprising operational transconductance amplifiers. The relaxation-oscillator technique offers a simple interfacing solution for resistive sensors [102]-[105]. These works convert the sensor resistance into measurable time or frequency, linearly. Many of these solutions do not require reference voltages [103]-[105]. However, the output-quantity (time or frequency) of the schemes can depend on many non-ideal parameters such as capacitor drift, power supply variations, etc. A special relaxation-oscillator circuit that uses matched reference voltages and renders immunity to many circuit non-idealities has been discussed in [102]. The circuit proposed in [143] also works based on the relaxation oscillator principle. This circuit uses a new calibration stage (and hence, needs a higher execution time) to give a precision output, devoid of the effect of capacitor drift and power supply variations. The scheme developed in [102], [110] is useful for a wide range of resistance measurements but requires (matched) bipolar-reference voltages and a calibration mechanism to nullify the effect of the switch resistances. In addition, these schemes require a long conversion time to measure high-resistances.

Dual-slope-based digitizing circuits inherently have the ability to minimize the effect of interferences as the integration time is well selected. These types of interfaces are proposed for capacitive angle sensors and resistive sensors in [56], [80]-[82], [84]-[87], [89]. Among these schemes, dual-slope-based interfaces for SE, DS, HB, and FB resistive sensors are described in [56], [80]-[82], [84]-[87], [89]. Such dual-slope digitizers have also been reported for other sensor types like capacitive angle sensors [83]. Each of these works [80]-[82], [84]-[86] is tested for a particular configuration only. Moreover, the current through the resistive sensors is not a preset-value, which is desired for some of the SE sensors [99], [100]. In fact, the current needs to be preset to specific values (ranging from μA to $\approx 30 \text{ mA}$) depending on the sensor application [100]. In addition, the dual-slope scheme requires precision (matched) reference voltages.

Alternately, the direct sensor to microcontroller interfaces for resistive sensors has been illustrated in [90]-[94], [135], [136]. The scheme in [90] is affected by the pin-resistance of the microcontroller employed. A scheme with compensation for pin-resistances has been reported in [91]. This scheme, however, assumes that the resistances of the different pins are equal. The nonlinearity of this scheme [90] is higher, especially for MR-based sensors. A similar approach proposed in [93], [94] is suitable, especially, for SE-type sensors. Though this method is simple, it may require additional charging cycles to compensate the effects of pin-resistances of the microcontroller and switch-resistances and hence higher conversion time is needed. Also, the direct microcontroller approach assumes that the pin resistances and threshold voltages of the microcontroller are the same over a cycle of its operation. A simple resistance-interfacing method using a suitable digital device (e. g., microcontroller, field-programmable gate array) can be inferred from [135] and [136]. An enhanced version of [135] and [136] has been developed for capacitively-coupled resistive sensors and reported in [106]. These works [106], [135], [136] require more than two conversion cycles, and the pin resistance and mismatch in the threshold voltage of the digital devices can lead to an output error. The conversion time can be reduced by using an approximation method in [112] or a modified discharge process in [113]. Latter is done using an optimally selected small-valued calibration resistor. Similarly, the conversion time can be lowered using a moving-threshold algorithm [111] in relaxation-oscillator-based interfaces. However, the nonlinearity error becomes high ($\approx 4\%$) in [111].

There are some other techniques are also proposed for resistive sensors. A high-resolution digitizer using sigma-delta architecture [101] needs a complex circuit. Dual-mode adaptive principle has been employed in [137] to measure low-and high-valued resistances with low power consumption. The high-resistance ($> 300\text{ k}\Omega$) measurement employs a resistance-to-digital converter, and the low-resistance ($< 300\text{ k}\Omega$) is done using an adaptive current source [137]. Another circuit that can measure the resistance, as well as the power associated with a sensor, is illustrated in [107]. The thermal conductivity of resistive carbon dioxide sensors was measured in

[108]. The improved range and accuracy can be obtained using a self-balancing digitizer for Wheatstone bridges [109]. An interface circuit useful for high-resistance measurement is illustrated in [138]. The principle of pulse width modulation has been employed in [139] for low-resistance determination.

Based on the above discussions, it can be concluded that the existing digital interfaces possess significant issues such as circuit complexity, the need for reference voltage, long conversion time, dependence on power-supply and capacitor drifts, and other non-idealities. This chapter proposes a novel dual-slope-based digitizing interface that can overcome the demerits of the above schemes. This circuit can interface with various types of resistive sensor configurations and provide constant-current excitation.

2.3. Digitizing Circuit for Resistive Sensors

The circuit schematic of the proposed Digitizing Circuit for Resistive sensors (DCR) is shown in Fig. 2.1. The circuit consists of an auxiliary section, made of Op-amp A_1 and the resistive-sensor elements and a dual-slope section. Latter is realized using a switch S_W , an integrator A_2 , a comparator A_3 , and a Timing and Logic Unit (TLU). This DCR architecture is an improved version of the dual-slope-based works presented in [80]-[82] and [84]. The novel design of the DCR ensures many positive features over the existing dual-slope-based and other schemes, as listed below.

1. Ability to interface resistive sensors to a dual-slope architecture using just one reference voltage source.
2. Preset-excitation current facility, which helps to control the self-heating errors for SE sensors (like, RTD).
3. The on-resistance of the switch does not affect the present scheme, which allows the use of low-cost switch ICs.
4. Negligible/low effect of other non-ideal parameters, like bias current, offset voltage, and independence from sensor-resistance mismatches (in the case of bridge-connected sensors).

5. Non-requirement of costly Instrumentation Amplifier (IA) and multiple switches.
6. Renders good performance with different types of resistive sensors (like, GMR, RTD) present in different configurations and/or operating ranges.

The working of this circuit with the aforementioned features is explained next.

2.3.1. Working of DCR

The sensor in Fig. 2.1 (highlighted in blue) can represent various types of resistive-sensor configurations. Let us assume, for the time being, that a SE sensor is present. In the case of SE resistance topology, R_X represents the sensor element and R_S is a standard resistance. The necessary adaptations required for other sensor topologies will be discussed in Section 2.3.2. In other sensor configurations (like DS, QB, HB), R_X and R_S stand for the elements of the respective topologies. The Op-amp A_1 provides the following purposes – (i) enabling of the circuit operation using a single reference voltage, (ii) the ability to excite the sensor, R_X (in case of SE sensor) with a constant current, and (iii) capability for high-current excitation of the SE sensor, R_X , using low-cost Op-amps. A detailed explanation of these studies will be given in the sequel.

The operation of the DCR is controlled by the switch S_W and the TLU using a control signal, V_C . The DCR operates in two modes. The first mode is an integration mode of duration T_1 . The second mode is a de-integration mode of duration T_2 . During T_1 , the control signal V_C is set to ‘0 (LOW)’ to ensure that the switch S_W is at position-1. Then, the output of A_1 (say, V_{A1}) gets fed as the input to the integrator. The equation

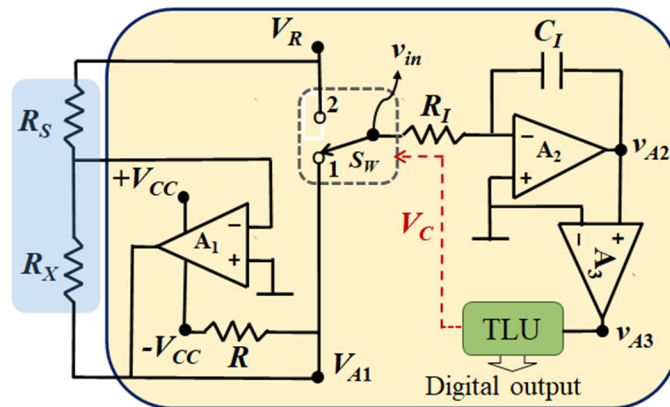


Fig. 2.1. Proposed circuit diagram of the DCR, based on an improved dual-slope technique.

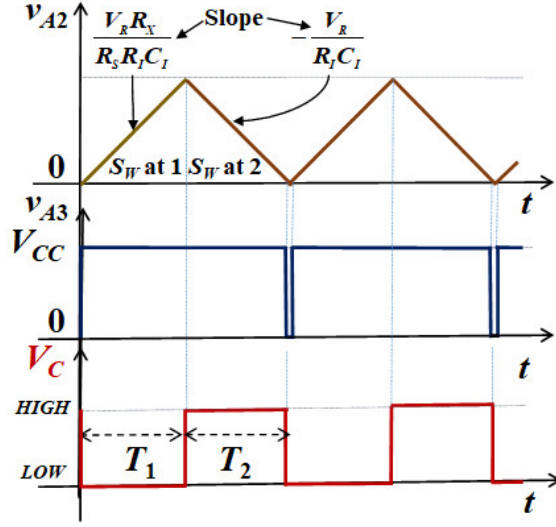


Fig. 2.2. Output waveforms, observed at the nodes v_{A2} and v_{A3} are figured here. The control signal V_C given by TLU is also plotted.

of V_{A1} can be derived and obtained as $V_{A1} = -(R_X / R_S) \times V_R$, where V_R is the reference voltage. As a result, the integrator-output (v_{A2}) charges linearly as shown in Fig. 2.2. The expression for v_{A2} is given in (2.1).

$$v_{A2}(t) = \frac{-V_{A1}}{R_I C_I} t = \left(\frac{V_R}{R_S R_I C_I} \right) \times R_X \times t \quad (2.1)$$

This charging process continues during the first mode, till a preset time of T_1 seconds. In other words,

$$v_{A2}(T_1) = \left(\frac{V_R}{R_S R_I C_I} \right) \times R_X \times T_1 \quad (2.2)$$

The switch location is now shifted to position-2 by setting $V_C = \text{logic-high}$ (see Fig. 2.2). Now the voltage V_R gets linked to A_2 . As a result, the integrator output, v_{A2} ramps down towards zero and follows (2.3).

$$v_{A2}(t) = v_{A2}(T_1) - \frac{V_R}{R_I C_I} (t - T_1) \quad (2.3)$$

The comparator A_3 detects the zero-crossings of v_{A2} . The TLU stops the de-integration mode when a zero-crossing is detected. Thus, v_{A2} follows a triangular-shaped waveform as shown in Fig. 2.2. In other words, $v_{A2}(T_1 + T_2)$ should be equal to 0. Applying this condition to (2.3) and simplifying, we get (2.4).

$$\frac{T_2}{T_1} = \frac{R_X}{R_S} \quad (2.4)$$

Equation (2.4) clearly evidences that a linear estimate of R_X can be obtained by the measurement of time T_2 . The resistance R_X can be found by using $R_X = R_S(T_2 / T_1)$. The fractional resistance change of R_X can also be found using (2.5) if R_X equals $R_0(1 + x)$.

$$x = \frac{T_2 R_S - T_1 R_0}{T_1 R_0} \quad (2.5)$$

By choosing R_S equal to the nominal-resistance of R_X (i. e., R_0), (2.5) simplifies to,

$$x = \frac{T_2 - T_1}{T_1} \quad (2.6)$$

Thus, x can be found using (2.6). The present approach not only requires a single positive reference-voltage V_R but also provides independence from V_R and the drift of passives, R_I and C_I of the integrator. The cycle explained above can be repeated (see Fig. 2.2) for continuous resistance-to-digital conversion.

It should be noted that the current flowing through the sensor in SE configuration is equal to V_R / R_S . Therefore, the presented digitizer has the facility for exciting the sensor with a preset current. In addition, it can be seen from Fig. 2.1 that a resistance, R is connected between the node V_{A1} and the negative power supply ($-V_{CC}$) of A_1 . This allows the majority of the excitation current to flow into $-V_{CC}$ (through R) and thus bypass the Op-amp-output. This helps to avoid the use of expensive and high-current-rated Op-amps to realize A_1 . The value of R can be derived using the expression of the excitation current ($= V_R / R_S$) as in (2.7).

$$\frac{V_R}{R_S} = \frac{V_{A1} + V_{CC}}{R} = \frac{-V_R (R_X / R_S) + V_{CC}}{R} \quad (2.7)$$

Simplifying (2.7), the value of R can be obtained as (2.8).

$$R = \frac{(V_{CC} R_S - V_R R_X)}{V_R} \quad (2.8)$$

The nominal value of R_X can be used in (2.8) to find R . This resistance will ensure zero Op-amp output current when $R_X = R_0$ and reduced Op-amp output current at other values of $R_X (\neq R_0)$.

2.3.2. Adaptation to different sensor types

The operation of DCR was explained by considering a SE resistive sensor in the previous section. The proposed circuit can be easily extended to interface various types of sensor resistances and render a direct-digital indication of the fractional resistance change.

2.3.2.1. QB sensor configuration

As seen from Fig. 1.5(c), one of the bridge elements can vary with respect to the measurand. Let us consider that the varying element is replaced by R_X of DCR and the fixed element of the same arm as R_S . Thus, the fractional resistance change of QB sensor configuration can be found using (2.6). Here the variable resistance of QB is equal to $R_0 (1 + x)$.

2.3.2.2. DS interfacing

In the case of DS interfacing [see Fig. 1.5(b)], both R_X and R_S will vary in a push-pull manner. In other words, $R_X = R_0 (1 + x)$ and $R_S = R_0 (1 - x)$. For such a case, the value of x can be calculated using (2.9).

$$x = \frac{T_2 - T_1}{T_2 + T_1} \quad (2.9)$$

2.3.2.3. Inverse-resistive sensor interfacing

Some of the DS possess inverse characteristics [101] (i. e., IDS). Then, $R_X = R_0 / (1+x)$ and $R_S = R_0 / (1-x)$. The measured x can be found for these types of sensors using (2.10).

$$x = \frac{T_1 - T_2}{T_1 + T_2} \quad (2.10)$$

From equations (2.6), (2.9), and (2.10), it can be concluded that the fractional change in resistance (x) can be calculated for various types of sensors by measuring time duration. The TLU measures the time duration T_2 and then computes x using the

relevant equation. The next section discusses the various non-ideal parameters and their effects on the DCR output.

2.4. Error Analysis of DCR

The components and Op-amps used to realize DCR can have their inherent error sources. The effect of these error sources is analyzed in this section. The various important error sources are modeled and represented in Fig. 2.3.

2.4.1. Errors due to Op-amp A₁

The main static error sources of A₁ are the bias-current and offset-voltage (say, V_{OS1}). Let the input current flowing to the inverting terminal of A₁ be I_{N1} . Then the output voltage of A₁ gets modified to V_{A1}' . The equation of V_{A1}' is given in (2.11).

$$V_{A1}' = V_{OS1} \left(\frac{R_X + R_S}{R_S} \right) - V_R \left(\frac{R_X}{R_S} \right) + I_{N1} R_X \quad (2.11)$$

This change in voltage alters the T_2/T_1 ratio as $(T_2/T_1)^a$, which is given in (2.12).

$$\left(\frac{T_2}{T_1} \right)^a = \frac{R_X}{R_S} - I_{N1} \frac{R_X}{V_R} - \frac{V_{OS1}}{V_R} \left(\frac{R_X + R_S}{R_S} \right) \quad (2.12)$$

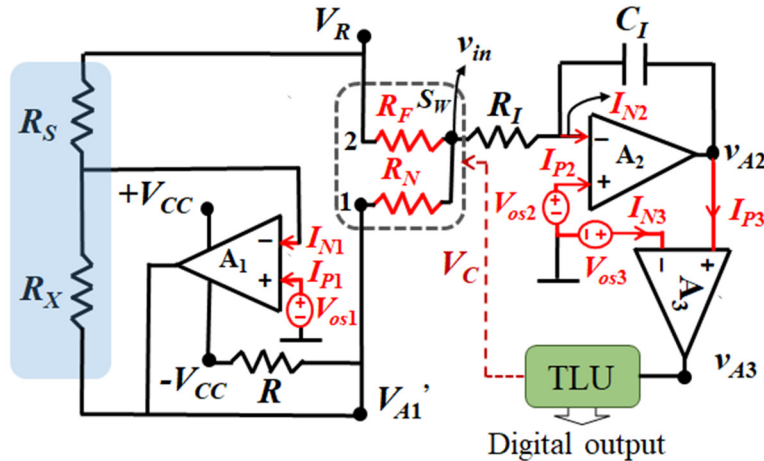


Fig. 2.3. Error sources of the proposed DCR are added to Fig. 2.1 and presented here, whenever the switch is located at position-1. I_P and I_N represents the bias currents of the Op-amps and V_{OS} is the offset voltage. Resistances, R_N and R_F are the on and off-resistance of the switch, S_W .

The expression given in (2.12) is valid for all types of sensor configurations. The maximum percentage Full-Scale error (e_{FSE}) can be calculated using $[(T_2 / T_1)^a - (T_2 / T_1)] / FSS \times 100 \%$, where FSS refers to the Full-Scale Span. This expression is also given in Appendix A. It shows that the maximum e_{FSE} is 0.01 % among the SE, DS, and HB configurations when A_1 is realized using OP07 IC.

2.4.2. Errors due to Op-amp A_2

The static non-idealities (i. e., I_{N2} , V_{OS2}) of Op-amp A_2 change the output voltage of the integrator. The modified equation for $v_{A2}'(T_1)$ and $v_{A2}'(T_1 + T_2)$ is given in (2.13).

$$\begin{aligned} v_{A2}'(T_1) &= \left(\frac{V_R R_X + V_{OS2} R_S + I_{N2} R_S R_I}{R_S R_I C_I} \right) T_1 \\ v_{A2}'(T_1 + T_2) &= v_{A2}'(T_1) - \left(\frac{V_R - V_{OS2} - I_{N2} R_I}{R_I C_I} \right) T_2 = 0 \end{aligned} \quad (2.13)$$

Using the charge balance condition, the modified value $(T_2/T_1)^b$ of T_2/T_1 becomes as (2.14).

$$\left(\frac{T_2}{T_1} \right)^b \approx \left(\frac{T_2}{T_1} \right) + \frac{V_{OS2} + I_{N2} R_I}{V_R} \quad (2.14)$$

The resulting error amounts to 0.01 % while using OP07 IC for A_2 .

2.4.3. Errors due to Op-amp A_3

The static non-idealities of Op-amp A_3 do not affect the output (T_2 / T_1) of the proposed DCR. The offset voltage of Op-amp A_3 gives the DC offset to the voltage of v_{A2} . However, the ratio, T_2/T_1 is independent of this DC offset. Hence, the offset voltage of A_3 does not cause any error in the output. The delay of the LM311 comparator (A_3) is in the range of nanoseconds (ns). This small delay has a negligible effect on the output. The noise voltages present at the input of the comparator can slightly alter the time instance of the *HIGH* to *LOW* transition, which signals the end of the de-integration period T_2 . Let us assume that E_{n1} and E_{n2} , respectively, stand for the amplitude of noise voltages at the start and end of a cycle of operation. Then, $v_{A2}(T_1)$

will get altered by $\pm E_{n1}$. Likewise, the *HIGH* to *LOW* transition of v_{A3} will occur when $v_{A2}(T_1+T_2)$ crosses $\pm E_{n2}$. The modified T_2/T_1 can be expressed as in (2.15).

$$\left(\frac{T_2}{T_1}\right)^c = \frac{R_X}{R_S} + \frac{\Delta E_n R_I C_I}{V_R T_1} \quad (2.15)$$

Here, the worst-case values of ΔE_n equal $\pm (E_{n1} + E_{n2})$. The resulting error was found to be negligible for typical noise voltages present in the circuit prototype developed.

2.4.4. Errors due to Switch Resistance

Let R_N and R_F be the on and off-resistance of the switch, S_W . The non-ideal nature of the switch may cause an error in the output and the positions of R_N and R_F during T_1 are illustrated in Fig. 2.3. Their locations will interchange during T_2 . These additional resistances change the T_2/T_1 ratio to (2.16).

$$\left(\frac{T_2}{T_1}\right)^d = \frac{(R_I + R_N)R_S - (R_I + R_F)R_X}{(R_I + R_N)R_X - (R_I + R_F)R_S} \quad (2.16)$$

This alteration in ratio gives a maximum e_{FSE} of 0.003 % among SE, DS, and HB configurations when CD4053 IC acts as S_W .

The delay of the switch is very less (in ns) compared to the typical values of T_1 and T_2 . Hence, the delay of the switch will have a negligible effect.

2.4.5. Errors due to the Environmental Temperature (θ)

A change in the temperature can affect (1) the parameters (I_P , I_N , V_{OS} , etc.) of the Op-amps and (2) the sensor elements. The temperature dependence, in case of a sensor, depends on the sensor type as well as its configuration (SE, HB, and DS). Detailed simulation and experimental studies were carried out to study the temperature dependence of the proposed technique. These studies will be elaborated in Section 2.8.

2.5. Simulation Studies of DCR

Initial verification of the proposed DCR was done by simulation, using LTspice software. The Op-amps A_1 and A_2 were modeled to have the specifications of

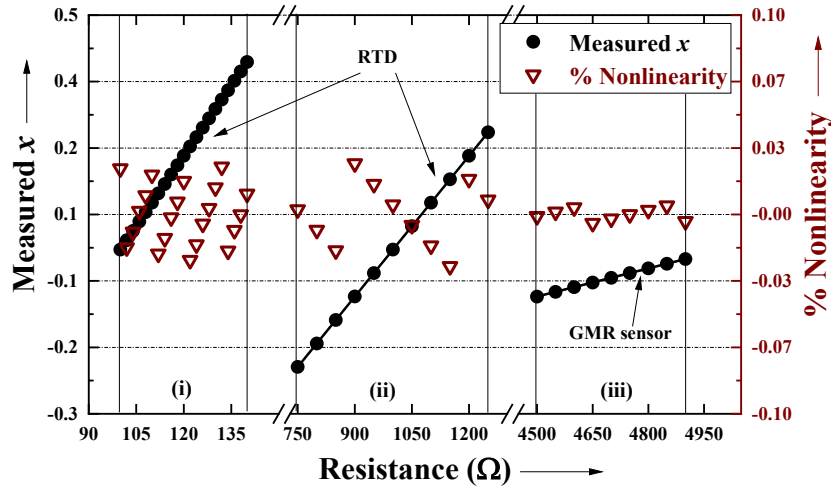


Fig. 2.4. Simulation results of the proposed DCR is shown here for SE/HB sensor interface, ((i) RTD-Pt100, (ii) RTD-Pt1000, and (iii) GMR-AA004).

the OP07 IC, and A_3 was configured by using LM311 IC specifications. The open-collector resistance required for this IC was chosen as 1 k Ω . This resistance could be increased to reduce the power consumed by this IC, at the cost of its higher output transition times. The resistor R_I and capacitor C_I were chosen as 100 k Ω and 100 nF, respectively. The preset-time T_1 was fixed as 5 ms. The switch, S_W was configured to have the CD4053 IC characteristics. The reference voltage V_R was chosen to have LM385-2.5 IC specifications, and the power supplies for Op-amps were chosen as

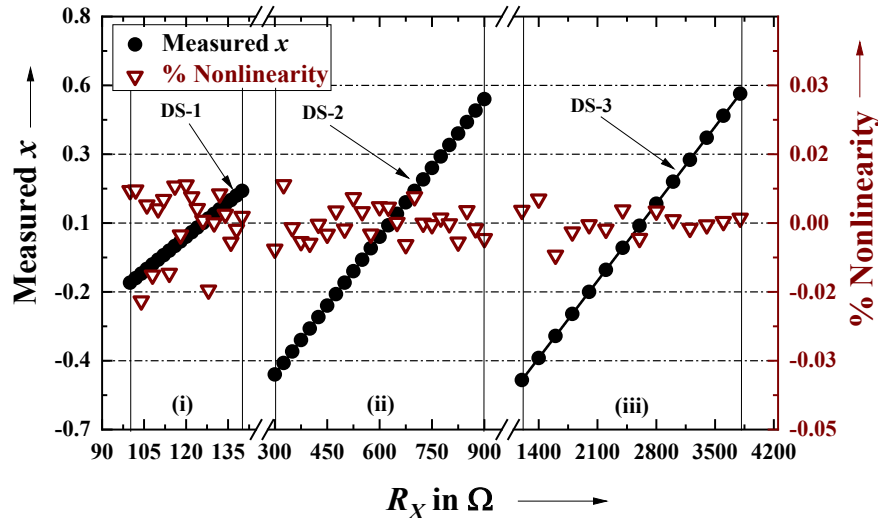


Fig. 2.5. Simulation results of the proposed DCR with DS, ((i) DS-1 (Potentiometric sensor – P11S [141]), (ii) DS-2 [101], (iii) DS-3 (Rectilinear displacement transducer-LT-150 [33])).

Table 2.1

Results obtained from Simulation and Emulation Studies

Sensor	Resistance range (k Ω)	Sensor model	e_{NL}^*		Value of R (Ω)	Step size (Ω)	Resolution in m Ω
			S*	E*			
SE & HB	0.1 - 0.14	Δ	0.02	0.04	260	2	1
	0.75 - 1.25	\diamond	0.03	0.03	---	50	1
	4.5 - 5	\blacklozenge	0.01	0.06	---	50	60
DS	0.1 - 0.14	∇	0.02	0.04	260	2	1
	0.3 - 0.9	\square	0.01	0.02	300	25	6
	1.2 - 3.8	\clubsuit	0.01	0.01	---	200	30

S - Simulation, E - Emulation, Δ - RTD-Pt100, \diamond - RTD-Pt1000, \blacklozenge - GMR-AA004, ∇ - Potentiometric sensor-P11S, \square - Sensor used in [101], \clubsuit - Rectilinear displacement transducer-LT-150

± 10 V. A monostable-multivibrator was designed using 555 timer IC (TLU) to produce the control signal, V_C .

The simulation was done for different types of sensor configurations (like SE, DS, and HB). Initially, the low resistance measurement was done by using RTD-Pt100 [140] characteristics in which R_X was varied from 100 Ω to 140 Ω and R_S was kept at 100 Ω . This was done to show the interfacing capability of DCR with the SE sensor model. The resistor R was connected and chosen as 260 Ω [to satisfy (2.8)] for this case. Next, the resistance, R_X was varied from 750 Ω to 1250 Ω , and R_S was kept at 1000 Ω to study the RTD-Pt1000 characteristics. The resistor R was not needed for these high resistance measurements. Finally, for the study of HB-type sensors, the R_X was varied from 4.5 k Ω to 5 k Ω to model the characteristics of the GMR sensor [37]. This case used R_S as 5 k Ω . All of the above-discussed cases were simulated, and the results obtained from the above simulation studies are plotted and shown in Fig. 2.4. The graphs show that the output of DCR follows a linear relation with the change in sensor resistance, R_X . The percentage nonlinearity error (say, e_{NL}) was found by using the following relation: $e_{NL} = [x - (S \times x^* + I)] / \text{FSS} \times 100\%$ (also given in Appendix A). Here, x^* denotes the actual resistance, and S and I represent the slope and intercept of the best fit line of x^* with respect to x . It shows that the maximum e_{NL} is 0.03 %.

Similarly, the differential sensor characteristics were simulated for three different cases. Initially, it was done with $100\ \Omega$ to $140\ \Omega$ [141] with $R = 260\ \Omega$. Later, the study was conducted for $300\ \Omega$ to $900\ \Omega$ [101] (with $R = 300\ \Omega$) and finally, for $1.2\ \text{k}\Omega$ to $3.8\ \text{k}\Omega$ [33]. All the cases were simulated, and the corresponding graphs were plotted between measured x and input resistance (R_X). This is shown in Fig. 2.5. The relation between the input and output quantities is linear. The measured e_{NL} is also present in Fig. 2.5, and the observed maximum e_{NL} for all cases is tabulated in Table 2.1. The worst-case e_{NL} is $0.02\ \%$. The step size of resistance and the resolution of all cases are also present in Table 2.1. From Table 2.1, it can be inferred that the proposed DCR shows low nonlinearity and high resolution.

2.6. Emulation Studies

The DCR was further verified using emulation studies. The components selected for emulation were similar to the components used in the simulation. The passive components were tolerant to $1\ \%$. The time-related measurements (i. e., estimation of T_1 and T_2) were performed with the help of the ATSAM3X8E microcontroller [142] present in the Arduino-Due microcontroller board. One of the timer/counter modules of the microcontroller was configured for the above purpose.

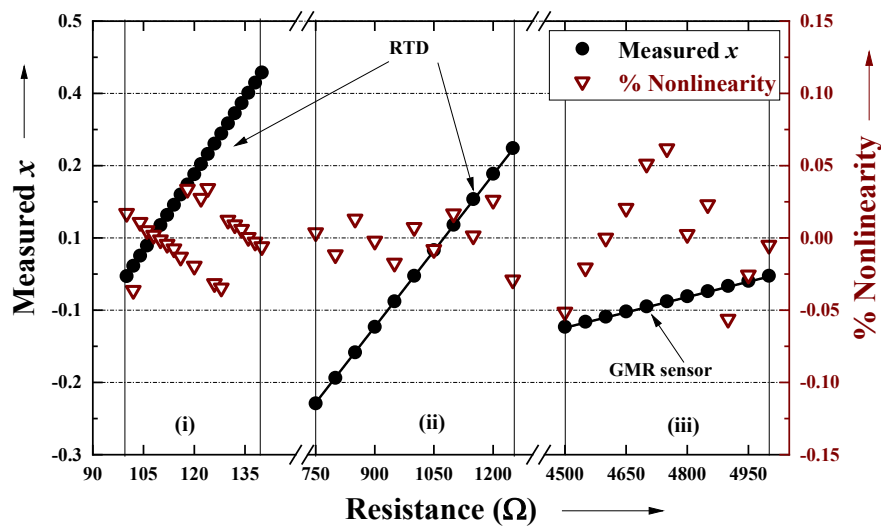


Fig. 2.6. Emulation results of the proposed DCR with SE/HB sensor, ((i) RTD-Pt100, (ii) RTD-Pt1000, and (iii) GMR-AA004).

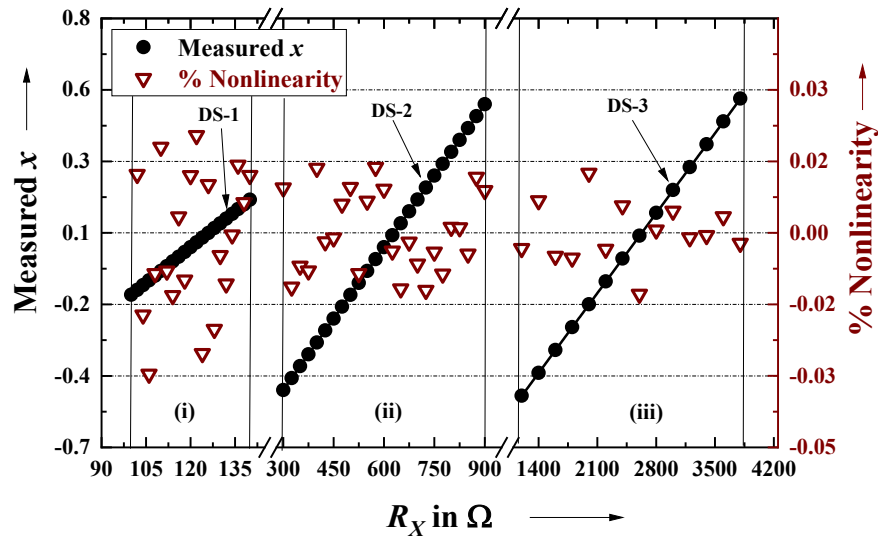


Fig. 2.7. Emulation results of the proposed DCR is shown here for DS interface, ((i) DS-1 (Potentiometric sensor – P11S [141]), (ii) DS-2 [101], (iii) DS-3 (Rectilinear displacement transducer-LT-150 [33])).

The timer/counter module has the following specifications: timer/counter-0, 32-bit timer/counter, 656.25 kHz clock frequency with approximately 1.5 μ s resolution. The logic signal, V_C was also generated using the digital input-output pin of the same microcontroller. The precision and resolution were improved by averaging 50 samples and rounding the output samples to 5 digits after the decimal place.

Initially, the SE and HB-type sensors were interfaced. The circuit was seen to exhibit dual-slope behavior [80]-[82]. The measured ‘ x ’ was seen to obey a linear pattern with x . This can be seen in Fig. 2.6. The observed e_{NL} values are also plotted in

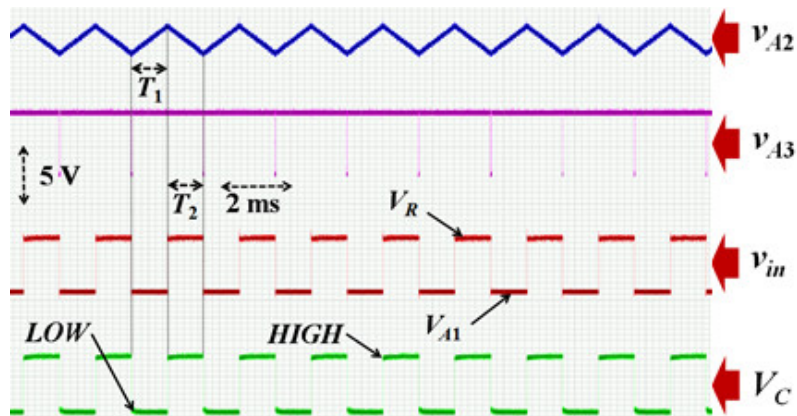


Fig. 2.8. Screenshot of waveforms observed using oscilloscope at different nodes of DCR at R_X and $R_S = 5 \text{ k}\Omega$.

the same graph (right Y-axis). The maximum value of e_{NL} observed from SE and HB models is 0.06 %. These results as well as corresponding resolutions are tabulated in Table 2.1. Similarly, the interface results of DS are plotted in Fig. 2.7. The maximum e_{NL} and resolution values for DS-DCR interfacing are given in Table 2.1. The oscilloscope waveforms observed at different nodes (v_{in} , v_{A2} , v_{A3} , and control signal V_C) are shown in Fig. 2.8. These waveforms were similar to that of Fig. 2.2. The power consumed by the developed circuit was computed and found to be around 30 mW. All electronic components, except for the microcontroller, were considered for the above computation. This was because the microcontroller was just used to mimic the TLU for the prototype developed. This board has many components/sections which are not needed for the operation of the TLU. In addition, the power consumption of 30 mW is also comparable with existing interfaces for resistive sensors [90]-[93], [143]-[145]. For microcontroller-based prototypes, techniques like clock frequency reduction, lowering of supply voltage, optimization, etc. [142] could also be employed for power reduction.

2.7. Performance Verification with Actual Sensors

The emulation tests, reported in Section 2.6, revealed the specifications (e. g., e_{NL} , resolution) of the DCR. Now, the DCR is interfaced and tested with actual sensors to clearly evidence its real-time performance and study the interfacing issues of the sensor + DCR systems.

2.7.1. Tests with RTD (SE Sensor)

An RTD (a representative SE sensor) was interfaced with DCR and tested. This combined system has not only the inherent merits of RTD for measurements of temperature, θ but also, possesses lower complexity and conversion time than [60], [80]. The details of the experimentation are given below.

2.7.1.1. Characterization of RTD

The experimental setup used for characterizing the RTD is shown in Fig. 2.9. Pt100 was the RTD used, and the reference θ was measured using LM35 IC [147]. This

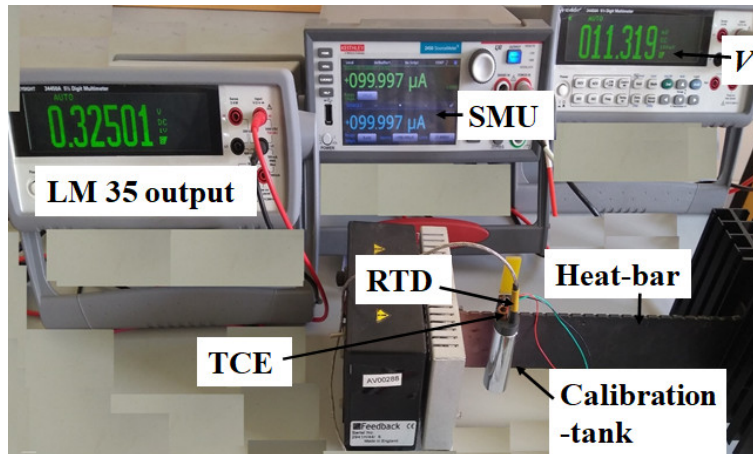


Fig. 2.9. Characterization setup of RTD-Pt100 sensor.

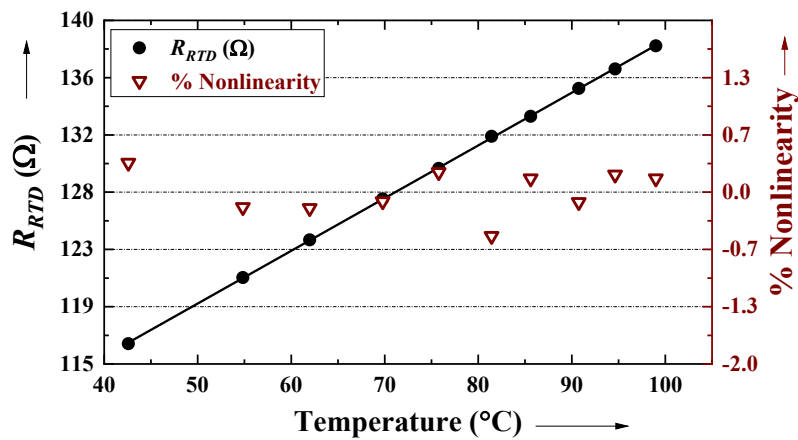


Fig. 2.10. Characterization of RTD-Pt100 sensor is shown here. The measured e_{NL} is also plotted in this graph.

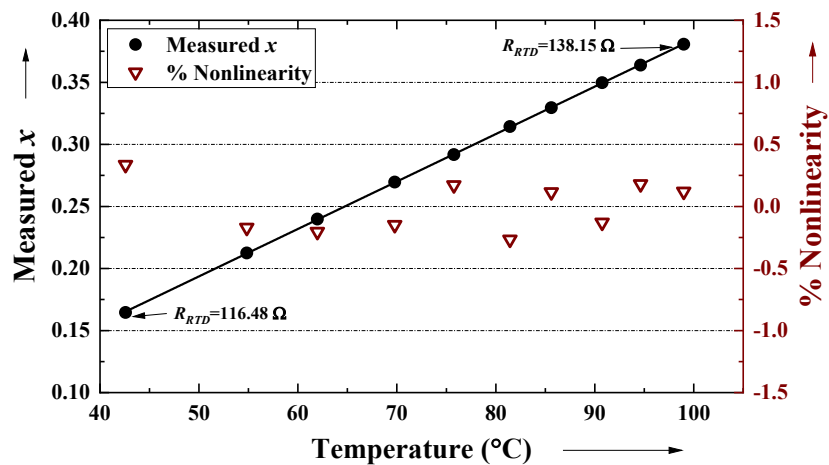


Fig. 2.11. RTD-DCR interface results are figured here. The measured e_{NL} is also shown.

LM35 IC itself has an inherent nonlinearity of 0.2 % [147]. This IC is expected to

produce a high precision output. These parts are placed in a Thermally-Conductive-Enclosure (TCE) made of copper material (high thermal conductivity of $223 \text{ W.m}^{-1} \cdot \text{K}^{-1}$). The setup comprises a heat-bar that provides different θ along its length and a calibration tank in which the TCE is placed. The self-heating error is reduced by choosing the excitation current (say, I) of the RTD as $100 \mu\text{A}$. This current was provided using a Source Measurement Unit (SMU) from Keithley Instruments (model: 2450). The above setup was used to expose the RTD to different temperatures. The resistance (say, R_{RTD}) of the RTD was noted for each θ using a 5.5-digit Multimeter, and the value of R_{RTD} is found using $R_{RTD} = V/I$, where V is the voltmeter reading. The R_{RTD} was plotted against the reference θ and given in Fig. 2.10. The nonlinearity, e_{NL} of the RTD employed can be seen to be less than 0.51 %.

2.7.1.2. RTD-DCR system

The RTD sensor was inserted in place of R_X (see Fig. 2.1) and tested with the DCR at different temperatures. The output x versus input θ graph is plotted and given in Fig. 2.11. The output can be seen to obey a linear relation with x . The worst-case e_{NL} is less than 0.34 % during the experiments. The nonlinearity observed during this experimentation can be seen to be lower when compared to the characterization results. This can be due to multiple cases. Firstly, the error values of SMU and the multimeter are not included in the characterization phase. Secondly, the overall experimental nonlinearity need not be the additive value of nonlinearities obtained from the sensor and circuit, and finally, the circuit was seen to reduce the sensor-error at the maximum error point of the characterization results. The conversion time is 10 ms, lower than the reported values in [80], [82], and [91].

2.7.2. Interfacing with GMR Sensor

As mentioned in Section 1.3.1.6, GMR sensors are low-cost and low-power devices that provide high-sensitivity magnetic field measurements. A typical GMR sensor AA004 IC is selected. This IC is present in the HB configuration. It is interfaced and tested with the DCR circuit. As discussed in Section 1.3.2, two elements of the GMR sensor (say, R_{X1} and R_{X2}), respond linearly to the magnetic field (say, B_{EXT}), while

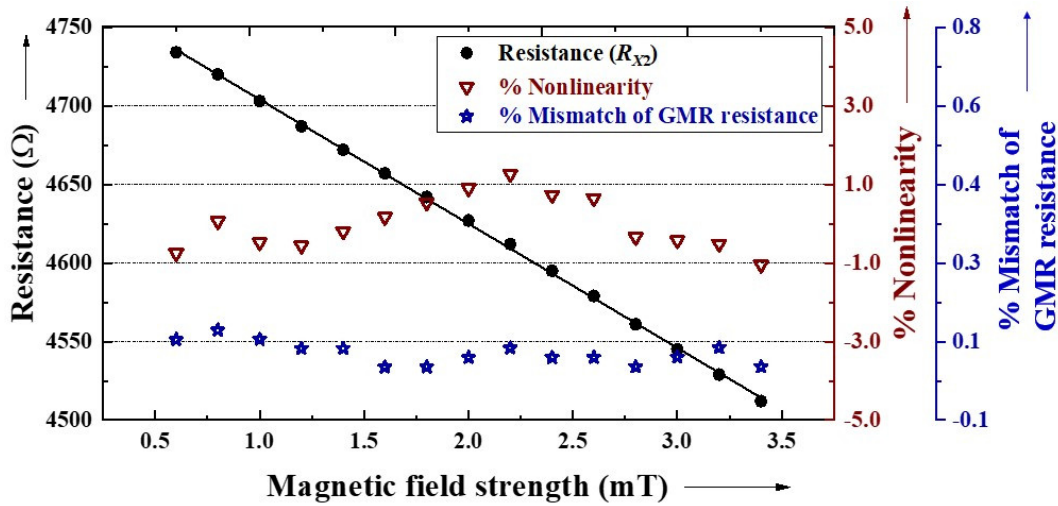


Fig. 2.12. Characterization of GMR sensor is shown here. The measured e_{NL} and mismatch between GMR elements are also plotted in this graph.

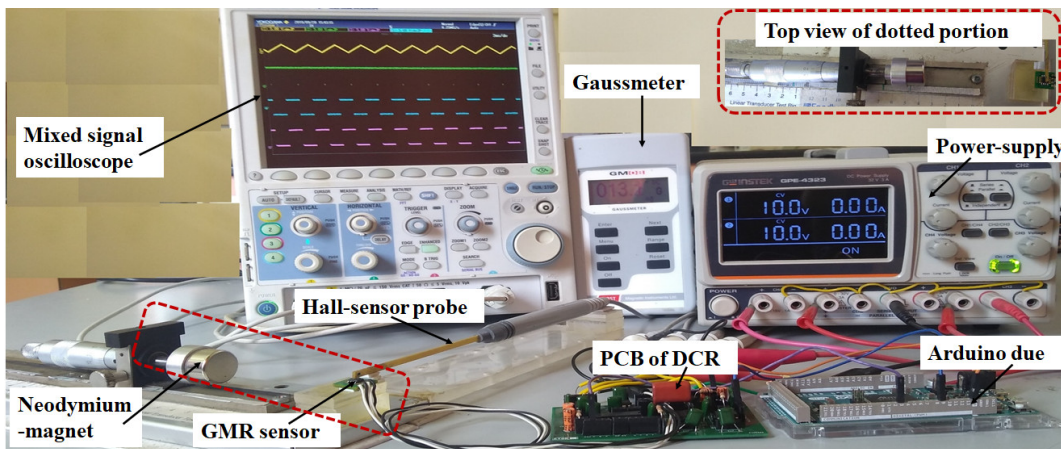


Fig. 2.13. Experimental setup used for GMR sensor interface with DCR is shown here.

the other two elements (say, R_{S1} and R_{S2}) act as shielded and constant resistance with respect to B_{EXT} . The characterization procedure reported in [148] was used to cross-check the nature of the above elements. A gaussmeter GM08 from Hirst Magnetics Instruments Ltd. was used to perform reference field estimation. It was seen that R_{X1} and R_{X2} vary linearly with B_{EXT} for $B_{EXT} \in (0.5 \text{ mT}, 3.5 \text{ mT})$. This can be inferred from Fig. 2.12. The maximum e_{NL} of R_{X1} (or R_{X2}) is 1.26 %, and the worst-case mismatch between these elements is 0.1 % (5Ω). The value of R_{S1} and R_{S2} were found as 4770Ω and 4794Ω , respectively, from these studies.

Next, the GMR sensor was connected with the PCB of the DCR as shown in Fig. 2.13. The resistances, R_X and R_S (in Fig. 2.1) were replaced, respectively, with R_{X1}

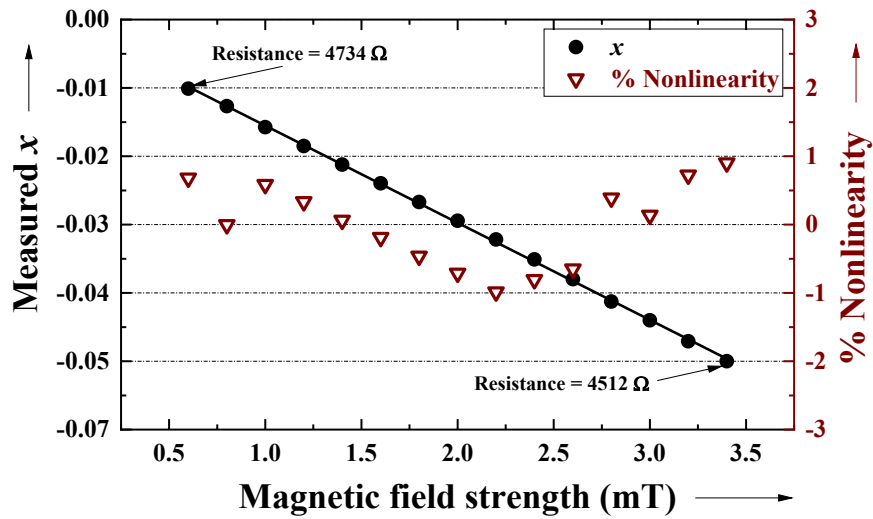


Fig. 2.14. GMR-DCR interface results are shown here. The measured e_{NL} is also depicted for each step of magnetic field.

and R_{S1} of the GMR sensor. The output (x) of the DCR was noted for different values of B_{EXT} . The setup in Fig. 2.13 (see inset) has the necessary mechanical provision to apply different B_{EXT} on the GMR sensor. The input (B_{EXT}) versus output (x) characteristics follows the expected linear variation [see Fig. 2.14]. The worst-case e_{NL} is 0.98 %. The main portion of this e_{NL} is contributed by the GMR sensor itself. It should also be noted that the developed GMR-DCR system ($e_{NL} = 0.98\%$) is better than the existing digitizers for GMR sensors [81], [84].

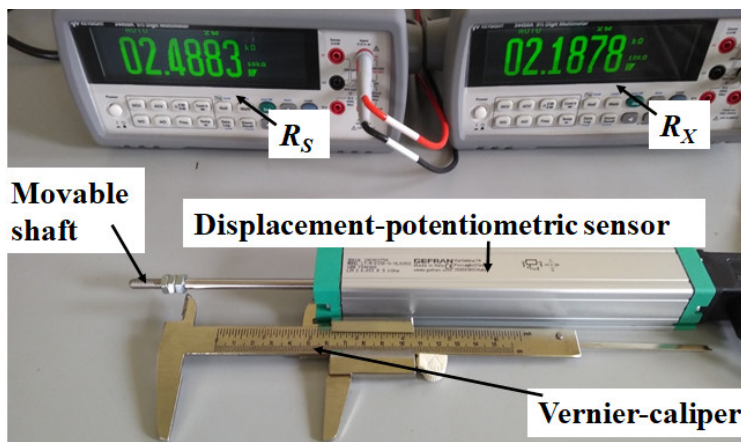


Fig. 2.15. Characterization setup for rectilinear displacement transducer-LT-150.

2.7.3. Tests with a Commercial Differential-Sensor

Tests were also conducted with a rectilinear displacement transducer (a DS-type sensor) to further evidence the versatility of DCR as a resistive sensor-interface. This easy-to-use and low-cost transducer can serve for the estimation of many measurands (e. g., pressure, airflow [5]). First, the differential resistance of the transducer was measured for different displacements of the shaft, with the help of a 5.5-digit multimeter. The true displacement was measured using a vernier caliper. The experimental setup used for this characterization can be seen in Fig. 2.15. The resistance of the transducer is linearly varying with shaft displacement, and the maximum e_{NL} is found to be 0.1 %.

Next, the differential sensor was linked with the DCR circuit, as mentioned in Section 2.3.2. The output, x in (2.9) was noted for different displacements. The results obtained are shown in Fig. 2.16 (data are attached in Appendix B.1). The maximum e_{NL} is very low (≈ 0.1 %). These results clearly show the adaptability of the developed DCR for the DS-type sensors.

2.8. Temperature-Stability Studies

The simulation environment was enhanced to study the temperature dependence of the DCR. The temperature-related drifts of I_B , V_{OS} , etc. of the Op-amps

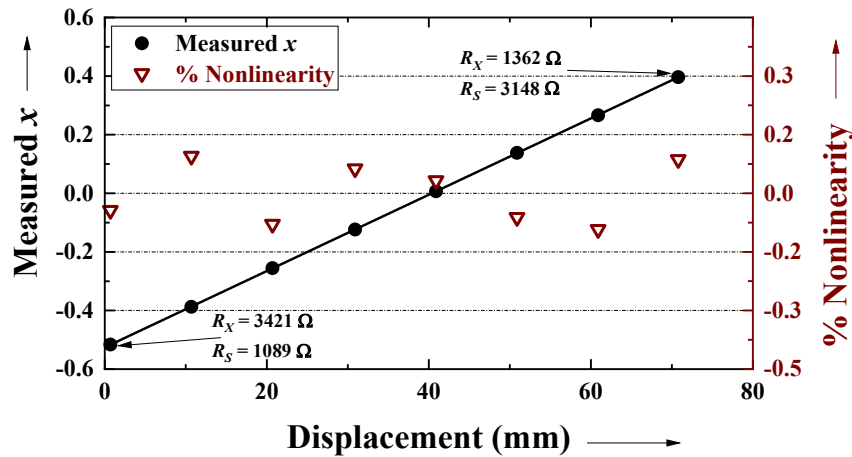


Fig. 2.16. DCR interface results with rectilinear displacement transducer-LT-150 is plotted here.

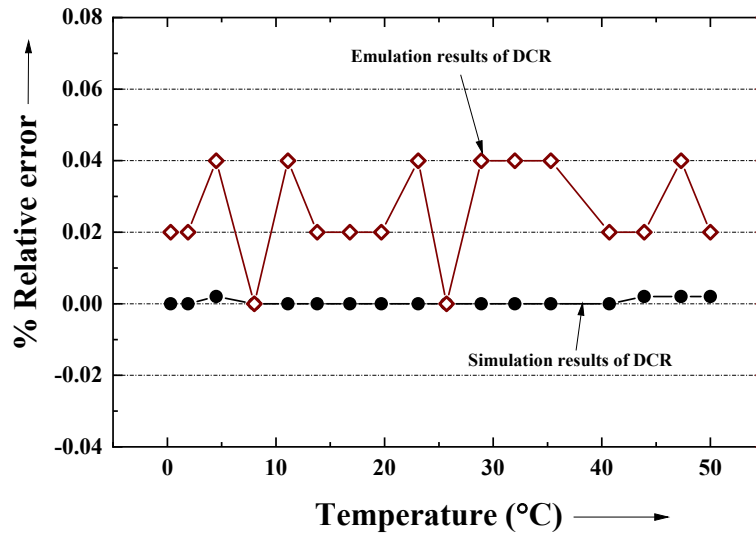


Fig. 2.17. Simulation and the experimentation results of the DCR at different temperatures (except sensor elements) are plotted.

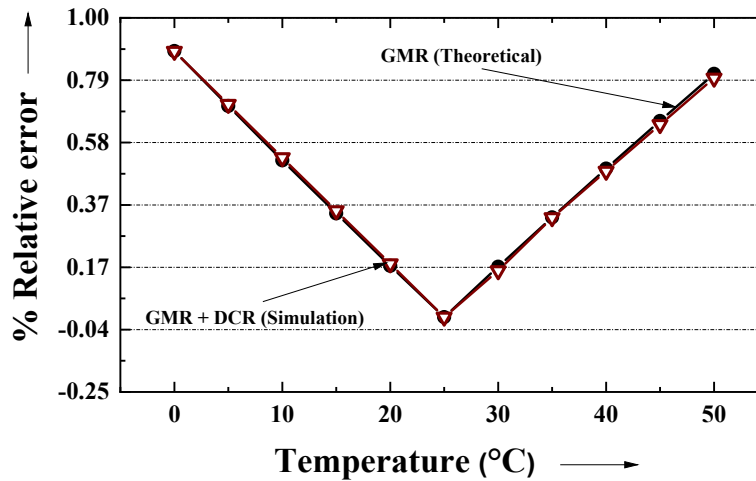


Fig. 2.18. Measured error of the GMR sensor alone (theoretical), and with DCR (simulation) is plotted.

are suitably modeled in the software. Initially, the studies were done to identify the temperature dependence of the DCR alone for a temperature range of 0°C to 50°C, a common range for electronic systems [94]. This was done by keeping the sensor elements constant throughout the temperature (θ) range [94]. The relative error (say, e_{REL}) at different θ from the nominal-case (25°C) was noted as per equation, $e_{REL} = [x - x^*] / x \times 100 \%$, where x^* and x , respectively, are the fractional resistance change at a particular θ and 25°C (expression is also given in Appendix A). The error, e_{REL} , so obtained is plotted and given in Fig. 2.17. The worst-case temperature stability for the

DCR is almost constant and negligible [see Fig. 2.17]. This shows that the DCR exhibits good performance against temperature drifts. This was also cross-checked using experimental studies. The developed DCR circuit (except the TLU and the sensor elements) was kept inside the climatic chamber (from Weisstechnik). The reference θ of the circuit was measured using an LM35 sensor IC. The experimentation was carried out by varying the θ from 0°C to 50°C. The resulting e_{REL} with respect to the room temperature (i. e., $\theta = 25^\circ\text{C}$) was plotted in Fig. 2.17. The observed maximum error is 0.04 %, which is close to the simulation studies.

Similarly, the temperature dependence of a GMR-DCR system is also studied. The temperature model of the GMR (AA004 IC) sensor, present in HB configuration, was obtained from [37] and simulated with DCR. The obtained results are plotted and given in Fig. 2.18. The worst-case e_{REL} was noted to be less than 0.9 %. This temperature dependence is mainly contributed by the sensor and not DCR. For instance, the temperature-related error of the GMR sensor bridge is derived from the datasheet [37] and plotted for $\theta \in (0, 50^\circ\text{C})$ in Fig. 2.18. It shows that the (theoretical and simulation) results related to the GMR sensor closely follow each other. Thus, the temperature dependence of the DCR is quite low.

2.9. Summary

The design and performance of the developed DCR circuit for a broad class of resistive sensors were extensively studied in this chapter. The maximum experimental nonlinearity error obtained was 0.06 %. The temperature-related error of the DCR circuit is less than 0.04 % for a deviation of 25°C. The developed scheme uses a dual-slope circuit with one reference voltage and low conversion time and renders comparable/better performance with respect to the prior art. The novel design philosophy used also ensures negligible dependence on many circuit non-idealities (like passive components drift, switch resistance, and Op-amp non-idealities) and allows preset-current excitation. The nonlinearity, e_{NL} can be further reduced by increasing the conversion time. This means that the conflicting requirements of e_{NL} and

speed of operation should be properly decided, based on the application demands. Nevertheless, the developed digitizer acts as an accurate and efficient dual-slope-based interface for a broad class of non-remote resistive sensors, as proven by the extensive analysis, simulation, and experimental results. It can be seen that the developed DCR requires a reference voltage in its architecture. In addition, it is not suitable for wide-span sensors. Relaxation oscillator-based interfaces that can solve these problems are discussed in the next chapter.

Chapter 3

Relaxation Oscillator-based Digital Techniques for Resistive Sensors

3.1. Introduction

In this chapter, efficient Relaxation-oscillator-based Digitizers for Resistive-sensors (RDR) are proposed. The scheme provides a direct-digital indication of the measurand, sensed by a resistive transducer. This relaxation-oscillator-based circuit provides many meritorious features such as (1) Simple architectures, that use no reference voltages, for resistive sensors, (2) Use of novel compensation functions, rendering an output free from the effect of power supply and capacitor drifts, (3) Linear digital output, without any separate ADC, in low conversion time, (4) Suitability for SE and QB-type resistive sensors, and (5) Negligible effect of many circuit non-ideal parameters, such as bias current and offset voltage of Op-amps, switch on-resistance and diode non-idealities, and no undesired saturation-related effects for the integrator. Further, a novel relaxation-oscillator technique is proposed for interfacing with wide-span resistive sensors. This circuit has the tendency of conversion time reduction technique, used to reduce the conversion time even for high resistance measurement. The methodology and their performance studies are explained in the upcoming sections.

This chapter is partially adapted from the post-print versions of

(1) Elangovan K and Anoop C. S., "Simple and Efficient Relaxation-Oscillator-Based Digital Techniques for Resistive Sensors — Design and Performance Evaluation," in *IEEE Transactions on Instrumentation and Measurement*, vol. 69, no. 9, pp. 6070-6079, Sept. 2020.

(2) Elangovan K and Anoop C. S., "Evaluation of New Digital Signal Conditioning Techniques for Resistive Sensors in Some Practically Relevant Scenarios," in *IEEE Transactions on Instrumentation and Measurement*, vol. 70, pp. 1-9, 2021, Art no. 2004709.

3.2. Relaxation oscillator-based Digitizer for Resistive sensors (RDR)

The working principle of the Relaxation-oscillator-based Digitizers for Resistive sensor (RDR) circuits is described in this section. The circuit schematic of these digitizers is shown in Section 3.2.1. This is followed by design criteria for the above digitizers. The proposed circuits, using simple architectures, process and render a direct-digital output proportional to the sensor resistance.

3.2.1. Working Principle of Digitizer (RDR)

As shown in Fig. 3.1, the RDR interfaces a resistive sensor (say, R_X) to a relaxation-oscillator-based architecture. The resistive sensor can be present in the SE form or QB form. In the former case, R_S is a standard resistance, while R_S refers to a shielded/fixed sensor resistance in the case of QB-type sensors. Such a shielded resistance will remain invariant with respect to the measurand. The circuit architecture consists of an integrator made of Op-amp OA, a comparator OC, a Timing and Logic Unit (TLU), switch S_W , diode D , and few other auxiliary elements.

Let v_{OA} and v_{OC} , respectively, stand for the output of the integrator OA and the comparator OC. Likewise, v_O represents the input to the TLU. It can be observed from Fig. 3.1 that a compensation resistor R_C has been placed between the nodes v_{OC} and v_O . This resistor ensures that the output, v_{OA} does not reach the saturation limits (detailed

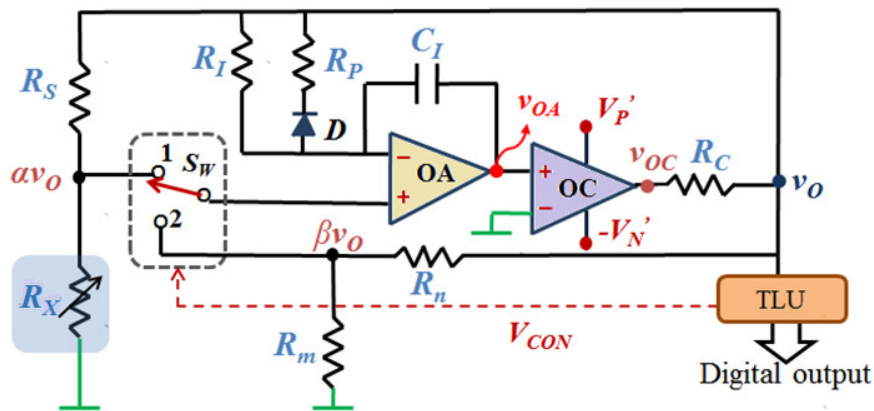


Fig. 3.1. Circuit diagram of the proposed relaxation-oscillator-based digitizer, RDR.

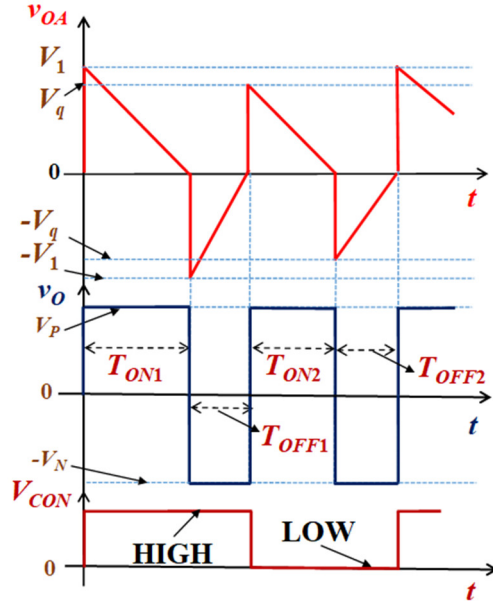


Fig. 3.2. Important node (v_{OA} and v_O) voltages of RDR and the control signal V_{CON} are shown here.

explanation will be given later). The typical waveforms of the signals v_{OA} and v_O are shown in Fig. 3.2. The signal v_{OA} has V_1 and $-V_1$ as the limiting values. Similarly, the (positive and negative) peak voltages of v_O are represented as V_P and $-V_N$ [see Fig. 3.2]. Note that V_P may not be exactly equal to V_N (due to the differences/variations in power-supply levels).

RDR works in two modes - a measurement mode (mode-M) and a compensation mode (mode-C) as explained below. The mode selection is accomplished using S_W and a digital signal V_{CON} issued by the TLU. The switching logic is given in (3.1).

$$\begin{aligned}
 S_W \Rightarrow 1; V_{CON} = 1 & \text{ (mode-M)} \\
 S_W \Rightarrow 2; V_{CON} = 0 & \text{ (mode-C)}
 \end{aligned} \tag{3.1}$$

3.2.1.1. Mode-M

The TLU places the switch S_W to position-1 in this mode (by setting $V_{CON} = HIGH$). This causes the half-bridge comprising R_X and R_S to get linked to the integrator. Let us consider the time duration (see Fig. 3.2), where v_{OA} is ramping down from V_1 (i. e., when $v_O = V_P$). The expression of v_{OA} can be written as in (3.2).

$$v_{OA} = V_1 - \left(\frac{v_O - \alpha v_O}{R_I C_I} \right) t \quad (3.2)$$

The steady-state value of V_1 has been shown to be $\alpha (V_P + V_N)$ [148], where $\alpha = R_X / (R_X + R_S)$. The voltage, v_{OA} obeys the above pattern for a time T_{ON1} till it crosses zero (i. e., when v_O makes a transition to $-V_N$). The equation of T_{ON1} can be derived from (3.2) and obtained as:

$$T_{ON1} = \left(\frac{\alpha}{1-\alpha} \right) \left(\frac{V_P + V_N}{V_P} \right) R_I C_I = \frac{R_X}{R_S} \left(\frac{V_P + V_N}{V_P} \right) R_I C_I \quad (3.3)$$

Now, the negatively-saturated v_O will make the output, v_{OA} ramp up towards zero. The equation of v_{OA} for this case is: $v_{OA} = -V_1 - [(v_O - \alpha v_O) / (R_I \parallel R_P) C_I] \times (t - T_{ON1})$. Let the signal, v_{OA} reach zero at $t = T_{ON1} + T_{OFF1}$, where T_{OFF1} is off-time duration. Substituting $v_{OA}(T_{ON1} + T_{OFF1}) = 0$, we get:

$$T_{OFF1} = \left(\frac{\alpha}{1-\alpha} \right) \left(\frac{V_P + V_N}{V_N} \right) (R_I \parallel R_P) C_I = \frac{R_X}{R_S} \left(\frac{V_P + V_N}{V_N} \right) (R_I \parallel R_P) C_I \quad (3.4)$$

The diode D becomes active only when v_O is in negative saturation (during T_{OFF1}).

3.2.1.2. Mode-C

Next, the circuit is changed to mode-C by setting $V_{CON} = 0$. In this case, the resistors R_m and R_n get connected to the integrator. Here, the peak voltage levels will become $\pm V_q$ where $V_q = \beta (V_P + V_N)$ and $\beta = R_m / (R_m + R_n)$. This can be seen in Fig. 3.2. The ON-time (say, T_{ON2}) of v_O can be obtained by replacing the ratio R_X / R_S in (3.3) with R_m / R_n . In other words,

$$T_{ON2} = \left(\frac{\gamma}{1-\gamma} \right) \left(\frac{V_P + V_N}{V_P} \right) R_I C_I = \frac{R_m}{R_n} \left(\frac{V_P + V_N}{V_P} \right) R_I C_I \quad (3.5)$$

As shown in Fig. 3.2, the off-time of mode-C will also have a reduced value. It can be clearly seen from (3.3) that T_{ON1} gives a linear measure of R_X but gets affected by non-idealities like variations of V_P and V_N (and their absolute values) and drift of

passive components (R_I , C_I). These effects can be compensated by using the function F_1 , given in (3.6).

$$F_1 = \frac{T_{ON1}}{T_{ON2}} = \left(\frac{R_n}{R_S R_m} \right) R_X \quad (3.6)$$

This means that the unknown sensor resistance, R_X can be easily found as $R_X = F_1 (R_m R_S / R_n)$. Thus, RDR provides a relaxation-oscillator methodology to measure R_X , without being affected by both capacitor and power supply drifts. The RDR circuit also has minimal dependence on other non-ideal parameters, like the on-resistance of the switch and non-ideal nature of the diode D , etc. (details will be explained in Section 3.4). Further, the compensation mode can be run periodically (and not after every mode-M) and the corresponding T_{ON2} can be stored and used.

The time durations, T_{ON1} , T_{ON2} , and T_{OFF1} are measured in the TLU. The TLU contains a TTL-compatible comparator and a timer/counter. It listens to the zero-crossing of v_O and then gives out the indication of R_X using (3.6). Alternatively, the time durations can be measured with the help of time-to-digital converters [149]. In addition, the scheme has facility to provide reduced conversion time. Thus, RDR obtains a linear digital indication of R_X using a simple and low-cost architecture. Note that digital output is obtained without using any ADC or additional switches.

3.2.2. Modified RDR (RDR*)

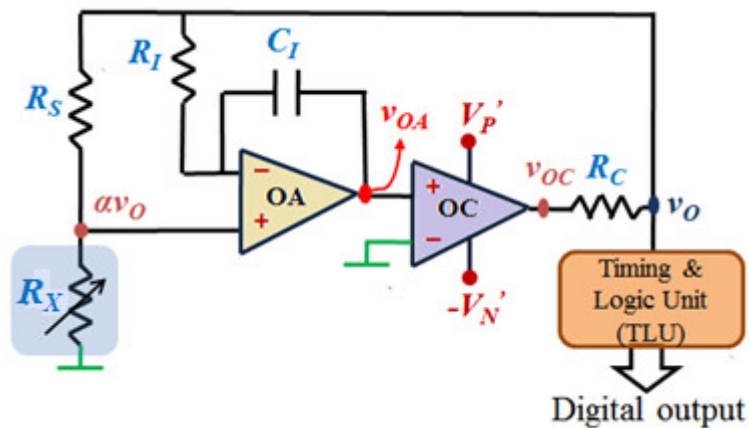


Fig. 3.3. Circuit diagram of the proposed relaxation-oscillator-based digitizer (i. e., RDR*).

As discussed in the working of RDR, the output can be obtained using two conversion cycles. This can be reduced using a simplified model of RDR (named RDR*), at the cost of dependence on drifts of a capacitor. The circuit diagram of RDR* is shown in Fig. 3.3. The working of RDR* is similar to RDR. Here, the auxiliary arm contains the resistors, R_m and R_n , resistor, R_P , and the diode, D is not used. Thus, the expression for T_{ON} is similar to (3.3) and T_{OFF} can be obtained by replacing $R_I \parallel R_P$ with R_I . The linear estimate of R_X can be obtained by measuring either T_{ON} or T_{OFF} . However, these quantities depend on the power-supply voltages (V_P , V_N) and their variations. The effect of these undesired parameters can be removed by using a new compensation function, F_2 given in (3.7).

$$R_X = \frac{F_2 R_S}{R_I C_I} = \left(\frac{T_{ON} \times T_{OFF}}{T_{ON} + T_{OFF}} \right) \frac{R_S}{R_I C_I} \quad (3.7)$$

The waveforms of RDR* are also similar to RDR except for the mode-C and increased T_{OFF} . It is evident from (3.7) that the estimated R_X is independent of power-supply variations. RDR* has an even lower conversion time as it works on a single-mode operation, but needs stable capacitors. One of the simple methods (RDR or RDR*) can be chosen for non-remote resistive sensors, based on the application and use.

3.2.3. Important Design Criteria for RDR and RDR* Systems

The integrator Op-amp, OA and comparator Op-amp, OC will be implemented using different ICs, and they may be associated with different load resistances. As a result, the saturation voltages (say, $\pm V_{sat}$) of OA may not be equal to the limiting values of v_{OC} . It can be shown that v_{OC} and v_O obey (3.8).

$$v_O = \frac{v_{OC}}{k}; \text{ where } k = \left[\frac{R_C}{R_X + R_S} + \frac{(1-\alpha)R_C}{R_I} + 1 \right] \quad (3.8)$$

The proper operation of the integrator OA (and RDR) can be ensured if the signal v_{OA} remains in the linear operating range, i. e., $\alpha (V_P + V_N) < V_{sat}$. This means that k should be greater than $\alpha (V_P' + V_N') / V_{sat}$, where V_P' and V_N' are the saturation

voltages of OC. This condition can be rewritten with the help of (3.8) as in (3.9), where R_{Xmax} is the maximum resistance of the sensor.

$$R_C \geq \frac{R_I}{(R_I + R_S)} \left[R_{Xmax} \left(\frac{V_P' + V_N'}{V_{sat}} - 1 \right) - R_S \right] \quad (3.9)$$

In other words, the compensation resistor, R_C satisfying (3.9) can be used to ensure the proper working of the RDR circuits. The values of the other passives R_I and C_I affect T_{ON} and T_{OFF} and can be selected based on the desirable conversion times.

The RDR circuits, discussed above, are not suited for the wide-span processing of R_X . It is mainly due to the saturation-related constraints of Op-amp OA. In other words, the selection of resistor, R_C is difficult for a wide range of operations. Moreover, there is no facility to reduce the execution time, especially for wide-span operations. Therefore, an enhanced circuit is developed to solve these issues and is discussed next.

3.3. Relaxation oscillator-based Digitizer for Resistive sensors with Wide-span (RDR_w)

The architecture and working of the proposed Relaxation oscillator-based Digitizer for Resistive sensors with Wide-span (RDR_w) are discussed in this section.

3.3.1. Principle of Operation of RDR_w

The circuit schematic of RDR_w is shown in Fig. 3.4. The RDR_w basically interfaces the resistive sensor (marked as R_X and R_S) to the digitizer. Latter consists of an integrator OP1, a comparator OP2, a switch (say, S_w), a Programmable Gain Amplifier (PGA), and a Timing and Logic Unit (TLU). The TLU helps to control the RDR_w operation and measure the time durations of the comparator-output (say, v_2). Note that the PGA can be even replaced by a fixed gain amplifier. However, the use of a PGA, over the fixed gain amplifier, will help to reduce the conversion time. The details about the utility of the PGA will be explained later. For the time being, assume that the gain of the PGA is G . The typical waveforms at the cardinal nodes (i. e., v_1

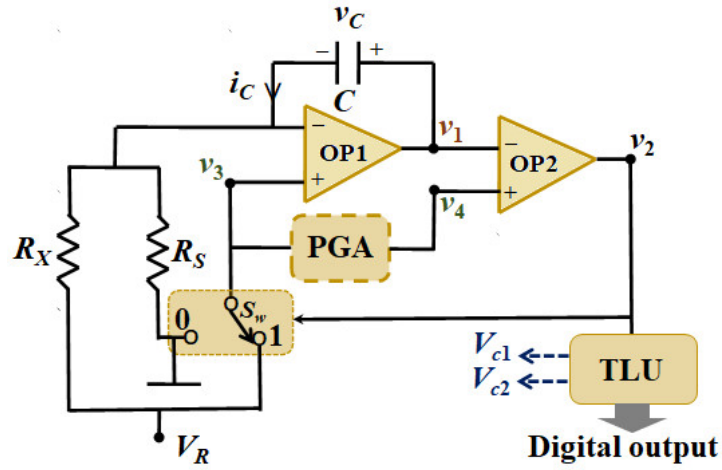


Fig. 3.4. Circuit diagram of relaxation oscillator-based digitizer for resistive sensors with wide-span (RDR_w).

and v_2) of RDR_w are shown in Fig. 3.5. The equation of the input (say, v_3) and output (say, v_4) of the PGA, for different switch positions, are given in (3.10), where V_R is DC reference voltage.

$$\begin{aligned} v_3 &= V_R \text{ and } v_4 = GV_R; S_w \rightarrow 1 \\ v_3 &= v_4 = 0 \quad ; S_w \rightarrow 0 \end{aligned} \quad (3.10)$$

Initially, assume that the comparator-output, v_2 is at logic-high. In this case, the switch S_w will be at position-1. This configuration ensures that $v_3 = V_R$ {vide (3.10)}

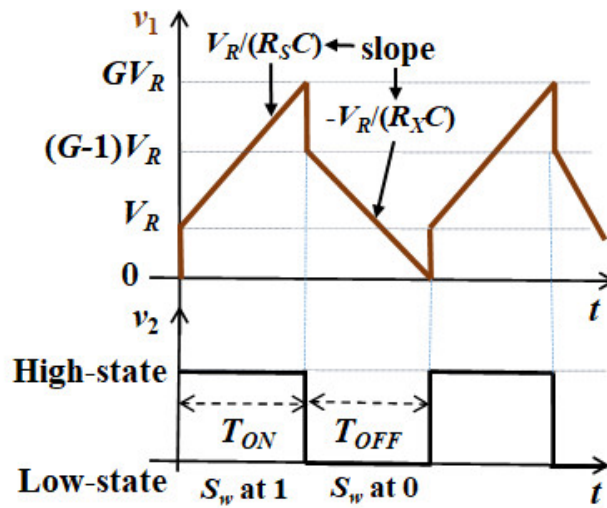


Fig. 3.5. Node (v_1 and v_2) voltage waveforms of RDR_w.

and $v_4 = GV_R$. The current (say, i_C) through the capacitor will be equal to $i_C = V_R / R_S$. As a result, the integrator output (v_1) will charge up as shown in (3.11) and Fig. 3.5.

$$v_1(t) = V_R + \left(\frac{V_R}{R_S C} \right) t \quad (3.11)$$

The expression given in (3.11) will be obeyed till $v_1 < v_4 (= GV_R)$. When v_1 crosses GV_R , the comparator output, v_2 will shift to its low-state. In this phase, the switch will be at position-0, causing $v_3 = v_4 = 0$. The capacitor will retain its voltage, v_C of $(G-1)V_R$ during this switching instant. Hence, the voltage, $v_1 (= v_3 + v_C)$ will be reduced to $(G-1)V_R$. The ON-time duration (say, T_{ON}) of v_2 can be found by substituting $v_1(T_{ON}) = GV_R$ in (3.11). Thus, the equation of T_{ON} can be obtained as given in (3.12).

$$T_{ON} = (G-1)R_S C \quad (3.12)$$

The subsequent variations of node voltages are depicted in Fig. 3.5. The current of $i_C = -V_R / R_X$ will flow through the capacitor when the switch position is changed to 0. The voltage, v_1 will decrease from $(G-1)V_R$ with a slope of $-V_R / (R_X C)$. This discharging will pursue till v_1 becomes v_4 (i.e., 0). At this moment, v_2 will switch back to high-state and be set to GV_R , and the cycle will repeat afterward [see Fig. 3.5]. The off-time duration (say, T_{OFF}) of v_2 can be derived as given in (3.13).

$$T_{OFF} = (G-1)R_X C \quad (3.13)$$

A function F can be defined as in (3.14) and further simplified using (3.12) and (3.13).

$$F = \frac{T_{OFF}}{T_{ON}} = \frac{R_X}{R_S} \quad (3.14)$$

In the case of SE-based configuration, R_X can be the resistive sensor and R_S can be a standard resistor. Thus, the sensor-resistance, R_X can be found using (3.14) as $R_X = FR_S$ or $R_X = (T_{OFF} / T_{ON}) \times R_S$. The duration of T_{ON} and T_{OFF} is measured by interfacing the output, v_2 to the timer of TLU, with the help of its digital port. Thus, the proposed RDR_w can give a direct-digital output using just one reference voltage. On the other hand, the schemes in [102] and [110] require bipolar reference voltage

sources. A mismatch between these references can lead to an output error. Note that the output is also immune to G , C , V_R , and their variations. In addition, the integrator output, v_1 always remains within well-defined limits, regardless of the value of R_X (note: the RDR circuit discussed in the previous section, gets saturated for large-valued resistors). This feature of RDR_w also aids in the measurement of R_X with a wide range.

3.3.1.1. Adaptation to differential-sensors (DS)

The elements, R_X and R_S can constitute the DS. Let, x be the fractional change of the measurand. Then, $R_X = R_0(1 + x)$ and $R_S = R_0(1 - x)$, where R_0 represents the nominal resistance of the sensor. Then, ‘ x ’ can be found with the help of the RDR_w using the function given in (3.15).

$$x = \frac{R_X - R_S}{R_X + R_S} = \frac{T_{OFF} - T_{ON}}{T_{OFF} + T_{ON}} = \frac{F - 1}{F + 1} \quad (3.15)$$

3.3.1.2. DS with inverse characteristics

Some of the differential sensors have an inverse relationship with respect to x . Such inverse-differential sensors (IDS) will follow $R_X = R_0 / (1 + x)$ and $R_S = R_0 / (1 - x)$ [134]. These sensors can also be interfaced with RDR_w and the measurand, ‘ x ’ can be found using the relation $(T_{ON} - T_{OFF}) / (T_{ON} + T_{OFF})$.

From the above discussions, it can be inferred that the proposed circuit, given in Fig. 3.4 is useful to measure the resistance of SE, DS, and IDS type resistive sensors using a single conversion cycle (i. e., $T_{ON} + T_{OFF}$).

3.3.2. Role and Design of PGA

The PGA can be intelligently designed to optimize the RDR_w performance, especially for SE-type sensors with a wide-span. Let the limiting values of the sensor resistance, R_X be R_{Xmin} and R_{Xmax} . In Section 3.3.1, the PGA gain was assumed to be equal to G . The off-time duration (T_{OFF}) and conversion time will have a large dynamic range for cases where $R_{Xmax} \gg R_{Xmin}$. This scenario will lead to two issues, namely, (i) Off-time durations can become very low when $R_X \rightarrow R_{Xmin}$, which brings in the adverse effects of the TLU resolution and the dynamic parameters of Op-amps, and (ii) T_{OFF}

and maximum conversion time (say, T_{cmax}) will become very high when $R_X \rightarrow R_{Xmax}$. For example, if $R_{Xmin} = 1 \text{ k}\Omega$ and $R_{Xmax} = 1 \text{ M}\Omega$, then $T_{OFF} \in (500 \text{ }\mu\text{s}, 500 \text{ ms})$ for $G = 6$ and $C = 100 \text{ nF}$. As a result, T_{cmax} of the RDR_w circuit becomes 550 ms when $R_S = 100 \text{ k}\Omega$.

The aforesaid issues could be solved by assigning different gains [see (3.13)] for various regions of R_X , as outlined below. Assume that T_{Xmin} and T_{Xmax} are the desired values of minimum and maximum off-times of the RDR_w scheme. The value of T_{Xmin} should be high enough so as to minimize the effects of TLU resolution and slew-rate of the Op-amps. T_{Xmax} depends on the desired conversion time. T_{Xmax} equals $T_{cmax} - T_{Smax}$, where T_{Smax} represents the maximum ON-time of RDR_w. T_{Smax} can be found using (3.12) by substituting $G = T_{Xmax} / \left(C \times \sqrt[N_R]{(R_{Xmin})^{N_R-1} R_{Xmax}} \right) + 1$. Then, the resistance, R_X can be separated into different regions. The number of regions of operation (say, N_R) can be selected as in (3.16). In (3.16), $\lceil \cdot \rceil$ represents the ceil function.

$$N_R = \left\lceil \log_k \left(\frac{R_{Xmax}}{R_{Xmin}} \right) \right\rceil; \text{ where } k = T_{Xmax} / T_{Xmin} \quad (3.16)$$

From (3.16), it can be seen that N_R will depend on the T_{Xmax} (as well as T_{cmax}). Then, the span of an i^{th} region can be written as $\left(\sqrt[N_R]{(R_{Xmin})^{N_R-i} (R_{Xmax})^i}, \sqrt[N_R]{(R_{Xmin})^{N_R-i-1} (R_{Xmax})^{i+1}} \right)$. Here, i vary from 0 to N_R-1 . The gain (say, G_i) for the i^{th} region can be expressed as in (3.17).

$$\text{Gain}(G_i) = \frac{T_{Xmin}}{C \times \sqrt[N_R]{(R_{Xmin})^{N_R-i} (R_{Xmax})^i}} + 1 \quad (3.17)$$

Using the above approach, T_{cmax} will set reduced as shown in (3.18). Note that conversion time without PGA was higher than T_{cmax} in (3.18) and T_{cmax} equaled $(G_0 - 1) (R_S + R_{Xmax}) C$.

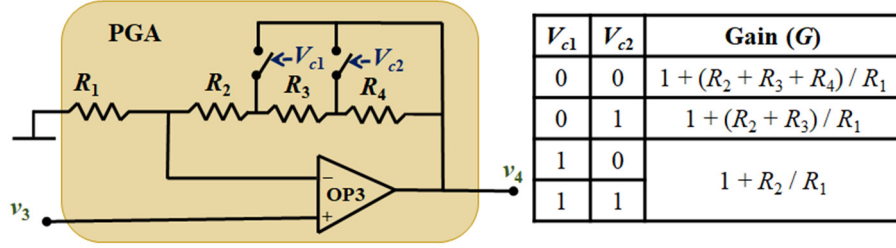


Fig. 3.6. Internal structure of the PGA that could be used along with RDR_W . This circuit is suited for the triple operation of RDR_W ($N_R = 3$). It could be suitably extended or reduced for $N_R \neq 3$.

$$T_{cmax} = \left[(G_0 - 1)C \left(R_S + \sqrt[N_R]{(R_{Xmin})^{N_R-1} R_{Xmax}} \right) \right] \quad (3.18)$$

The value of R_S and C of RDR_W can be chosen such that they help to satisfy the aforementioned conditions.

Let us consider a typical example, where $R_X \in (1 \text{ k}\Omega, 1 \text{ M}\Omega)$. Assume, the required T_{Smin} and T_{Xmin} are $500 \mu\text{s}$ which helps to avoid the issue (i). Let T_{Xmax} be 5 ms . From (3.16), it can be found that $k = 10$ and N_R equals 3. Thus, the different regions can be obtained as $(1 \text{ k}\Omega, 10 \text{ k}\Omega)$, $(10 \text{ k}\Omega, 100 \text{ k}\Omega)$, and $(100 \text{ k}\Omega, 1 \text{ M}\Omega)$. The gain values (say, G_0, G_1, G_2 , respectively) for these regions can be found using (3.17) as 6, 1.5, and 1.05. Using this approach, T_{cmax} of the developed prototype can be achieved as 55 ms when using $C = 100 \text{ nF}$ and $R_S = 100 \text{ k}\Omega$. This is approximately ten times lower than the value obtained using the fixed value of the gain.

The above logic can be realized with the help of the TLU and the PGA. A typical circuit of the PGA which could be used with the RDR_W , is shown in Fig. 3.6. This PGA is suited for $N_R = 3$. It accepts the signal, v_3 , and provides its output to the positive terminal, v_4 of OP2. The circuit consists of four resistors (R_1 to R_4) and two switches, controlled by digital signals, V_{c1} and V_{c2} from TLU. The gain, G_i of this circuit for different combinations of V_{c1} and V_{c2} is also illustrated in Fig. 3.6. Thus, the required gain, (G_i) can be selected for the RDR_W , depending on the value of sensor resistance. This selection process can be automated using a suitable program in TLU (shown in Section 3.7). This PGA circuit can be easily extended/reduced for cases where $N_R \neq 3$. In such cases, the various gains can be achieved by appropriately adding or removing the feedback resistors, switches, and associated control signals of PGA.

For instance, an RDR_W with N_R regions, requires a PGA with N_R number of feedback resistors, $(N_R - 1)$ numbers of switches, and control signals.

3.4. Error Analysis

Non-ideal nature of the circuit components and sensor parameters can affect the working of the proposed interfaces. The effect of these parameters is studied, quantified, and detailed next.

3.4.1. Analysis of RDR

3.4.1.1. Parameters of OA and OC

The bias current of OA can change the time durations, T_{ON1} and T_{ON2} . These alterations in T_{ON1} and T_{ON2} change the function F_1 to F_1' , which is given in (3.19), where $\beta = R_m / (R_m + R_n)$, $p = i_{P1}R_S$, and $n = i_{N1}R_I$.

$$F_1' = F_1 \left[\left(\frac{1-\alpha}{1-\beta} \right) \left(\frac{V_P(1-\beta) + \beta p - n}{V_P(1-\alpha) + \alpha p - n} \right) \right] \quad (3.19)$$

The resulting error in F_1 is merely 0.005 % for a typical bias current of 2 nA (e.g., OP07 IC). The effect of the offset voltage (V_{OS1}) of OA can be computed in a similar manner as that of bias current using (3.19), and the modified function (F_1') equals:

$$F_1' = F_1 \left[\left(\frac{1-\alpha}{1-\beta} \right) \left(\frac{V_P(1-\beta) - V_{OS1}}{V_P(1-\alpha) - V_{OS1}} \right) \right] \quad (3.20)$$

The error due to F_1' for the V_{OS1} of the OP07 IC is just 0.002 %. The drift of V_{OS} is also considered. A typical, drift $\Delta V_{OS1}/\Delta T$ of OP07 IC (1.3 $\mu\text{V}/^\circ\text{C}$) introduces negligible error in output for a ΔT of 10 $^\circ\text{C}$. The offset of OC will not introduce any error in the output of RDR.

3.4.1.2. Non-ideal parameters of the diode

The parameters, ON-state forward voltage drop of the diode (say, V_γ) and on-resistance (say, R_f) of the diode can affect the off-times of RDR. Since the function F_1 depends only on ON-times, there is no effect due to V_γ and R_f . The off-resistance (say,

R_r) of the diode will modify T_{ON} to T_{ND1} as given in (3.21) for mode – M.

$$T_{ND1} = \frac{R_X}{R_S} \left(\frac{V_P + V_N}{V_P} \right) \{ R_T \parallel (R_P + R_r) \} C \quad (3.21)$$

The ON-time of mode-C can be obtained from (3.21) by using R_n and R_m , in place of R_S and R_X . The effect of R_r gets nullified on the computation of F_1 .

3.4.1.3. Switch resistance

The selection of modes is done using the switch, S_W . The finite on-resistance (R_N) and off-resistance (R_{OF}) of S_W may cause an error in the output. Due to these finite resistances, the function F_1 gets altered as given in (3.22), where $q_1 = \beta / \alpha$ and $q_2 = (1 - \alpha) / (1 - \beta)$.

$$F_1' = F_1 \left(\frac{R_{OF} + q_1 R_N}{R_{OF} + R_N / q_1} \right) \left(\frac{R_{OF} + q_2 R_N}{R_{OF} + R_N / q_2} \right) \quad (3.22)$$

The resulting error is negligible for the parameters of a typical switch IC [150].

3.4.1.4. Bandwidth and slew-rate considerations

Op-amp OA has a finite bandwidth (say, f_B). This can cause the output v_{OA} to have a steady-state delay (say, τ) of $1/(2\pi f_B)$ with respect to the ideal waveforms [151]. As a result, the value of T_{ON} and T_{OFF} gets altered by τ s. For OP07 IC, $f_B = 0.6$ MHz and τ work out to be very small (≈ 0.26 μ s) when compared to T_{ON} and T_{OFF} . As a result, the f_B of OA does not have a significant effect on the operation of the proposed circuits. Similarly, the slew rate of Op-amp can also affect the output. For instance, the output, v_O may become trapezoidal if $(V_P + V_N) / SR$ becomes close to T_{ON} or T_{OFF} . This may cause non-linearity in the integrator-output, v_{OA} . However, these effects are negligible in the present case as $(V_P + V_N) / SR$ (≈ 50 μ s) is quite small to typical T_{ON} and T_{OFF} (≈ 15 ms).

3.4.1.5. Considerations of TLU

Let us consider that ' f_c ' is the clock frequency of the TLU. Then $T_{ON} = N_{ON} T_C$, where N_{ON} is the digital-counts corresponding to T_{ON} and $T_C = 1/f_c$. The output function, F_1 simplifies to N_{ON1}/N_{ON2} . The timer/counter may suffer from time-base

inaccuracies, counting errors, etc. This can deviate the function, F_1 from its ideal values. For instance, a counting error of ± 1 in the timer module of RDR can lead to an output-error of 0.08 % for $f_c = 656.25$ kHz.

3.4.2. Analysis of RDR_w

The proposed RDR_w circuit has many merits like independence from drifts of G , V_R , and C . However, a few non-ideal sources can lead to an error. The error sources of Op-amps and switch can cause an error in the RDR_w output. These sources can be modeled as indicated in [4], [85], [148] and their effects are described below.

3.4.2.1. Effects due to switch and the Op-amps

The bias current, offset voltage, and resistances of S_w of the RDR_w were modeled. The switch, S_w is directly linked to the non-inverting terminal of the Op-amp OP1 and OP3 (Op-amp used in PGA). Thus, the on and off-resistances of S_w will cause only a negligible error. Let us consider that the bias current of the Op-amp OP1 and OP3, is I_{B1} and I_{B3} , respectively. The offset voltages of these Op-amps can be considered V_{os1} and V_{os3} . In presence of these elements, the function F will get modified to F^* . The expression of F^* is given in (3.23), where $R_{sen} = R_X + R_S$, $m = V_{os1}R_{sen}$, and $n = I_{B1}R_XR_S$.

$$F^* = \frac{V_R R_X + V_{os1} R_{sen} + I_{B1} R_X R_S}{V_R R_S - V_{os1} R_{sen} - I_{B1} R_X R_S} = \frac{V_R R_X + m + n}{V_R R_S - m - n} \quad (3.23)$$

From (3.23), it can be noted that the terms of V_{os3} and I_{B3} of Op-amp OP3 will not affect the output. The error, e_{FSE} is found using (3.23) and (3.14) and it is given in (3.24), where $FSS = R_{Xmax} - R_{Xmin}$.

$$\% e_{FSE} = \frac{R_{sen} (m + n)}{R_S \times FSS \times (V_R R_S - m - n)} \times 100\% \quad (3.24)$$

It can be observed from (3.24) that the error will increase with the sensor resistance, R_X . The magnitude of the errors is evaluated by using the values of V_{os1} (≈ 60 μ V) and I_{B1} (≈ 2 nA) of OP07 IC in (3.24). As far as SE-type sensors are concerned, the worst-case deviation of the function F^* (from F) will amount to 0.24 %, when R_X varies from

1 k Ω to 1 M Ω . Similarly, the nonlinearity, e_{NL} is found as 0.04 % for SE-type sensors. For DS, the estimated value of $x = (F^* - 1) / (F^* + 1)$ will suffer a worst-case deviation of 0.01 %.

3.4.2.2. Errors due to TLU

The time measurements of the RDR_w are done by using the timer/counter modules. Let N_{ON} and N_{OFF} be the counter-outputs such that $F = N_{OFF} / N_{ON}$. Then, $N_{ON} = T_{ON} \times f_C$ and $N_{OFF} = T_{OFF} \times f_C$. A counting error of $\pm \Delta N$ of the timer/counter module can modify F to $F^\#$, whose expression is given in (3.25).

$$F^\# = \frac{(N_{OFF} \pm \Delta N)}{(N_{ON} \pm \Delta N)} \quad (3.25)$$

The worst-case deviation of $F^\#$ from F will be around 0.02 % for an ΔN of 1 and f_C of 656.25 kHz. This f_C value corresponds to the timer/counter-0 module of the TLU used in the prototype.

3.4.2.3. Effect of slew-rate and delay of op-amps

The errors due to the slew-rate and delay of Op-amps can be reduced by choosing T_{ON} and T_{OFF} to be much greater than a few hundred 100 μs [102]. The logic described in Section 3.3.2 also aids in making the aforesaid selection.

3.4.2.4. Few practical considerations

The realistic limits of the resistance measurement of RDR_w depend on a number of factors such as the resolution of the timer/counter modules [142], limitation imposed by the (positive) Op-amp power supply (say, V_{CC}), power line interference [152], [153] and circuit noise, slew-rate of the Op-amps, and input resistance of OP1. The lower limit (R_{Xmin}) is given in (3.26), where G_{max} is the maximum value of the gain.

$$\frac{T_{Xmin}}{(G_{max} - 1)C} = \frac{V_R T_{Xmin}}{(V_{CC} - V_R)C} \quad (3.26)$$

From the above relation, it can be seen that R_{Xmin} depends on V_{CC} , V_R , C , and T_{Xmin} . Similarly, the upper limit is much lower than the input resistance of the Op-amp OP1.

Further, it can be seen from (3.23) that an increased R_{Xmax} leads to a higher error. Thus, I_{B1} and V_{os1} can also be accounted, while choosing R_{Xmax} . The number of regions (N_R) can be selected as (3.16). However, an increased value of N_R will require increased complexity and transient time and needs low-valued resistors in the PGA circuit. By considering the above facts, the developed RDR_w prototype can effectively measure R_X ranging from 100 Ω to 100 M Ω .

3.5. Performance Verification of RDR Circuits

The performance of the RDR circuits was initially verified using simulation and then by emulation studies. Finally, the GMR sensor was interfaced with the developed RDR circuits. Details are given below.

3.5.1. Simulation Studies

The proposed circuits were modeled, simulated, and their performance was studied using LTspice software. Details of the studies were categorized below.

3.5.1.1. Simulation studies of RDR circuit

The Op-amp OA and OC were designed to have the specifications of OP07 and LF356 IC, respectively. The Op-amps were powered by a ± 5 V supply. The resistor (R_I) and capacitor (C_I) were chosen as 100 k Ω and 100 nF. The resistor R_C was selected as 10 k Ω such that it satisfies (3.9). The resistor, R_P was selected as 100 k Ω so that the $T_{OFF} \approx T_{ON} / 2$. The resistor R_m and R_n were selected as 4.7 k Ω and 5.6 k Ω , respectively. Switch S_W and diode D were configured, respectively, to have the specifications of MAX 4053 IC and 1N4007. The selection of R_X and R_S is dependent upon the sensor and its configurations (SE or QB). Resistor R_S was selected as 5 k Ω , and the sensor resistor R_X was varied from 5 k Ω to 4.5 k Ω with the step size of 50 Ω . This was done to mimic the characteristics of a commercial Giant-magneto resistance (GMR) sensor [37]. The values of T_{ON1} , T_{ON2} , and T_{OFF1} and the function F_1 were observed for each step. A graph of F_1 versus R_X is plotted and given in Fig. 3.7. The graph clearly shows

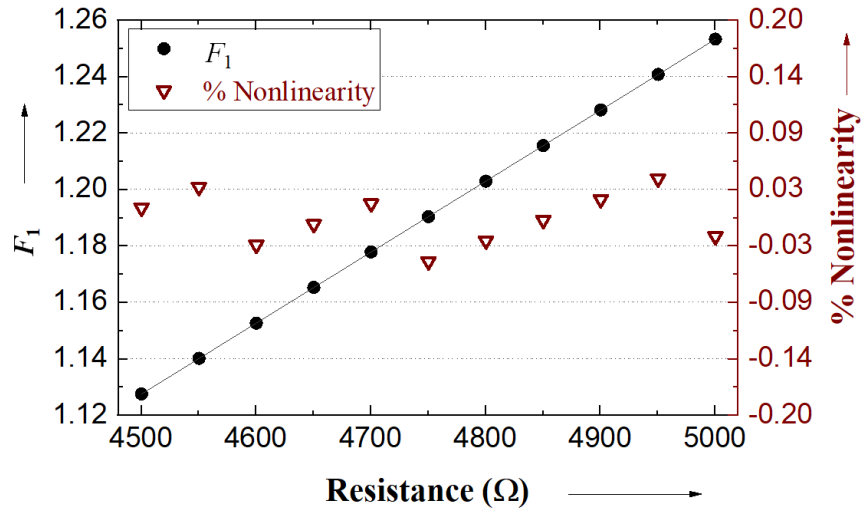


Fig. 3.7. Results obtained from simulation studies for RDR.

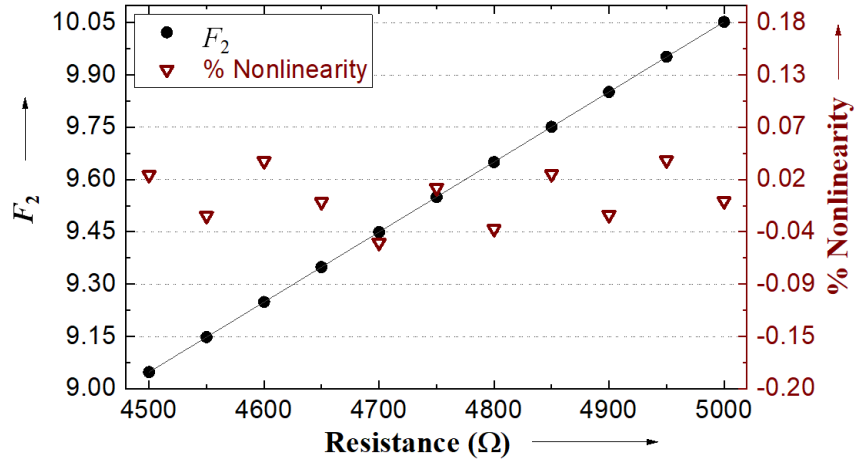


Fig. 3.8. Results obtained from simulation studies for RDR*.

that F_1 obeys a linear relationship with R_X . The nonlinearity, e_{NL} of F_1 for each value of R_X was calculated and plotted in Fig. 3.7. The maximum e_{NL} is merely 0.04 %.

3.5.1.2. Simulation studies of RDR*

RDR* was designed using similar components, given in Section 3.5.1.1. The circuit was simulated for the resistance characteristics in [37]. The output F_2 was measured and plotted against R_X and shown in Fig. 3.8. The nonlinearity, e_{NL} obtained from the plot is 0.05 %. Some of the sensors (like RTD-Pt1000) have low resistance values. To simulate this scenario, the RDR* circuit was tested for such cases where R_X varies from 0.9 kΩ to 1.1 kΩ. The maximum e_{NL} obtained for this case is also less than

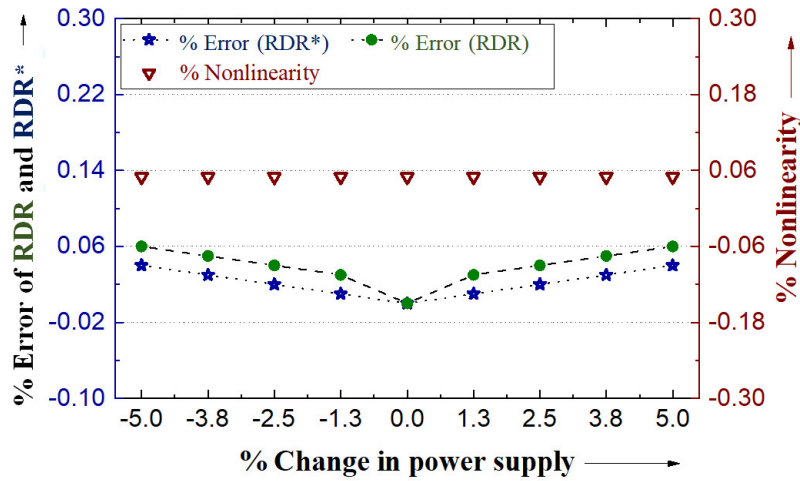


Fig. 3.9. Simulation results showing the immunity of the proposed schemes to power-supply drifts.

0.05 %. The effect of power-supply drifts on the performance of RDR and RDR* was also checked, and the results are shown in Fig. 3.9. It can be seen from Fig. 3.9 that the worst-case errors (e_{NL} and e_{REL}) of RDR remain very low for drift $< 5\%$.

3.5.2. Emulation Studies

The RDR circuits were implemented and tested for further performance validation. The components used in the hardware model were similar to those employed in the simulation. Resistors used were tolerant to 1 %. The TLU was realized using LM311 IC and one of the timer/counter modules of the ATSAM3X8E

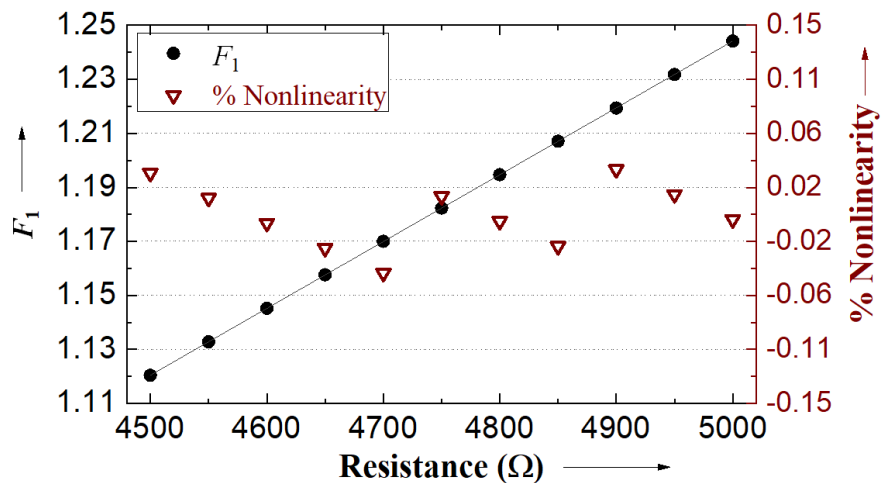


Fig. 3.10. Linear transfer characteristics of RDR obtained on emulation studies.

microcontroller [142]. The timer/counter module has the specifications of timer/counter-0, 32-bit timer/counter, and 656.25 kHz clock frequency with 2 μ s resolution. The output signal from the comparator (OC) is a bipolar signal, v_O (see Fig. 3.2), and the timer can accept only unipolar signals. The necessary bipolar-to-unipolar conversion was accomplished using the LM311 IC. Note that the LM311 IC, itself, cannot be used to implement the comparator OC. This will not ensure the proper working of the developed circuits as zero current will flow through the capacitor when output v_O is zero. The timer module can be replaced by an adequate digital platform in standalone applications.

The resistance, R_X was mimicked with the help of a precision decade resistance box. The TLU, connected to v_O , measured T_{ON} and T_{OFF} and computed the appropriate function (F_1 or F_2). The precision was improved by averaging of few output samples and rounding off to three digits (after the decimal point). The resolution of this setup was approximately 0.5 Ω for RDR and RDR* systems. The function, F_1 and F_2 were recorded for different values of $R_X \in (4.5 \text{ k}\Omega, 5 \text{ k}\Omega)$, and the associated plots are given in Fig. 3.10 and Fig. 3.11. As expected, the functions are linear with R_X and the worst-case e_{NL} is 0.05 % for RDR and 0.08 % for RDR*. The power consumption of the RDR and RDR* was found to be around 25 mW and 22 mW, respectively. The microcontroller board was not considered for the above power computations. This was because the board has many other components/sections which are not used/needed for

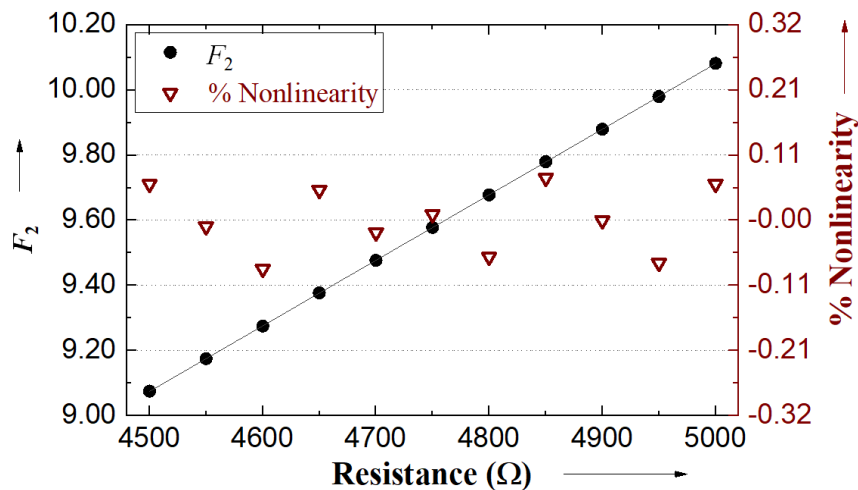


Fig. 3.11. Emulation results of RDR*. Measured e_{NL} is also plotted.

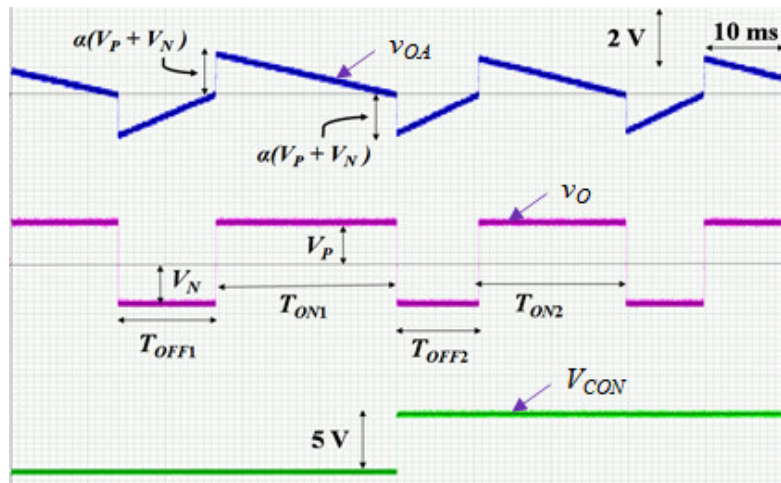


Fig. 3.12. Screenshot of the waveforms at important nodes of RDR. These waveforms are closely matched with the expected nature (see Fig. 3.2).

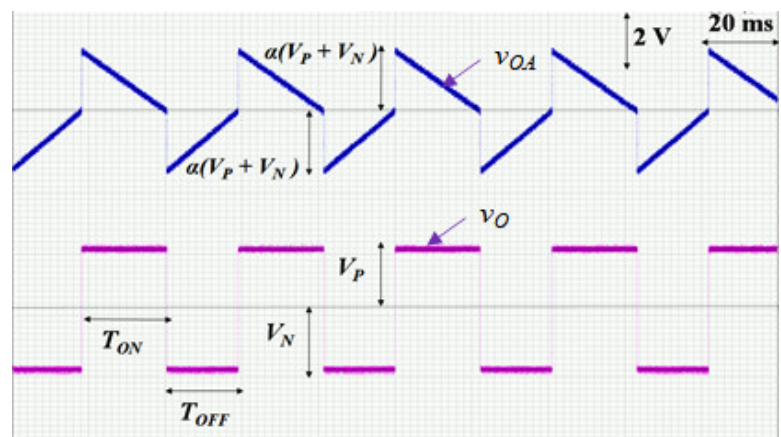


Fig. 3.13. Oscilloscope waveforms at important nodes of RDR*. Waveforms are matched with the expected results and shows relaxation oscillator behavior.

the time computations. Among the main components (Comparator OC, Switch, and LM 311 IC) considered, the integrator OA was observed to consume a significant portion of the power. The power consumed by the developed circuits is also comparable with the existing interface circuits for similar applications [145]. The waveforms at the important nodes of the RDR were recorded in an oscilloscope for cross-checking the methodology. These waveforms (given in Fig. 3.12) bear a close resemblance with the expected plots given in Fig. 3.2. Similarly, the waveforms of the RDR* circuit were also captured (See Fig. 3.13).

3.6. Performance Evaluation of RDR and RDR* with GMR Sensors

In this section, the developed RDR and RDR* are interfaced with commercially available GMR sensors, and the ability of the GMR + RDR systems to act as a linear magnetometer is verified. A brief explanation is given below.

3.6.1. GMR Sensors and Existing Interfaces

GMR sensors are low-cost, small-sized and rugged magnetometers that can be used to measure low magnetic fields (range ≈ 0.1 mT to 10 mT). These sensors also have high sensitivity and consume less power. These qualities make the GMR sensor an excellent choice for automotive and other industrial applications. Typically, these sensors are available in a bridge form, comprising two sensing GMR elements and two other magnetically-shielded GMRs. The resistance of the sensing GMR elements varies linearly with the applied field. As with other sensors, efficient electronic interfaces are required for GMR sensors as well. Application notes [37] prescribe the use of an IA and an ADC to condition the GMR sensor output. However, this costly interface yields a nonlinear output response. An alternate analog linearization circuit in [78] uses a reference voltage and a linearization Op-amp for GMR sensors. A dual-slope-based digitizer for the GMR sensor [81] provides a linear indication of the field but requires a long conversion time. The above discussion clearly shows that existing interfaces for

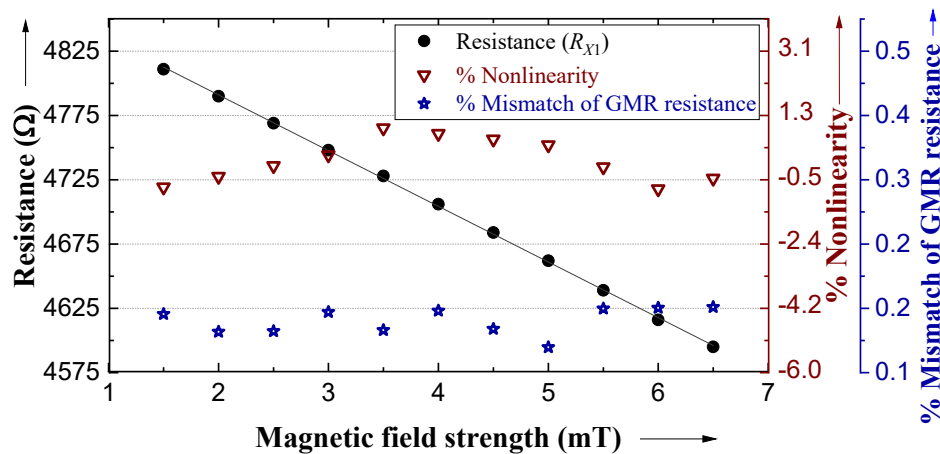


Fig. 3.14. Results obtained from characterization of AA005 GMR sensor IC.

GMR sensors have demerits like high cost, non-linear response, the need for reference voltage, etc. The developed simple RDR circuits are interfaced with a GMR sensor to realize a linear and efficient magnetometer.

3.6.2. Sensor-Characterization Studies

The GMR sensor was characterized first before interfacing with the RDR circuits. Two GMR ICs (AA004 and AA005 from NVE Corp.) of different measurement ranges were selected and studied. The procedure for the calibration of

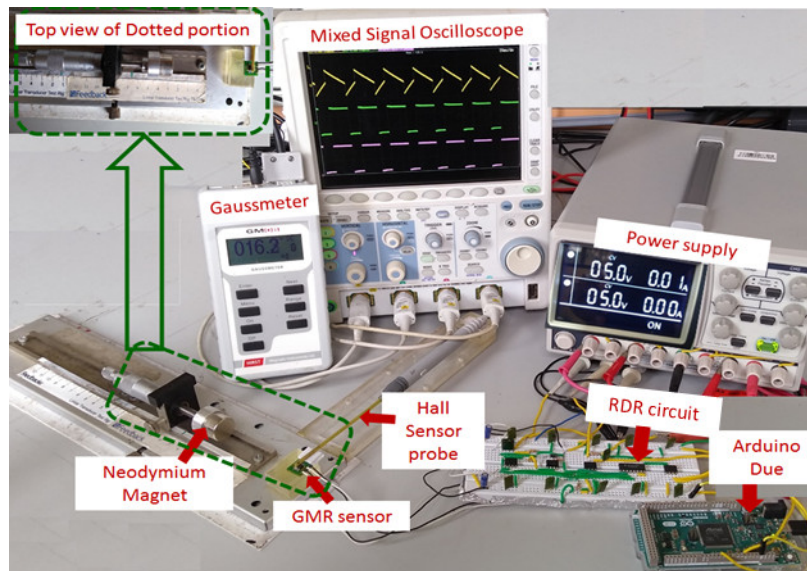


Fig. 3.15. Photograph of the developed RDR circuit being tested with a commercially available GMR sensor.

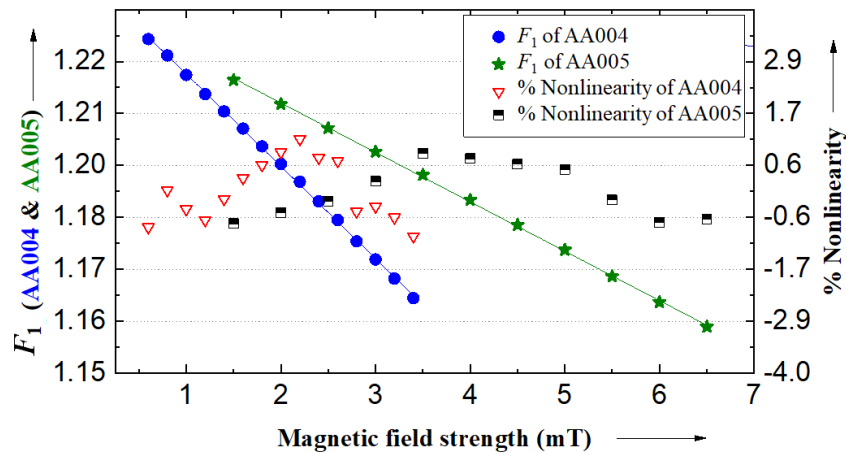


Fig. 3.16. Output of RDR observed when interfaced with GMR sensors.

GMR sensors was detailed in Section 2.7.2. These studies show the linear variation of sensing-GMR resistance (R_X) with B_{EXT} , belonging to the prescribed range (0.5 mT, 3.5 mT) of the IC. The maximum e_{NL} of R_X was obtained as 1.26 %. The worst-case mismatch is 5 Ω (0.1 %). The shielded GMR resistors were obtained as 4770 Ω and 4794 Ω from the above studies. Similar results were obtained when AA005 IC was characterized in its prescribed range of $B_{EXT} \in (1 \text{ mT}, 7 \text{ mT})$. The values of the shielded resistance were 4892 Ω and 4884 Ω . The linear response, e_{NL} , and mismatch pertaining to the AA005 IC can be inferred from Fig. 3.14. These studies show that the GMR sensors consist of linear variable-resistive elements for which the developed RDR and RDR* can be used as an interface.

3.6.3. Tests of the Combined GMR-RDR Instrumentation System

The GMR sensors, characterized in Section 3.6.2 were interfaced with the developed RDR and RDR*. A sensing resistance of the GMR sensor was used as R_X , whereas R_S was substituted with a shielded GMR resistance. A snapshot of the experimental setup is shown in Fig. 3.15. This figure shows the test-rig and other equipment used to test the developed RDR. The output F_1 of the RDR was noted for each B_{EXT} . The results obtained with AA004 and AA005 IC are shown in Fig. 3.16. Linear transfer characteristics can be seen in Fig. 3.16. Maximum e_{NL} was 1.15 % for

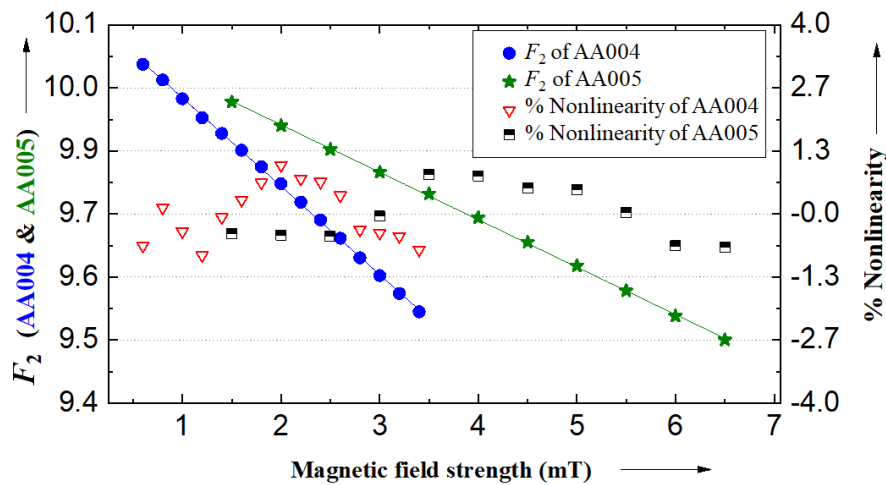


Fig. 3.17. Output versus magnetic field characteristics of GMR-RDR* instrumentation system.

AA004 sensor and 0.84 % for AA005 sensor. Similarly, the expected performance was also rendered by the RDR*. The results obtained with RDR* studies are shown in Fig. 3.17. The nonlinearity, e_{NL} of RDR* with the AA004 sensor was 1.03 % and that with AA005 was 0.83 %. The nonlinearity, e_{NL} observed in the GMR-RDR-based experiments is higher than e_{NL} values obtained in emulation studies. The increased e_{NL} is mainly contributed by the GMR sensor itself (see Fig. 3.14).

The RDR circuits, discussed above, are not suited for the wide-span processing of R_X . Moreover, there is no facility to reduce the execution time. The enhanced RDR_w, which was proposed to resolve these issues, is tested for performance in the next section.

3.7. Performance Verification of RDR_w Circuit

The RDR_w circuits were evaluated for performance using several tests, as described in the forthcoming sub-sections.

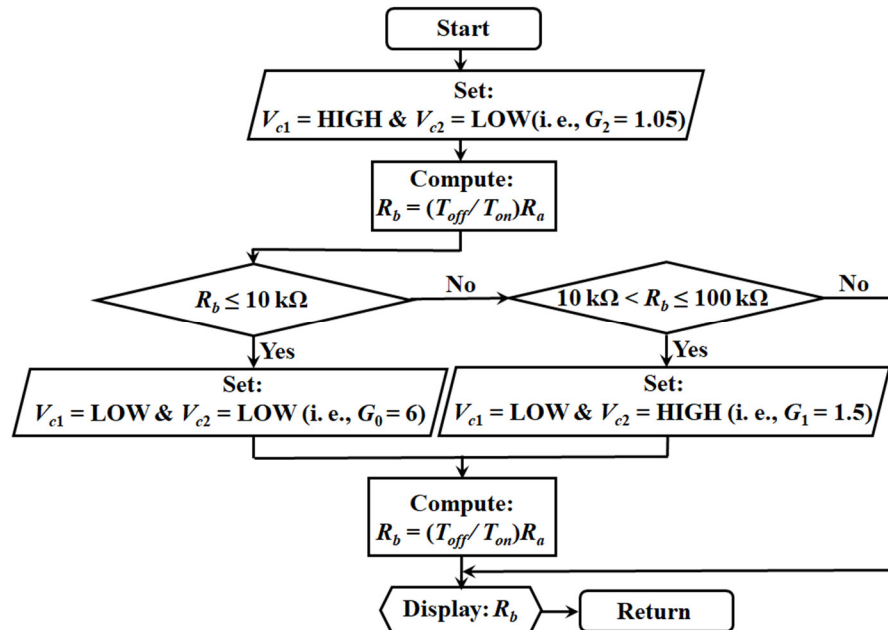


Fig. 3.18. Sequence of steps followed by TLU to compute R_b in RDR_w.

3.7.1. Simulation and Emulation Studies of RDR_w

The RDR_w was studied in simulation and using hardware-based emulations. LTspice was the simulation tool used, while the emulation studies were carried out using a bread-boarded model. Commercially available components were used in these studies. OP07 IC was used to realize the Op-amps (OP1 and OP3), and the comparator OP2 was developed using LM311 IC. All switches of RDR_w were implemented using MAX4053 IC, while the reference voltage $V_R (=1.2\text{ V})$ was built using LM385-1.2 IC. The power supply voltages used were $\pm 8\text{ V}$. The TLU was realized using an Arduino Due board which uses ATSAM3X8E as the microcontroller. The time measurements were done with the help of a timer/counter-0 module. An equivalent logic was used in

Table 3.1

Details and Results of Simulation and Emulation Studies of RDR_w

Circuit	Sensor model	Sensing element	Resistance range in k Ω	Gain	% e_{NL}	
					S	E
RDR _w	SE	R_X	1 – 10	$G_0 = 6$	0.04	0.07
			10 – 100	$G_1 = 1.5$		
			100 – 1000	$G_2 = 1.05$		
	DS	$R_X \& R_S$	10 – 110	1.05	0.05	0.07

S – Simulation results, E – Emulation results

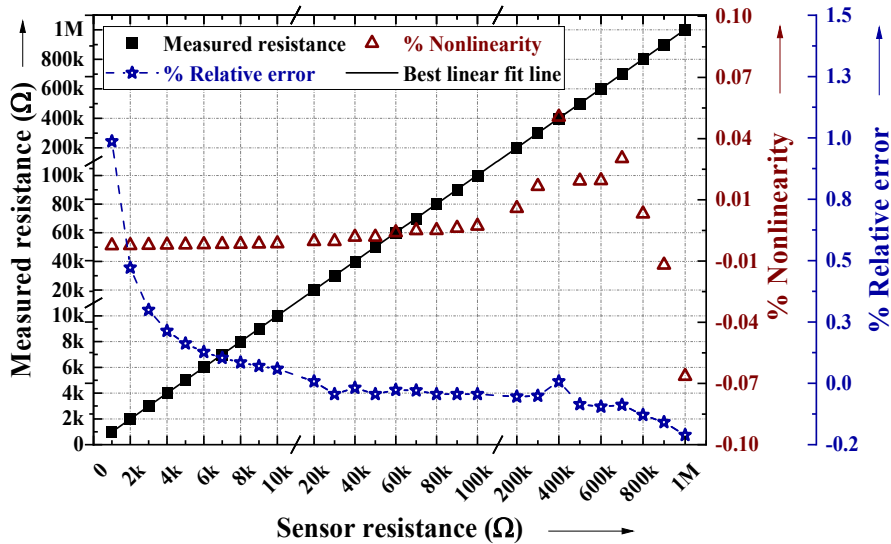


Fig. 3.19. Input-output characteristics of the developed RDR_w during hardware-based tests with SE-type sensor.

LTspice for simulations. The gain selection logic, as shown in the flowchart in Fig. 3.18, was implemented in the TLU.

First, the efficacy of RDR_w for SE-type was investigated. The resistor R_S was fixed as 100 k Ω . The sensor resistance, R_X was varied over a wide range (i. e., from 1 k Ω to 1 M Ω). A limit of 5 ms was taken for the T_{Xmax} , and T_{Xmin} was set to 500 μ s, based on the resolution of TLU and slew-rate considerations of Op-amps. Using (3.16), N_R was obtained as 3. The three regions are namely (1 k Ω , 10 k Ω), (10 k Ω , 100 k Ω), and (100 k Ω , 1 M Ω) for this case. The gain for each range was decided based on (3.17) and summarized in Table 3.1. The output, F was measured for different values of $R_b \in$ (1 k Ω , 1 M Ω) and the results are given in Table 3.1. The measured resistance was found to vary linearly with input resistance. The maximum e_{NL} observed from the simulation is 0.04 %. The linear input-output characteristic obtained from emulation studies is plotted and given in Fig. 3.19 (corresponding data are attached in Appendix B.2). It can be seen from Fig. 3.19 that the maximum e_{NL} observed from emulation is 0.07 %. The measured e_{REL} is also plotted in Fig. 3.19. The observed maximum error from Fig. 3.19 is 1 %. Thus, the above simulation and hardware studies corroborate well with each other as well as with the theoretical expectations. The power consumed by this prototype RDR_w was around 62 mW. The cardinal voltage waveforms of RDR_w observed using an oscilloscope are shown in Fig. 3.20. Fig. 3.20(a) shows the waveform in the first region of operation when $R_X = 5$ k Ω . The oscillogram when

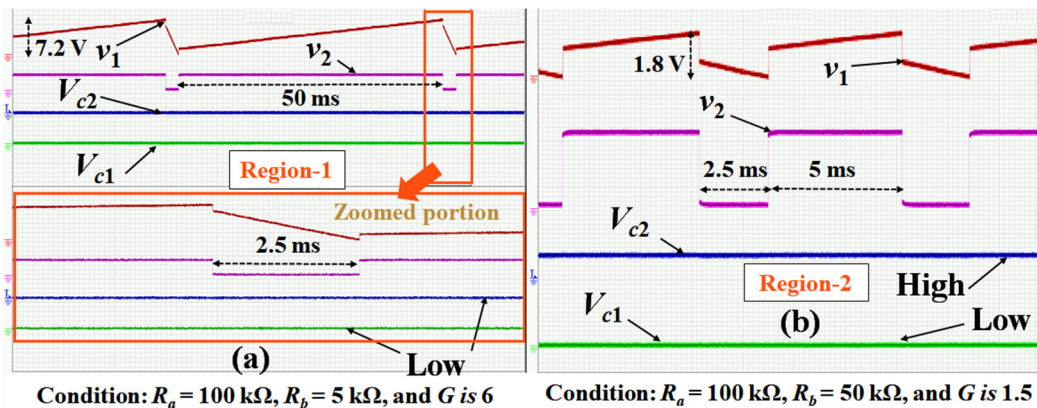


Fig. 3.20. Cardinal waveforms observed at different nodes of the proposed RDR_w are presented here. The waveforms in (a) and (b) are captured respectively, in region-1 and region-2 of RDR_w operation.

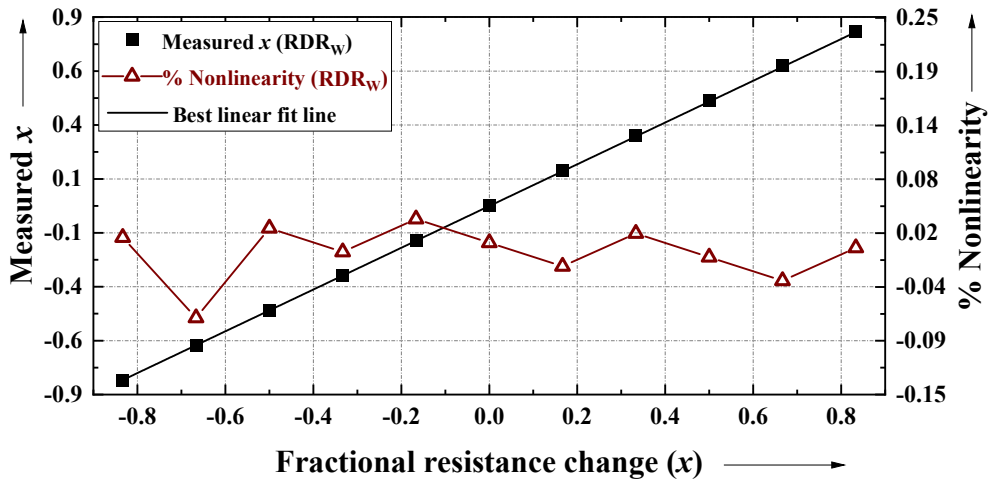


Fig. 3.21. Test results obtained on interfacing RDR_w with DS-type. e_{NL} of RDR_w on interfacing with DS is also plotted.

$R_X = 50 \text{ k}\Omega$ (second region) is given in Fig. 3.20(b). These waveforms are matched with Fig. 3.5. Similarly, the evaluation of RDR_w with DS was carried out. Here, R_0 was set to $60 \text{ k}\Omega$, and ‘ x ’ was varied from -0.83 to 0.83 . The output ‘ x ’ of the RDR_w was measured with the help of (3.15). The plot of the input-output characteristics is shown in Fig. 3.21. The emulation e_{NL} values for different values of x are also plotted in Fig. 3.21. The worst-case e_{NL} is 0.07% .

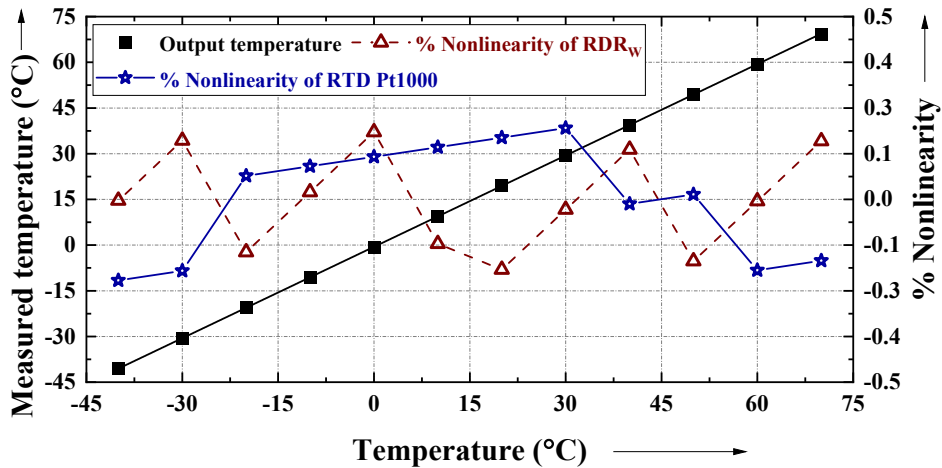


Fig. 3.22. Experimental results of the developed RDR_w when it is interfaced with the RTD-Pt 1000 temperature sensor. The inherent e_{NL} of the sensor is also plotted here.

Table 3.2

Estimated Values of Statistical Performance Parameters

Parameters	RDR _w	
	10 k Ω	100 k Ω
Signal-to-noise ratio (dB)	69.58	73.99
Standard deviation (%)	0.03	0.01
Resolution (ENOB) (bits)	11.3	12
Repeatability error (%)	0.001	0.01

3.7.2. Experimental Studies of RDR_w Circuit with RTD characteristics

The real-time capability of RDR_w towards SE sensor interfacing was further validated using RTD-Pt1000 temperature sensor characteristics [154]. The sensor has an inherent e_{NL} of 0.22 % for the range of -40 °C to 70 °C [154]. This sensor was emulated using decade resistance boxes. The output (plotted in Fig. 3.22) was seen to obey a linear relation with temperature. The maximum e_{NL} is 0.2 %, as can be seen from the scatter + dashed-line plot of Fig. 3.22. The measured e_{NL} is higher in experimental studies than in the emulation and it is mainly due to the inherent e_{NL} of the temperature sensor.

3.7.3. Additional Performance Tests

The performance parameters like Signal-to-Noise Ratio (SNR), Standard deviation (σ), Effective Number Of Bits (ENOB), and Repeatability Error (R_E) were found for RDR_w. The expressions used to compute these parameters are given in Appendix A.

The above studies were done for SE-type sensor configuration for two values of R_X (i. e., 10 k Ω , and 100 k Ω). The results were obtained using 400 consecutive measurements. The values estimated for the performance parameters are given in Table 3.2. From Table 3.2, it can be observed that the RDR_w has an SNR of 73.99 dB. Similarly, the repeatability error is also admirable (≈ 0.01 %). In addition, the above results are also comparable with the schemes in [60], [102], [155]-[157]. These results

Table 3.3

Comparison Study of Proposed Techniques with Existing Interface Circuits

Parameters	[98]	[81]	[91]	[101]	[102]	[103]	[105]	[158]	[60]	[93]	[94]	[80]	[82]	[159]	[110]	DCR	RDR	RDR*	RDR _w	
Technique	PWC	DS	DM	Σ - Δ	RO				DM			DS		3 PT	RO	DS	RO			
Sensor configuration	QB	HB	DS		SE	QB & FB	SE	FB	SE			FB		SE	SE, DS, HB	SE & QB		SE & DS		
Need of V_R	Yes		No	Yes		No		Yes	No			Yes	No	Yes		No		Yes		
Suitability for wide range measurement	No				Yes	No								Yes	No			Yes		
Facility to reduce conversion time	No																			Yes
Current preset facility	No															Yes	No			
Power supply effects	Yes	No	Yes	No	Yes						No	Yes		No						
Conversion time reduction	No																		Yes	
% e_{NL}	0.06	0.26	0.01	0.15	0.06	1	0.1	2	0.06	NA		0.2	0.5	1	0.06	0.05	0.08	0.07		
Resolution	1 Ω	NA	13b	NA		1 Ω	0.1 μ s	0.4 μ Ω	0.03 Ω	1 $^{\circ}$ C	0.1 Ω	NA	12.6b	NA		0.06 Ω	0.5 Ω		12b	
Conversion time (ms)	14	100		40	1980	NA	124	NA	6	NA		100	330	80	1320	10	40		55	
Complexity	High	Low				High	Low	High	Low			High		Low						
Sensors considered	RTD	GMR	---			Humidity sensor, RTD	---	Pressure sensor	RTD			Load cell	Pressure sensor & Strain gauge	NA	RTD, Displacement sensor, GMR	GMR		RTD		
Special requirements	#	♣	♠	♣	♥	Complex circuit	---	♠			♣, ♥	♣	---	♣, ♥	---			Difficulty in resistor-selection		

PWC – Pulse Width Conversion, DS – Dual-Slope, DM – Direct Microcontroller, Σ - Δ – Sigma-Delta, RO – Relaxation Oscillator, 3 PT – 3 Point Technique, NA – Not Available, V_R – Reference voltage, b – bits, # - Current source, ♠ - Assumes that threshold voltage of the microcontroller is same during the charging and discharging phases ♥ - Bipolar matched reference voltages, ♣ - Intermittent calibration/compensation is needed to compensate for switch/pin resistances

show that the real-time performance of the developed circuits is satisfactory, and it can be useful for non-remote resistance measurement applications.

3.7.4. Comparison with State-of-Art

The developed DCR, RDR, RDR*, and RDR_w were compared with the state-of-art works. The outcome of the comparison is given in Table 3.3. Table 3.3 shows the various properties like the technique used, sensor configurations, conversion time, e_{NL} , resolution, etc. From Table 3.3, it can be observed that the RDR and RDR* show almost equal performance except for the conversion time. The RDR and RDR* show comparable/superior performance than the existing interfaces for resistive sensors. In addition, RDR and RDR* circuits do not require a reference voltage source. On the other hand, the developed RDR_w circuit is suitable for a wide range of resistance measurements. This circuit requires a single reference voltage source, and the output is independent of many circuit nonidealities. In addition, the facility of conversion time reduction is a superior feature than the existing techniques. This shows that high resistance can also be measured in low conversion time. However, the selection of passive components of PGA is difficult.

3.8. Summary

The elaborate analysis as well as simulation and experimental studies, given in the previous sections, proved the efficacy of the developed RDR circuits and their utility to build a linear GMR-based magnetometer. The developed novel GMR-RDR magnetometer provides better performance than existing interfaces for GMR sensors. The RDR circuits, in general, were also compared with different digital interfaces for non-remote resistive sensors. It is quite clear that RDR and RDR* systems offer an efficient interface for non-remote resistive sensors with many positive features such as simple design, non-requirement of V_R , low complexity, and negligible dependence on power-supply drifts, etc. compared to the existing digital interfaces. The performance parameters like e_{NL} , resolution, and conversion time were also superior or comparable with the existing schemes.

Later, an enhanced version of RDR (i. e., RDR_w) was proposed for wide-span resistive sensors. Design, working, and analysis of the RDR_w and their detailed performance evaluations were explained. Test results demonstrate that RDR_w served as a direct digitizer for resistive sensors in SE and DS configurations and they rendered all expected features. The performance of the developed schemes was also evaluated against existing works, and it can be deduced that the developed novel design of RDR_w is superior or equivalent, in most of the performance measures (conversion time, good linearity, high resolution), to the existing works for non-remote resistive sensors. In addition, the use of enhanced digitizing architectures with standard blocks such as integrator, comparator, and amplifier with tunable gain values are compatible for the VLSI implementation of the developed circuits [133]. Concluding, the developed RDR_w can serve as an efficient digital signal conditioner for resistive sensors, especially in various practical situations, where wide-span or non-remote measurement is required.

It can be inferred that the developed circuits (DCR, RDR, RDR*, and RDR_w) are not suitable for remotely located resistive sensors. Digitizing techniques that can work with remotely located resistive sensors are explained in the next chapter.

Chapter 4

Design of Digitizing Circuits for Remotely Connected Resistive Sensors

4.1. Introduction

In some of the industrial scenarios, resistive sensors need to be placed at remote locations, where it is difficult to accommodate the electronics. Measurement of water temperature in thermal power plants and oil temperature in petroleum industries are a few examples where remote measurement becomes important. In these situations, the electronics cannot be placed near to tank due to their hazardous nature of the plant. This chapter proposes two-wire, three-wire, and six-wire schemes for SE and bridge-based sensors. The two-wire scheme is useful where low cost and low complexity is the main concern. The three-wire scheme can be adapted where accuracy is an important need. Likewise, a six-wire scheme is essential for remotely-connected bridge sensors. Initially, the chapter reports enhanced interfaces, with inbuilt wire resistance compensation. The design of these interfaces is adapted/inspired from the methodology presented in Chapter 3. Later, a universal digitizer for bridge-connected resistive sensors is also detailed. This chapter first explains the existing interfaces for remote

This chapter is partially adapted from the post-print versions of

(1) Elangovan K and Anoop C. S., "Simple and Efficient Relaxation-Oscillator-Based Digital Techniques for Resistive Sensors — Design and Performance Evaluation," in *IEEE Transactions on Instrumentation and Measurement*, vol. 69, no. 9, pp. 6070-6079, Sept. 2020.

(2) Elangovan K and Anoop C. S., "Evaluation of New Digital Signal Conditioning Techniques for Resistive Sensors in Some Practically Relevant Scenarios," in *IEEE Transactions on Instrumentation and Measurement*, vol. 70, pp. 1-9, 2021, Art no. 2004709.

(3) Elangovan K and Anoop C. S., "An Efficient Universal Digitizer With Linear Transfer Characteristic for Resistive Sensor Bridges," in *IEEE Transactions on Instrumentation and Measurement*, vol. 70, pp. 1-4, 2021, Art no. 2004904.

Table 4.1

Literature map of Various Schemes for Remote Resistance Measurements

References	Adapted scheme/Number of wires needed	Adaptable configuration	Conversion cycles	Prototype developed				Comments
				% e_{NL}	% e_{REL}	Conversion time (ms)	Range (in dB) [#]	
[60]	Twin-diode/2-wire	SE	3	NA	0.06	5.3	3.52	Mismatch in upper threshold voltage of μc causes an error
[61]			2	0.3	0.12	2.58		* Needs to find transformation constant
[62]				0.1	0.9	0.2	20	Complex architecture and high error in output
[64]	Current conveyor-based/3 wire		Not applicable	NA	0.16	Not applicable	6.94	Complex architecture and no experimentally verified data
[114]	Direct interface/4-wire		3	0.02	NA	60	25.6	Excellent linearity, however, requires a number of μc pins and high-resolution μc to reduce the errors due to the counter.
[115]	Self-balance/4-wire		1	0.3		15.3	40	Complex circuit, requiring waveform generator
[85]	Dual-slope/5-wire	0.09		333		6.02	Complex architecture with more wires	

– Range (in dB) = $20\log(\text{Maximum measurable resistance}/\text{Minimum measurable resistance})$, NA – Not Available, * – Mismatch in diode ON-state forward voltage drop causes an output error, μc – Microcontroller.

resistive sensors in the next section. This is followed by the methodology and performance evaluation of the proposed digitizing interfaces for remote resistive sensors.

4.2. Interfaces for Remotely Connected Resistive Sensors

As discussed in Section 1.4.3, the resistance of connecting leads can introduce a measurement error, in case of remotely-linked resistive sensors. Hence, the digitizers should be equipped with adequate lead wire compensation techniques. A brief summary of such compensation methods was introduced in Section 1.5. A detailed explanation of the existing interfacing schemes adapted with the above methods is given next. The remote resistive sensors can be connected to the electronics using two or three or four or six wires. The detailed literature map is given in Table 4.1 for remote resistive sensors. The two-wire scheme can cause an error in the output. The two-wire measurement technique has been enhanced with the help of a twin-diode arrangement in [60]-[63], [143]. This helps to retain the benefit of reduced connecting leads (and hence, wiring infrastructure) and achieve independence from wire resistances. This scheme is only suitable for SE-based sensors. In addition, it is expected that the twin-diodes are matched. Any mismatch or deviation in the ON-state forward voltage drop of the diodes can lead to an output error in these schemes. It is practically difficult to ensure a low mismatch in diode ON-state forward voltage drop due to the dependency on many parameters including the current flowing through the diodes.

The above-discussed problem can be solved by using additional connecting wires. An analog interface realizing the three-wire technique is reported in [64], [65]. Similarly, a digitizing scheme interfacing a three-wire resistive sensor is available in [144], [155]. In three-wire technique, the mismatch in wire resistance can cause an error. However, the magnitude of this error is much smaller than the error present in the two-wire case [155]. Thus, the measurement philosophy of three-wire linked resistive sensing, followed in [64], [65], [144], [155], is advantageous over the technique followed in [60]-[63], [143]. Digitizing interfaces using more than three

wires are also being investigated and described in recent research [85], [86], [114], [115], [156]. A dual-slope circuitry is employed in [85]. However, the circuit in [85] needs an instrumentation amplifier which is costly. The digitizer proposed in [114] is developed for four-wire connected sensors in SE configuration. This circuit works based on the charge-discharge principle and requires three conversion cycles. This scheme is immune to the wire resistances and their mismatches. The work reported in [115] nullifies the effect of wire resistance using the self-balancing technique. The work reported in [156] uses a six-wire technique, for remote bridge-type sensors. This circuit works based on the dual-slope principle and shows an output that is independent of mismatches of wire resistances and parasitic elements of the sensor. Nevertheless, the use of a large number of wires can increase the system's cost.

This chapter initially discusses the design and working principle of the relaxation oscillator-based digitizer for remotely connected resistive sensors. This circuit requires a twin diode arrangement to nullify the effect of the connecting wire resistances. Later, the relaxation oscillator technique is enhanced to adapt with both SE and DS using one additional connecting wire. This three-wire scheme reduces the error present in the twin diode scheme as well. Finally, a dual-slope-based technique is proposed for remotely connected bridge-based resistive sensors. An extensive analysis of these circuits is given in the upcoming sections.

4.3. Digitizer for Remotely Connected Resistive Sensors

The working principle of digitizing interfaces for various types of remotely connected resistive sensors is discussed in this section.

4.3.1. Digitizer for Remote Resistive sensors (DRR-1)

The circuit diagram of the proposed digitizer for remote resistive (DRR-1) sensors is shown in Fig. 4.1. This circuit is improved from the relaxation oscillator technique presented in Section 3.2 and the two-wire method given in Section 4.2. The circuit retains all the benefits of the relaxation oscillator technique and provides wire resistance compensation. Here, the resistive sensor is shown as R_X . A single-element

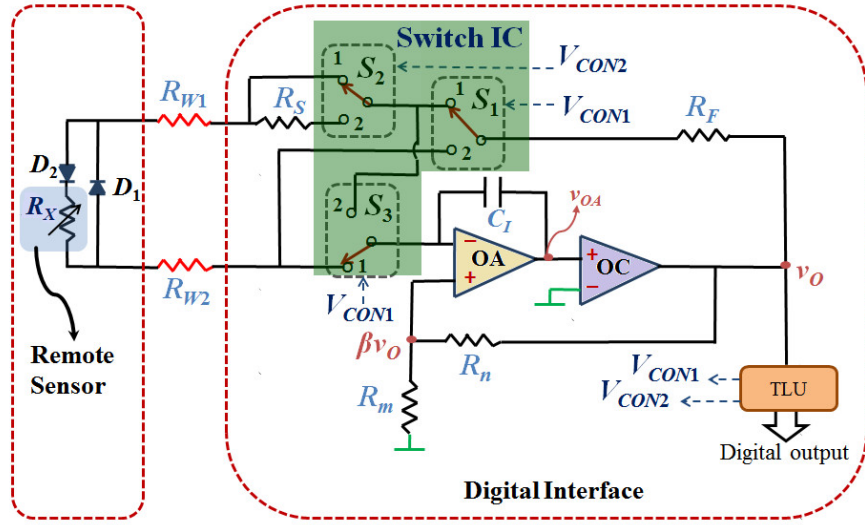


Fig. 4.1. Circuit diagram of the digitizer (DRR-1) for remote resistive sensors.

resistive sensor is considered, as this configuration was shown to exhibit significant error (vide Section 1.4.3). Two matched diodes D_1 and D_2 (marked in blue color) are placed, along with R_X , at the remote location as shown in Fig. 4.1. These elements (R_X , D_1 , and D_2) are connected to the DRR-1 using two wires of resistance R_{W1} and R_{W2} . The DRR-1 has a switch IC [150] comprising three switches S_1 , S_2 , S_3 , and resistances R_S and R_F . These switches, D_1 , D_2 , and an intelligent logic, controlled by the digital signals (V_{CON1} and V_{CON2}), help to achieve wire-resistance compensation, and the corresponding waveforms are depicted in Fig. 4.2. The switching logic can be easily understood in Table 4.2.

DRR-1 has three modes of operation executed in sequence. The status of the control signals and the position of switches for these modes are illustrated in Table 4.2. Table 4.2 also shows the effective input resistance (R_{eqi}) of the integrator in each mode. Here, R_{COM} is used to represent the common value of R_{eqi} , which is present in all three modes. It equals $R_F + R_{SW1} + R_{SW2} + R_{SW3} + R_{W1} + R_{W2}$, where R_{SW1} , R_{SW2} , and R_{SW3} correspond, respectively, to the on-resistances of switches S_1 , S_2 , and S_3 . In each mode, the DRR-1 will act as a relaxation oscillator and it will produce a square waveform, v_O [having T_{ON} and T_{OFF} as in Fig. 4.2]. The working mechanism of DRR-1 is the same as RDR circuits except for the input resistances of the integrator (R_{eq}). Thus, the expression for on-time (T_{ONi}) for i^{th} mode can be derived and written in (4.1).

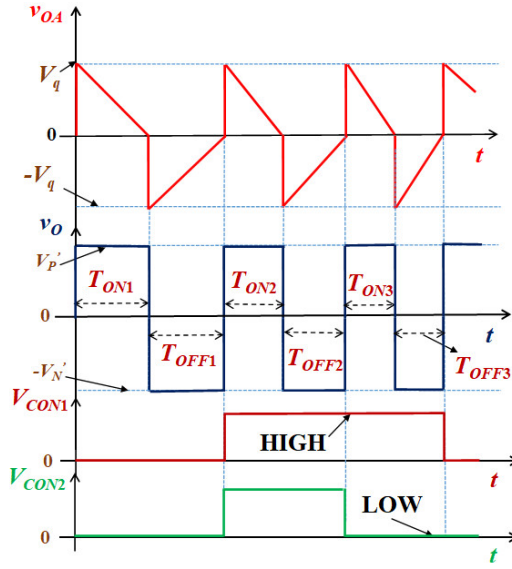


Fig. 4.2. Important waveforms of DRR-1. Control signals, V_{CON1} and V_{CON2} are also depicted.

$$T_{ONi} = kR_{eqi} \quad (4.1)$$

Here, the equation of k is as per (4.2).

$$k = \frac{\beta(V_p' + V_N')C_I}{V_p'(1 - \beta) - V_\gamma} \quad (4.2)$$

Here, V_γ denotes the ON-state forward voltage drop of the diode and $\beta = R_m / (R_m + R_n)$. In other words, the expressions of on-times follow (4.3).

$$T_{ON1} = k(R_G + R_{COM}); T_{ON2} = k(R_S + R_{COM}); T_{ON3} = k(R_{COM}) \quad (4.3)$$

T_{ON1} contains information about R_X . However, it depends on undesired parameters like

Table 4.2
Modes of Operation of DRR-1

Mode	Signal status		Position of switch			Input resistance (R_{eqi}) of integrator
	V_{CON1}	V_{CON2}	S_1	S_2	S_3	
1	0	0	1	1	1	$R_{eq1} = R_X + R_{COM}^*$
2	1	1	2	2	2	$R_{eq2} = R_S + R_{COM}^*$
3	1	0	2	1	2	$R_{eq3} = R_{COM}^*$

* R_{COM} – Common input resistance present in each mode

wire resistance (R_{W1} and R_{W2}), switch resistances (R_{SW1} , R_{SW2} , and R_{SW3}), and V_γ . An output, compensated from these non-idealities can be achieved by using the compensation function given in (4.4).

$$F_1 = \frac{T_{ON1} - T_{ON3}}{T_{ON2} - T_{ON3}} \quad (4.4)$$

Substituting (4.3) in (4.4), F_1 simplifies as in (4.5).

$$F_1 = \frac{k(R_G + R_{COM}) - k(R_{COM})}{k(R_S + R_{COM}) - k(R_{COM})} = \frac{R_X}{R_S} \quad (4.5)$$

Equation (4.5) clearly shows that F_1 provides a measure of R_X , without dependence on R_W . This proof shows the DRR-1 can provide an output proportional to R_X and independent of wire resistances. Hence, DRR-1 is suitable for remote resistive sensors. However, the DRR-1 scheme requires the availability of matched diodes. Any difference between the properties (such as ON-state forward voltage drop and on-resistance) of the diodes can bring considerable errors. The effect of these errors will be quantified and given in Section 4.4.1. An improved digitizer which is derived from the above issues is explained next.

4.3.2. Improved Relaxation Oscillator-based Digitizer (DRR-2)

The circuit schematic of the improved relaxation-oscillator-based digitizer for remote resistive sensors (DRR-2) is shown in Fig. 4.3. This circuit is an adapted version of RDR_W (discussed in Section 3.3). The DRR-2 connects the resistive sensor elements (R_X and R_S) to the electronic section, using three wires, each with resistance, of say, R_w . The major modification in the electronics of DRR-2 (when compared to RDR_W) includes a switch ' S_{w2} ' and a discrete resistor, R . A control signal, V_S sets the position of S_{w2} . The DRR-2 operates in two modes, depending on the state of V_S . In the first mode (say, mode-1), V_S will be in a high-state, which sets $S_{w2} \rightarrow 0$. Then, the DRR-2 works in the same manner as in RDR_W.

Let us consider that the output of the comparator, v_2 is at logic-high. This sets the switch, S_{w1} to position-1. This ensures that $v_3 = V_R$ and $v_4 = GV_R$ where G represents

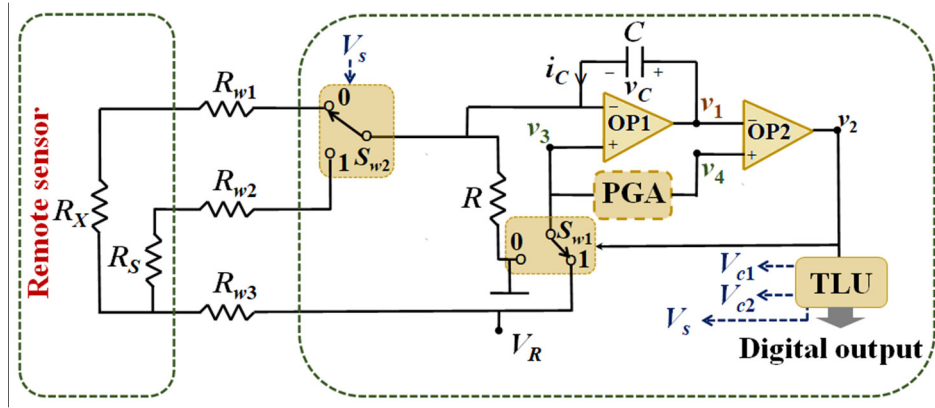


Fig. 4.3. Circuit schematic of the Digitizer for Remote Resistive sensors (DRR-2).

the gain of the PGA (PGA of DRR-2 plays a similar role as that of RDR_w). The current, i_C will be equal to $i_C = V_R / R$. As a result, the integrator output (v_1) will charge up to GV_R (see Fig. 4.4). The on-time duration (T_{ON1}) of the signal, v_2 is given in (4.6).

$$T_{ON1} = (G-1)RC \quad (4.6)$$

When v_1 crosses GV_R , the comparator output, v_2 will change to low-state. In this phase, the switch, S_{w1} will be at position-0, causing $v_3 = v_4 = 0$. Now, the current of $i_C = -V_R / (R_X + R_{S_{w2}} + 2R_w)$ will flow through the capacitor where $R_{S_{w2}}$ stands for the on-resistance of S_{w2} . At this instant, the integrator will start to discharge towards zero

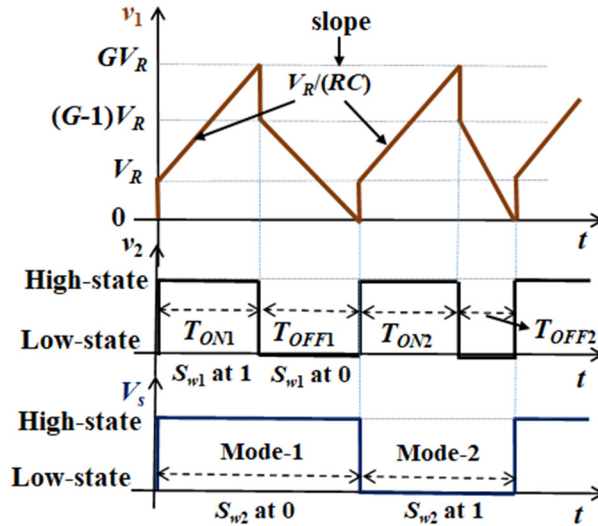


Fig. 4.4. Typical waveforms at the nodes v_1 and v_2 of DRR-2. Control signal, V_s is also depicted.

potential. This discharging will pursue till v_1 becomes v_4 (i.e., 0) (see Fig. 4.4). This indicates the start of the mode-2 operation. The off-time duration (say, T_{OFF1}) of v_2 can be derived as given in (4.7).

$$T_{OFF1} = (G-1)(R_X + R_{sw2} + 2R_w)C \quad (4.7)$$

Once mode-1 is over, mode-2 is initiated by placing $S_{w2} \rightarrow 1$ (i. e., $V_S = 0$). The on-time (say, T_{ON2}) of v_2 will remain the same as in mode-1 [see Fig. 4.4]. At the end on-time duration, the comparator alters the position of the switch, S_{w1} from 1 to 0. Thus, the integrator will start to discharge and the off-time (say, T_{OFF2}) will follow (4.8).

$$T_{OFF2} = (G-1)(R_S + R_{sw2} + 2R_w)C \quad (4.8)$$

Now, a function ' F_2 ' can be used to achieve independence from R_w . The expression of F_2 and its simplified version [obtained with the help of (4.6), (4.7), and (4.8)] is given in (4.9).

$$F_2 = \frac{T_{OFF1} - T_{OFF2}}{T_{ON1}} \quad (4.9)$$

Substituting (4.6), (4.7), and (4.8), the expression for F_2 can be simplified and given in (4.10).

$$F_2 = \frac{R_X - R_S}{R} \quad (4.10)$$

This equation clearly demonstrates that DRR-2 can render an output that depends on R_X and R_S , and not on R_w . The sensor, R_X being of SE-type, then the resistance of R_X can be found using F_2 , as written in (4.11).

$$R_X = F_2 R + R_S \quad (4.11)$$

In case DS is interfaced to the DRR-2 circuit, then the fractional resistance change ' x ' can be found using (4.10) and it is equal to $F_2 / 2$. This can be achieved by selecting the resistance R to be equal to R_0 (i. e., nominal resistance of the sensor).

Thus, the DRR-2 retains all the merits of RDR_w, and it uses an additional operational cycle and an intelligent methodology to achieve compatibility with remote-resistive sensors. In addition, the DRR-2 does not use matched diodes and it is suitable for DS. Hence, DRR-2 is expected to give better performance than DRR-1. Many of the industrial resistive sensors are available in bridge configurations (QB, HB, and FB). Next, a universal digitizer for remotely located resistive sensor bridges is proposed.

4.3.3. Universal Digitizer for Remotely Located Resistive-Bridge Sensors (DRR-3)

The DRR-3 circuit designed for a remote resistive bridge is shown in Fig. 4.5. The bridge, comprising the sensor elements (R_1 to R_4), is linked to the DRR-3 using a special wiring scheme (see Fig. 4.5). The circuit is made of two excitation-helper Op-amps A_1 and A_2 , an integrator A_3 , a comparator A_4 , and a Timing and Logic Unit (TLU). The wires are shown using six different resistors (R_{w1} to R_{w6}) to reflect the imbalanced wire impedances. Two switches S_1 and S_2 , controlled by the digital signals v_{c1} and v_{c2} from TLU, ensure the proper operation of DRR-3. These switches are set to position-0 if their control signal is logic-high and to position-1, otherwise. The operation of DRR-3 is explained next.

The DRR-3 ensures that the current through the wire impedances R_{w1} , R_{w3} , R_{w4} , and R_{w6} is zero. This sets $V_e = V_R$ and $V_g = 0$, where V_e and V_g are the voltages of

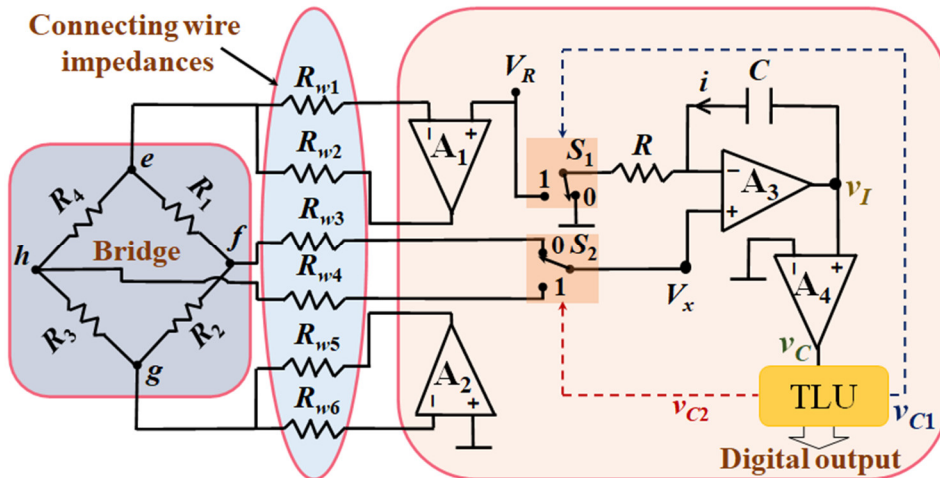


Fig. 4.5. Proposed DRR-3 circuit for bridge-connected resistive sensors.

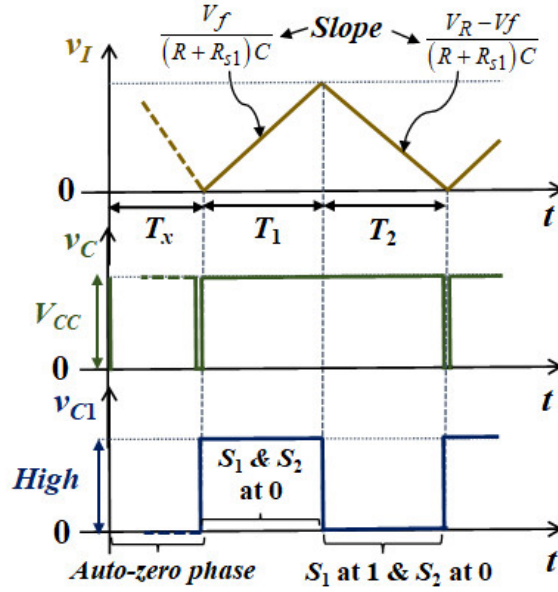


Fig. 4.6. Typical waveforms at the nodes v_I and v_C and the control signal, v_{C1} of DRR-3.

nodes- e and g . The wires having the impedances R_{w2} and R_{w5} complete the negative feedback of A_1 and A_2 . These wires will not affect the potential of nodes e and g . As a result, the bridge outputs, V_f and V_h will, respectively, be equal to $V_R \times R_2 / (R_1 + R_2)$ and $V_R \times R_3 / (R_3 + R_4)$.

The operation of the DRR-3 includes an auto-zero phase and a measurement phase. In the former phase, the integrator output, v_I is brought towards zero, from an arbitrary initial value. This is done by sensing the state of v_C and appropriately setting the position of the switch S_1 . For instance, S_1 will be set to position-1 if $v_C = \text{high}$ and position-0, otherwise. In this configuration, the voltage v_I will ramp towards zero, as shown in Fig. 4.6 [see the duration, T_x].

Next, the measurement phase is initiated. Assume, S_1 and S_2 are at position-0 (i. e., $v_{C1} = v_{C2} = \text{high-state}$). Then, $V_x = V_f$. In this case, a fixed current $i = V_f / (R + R_{s1})$ will flow through the capacitor C . Here, R_{s1} stands for the on-resistance of S_1 . Hence, the output voltage of the integrator will ramp up (see Fig. 4.6) and it follows (4.12).

$$v_I(t) = \frac{1}{C} \int i dt \quad (4.12)$$

This process will be continued for a preset duration of T_1 seconds, and $v_I(T_x + T_1)$ is

Table 4.3

Adaptable Bridge Configurations of DRR-3

Bridge type	Bridge elements	Time-based equations
QB	$R_1 = R_3 = R_4 = R_0, R_2 = R_x$	$R_x = (T_2 / T_1) \times R_0$
HB	$R_1 = R_3 = R_0, R_2 = R_4 = R_x$	
FB	$R_1 = R_3 = R_0 (1 - x), R_2 = R_4 = R_0 (1 + x)$	$x = (T_2 - T_1) / (T_2 + T_1)$
IFB	$R_1 = R_3 = R_0 / (1 - x), R_2 = R_4 = R_0 / (1 + x)$	$x = (T_1 - T_2) / (T_1 + T_2)$
R_x - sensor element, R_0 - Nominal value of the resistive sensor		

given in (4.13).

$$v_I(T_x + T_1) = \left(\frac{V_f}{(R + R_{s1})C} \right) T_1 \quad (4.13)$$

At the end of $T_x + T_1$, the TLU sets the switch S_1 to position-1. As a result, the current $i = (V_f - V_R) / (R + R_{s1})$. This discharges the signal, v_I towards the ground potential (i. e., threshold voltage of A4). The expression $v_I(t)$ follows (4.14).

$$v_I(t) = \left(\frac{V_f}{(R + R_{s1})C} \right) T_1 - \frac{V_R - V_f}{(R + R_{s1})C} (t - T_x - T_1) \quad (4.14)$$

As soon as $v_I(t)$ crosses zero, A4 will trigger a high-to-low transition at its output, which again sets the position of S_1 to 0. This will mark the end of one measurement cycle. Let T_2 be the duration of the discharge mode. By using the condition $v_I(T_x + T_1 + T_2) = 0$, the equation (4.15) can be obtained when $S_2 \rightarrow 0$.

$$\frac{T_2}{T_1} = \frac{V_f}{V_R - V_f} = \frac{R_2}{R_1} [S_2 \rightarrow 0] \quad (4.15)$$

It can be seen that the information about R_1 and R_2 can be extracted from (4.15). Equation (4.15) can be manipulated to adapt DRR-3 for all the bridge types. A summary of the time-based equations for different bridge types is given in Table 4.3. Latter also shows the nature of the sensor elements for each case. For example, in the case of a QB-type sensor, R_2 is the sensor resistance (R_x), and the other elements are

fixed at R_0 . Thus, the expression $(T_2 / T_1) \times R_0$ can give a linear estimate of R_X . Likewise, FB sensors obey $R_1 = R_3 = R_0 \times (1 - x)$ and $R_2 = R_4 = R_0 \times (1 + x)$, where x is the fractional change in resistance. The value of ‘ x ’ can be ascertained using the expression shown in Table 4.3. The DRR-3 expressions which are compatible with HB and Inverse Full-Bridge (IFB) are also given in Table 4.3. Thus, DRR-3 serves as a universal linear-digital interface for bridge-based measurements.

The DRR-3-output is unaffected by various parameters such as R_{s1} , V_R , R , C , and their drifts. In addition, the scheme nullifies the effects of wire impedances and their imbalances, if any. In the preceding explanation, switch S_2 was linked to position-0. The DRR-3 can also operate by setting S_2 to position-1 (i. e., $v_{c2} = \text{low-state}$). In this case, the voltage of node- h will be connected to V_x . The operation of DRR-3 will remain similar to the previous case. The equation of T_2 / T_1 can be obtained as in (4.16).

$$\frac{T_2}{T_1} = \frac{V_h}{V_R - V_h} = \frac{R_3}{R_4} [S_2 \rightarrow 1] \quad (4.16)$$

A linear estimate of R_X or x can be obtained using (4.16). This approach guarantees two benefits – (1) the effect of mismatch among the sensor elements can be avoided [160], (2) increased reliability for some bridge scenarios as the voltage of either node- f or h can be used as V_x (redundancy feature). A simplified version of DRR-3 can be used for non-remote resistive sensors. Here, the DRR-3 circuit can be further simplified by avoiding A_1 and A_2 . In other words, the node- e and $-g$ can be directly connected, respectively, to V_R and ground for such bridge scenarios.

Parasitic capacitors (say, C_p) can present (in parallel) with each of the sensor elements in few-bridge cases. The voltages at the nodes- f and h of the DC-excited DRR-3 are always a constant for a particular condition of bridge elements. Thus, the voltage across the C_p 's is also fixed, regardless of the transitions of the switch positions. Hence, the DRR-3 output is independent of C_p . Similarly, parasitic capacitances can be also present across the connecting wires. However, in the DRR-3 circuit, the voltage across these parasitic capacitors is a fixed value for a particular condition of the bridge elements. Therefore, the DRR-3 output is also immune to the effect of the parasitic

capacitance of the connecting wires.

4.4. Error Analysis

The error analysis of the DRR circuits is carried out, as explained next.

4.4.1. Errors Sources of DRR-1

The effect of different circuit parameters on DRR-1 is discussed in this subsection. As can be observed from (4.5), the DRR-1 gives an output, independent of many non-idealities including wire and switch resistances, and V_γ . However, the static non-idealities of OA and OC can modify its output function F_1 (to F_1^*). The modified function, F_1^* is given in (4.17).

$$F_1^* = F_1 \left[\frac{V_p'(1-\beta) - V_{OS1} - i_{N1}R_{eq2} - \beta i_{p1}R_n}{V_p'(1-\beta) - V_{OS1} - i_{N1}R_{eq1} - \beta i_{p1}R_n} \right] \quad (4.17)$$

In (4.17), the symbols V_{OS1} , i_{p1} , and i_{N1} are the offset voltage and bias current of OA. The expression (4.17) clearly shows that the DRR-1 is independent of the offset voltage (V_{OS2}) of OC. The error in F_1 is negligible if OP07 IC is used for the Op-amp OA. The effect of mismatch in V_γ of diodes is analyzed. The plot of relative error in the twin diode (e_{TWO}) scheme for different practical values of ΔV_γ [161], [162] is shown in Fig. 4.7. For instance, this error, e_{TWO} becomes significant (1.7 %) for a ΔV_γ of 2.5 mV.

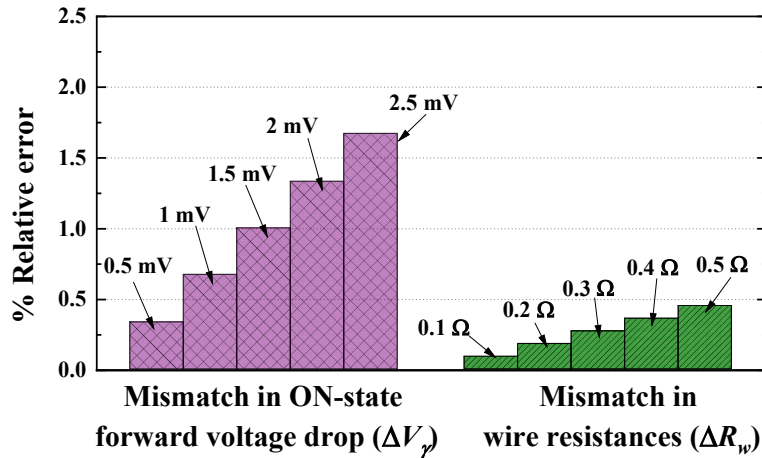


Fig. 4.7. Comparison study between the DRR-1 and DRR-2. Relative error is computed with respect to the ideal condition (i. e., $\Delta V_\gamma = 0$ or $\Delta R_w = 0$, as the case may be).

It is practically difficult to ensure low ΔV_γ as V_γ depends on many parameters including the current flowing through the diodes [161]. However, this error can be reduced using three wire technique as discussed next.

4.4.2. Error Sources of DRR-2

The important error sources of the DRR-2 circuit are identified and their effects are described next. The proof in Section 4.3.2 concluded that the on-resistance of S_{w2} does not affect the DRR-2. However, this proof assumed that the on-resistance is the same at both positions (position-0 and -1). Let us assume that the mismatch between the on-resistances of the practical switch used is ΔR_{sw} . This will alter the function F_2 as F_2^* , whose equation is given in (4.18).

$$F_2^* = F_2 + \Delta R_{sw} / R \quad (4.18)$$

From (4.18), it can be seen that ΔR_{sw} will cause an offset error in F_2 . This error will be 0.0005 % for ΔR_{sw} of 5 Ω and a typical $R = 100$ k Ω . Likewise, practical switches have finite off-resistances (say, R_{of}). This condition will modify the off-time durations, T_{OFF1} and T_{OFF2} . The modified expressions of these durations (say, T_{OFM1} and T_{OFM2}) are given in (4.19).

$$T_{OFM1} \approx (G-1)R_{X1}C; T_{OFM2} \approx (G-1)R_{X2}C \quad (4.19)$$

In (4.19), $R_{X1} \approx \{(R_{Sw2} + R_X) \parallel (R_{of} + R_S)\} + 2R_w$ and $R_{X2} \approx \{(R_{of} + R_X) \parallel (R_{Sw2} + R_S)\} + 2R_w$. Using (4.19) in (4.9), it can be observed that the error will increase with R_X . A maximum error of 0.2 % (SE case) is observed when MAX4053 IC served as S_{w2} . The nonlinearity, e_{NL} works out to be 0.04 %.

In Section 4.3.2, it was assumed that the resistances of all the connecting wires were equal to R_w . However, in practice, their values may differ slightly from each other. In the DRR-2 technique, the mismatch in wire resistance (say, ΔR_w) can cause an error, e_{THR} . However, the magnitude of e_{THR} is much smaller than the e_{TWO} present in the two-wire case, as illustrated in Fig. 4.7. A typical ΔR_w of 0.5 Ω [163] introduces a maximum

error (e_{THR}) of just 0.45 %. Thus, the three-wire linked resistive sensing, followed in DRR-2, has merits over the technique followed in DRR-1.

4.4.3. Error Sources of DRR-3

The effect of some error sources of DRR-3 has been covered in Section 4.3.3. The other nonidealities, especially those of circuitry, are detailed here. The presence of I_B and V_{os} of Op-amps can alter the (T_2/T_1) expression given in (4.15). The associated error (say, e_A) is given in (4.20).

$$\%e_A \approx (V_{err} / V_R) \times (1 + R_1 / R_2 + R_2 / R_1) \times 100\% \quad (4.20)$$

Here $V_{err} = 2V_{os} + I_B (R + R_{s1} + R_{w1})$. The IC OP07 ($I_B = 2$ nA, $V_{os} = 60$ μ V) was used to realize the Op-amps A₁, A₂, and A₃. By using (4.20), the maximum value of e_A works out to be 0.02 %.

The finite time resolution of the TLU can also lead to an output error. This error was found to be 0.09 % for the resolution of 2 μ s and $T_1 = 5$ ms. The effect of slew-rate and delay (≈ 50 ns) of the comparator can be avoided by selecting T_1 in milliseconds.

4.5. Performance Verification of DRR-1 Circuit

The DRR-1 circuit was evaluated for performance as described in the forthcoming subsections.

4.5.1. Simulation DRR-1

The simulation study of DRR-1 was done by using LTspice software. The Op-amp OA and OC were selected to mimic OP07 IC and LF356 IC characteristics, respectively. The resistance R_n was selected as 3.3 k Ω , while the other resistances (R_m , R_F , and R_S) were set as 1 k Ω . The diodes, D_1 and D_2 were made by using 1N4007 characteristics and the MAX4053 IC-based switch was used to realize the switch IC. The capacitor, C_I was selected as 1 μ F. The TLU was realized in such a way that it generate the control signals, V_{CON1} and V_{CON2} . The resolution of time duration

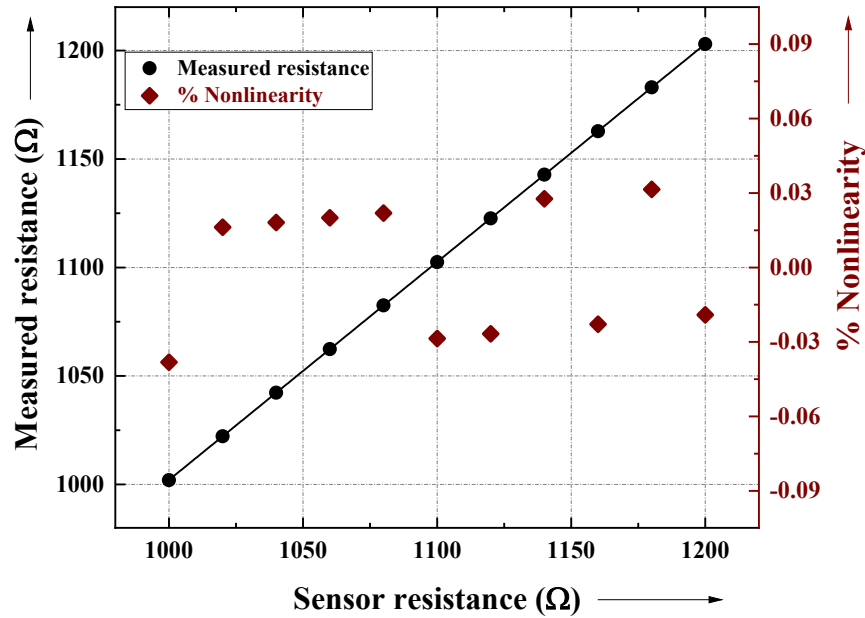


Fig. 4.8. Simulation results of input-output characteristics of DRR-1. Measured e_{NL} is also plotted.

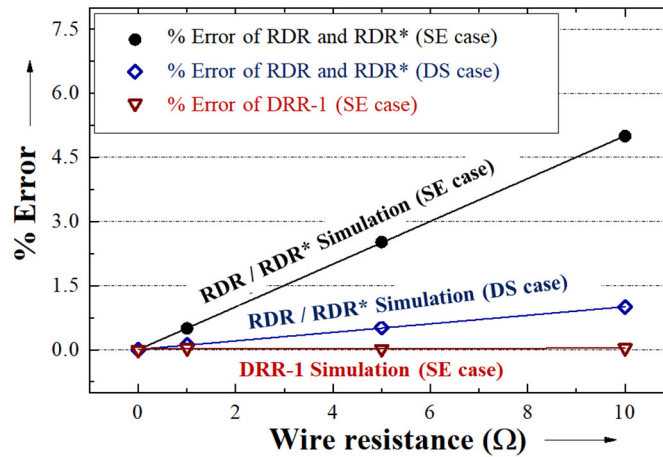


Fig. 4.9. Simulation plot showing the effect of wire-resistance on RDR, RDR*, and the compensated DRR-1.

measurement was kept at $1 \mu\text{s}$ to mimic with the TLU used in the developed prototype. The connecting wires and the sensor, R_X were realized using a decade resistance box. The resistor, R_X was varied from $1 \text{ k}\Omega$ to $1.2 \text{ k}\Omega$ to mimic the RTD-Pt1000 sensor characteristics. The output time durations were measured, and output resistance was also calculated. The transfer characteristics of DRR-1 are plotted in Fig. 4.8. The nonlinearity, e_{NL} was also calculated for each step of resistance values. The maximum observed e_{NL} is 0.04% .

Next, the efficacy of DRR-1 with respect to the immunity against wire resistance was also studied. Here, the sensor resistance was fixed as 1 k Ω and the wire resistances were changed to 0, 1 Ω , 5 Ω , and 10 Ω . The worst-case error (i. e., e_{REL}) was noted for each value of R_W and plotted and given in Fig. 4.9. The plot clearly shows that the function F_1 is not affected by the presence of R_W .

4.5.2. Emulation studies

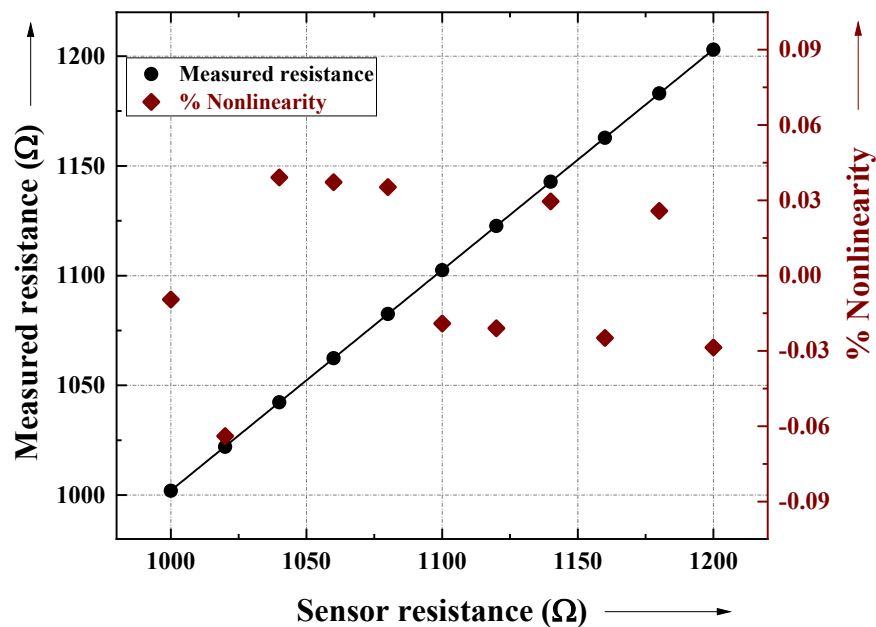


Fig. 4.10. Transfer characteristic of DRR-1 using emulation studies.

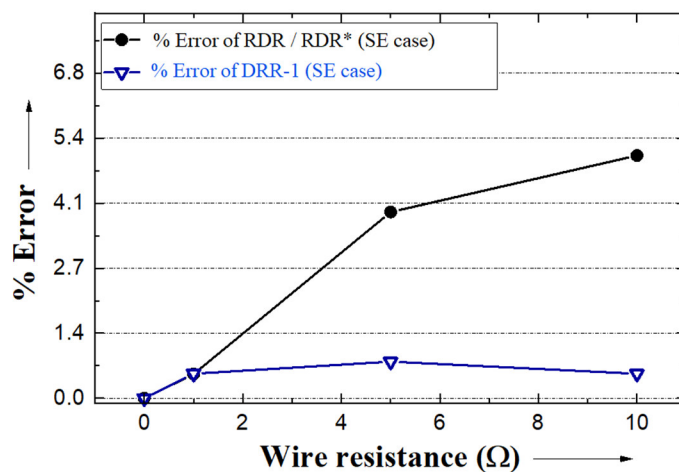


Fig. 4.11. Effect of wire-resistance on RDR, RDR*, and the compensated DRR-1 are shown here while interfacing with emulated RTD-Pt1000 temperature sensor.

Experimental studies were also carried out for DRR-1 with the remote-resistive sensor. The characteristics of RTD-Pt1000 were used for these studies. The components used in experimental studies have similar components used in the simulation studies. The wire resistances were kept as $10\ \Omega$. The sensor resistance, R_X was varied from $1\ \text{k}\Omega$ to $1.2\ \text{k}\Omega$. The relationship between input and output is plotted as a graph and given in Fig. 4.10. From Fig. 4.10, it can be observed that the relationship is linear and the maximum e_{NL} is $0.06\ \%$. These results are also similar to the results obtained using simulation studies. Next, different values of wire resistances (i. e., 0 , $1\ \Omega$, $5\ \Omega$, and $10\ \Omega$) were used to connect the sensors to the developed DRR-1 circuit. The worst-case error of the circuit was calculated and plotted in Fig. 4.11. It can be seen from Fig. 4.11 that the maximum error is less than $0.6\ \%$.

4.5.3. Comparison of DRR-1 with RDR

The developed DRR-1 is an adapted version of RDR and renders wire-resistance compensation. Therefore, the performance of DRR-1 was compared with RDR, in the context of wire-resistance compensation. The RDR and RDR* circuits were also simulated to show dependency on wire resistances and compared with the results of DRR-1. Here, SE and DS configurations were considered. The sensor resistance of RDR and RDR* circuits was kept as $1\ \text{k}\Omega$ and the effect of wire resistances was observed, and the results are plotted in Fig. 4.9. The error can be seen to increase with R_W for RDR and RDR* circuits. Fig. 4.9 also clearly shows that the error of the DS configuration is less than the SE configuration. Later, the above results were also verified with the emulation studies for SE configuration. As expected, the error of RDR/RDR* increases with wire-resistance (see Fig. 4.11). On the other hand, the DRR-1 output was almost independent of wire resistance (see Fig. 4.11). Hence, DRR-1 is suitable for remotely located resistive sensors.

4.6. Performance Verification of DRR-2 Circuit

The performance of the DRR-2 circuit is also analyzed using simulation and experimental studies, discussed next.

Table 4.4

Details and Results of Simulation and Emulation Studies of DRR-2

Circuit	Sensor model	Sensing element	Resistance range in $k\Omega$	Gain	% e_{NL}	
					S	E
DRR-2	SE	R_X	1 – 10	$G_0 = 6$	0.04	0.09
			10 – 100	$G_1 = 1.5$		
			100 – 1000	$G_2 = 1.05$		
S – Simulation results, E – Emulation results						

4.6.1. Simulation Studies of DRR-2

Simulation studies of DRR-2 were conducted with the help of LTspice software. Specifications of OP07 IC were used to realize the Op-amps (OP1 and OP3), and the comparator OP2 was developed using LM311 IC characteristics. All switches of DRR-2 were implemented using MAX4053 IC specifications, while the reference voltage V_R was kept as 1.2 V to mimic LM385-1.2 IC. The resistor, R was selected as 100 k Ω . The power supply voltages used were ± 8 V. The TLU was realized using suitable logic circuits to generate the control signals, V_s , V_{c1} , and V_{c2} . The gain selection logic (like RDR_w) was implemented in the TLU.

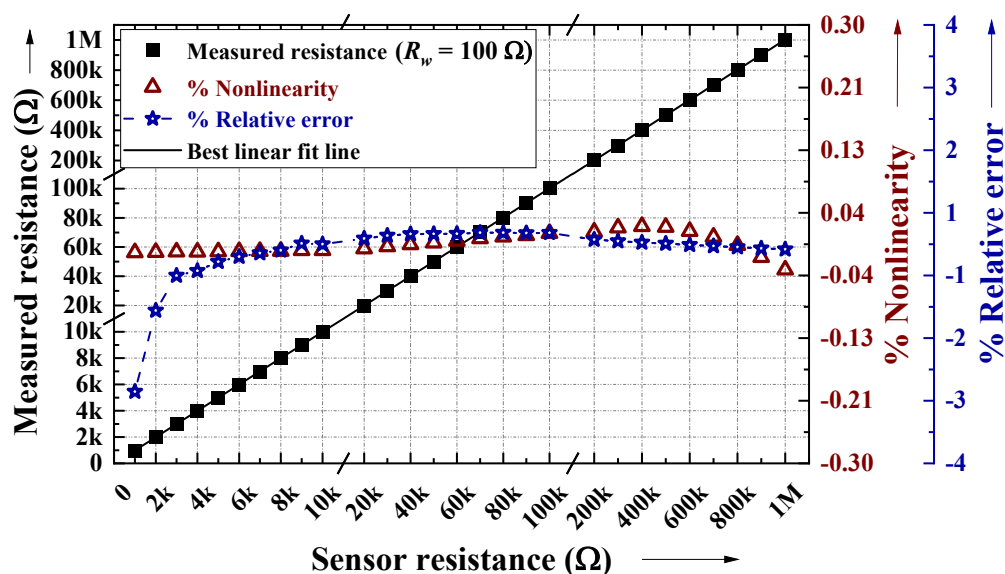


Fig. 4.12. Linear transfer characteristics obtained using simulation of DRR-2 with a remotely-located SE sensor.

Initially, the wire resistance R_w was taken as 100Ω . The SE-type sensor (R_X) was interfaced, through R_w 's, to the DRR-2. The resistor R_S was fixed as $100 \text{ k}\Omega$. The sensor resistance, R_X was varied over a wide range (i. e., from $1 \text{ k}\Omega$ to $1 \text{ M}\Omega$). The value of T_{Xmax} and T_{Xmin} was set like RDR_w . Using (3.16), N_R was obtained as 3. The three regions and gain selection for each range were decided like RDR_w and summarized in Table 4.4. The output, F_2 was measured for different values of $R_b \in (1 \text{ k}\Omega, 1 \text{ M}\Omega)$ and the results are given in Table 4.4. The output characteristics of DRR-2 observed from the simulation are plotted in Fig. 4.12. The measured resistance was found to vary linearly with input. The maximum e_{NL} of DRR-2 is merely 0.04% (refer Fig. 4.12, scatter plot). Similarly, the error, e_{REL} at each step of resistance is also plotted in Fig. 4.12 and the maximum error is 2.4% . This high error is expected, and it can be easily understood by deriving e_{REL} for DRR-2.

Further, the suitability of DRR-2 for remote measurements was checked for different values of $R_w \in (0, 100 \Omega)$. A typical value of $R_X = R_S = 10 \text{ k}\Omega$ is used for this study. The measured output resistance of DRR-2 for different R_w is shown in Fig. 4.13. It can be seen from Fig. 4.13 that the measured values of R_X are very close to the ideal

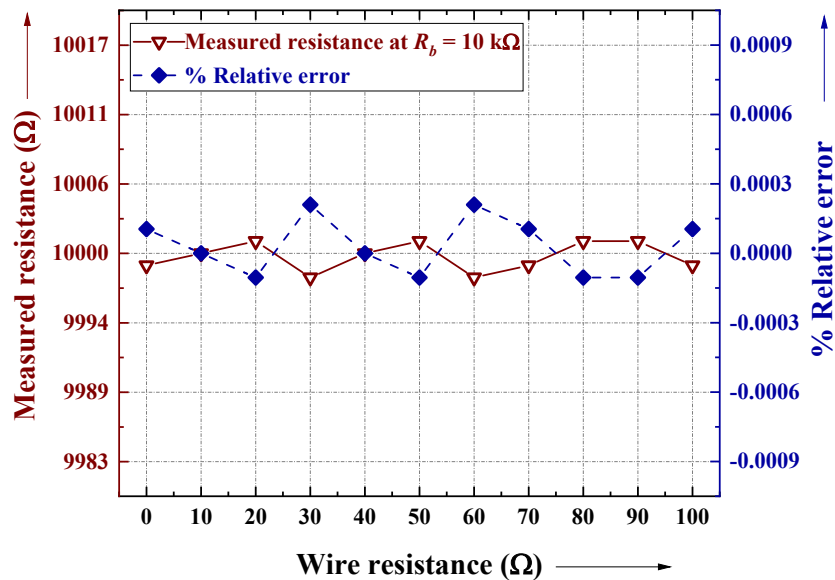


Fig. 4.13. Simulation test results depicted the immunity of the DRR-2 on the effect of the wire resistances.

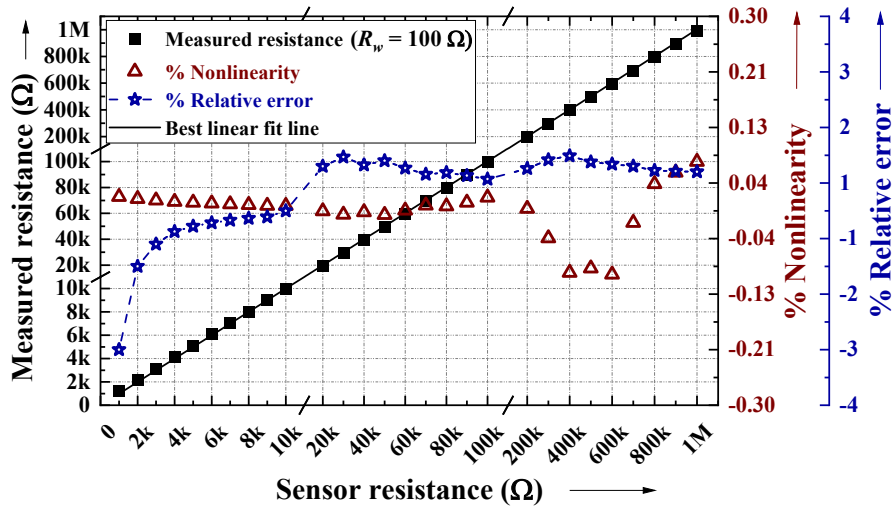


Fig. 4.14. Linear transfer characteristics obtained when a hardware prototype of DRR-2 is tested with a remotely-located SE sensor.

value of 10 k Ω . The output deviation (e_{REL}) for different R_w is also plotted in Fig. 4.13 (scatter + dashed-line plot). The maximum e_{REL} obtained from Fig. 4.13 is 0.0002 %.

4.6.2. Experimental Studies of DRR-2

The simulation results discussed above were also cross-verified with the help of experimental studies. The components used in the experimental studies have similar specifications discussed in simulation studies. The TLU was realized using the Arduino Due board which uses ATSAM3X8E as the microcontroller. The time measurements

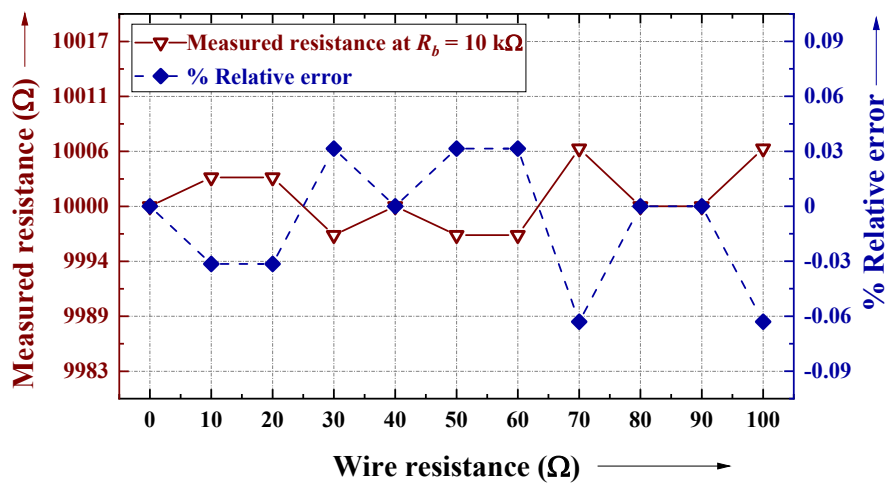


Fig. 4.15. Emulation test results depicted the immunity of the DRR-2 on the effect of the wire resistances.

were done with the help of a timer/counter-0 module. The resistance, R_X was varied from 1 k Ω to 1 M Ω (range \approx 60 dB). The output of the DRR-2 circuit was measured and linear input-output characteristics were observed. This can be seen from Fig. 4.14. The nonlinearity, e_{NL} and e_{REL} values are also measured and plotted in Fig. 12. The maximum values are 0.09 % and 2.5 %, respectively.

The effect of connecting wires was also verified using experimental studies. Here, the wire resistances were varied from 0 to 100 Ω with the step of 10 Ω . The sensor resistance, R_X was kept as 10 k Ω and the errors were measured. The results are plotted in Fig. 4.15 and the maximum error is less than 0.062 %.

The real-time capability of DRR-2 towards SE sensor interfacing was further validated using RTD-Pt1000 temperature sensor characteristics [154]. The sensor has an inherent e_{NL} of 0.22 % for the range of -40 $^{\circ}\text{C}$ to 70 $^{\circ}\text{C}$ [154]. This sensor was emulated using decade resistance boxes. Tests were done with DRR-2 for $R_w = 0 \Omega$ and $R_w = 100 \Omega$. The output characteristics of DRR-2 for $R_w = 100 \Omega$ are plotted and shown in Fig. 4.16. The nonlinearity, e_{NL} for different temperatures is also shown in Fig. 4.16. The maximum e_{NL} is around 0.2 %. The measured e_{NL} is higher in experimental studies than the emulation and it is mainly due to the inherent e_{NL} of the temperature sensor.

Finally, the performance parameters like SNR, ENOB, etc. were found for DRR-2 using standard definitions (given in Appendix A). These studies were done for

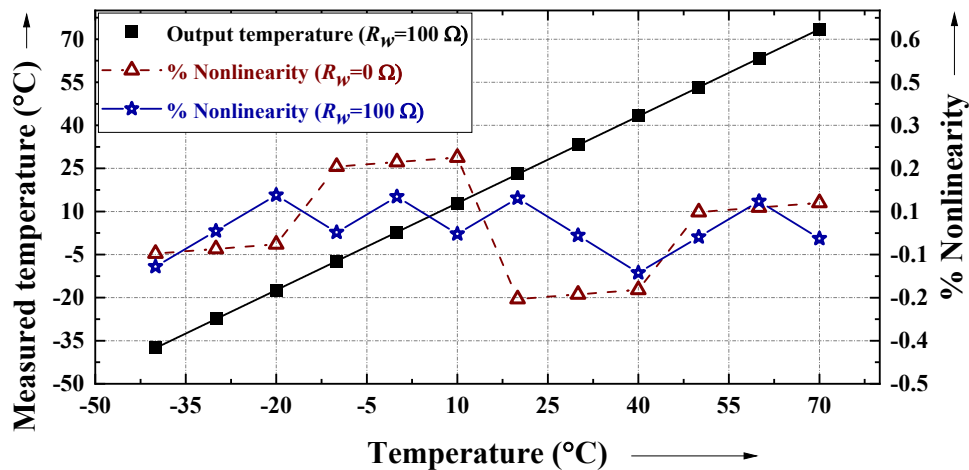


Fig. 4.16. Transfer characteristics and e_{NL} of DRR-2 + RTD system (remote case, $R_w = 100 \Omega$). Measured e_{NL} in remote and non-remote cases is also plotted.

Table 4.5

Estimated Values of Statistical Performance Parameters

Parameters	DRR-2		DRR-3
	10 k Ω	100 k Ω	140 Ω
Signal-to-noise ratio (SNR in dB)	58.57	54.56	61.2
Standard deviation (σ)	0.12	0.19	0.003
Resolution (ENOB) (bits)	9.44	8.8	9.9
Repeatability error (R_E)	0.004	0.08	0.01

SE-type sensor configuration for two values of R_X (i. e., 10 k Ω , and 100 k Ω). The results were obtained using 400 consecutive measurements. The values estimated for the performance parameters are given in Table 4.5. From Table 4.5, it can be observed that the DRR-2 has an SNR of 58.57 dB. Similarly, R_E is also admirable ($\approx 0.08\%$). In addition, the above results are also comparable with the schemes in [102], [157]. These results show that the real-time performance of the developed circuits is satisfactory.

4.7. Performance Verification of DRR-3 Circuit

The performance of the DRR-3 circuit was also studied with the help of simulation, emulation, and experimental studies. Details are given below.

4.7.1. Simulation Studies

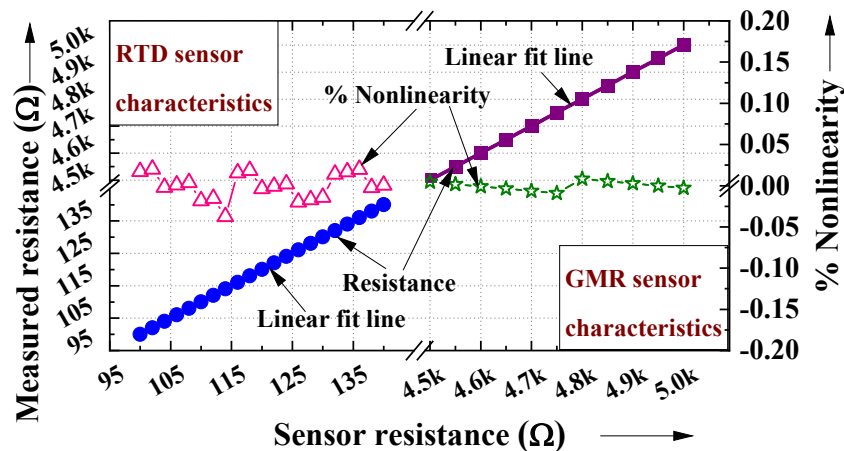


Fig. 4.17. Simulation results of interfacing RTD and GMR sensor with DRR-3. Measured e_{NL} is also plotted.

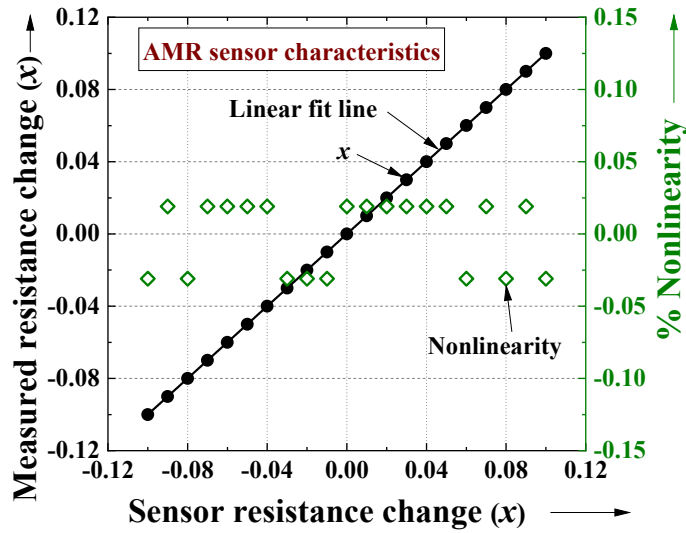


Fig. 4.18. Simulation results of DRR-3 with AMR sensor characteristics. Measured e_{NL} at each step of x is shown and the maximum e_{NL} is 0.03 %.

The simulation studies (tool: LTspice) were conducted to understand the performance of the proposed DRR-3 circuit. The Op-amps A_1 to A_3 were realized using OP07 IC specifications, while LM311 IC served as the Op-amp A_4 . The switches were implemented using CD4053 IC characteristics. The reference voltage, V_R was selected as 2.5 V to meet the specifications of LM385-2.5 V. Passive components were chosen as $R = 3.3 \text{ k}\Omega$ and $C = 1 \text{ }\mu\text{F}$. The TLU with $T_1 = 5 \text{ ms}$ was realized using the suitable logic circuit in LTspice. The resolution of the time measurement was kept as

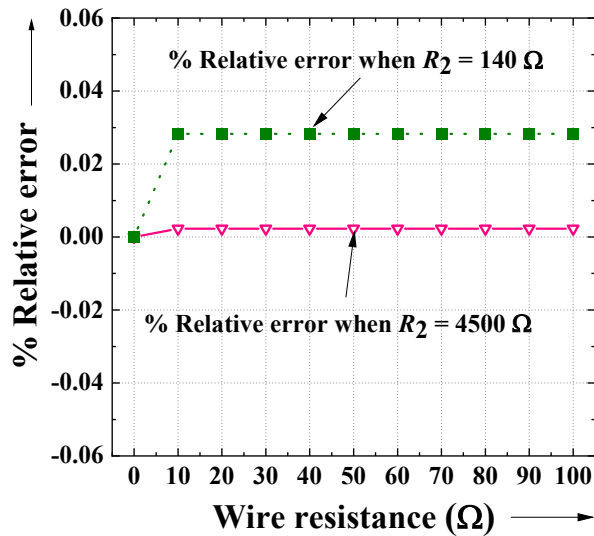


Fig. 4.19. Simulation study of effect of the wire impedance on the performance of DRR-3. Wire resistances were varied from 0 to 100 Ω and the maximum e_{REL} is 0.03 %.

1 μs . The DRR-3 circuit was interfaced with characteristics pertaining to three different sensor-bridge configurations. First, RTD sensor-based QB with $R_X \in (100 \Omega, 140 \Omega)$ and $R_0 = 100 \Omega$. Secondly, the HB configuration was tested using GMR sensor characteristics with $R_2, R_4 \in (4.5 \text{ k}\Omega, 5 \text{ k}\Omega)$ and $R_1 = R_3 = 5 \text{ k}\Omega$. Finally, an Anisotropic Magneto Resistance (AMR) sensor (FB) with $R_0 = 1 \text{ k}\Omega$ and $x \in (-0.1, 0.1)$ was interfaced with DRR-3. The transfer characteristics of DRR-3 were plotted. Fig. 4.17 shows the transfer characteristics of DRR-3 for RTD and GMR sensors, while the measured ‘ x ’ for AMR-sensor simulation is plotted in Fig. 4.18. The nonlinearity, e_{NL} values are also plotted in these figures. From these plots, it is evident that DRR-3 possesses a maximum e_{NL} of less than 0.04 % for all bridge configurations considered.

Tests of DRR-3 were also carried out with different values of connecting wire impedances (R_{w1} to R_{w6}) for QB configuration (keeping $R_2 = 140 \Omega$) as well as GMR sensors (keeping $R_2 = R_4 = 4.5 \text{ k}\Omega$). The wire impedances varied from 0 to 100 Ω . The error, e_{REL} due to wire impedances were computed with respect to the condition when all R_w ’s are zero and is plotted in Fig. 4.19. Fig. 4.19 shows that the maximum error is merely 0.03 % for both the bridge types.

4.7.2. Experimental Studies of DRR-3 Circuit

The hardware prototype of the DRR-3 was built using readily available components. The components used in simulation studies were utilized in experimental studies. The TLU with $T_1 = 5 \text{ ms}$ was realized using the ATSAM3X8E microcontroller.

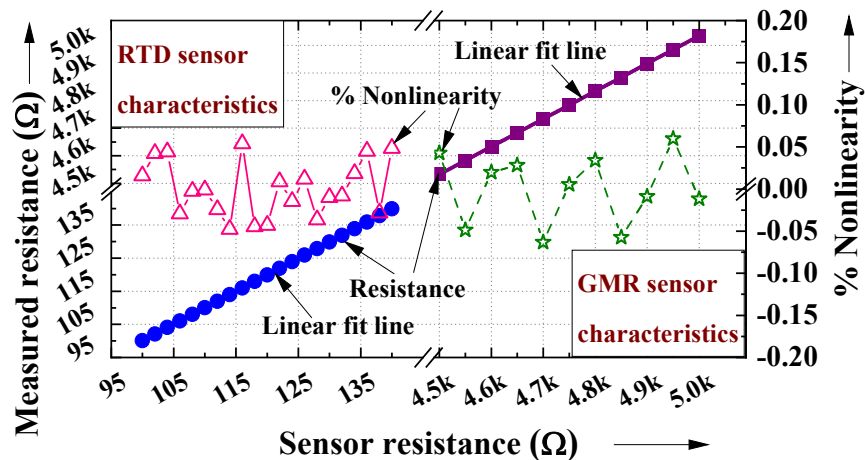


Fig. 4.20. Emulation results of interfacing RTD and GMR sensor with DRR-3.

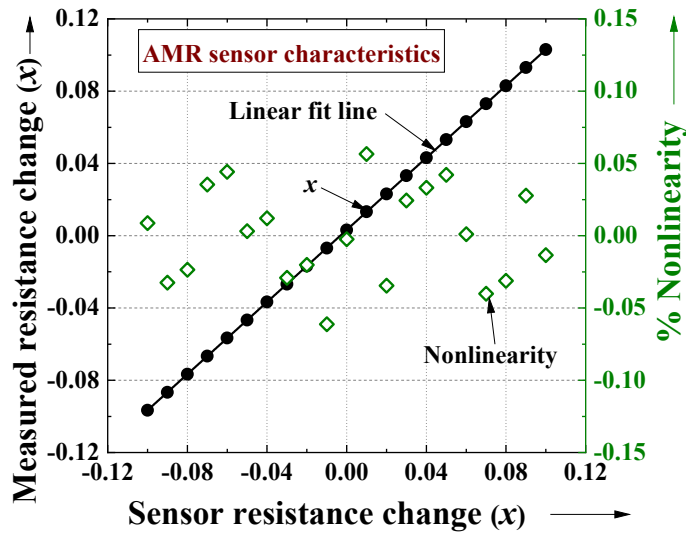


Fig. 4.21. Experimental tests of DRR-3 with AMR sensor characteristics.

The resolution of the above TLU ($\approx 2 \mu\text{s}$) will not have any considerable effect. The DRR-3 circuit was interfaced with characteristics pertaining to three different sensor-bridge configurations. First, RTD sensor-based QB and the HB configuration were tested using GMR sensor characteristics (similar to simulation studies). Finally, an AMR sensor was also interfaced with DRR-3. These characteristics were synthesized using precision decade resistances. The transfer characteristics of DRR-3 were recorded and plotted. Fig. 4.20 shows the transfer characteristics of DRR-3 for RTD and GMR sensors. Likewise, the AMR-sensor emulation is plotted in Fig. 4.21. The

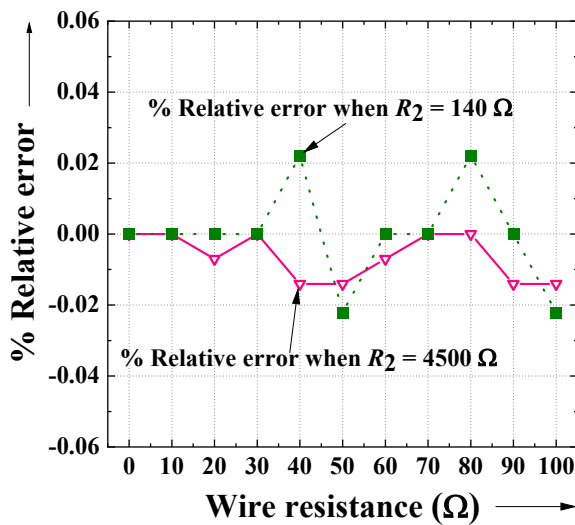


Fig. 4.22. Effect of the wire impedance on the performance of DRR-3.

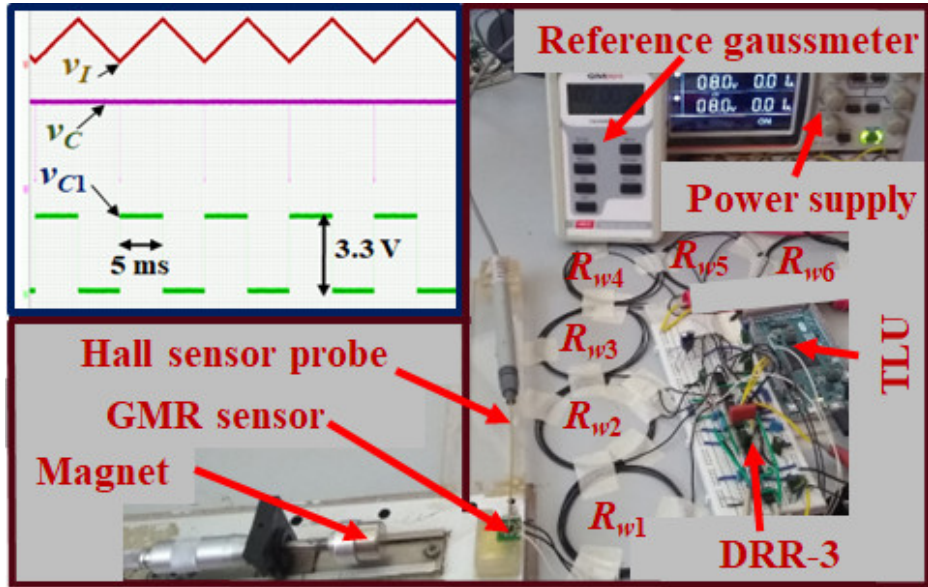


Fig. 4.23. Experimental setup of DRR-3 + GMR system with oscillogram in inset.

DRR-3 was seen to provide expected linear transfer characteristics that corroborate well with theoretical explanation and simulation results. The nonlinearity, e_{NL} values are also plotted and the maximum e_{NL} of less than 0.06 % is observed for all bridge configurations.

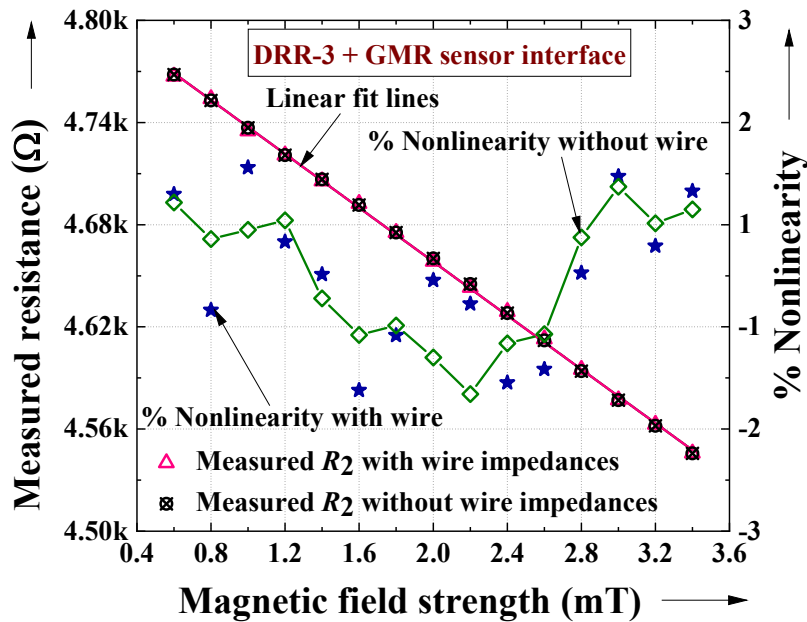


Fig. 4.24. Experimental interface results of DRR-3 with the AA004 GMR sensor.

The effect of connecting wire impedances was also studied using experimental studies. Here, the wire resistances varied from 0 to 100 Ω using precision decade boxes. This study was conducted for two different cases like simulation studies and the results are plotted in Fig. 4.22. The observed maximum error from Fig. 4.22 is 0.02 %.

The utility of DRR-3 towards interfacing with a typical GMR sensor (AA004 IC from NVE Corp.) was studied. This GMR sensor was interfaced with the DRR-3 using six long wires of an impedance of $\approx 1 \Omega$. A snapshot of the experimental setup is shown in Fig. 4.23. The sensor was excited with different values of $B_{EXT} \in (0.5 \text{ mT}, 3.5 \text{ mT})$ and the DRR-3 output was noted. A suitable magnet and traverse setup were used to apply B_{EXT} . The reference value of B_{EXT} was noted using the GM08 gaussmeter. Results obtained are plotted in Fig. 4.24 (Datasets can be viewed from Appendix B.3). Linear DRR-3 response with B_{EXT} was observed and the maximum e_{NL} is 1.16 % (which is lower than the inherent e_{NL} of the GMR sensor). The simplified DRR-3 version, without Op-amps A_1 and A_2 , was also tested for non-remote GMR sensors. The obtained output versus field characteristics matches well with the previous case [see Fig. 4.24].

Further, precision-related parameters of the DRR-3 were characterized using 400 repeated measurements in a hardware prototype (expressions are given in Appendix A). Initially, the QB-type sensors at a typical R_X of 140 Ω were tested. Results were given in Table 4.5. It was seen that the DRR-3 offers a high SNR of 61.2 dB and a small value of σ of 0.003 % and R_E of 0.01 %.

4.8. Comparison Studies

The developed DRR circuits were also compared with each other. The outcomes of the comparison study are given in Table 4.6. From Table 4.6, it can be observed that the developed DRR-1 circuit requires less number of connecting wires. The DRR-1 scheme also does not need any separate calibration to find the transformation constants. However, this circuit cannot adapt to wide-range sensors and exhibits saturation-related effects. The DRR-2 circuit shows a low error in the output

Table 4.6

Comparison Study between Developed DRR Circuits

Parameters		DRR-1	DRR-2	DRR-3
Adapted scheme/number of wires needed		Twin-diode/2-wire	Relaxation oscillator/3-wire	Dual-slope/6-wire
Adapted configuration		SE	SE, DS	Bridge
Ability to interface with wide-span sensors		No	Yes	Yes
Ability to reduce conversion time		No	Yes	No
Conversion cycles		3	2	1
Prototype developed	% e_{NL}	0.05	0.09	0.06
	% e_{REL}	NA	2.5	NA
	Conversion time (ms)	10	110	12
	Range (in dB) [#]	3.52	60	34
Comments		1. Mismatch in diode ON-state forward voltage drop causes an output error 2. Saturation related effects	1. Suitable for wide range of measurement 2. consumes high power and requires more count of components	1. Independent to wire resistance mismatches 2. Complex architecture with more wires
# - Range in dB = $20\log(\text{Maximum measurable resistance}/\text{Minimum measurable resistance})$, NA – Not available				

than the DRR-1. In addition, this circuit can be able to measure a wide range of resistances. The DRR-3 is independent of the mismatch in the connecting wires, and it has low conversion time (single conversion cycle) than the DRR-1 and DRR-2 circuits. Note that, the SE and DS configurations can also be interfaced with DRR-3 by forming the Wheatstone bridge. The other features of the developed circuits can be observed from Table 4.6.

The comparison between some of the existing digitizing interfaces for remotely connected resistive sensors was done and it is given in Table 4.1. This comparison considers the parameters such as methodology adapted, suitable configurations, e_{NL} , e_{REL} , etc. From Table 4.1, it can be observed that the scheme

developed using two-wire [60] has a low error in the output. However, this work considers the microcontroller threshold voltages are the same throughout the conversion time. The number of conversion cycles is reduced in [61] and [62]. The three-wire technique proposed in [64] requires current conveyors and it shows errors in output due to circuit nonidealities. In addition, the performance of the circuit is verified using only simulation studies. The four-wire technique reported in [114] is useful to avoid errors due to the mismatch of wire resistances. Likewise, the circuits developed in [115] and [85] are also useful to avoid mismatches in the wire resistances. However, these circuits [85], [114], [115] need complex circuit/high-resolution components to get their own merits. From Tables 4.1 and 4.6, it can be understood that the developed DRR circuits show superior/comparable performance than the existing circuits.

4.9. Summary

The developed DRR-1 employed a simple design, and it was equipped with novel compensation functions to provide a linear-digital indication of remote resistive sensors. Later, an efficient digital interface (DRR-2) for three-wire connected resistive sensors was presented in this chapter. The developed DRR-2 was suitable for wide-span sensors and possesses low error than DRR-1. Finally, the novel DRR-3 circuit has been designed and adapted for various bridge configurations. Using a simple architecture, DRR-3 provided effective compensation for many non-ideal industrial scenarios such as remotely located sensor bridges, bridges with parasitic elements and mismatches among its elements, etc. The performance of the developed DRR circuits was evaluated using various simulation and experimental tests. Test results demonstrate that DRR circuits served as a direct-digitizer for resistive sensors in SE, DS, and bridge configurations and they rendered all expected features. The performance of the developed schemes was also evaluated against existing works. DRR-1 circuit is mainly useful where low wiring infrastructure (results in low-cost), and low complexity are required. On the other hand, the DRR-2 circuit is essential

where accuracy is the main concern. Likewise, the DRR-3 circuit is useful for bridge-based sensor configurations. These circuits can be directly used in automotive applications. Here, the circuit components need to be replaced with automotive standard components. For example, the integrator can be modeled using TSZ181 IC [164] and the design of the comparator can be done using TS3021 IC [165]. The high-frequency conducted noise (≈ 100 kHz to 10 MHz) from electrical contacts and accessory drive/control motors [166] is minimized with the help of the integrator-based digitizer circuits which are present in this chapter. In automotive applications, harsh environments such as wide temperature extremes and random vibrations can affect the performance of the proposed circuits. Nevertheless, the developed DRRs can serve as an efficient digital signal conditioner for resistive sensors, especially in various practical situations, where wide-span and remote measurement is required.

The architecture of the digitizing circuits can be further reduced by using the charge-discharge-based technique. This ensures the utilization of a few passive components in the architecture. The methodology and the suitability of this scheme for remote resistive sensors are detailed in the next chapter.

Chapter 5

Improved Microcontroller-Based Digitizing Interface Circuits for Resistive Sensors in Different Configurations

5.1. Introduction

The digitizers for resistive sensors, discussed in previous chapters, were based on dual-slope and relaxation oscillator techniques. In this chapter, an alternate technique of microcontroller-based interfacing is explored for resistive sensors. Here, improved architectures based on microcontroller interfacing are proposed. The methodology of the proposed interfaces is discussed next.

5.2. Digitizing Interface for Resistive Sensors

This chapter discusses the design and analysis of Digitizing Interface for Resistive sensors (DIR). DIR operates on three-wire connected resistive sensors and provides a direct-digital output proportional to the sensor resistance or the measurand. The direct microcontroller interface basically comprises simple analog circuitry and a digital control-and-timing unit (CTU). The CTU intelligently controls the analog circuitry using different control signals such that the effect of many non-ideal parameters, including wire-resistances of three wires (R_{w1} , R_{w2} , and R_{w3}) are nullified. The new design proposed in this chapter ensures the following features.

- a. Adaptability with various types of resistive sensors
- b. Linear digital output using simple analog circuitry
- c. Ability to interface different remotely-located resistive sensors using only three

This chapter is partially adapted from the post-print version of Elangovan K, A. Antony, and Anoop C. S., "Simplified Digitizing Interface-Architectures for Three-Wire Connected Resistive Sensors: Design and Comprehensive Evaluation," in *IEEE Transactions on Instrumentation and Measurement*, vol. 71, pp. 1-9, 2022, Art no. 2000309.

conversion cycles

- d. Immunity against lead-wire resistances, permitting accurate measurements of low-valued resistive sensors
- e. No effects of microcontroller parameters such as threshold voltage, pin-resistance, resistance in the high-impedance state, etc., thus permitting precision measurements of high-valued and wide-range resistive sensors

The working and performance verification of the proposed digitizing interfaces are discussed in the upcoming sections.

5.2.1. Digitizing Interface for SE type Resistive Sensors (DIR-SE)

The circuit schematic of DIR-SE is shown in Fig. 5.1. DIR-SE consists of four switches named S_1 to S_4 , a resistor R_C used to charge the capacitor C , a comparator OP, a reference voltage, V_R , and two more resistors (R_m and R_n). The switches S_1 and S_2 are based on Single-Pole Single-Throw (SPST) topology, while S_3 and S_4 are Single-Pole Double-Throw (SPDT) switches. As shown in Fig. 5.1, these switches are controlled using the digital signals (v_{C1} , v_{C2} , and v_{C3}) generated by the CTU. The control strategy used is illustrated in the following equations.

$$\begin{aligned} S_1 \rightarrow \text{ON}, S_2 \rightarrow \text{OFF}; v_{C1} = \text{High} \\ S_1 \rightarrow \text{OFF}, S_2 \rightarrow \text{ON}; v_{C1} = \text{Low} \end{aligned} \quad (5.1)$$

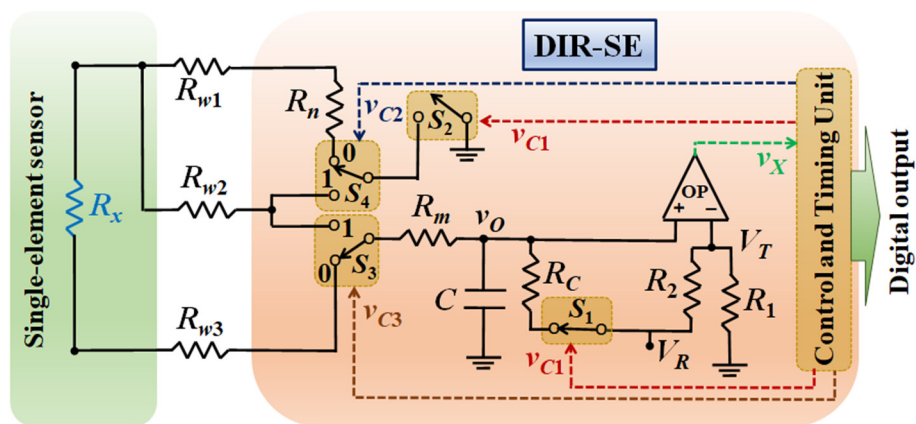


Fig. 5.1. Proposed digitizing interface (DIR-SE) for remotely connected three wire single element resistive sensor.

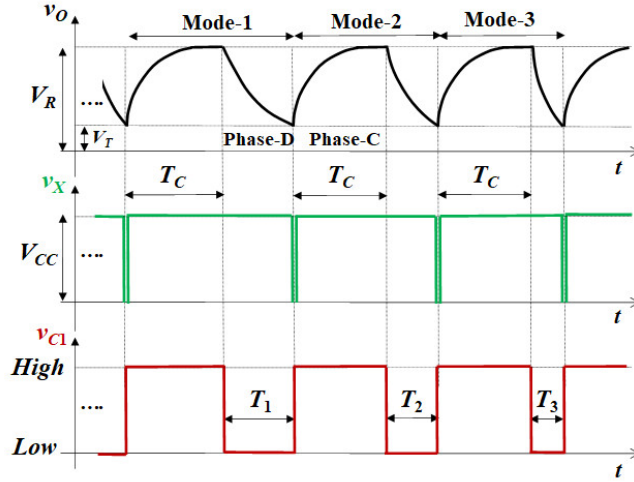


Fig. 5.2. Various node voltages (v_O and v_X) and control signal (v_{C1}) waveforms of DIR-SE.

$$\begin{aligned}
 S_3 \rightarrow 0; v_{C3} = \text{Low} & \quad S_4 \rightarrow 0; v_{C2} = \text{Low} \\
 S_3 \rightarrow 1; v_{C3} = \text{High} & \quad S_4 \rightarrow 1; v_{C2} = \text{High}
 \end{aligned} \tag{5.2}$$

The potential, v_O and the voltage, $V_T = V_R \times R_1 / (R_1 + R_2)$ are the inputs to the comparator OP. Latter's output acts as a trigger for the CTU. As shown in Fig. 5.2, the sensor resistance (say, R_x) can be found using DIR-SE with the help of three modes of operation. Each mode contains a charging phase and discharging phase, as explained next.

The charging phase (phase-C) is initiated by setting v_{C1} to high-state. As given in (5.1), switch S_1 will be ON and S_2 will be OFF, in this condition. Table 5.1 also illustrates the switch conditions. This causes the capacitor, C to charge toward V_R . This charging is allowed for a predefined duration (say, T_C). The values of R_C , C , and T_C are selected such that v_O reaches V_R at the end of T_C .

Each phase-C is followed by a corresponding discharging phase (phase-D). In phase-D, v_{C1} is made low to set $S_1 \rightarrow$ OFF and $S_2 \rightarrow$ ON. In this case, the capacitor will discharge through a resistive path, having a resistance R_{eqi} for the i^{th} mode. The value of R_{eqi} is decided by the intelligent positioning of other two switches, S_3 and S_4 [see (5.2) and Table 5.1]. In Table 5.1, R_{com} is the common resistances that occur in all the discharging modes, and R_{s2} , R_{s3} , and R_{s4} represent the ON-resistances of the

Table 5.1

Switch Positions Based on the Different Modes of DIR-SE

Mode	Phase	Switch positions				Equivalent resistance of i^{th} mode discharge phase (R_{eqi})
		S_1	S_2	S_3	S_4	
1	C	ON	OFF	--	--	---
	D	OFF	ON	0	0	$R_x + R_n + R_{w1} + R_{w3} + R_{com}$
2	C	ON	OFF	--	--	---
	D	OFF	ON	0	1	$R_x + R_{w2} + R_{w3} + R_{com}$
3	C	ON	OFF	--	--	---
	D	OFF	ON	1	0	$R_n + R_{w1} + R_{w2} + R_{com}$
C – Charge, D – Discharge, $R_{com} = R_m + R_{s2} + R_{s3} + R_{s4}$						

switches S_2 to S_4 , respectively. As given in Table 5.1, R_{com} equals $R_m + R_{s2} + R_{s3} + R_{s4}$.

The equation for discharge of v_O can be expressed as in (5.3).

$$v_O(t) = V_R e^{-t/[R_{eqi} \times C]} \quad (5.3)$$

Once v_O crosses V_T , the comparator output, v_X becomes high to low, triggering the end of a given mode. After this instance, the subsequent mode is initiated (see Fig. 5.2) and the cycle of operation continues. The phase-C operation is the same for all modes, while the switch-states for different phase-D are as given in Table 5.1. The discharge duration (say, T_i) for the i^{th} mode can be written, with the help of (5.4), as follows:

$$T_i = R_{eqi} C \ln \left(\frac{V_R}{V_T} \right) = R_{eqi} K, \text{ where } K = C \ln \left(\frac{V_R}{V_T} \right) \quad (5.4)$$

In other words, the discharge duration (T_1) for the first mode is $T_1 = K \times (R_x + R_n + R_{w1} + R_{w3} + R_{com})$. Likewise, the discharge durations for second and third modes can be obtained (vide Table 5.1) as $T_2 = K \times (R_x + R_{w2} + R_{w3} + R_{com})$ and $T_3 = K \times (R_n + R_{w1} + R_{w2} + R_{com})$. Now, consider the following function F_1 shown in (5.5).

$$F_1 = \frac{T_1 - T_3}{T_1 - T_2} R_n = \frac{R_{eq1} - R_{eq3}}{R_{eq1} - R_{eq2}} R_n = R_x \quad (5.5)$$

Assuming equal values of wire resistances ($R_{w1} = R_{w2} = R_{w3}$), the function F_1 simplifies to R_x . The time durations T_1 to T_3 can be measured in the CTU (e. g., using

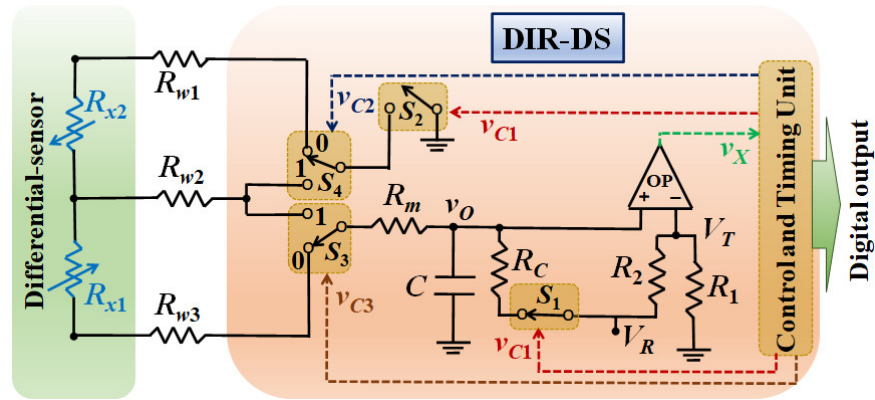


Fig. 5.3. Circuit diagram of the proposed digitizing interface (DIR-DS) for three wire remote differential sensor.

a timer). CTU can also be programmed to compute the function F_1 and thus, provide a linear digital indication of R_x . The generation of logic signals can also be done with the help of a simple digital circuit (e. g., D flip-flop and inverter). An explicit time-to-digital IC can be used for the measurement of time durations. It can also be observed that the function, F_1 is independent of wire and switch resistances, capacitor, C , and the (stable) reference voltages (V_R and V_T). Thermal variations would not cause any significant effect during the (low) conversion time of the proposed DIR-SE. However, any mismatches among wire resistances (or switch resistances) can introduce some errors, as will be described in Section 5.3.1.

5.2.2. Digitizing Interface for DS-type Resistive Sensors (DIR-DS)

The DIR-SE can be easily adapted for differential sensors (say, R_{x1} and R_{x2}). The adapted circuit (say, DIR-DS) is shown in Fig. 5.3. The main difference is that the resistances, R_x and R_n will be replaced by R_{x1} and R_{x2} , respectively. The sensor elements R_{x1} and R_{x2} follow the equation, $R_{x1} = R_o (1 + x)$ and $R_{x2} = R_o (1 - x)$, where R_o is the nominal resistance and x is the fractional resistance change of the DS. The DIR-DS, like DIR-SE, also has a triple-mode operation executed in sequence. Each mode comprises phase-C and phase-D. The switch positions for different phases are the same as DIR-SE (see Table 5.1).

The equivalent resistance (R_{eqi}) for discharging phase can be obtained from Table 5.1, after replacing R_x with R_{x1} and R_n with R_{x2} . With the help of three discharging times (T_1 , T_2 , and T_3), the following expressions can be written for R_{x1}/R_{x2} and ‘ x ’.

$$\frac{R_{x1}}{R_{x2}} = \frac{T_1 - T_3}{T_1 - T_2} = F_2; \quad x = \frac{F_2 - 1}{F_2 + 1} \quad (5.6)$$

CTU measures T_1 to T_3 and then computes and outputs a digital estimation of x as given in (5.6). From (5.6), it can be observed that the estimated x is also independent of the voltages V_R and V_T , capacitor drift, and wire and switch resistances. This assumes $R_{w1} = R_{w2} = R_{w3}$ and that the switches, S_3 and S_4 have equal on-resistance at their positions (position-0 and-1). The proposed DIR-DS can also be able to measure the x of the DS with inverse characteristics. Here, the sensor resistances vary as, $R_{x1} = R_o / (1 + x)$ and $R_{x2} = R_o / (1 - x)$. This can be obtained by using $x = (1 - F_2) / (1 + F_2)$ relation.

5.2.3. Digitizing Interface for Bridge-type Resistive Sensors (DIR-B)

The proposed digitizing interface suitable for bridge-type resistive sensors is shown in Fig. 5.4. The elements R_{x1} to R_{x4} contribute to the resistive bridge. This circuit additionally requires one Single Pole Quadruple Throw (SPQT) switch (i. e, S_4) and one more control signal than the DIR-SE/DIR-DS. The sensor bridge can be either HB or FB. The position of the switches for all three modes is tabulated in Table 5.2. An HB-based sensor is considered for now. In mode-1 (phase-D), the switches S_3 and S_4 are configured to be at position-0. This makes the capacitor to discharge through a R_{eq1} of $R_x \parallel (R_x + 2R_o) + R_{com} + R_{w2} + R_{w3}$. Here, it is assumed that $R_{x1} = R_{x4} = R_x$ and $R_{x2} = R_{x3} = R_o$ (nature of ideal HB-type sensor). The value of R_{eq1} and discharging resistances for other modes are also shown in Table 5.2.

Using the different R_{eqi} , the function F_3 [given in (5.7)] can be derived to find the unknown resistance or the measurand.

$$F_3 = \left(\frac{T_1 - T_3}{T_2 - T_3} \right) = \left(\frac{R_{eq1} - R_{eq3}}{R_{eq2} - R_{eq3}} \right) \quad (5.7)$$

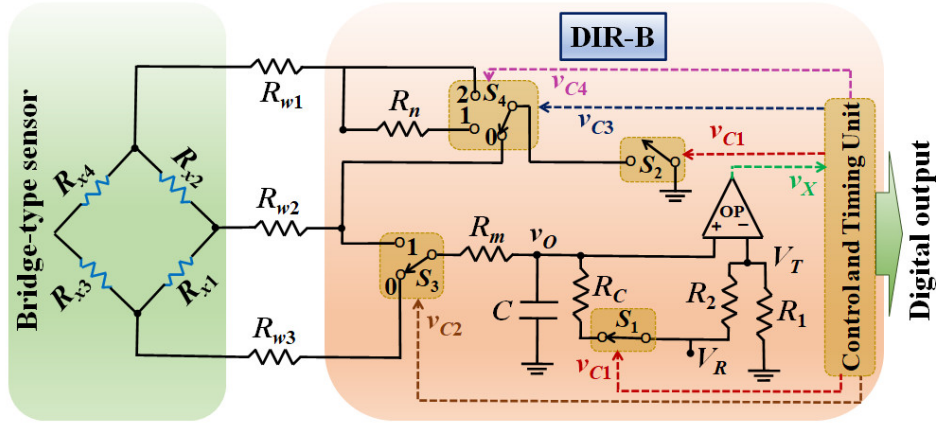


Fig. 5.4. Digitizing interface (DIR-B) for bridge-type resistive sensors.

Table 5.2

Switch Positions Based on the Different Modes of DIR-B

Mode	Phase	Switch positions				Equivalent resistance of i^{th} mode discharge phase (R_{eqi})
		S_1	S_2	S_3	S_4	
1	C	ON	OFF	--	--	---
	D	OFF	ON	0	0	$R_x \parallel (R_x + 2R_o) + R_{com} + R_{w2} + R_{w3}$
2	C	ON	OFF	--	--	---
	D	OFF	ON	1	1	$R_o \parallel (R_o + 2R_x) + R_n + R_{com} + R_{w1} + R_{w2}$
3	C	ON	OFF	--	--	---
	D	OFF	ON	1	2	$R_o \parallel (R_o + 2R_x) + R_{com} + R_{w1} + R_{w2}$

On further simplification, using resistance values in Table 5.2, the function F_3 simplifies to (5.8).

$$F_3 = \frac{R_x^2 - R_o^2}{2R_n(R_x + R_o)} = \frac{R_x - R_o}{2R_n} \quad (5.8)$$

From (5.8), the sensor resistance of HB can be found using (5.9) where R_x is the variable resistance and R_o is the constant.

$$R_x = 2 \left(\frac{T_1 - T_3}{T_2 - T_3} \right) R_n + R_o = 2F_3 R_n + R_o \quad (5.9)$$

Similarly, 'x' of the FB sensor can also be found using the DIR-B circuit. Here, $R_{x1} = R_{x4} = R_o(1 + x)$, $R_{x2} = R_{x3} = R_o(1 - x)$ and R_n can be selected as R_o . Then x equals F_3 .

The above expressions show that the DIR-B possesses all the positive features as that of DIR-SE and DIR-DS. Note that, the DIR circuits can measure the sensor resistances within a maximum conversion time, t_c , where $t_c = 3T_C + T_1 + T_2 + T_3$.

5.3. Error Analysis

The analysis in Sections 5.2.1 to 5.2.3 assumes that the components and wires present in the circuits are ideal. This section considers various error sources and the details are given below.

5.3.1. Mismatches among Connecting Wire Resistances and Switch Resistances

The resistances of the connecting wires may differ from each other. Let us consider that ΔR_w stands for mismatch among R_w 's. Similarly, there can be differences (say, ΔR_s) in the on-resistance of the different switches of the DIR circuits. These parameters can develop an error in the output of the DIR schemes. For instance, the modified value (say, R_x^a) of DIR-SE output can be derived and obtained as in (5.10).

$$R_x^a = \left(\frac{R_x + \Delta R_s + \Delta R_w}{R_n + \Delta R_s + \Delta R_w} \right) R_n \quad (5.10)$$

The maximum value of ΔR_s of the switch IC (MAX 4053) employed is 12 Ω . Considering $\Delta R_w = 0.5 \Omega$ and $\Delta R_s = 12 \Omega$, the parameters, e_{REL} and e_{NL} works out to be 3.7 % and 0.02 %, respectively, for RTD-Pt100 sensor (at $R_x = 80 \Omega$) + DIR-SE system interface. Note that, this error can be reduced using the switches having lower ΔR_s (such as, CD74HC4052 IC, TMUX6209 IC) for DIR circuits.

The modified output expressions (x^a and R_x^a) of DIR-DS and DIR-B can be written as in (5.11).

$$x^a = \frac{R_{x1} - R_{x2}}{R_{x1} + R_{x2} + 2\Delta R_s + 2\Delta R_w}, R_x^a = R_x + \frac{\Delta R_w + 2\Delta R_s}{R_x + R_o} \quad (5.11)$$

The parameters, e_{NL} and e_{REL} values, for the above cases, can also be computed for the sensor being interfaced.

5.3.2. CTU Errors

The discharge times of DIR circuits are measured by using a timer/counter module of CTU. This module may exhibit an error of $\pm \Delta T$. This modifies the output of DIR-SE as in (5.12).

$$R_x^b = \left[\frac{(T_1 \pm \Delta T) - (T_3 \pm \Delta T)}{(T_1 \pm \Delta T) - (T_2 \pm \Delta T)} \right] R_n \quad (5.12)$$

It can be observed that the maximum e_{NL} for the DIR-SE circuit is 0.02 % and e_{REL} is 0.3 %, respectively, with the RTD-Pt100 interface. The above errors are calculated for a module with $\Delta T = \pm 2 \mu s$ [142], used for the developed prototype. Similarly, the timer/counter may encounter computational delays. However, their effect can be minimized by keeping the discharge time durations (T_1 to T_3) in the order of milliseconds. A similar error of $\pm \Delta T$ may be present in DIR-DS and DIR-B output as well.

5.3.3. Mismatch in Nominal Resistance of the Sensor

In an ideal case, the R_o of R_{x1} is the same as the R_o of R_{x2} . The practical mismatches between these elements can alter the DIR-DS and DIR-B circuit outputs, as expressed in (5.13) and (5.14).

$$x^b = \left(\frac{F_2 R_{o2} - R_{o1}}{F_2 R_{o2} + R_{o1}} \right) \quad (5.13)$$

$$R_x^b = 2 \left[\frac{(R_{x1} - R_{o2})(R_{o3} + R_{x4})}{R_{x1} + R_{o2} + R_{o3} + R_{x4}} \right] + R_o = 2F_3^b + R_o \quad (5.14)$$

Here, R_{o2} and R_{o3} are the nominal resistance of R_{x2} and R_{x3} . Likewise, the output of the FB configuration is modified as F_3^b .

5.3.4. Other Non-idealities

The comparator OP may have an offset voltage. This will alter the threshold voltage levels (i. e., V_T will change from its original value). The tolerance of R_1 and R_2 can also alter V_T . This change can alter the time durations, T_1 to T_3 . Similarly, the drift in the reference voltage, V_R also modifies the time durations. However, the functions F_1 to F_3 are independent of V_T and V_R . The effect of interference/noise present at V_T as well as the sensor has a negligible effect when the values of the components are constant during one conversion time.

From the above studies, it can be inferred that error sources of the proposed DIR circuits generate a low error in the output.

5.4. Performance Verification of the DIR Circuits

The performance of the DIR circuits was checked using a number of extensive experimental studies. These studies are described in the following subsections.

5.4.1. Emulation Studies of DIR-SE

The DIR-SE circuit was bread-boarded and evaluated for performance. The charging resistor R_C and the capacitor was selected, respectively as 150Ω and $2 \mu\text{F}$. The value of R_m was taken as $1 \text{ k}\Omega$. The reference voltage, V_R was realized using

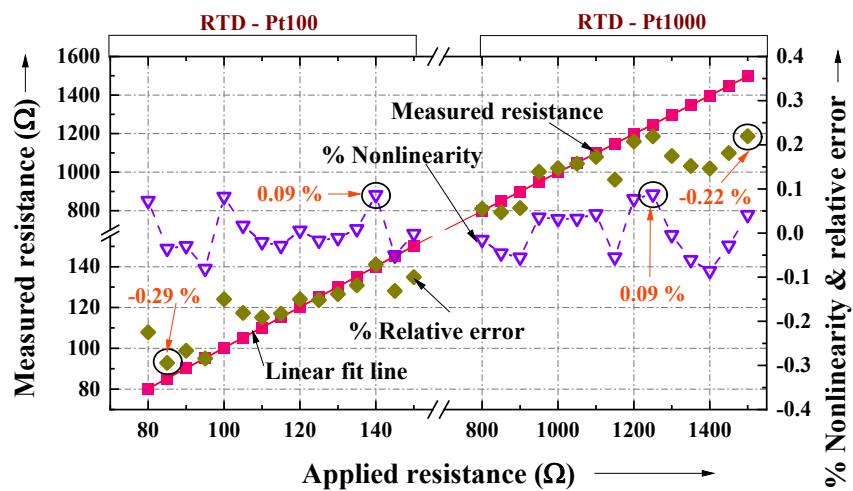


Fig. 5.5. Emulation results of the proposed DIR-SE with RTD-Pt100 sensor and RTD-Pt1000 sensor-based SE sensors.

LM385-2.5 IC (nominal value = 2.5 V and temperature coefficient = 150 ppm/°C). The threshold voltage, V_T of the comparator was kept at 1.12 V using $R_1 = 1.46 \text{ k}\Omega$ and $R_2 = 1.8 \text{ k}\Omega$. These precision voltages decide the charging and discharging thresholds of the capacitor, thereby giving precision measurements. The comparator OP was modeled using LM311 IC. The switches S_1 to S_4 were designed using MAX4053 ICs. The wire resistances (R_{w1} to R_{w3}) were kept as $11 \text{ }\Omega$ to mimic the 30 m of 30 standard wire gauge copper wire [163]. The CTU was realized using an ATSAM3X8E microcontroller [142] placed in Arduino Due platform. The time durations, T_1 to T_3 were measured using the timer/counter modules with the specifications of timer/counter-0, 32-bit, and the clock frequency is 656.25 kHz [142]. This microcontroller is programmed to maintain the predefined charging time, T_C as 5 ms, generate control signals, and measure T_1 , T_2 , and T_3 . This microcontroller board has many components/sections which are not needed for the operation of the CTU. In other words, limited functionality is only needed. Hence, the existing processing platform available in the overall system architecture can be used along with this circuit as well in real-time applications. The resistor, R_n was chosen as the nominal value of R_x (i. e., $100 \text{ }\Omega$ for RTD-Pt100 and RTD-Pt1000 has $1 \text{ k}\Omega$).

The sensor resistance, R_x was varied in accordance with RTD-Pt100 [140] for a temperature range ($-50 \text{ }^\circ\text{C}$, $130 \text{ }^\circ\text{C}$). This corresponds to $R_x \in (80 \text{ }\Omega, 150 \text{ }\Omega)$. This variation of R_x was realized using a precision decade resistance box from Zeal Pvt. Ltd. (specifications: resolution $1 \text{ }\Omega$ and accuracy 0.1%) and it was cross-verified using a 5.5-digit multimeter (model no: 34450A) from Keysight Tech. The step size of variation was $5 \text{ }\Omega$. The output of the DIR-SE was recorded for each step of R_x . The plot of input-output characteristics of DIR-SE is shown in Fig. 5.5. The parameters, e_{NL} and e_{REL} of DIR-SE output are estimated and plotted in Fig. 5.5 (see scatter plot). The datasets are attached in Appendix B.4. DIR-SE can be seen to render a linear transfer characteristic, with $e_{NL} < 0.09 \%$ and $e_{REL} < 0.29 \%$. It can be seen that the error obtained from emulation is different and lower than the theoretically predicted value (refer to Section 5.3.1). This is mainly due to the actual value of ΔR_s being lower than the worst-case value of $12 \text{ }\Omega$. These results were also verified in the simulation model

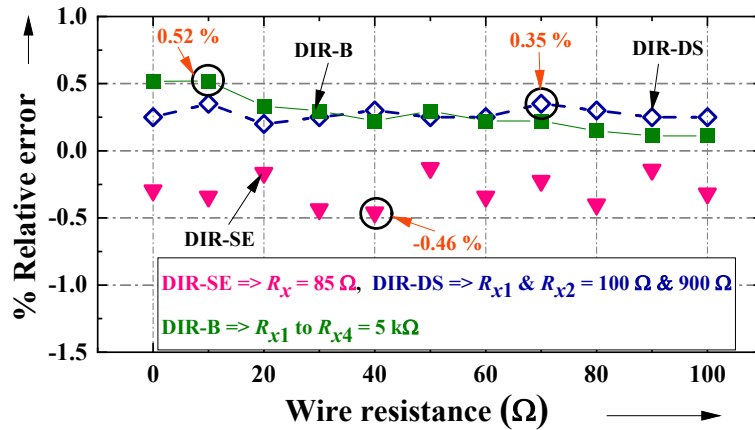


Fig. 5.6. Results depict the low dependence of wire resistances on the performance of DIR circuits.

(Tool: LTspice from Linear Technology Inc.) of DIR. The results from simulation and emulation studies followed each other closely, as will be discussed in Section 5.5.3.

Further, the versatility of DIR-SE is also checked by interfacing with another sensor (RTD-Pt1000) of different nominal resistance. The output of the CTU was obtained for each step of R_x and plotted and given in Fig. 5.5. The DIR-SE gives good performance in this case as well. The parameters, e_{NL} and e_{REL} were, respectively, less than 0.09 % and 0.22 %. The power consumption of the DIR-SE circuit is found to be around 12 mW. Further, the DIR-SE circuit was tested for a wide range of operations. In this case, R_x was varied from 1 kΩ to 1 MΩ, and the measured e_{NL} is less than 0.22 %.

Next, the emulation was done to verify the dependence of the wire resistances. The wire resistance (R_{w1} to R_{w3}) was varied from 0 Ω to 100 Ω, in steps of 10 Ω. R_x was fixed as 85 Ω as this value of R_x shows the maximum error (see Fig. 5.5). The e_{REL} (defined with respect to 85 Ω) is noted for different values of wire resistances and it is plotted in Fig. 5.6. From Fig. 5.6, it can be observed that the absolute value of relative error in R_x measurement, for $R_w \in (0 \Omega, 100 \Omega)$, is ranging from 0.13 % to 0.46 %. Hence, this result clearly conveys that the wire resistances have a low influence on the performance of DIR-SE.

5.4.2. Emulation Studies of DIR-DS

The DIR-DS was built and interfaced with differential-type sensors. The components used in DIR-DS were the same as in DIR-SE, except for R_n (note, R_n is not present in DIR-DS). The DS resistance were emulated to mimic the characteristics of PTV09A-2 020F-B102 potentiometric sensor [167] and LT-150 displacement sensor [33]. In the first case, the sensor specifications [167] used were $R_o = 500 \Omega$ and $x \in (-0.8, 0.8)$. The second sensor was chosen to have $R_o = 2.5 \text{ k}\Omega$ and $x \in (-0.6, 0.6)$ [33]. In both cases, the output of DIR-DS was noted for different x values. The resulting output characteristics with R_{x1} are plotted and given in Fig. 5.7. The linear variation of measured resistance can be observed from these plots. The parameters, e_{NL} and e_{REL} of these DIR-DS measurements were less than 0.07 % and 0.3 %, respectively (see scatter plot in Fig. 5.7).

The wire resistance effects of the DIR-DS circuit were also verified in emulation studies. This was done by varying R_{w1} to R_{w3} from 0Ω to 100Ω by keeping R_{x1} and R_{x2} as 100Ω and 900Ω (condition for maximum error, observed from Fig. 5.7). The observed errors for each step of wire resistance are plotted in Fig. 5.6. From Fig. 5.6, it can be inferred that the error does not vary much with R_w . The maximum error is less than 0.35 %.

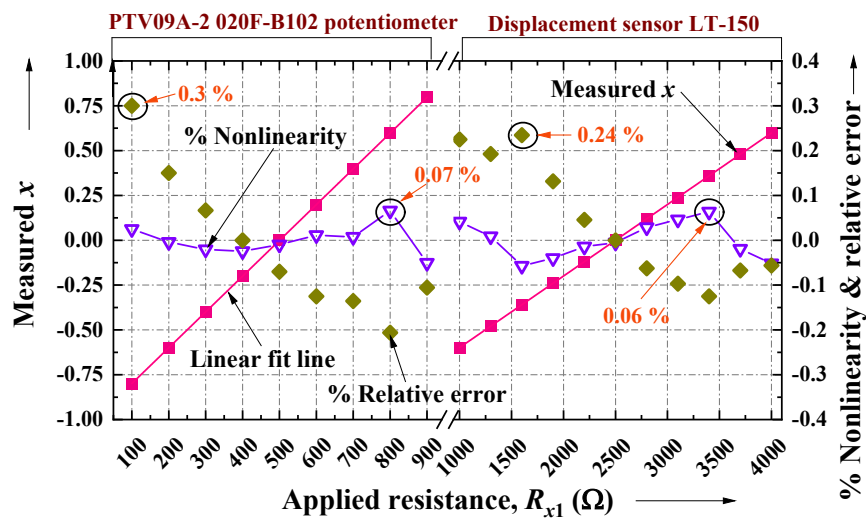


Fig. 5.7. Emulation results of the proposed DIR-DS with two types of commercial differential sensors.

5.4.3. Performance Studies of DIR-B

The DIR-B circuit was also evaluated for performance. All the components of DIR-B were similar to DIR-SE/DIR-DS, and the switch S_4 was designed using MAX4052 IC. Two bridge-sensors were selected for emulation study. First sensor used is AA004 GMR IC [37] (an HB sensor). Second sensor is a FB-type AMR sensor IC [168]. For the first sensor, R_{x2} and R_{x3} were set as $5\text{ k}\Omega$, and R_{x1} and R_{x4} were varied from $4.5\text{ k}\Omega$ to $5\text{ k}\Omega$. The AMR sensor characteristics were emulated with $R_o = 1\text{ k}\Omega$ and $x \in (-0.1, 0.1)$. The measured resistance from DIR-B is plotted with R_{x1} and shown in Fig. 5.8. The maximum e_{NL} and e_{REL} of these measurements are 0.17% and 0.4% , respectively. This can be visualized from the scatter plots in Fig. 5.8. Similar linear transfer relation of DIR-B was observed with AMR sensor characteristics. The power consumption of the DIR-B is found as 17 mW . The DIR schemes can be seen to consume lower power than the similar microcontroller-based resistive-digitizers in [60], [114], and [136]. This is because the developed DIR utilizes the microcontroller only for the generation of control signals and time measurements.

The effect of the wire resistances on DIR-B was also checked. The sensor resistances were fixed as $5\text{ k}\Omega$. The output of DIR-B did not vary with respect to R_w for $R_w \in (0\text{ }\Omega, 100\text{ }\Omega)$. The results are plotted in Fig. 5.6, and the worst-case error is 0.52% . Further, the conversion time (t_c) of the developed DIR circuits was also found.

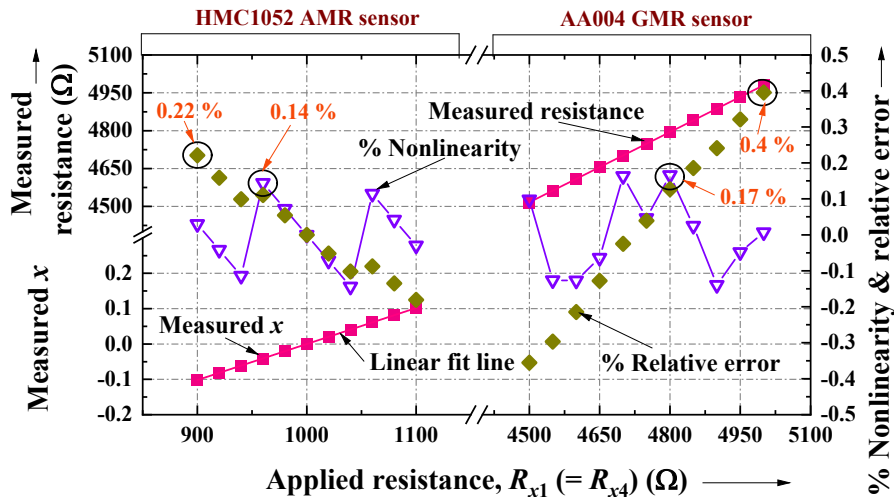


Fig. 5.8. Results of the proposed DIR-B are plotted when interfaced with magneto-resistance-based bridge sensors.

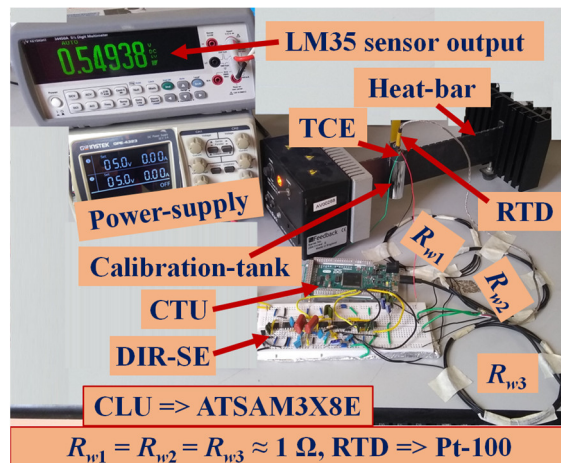


Fig. 5.9. Photograph of the experimental setup used for RTD sensor interface with DIR-SE. The values of t_c are 30 ms and 38 ms for DIR-SE and DIR-DS, respectively. The DIR-B circuit has a t_c of 42 ms. From the above various results, it can be inferred that the developed DIR schemes produce a linear digital output independent of various non-idealities like wire and switch resistance, threshold voltage of microcontroller, etc.

5.5. Experimental Studies of the DIR Circuits

The real-time performance of the developed DIR circuits was verified by interfacing various types of commercial sensors. Initially, these sensors were characterized to find their inherent errors. The experimental procedure for

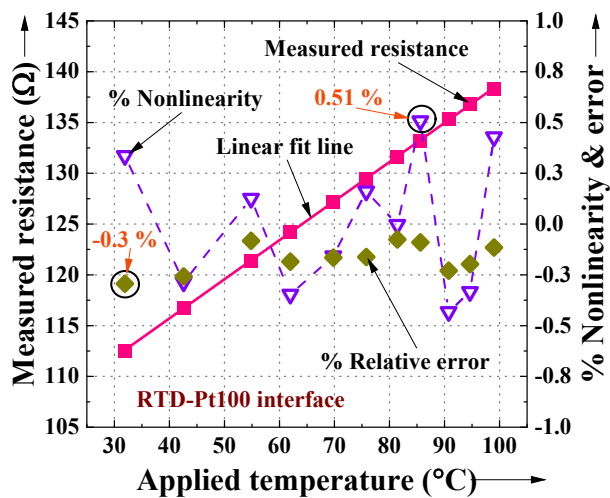


Fig. 5.10. Experimental results of the developed DIR-SE with RTD-Pt100 sensor.

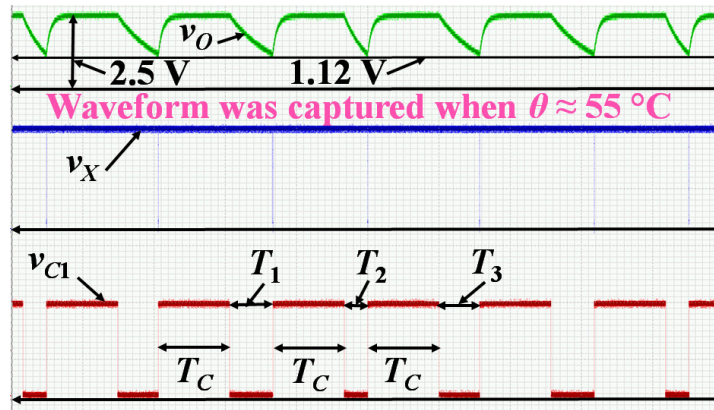


Fig. 5.11. Oscilloscope waveforms of RTD + DIR-SE circuit at $\theta = 55^\circ\text{C}$. Here T_C is fixed as 5 ms and the x-axis is 5ms/division.

characterization is present in [134]. Later, the estimation of the static performance parameters was also performed in this section.

5.5.1. Experimental Studies with Commercial Sensors

The DIR-SE was evaluated with a temperature measurement setup, in which RTD-Pt100 was used as the basic resistive sensor. A photograph of this experimental setup is shown in Fig. 5.9. The calibration-tank, containing water, was moved on the heat-bar. The heat-bar has different temperatures (say, θ) along its length. Thus, the resistance of the RTD will vary with respect to the position of the calibration-tank on the heat bar. The reference θ was measured using an LM35 sensor which was placed inside the Thermally-Conductive Enclosure (TCE). The water temperature was varied from 32°C to 99°C . The relation between measured resistance and θ using DIR-SE is

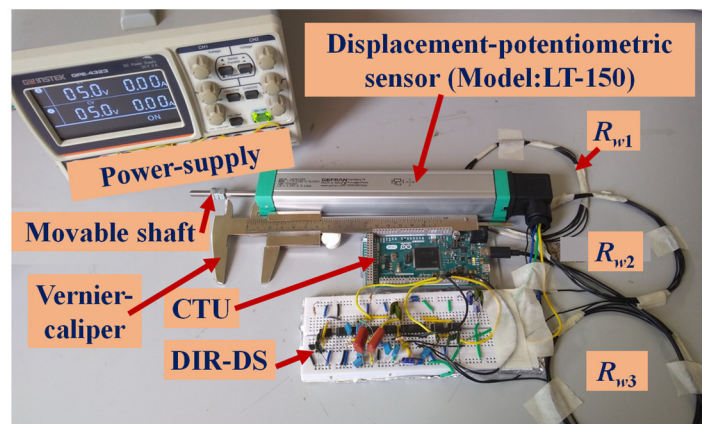


Fig. 5.12. Photograph of the experimental setup used for RTD sensor with DIR-DS.

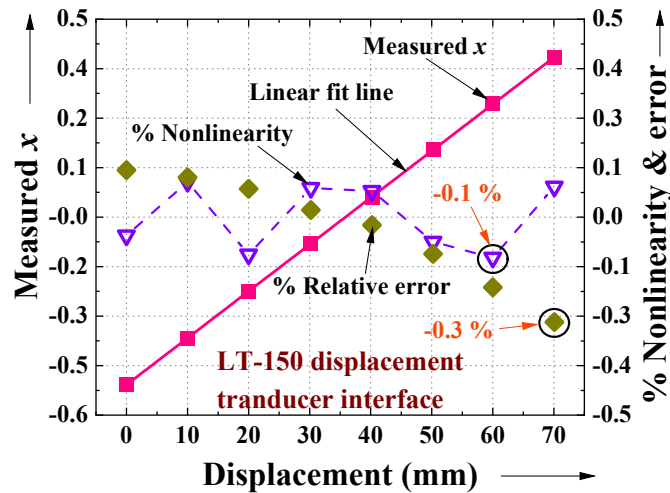


Fig. 5.13. Experimental results of the developed DIR-DS with displacement sensor.

linear and the same is plotted in Fig. 5.10. The measured e_{NL} values are also plotted as a line + scatter plot, and the maximum e_{NL} is 0.51 %. The value is higher than the e_{NL} observed in the emulation studies. This is because the inherent e_{NL} of the RTD sensor is around 0.59 % [134]. Similarly, the error, e_{REL} was also found with respect to the sensor output, and the maximum e_{REL} is 0.3 %. The oscilloscope waveforms were recorded at $\theta \approx 55^\circ\text{C}$ given in Fig. 5.11.

Later, the LT-150 displacement transducer was interfaced with DIR-DS. The experimental setup used for this interface is shown in Fig. 5.12. Here, the displacement (say, d) of the shaft varied from 0 mm to 70 mm (reference: vernier-caliper). The measured x versus d is plotted in Fig. 5.13. From Fig. 5.13, it can be inferred that the

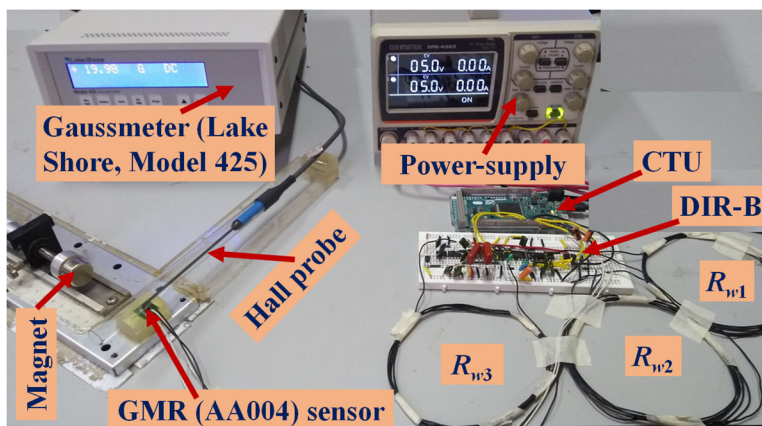


Fig. 5.14. Photograph of the experimental setup used for the interface of GMR sensor with DIR-B.

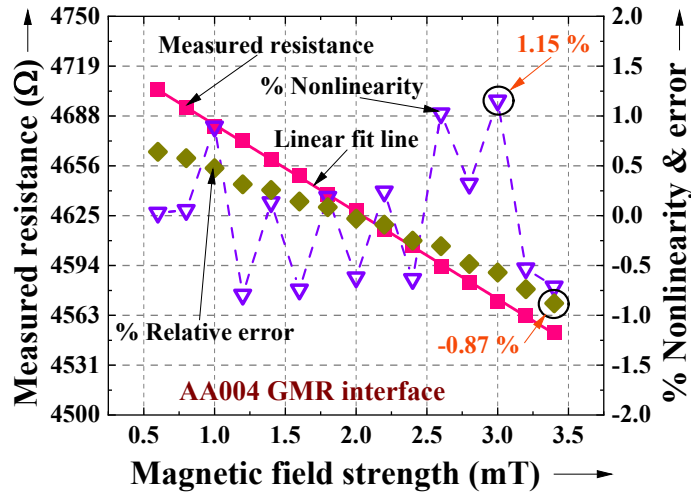


Fig. 5.15. Experimental results of the developed DIR-B with GMR sensor.

maximum e_{NL} is 0.1 %. At the same time, the parameters, e_{NL} and e_{REL} between the sensor and DIR-DS were found as 0.11 % and 0.27 %, respectively.

Finally, the AA004 GMR sensor was interfaced with the DIR-B. Here, the $B_{EXT} \in (0.5 \text{ mT}, 3.5 \text{ mT})$ was generated using a magnet. The reference field was estimated using Lakeshore (model: 425) gaussmeter. The experimental setup can be seen from Fig. 5.14. The relation between measured resistance and B_{EXT} is given in Fig. 5.15. It can be observed that the DIR-B circuit possesses e_{NL} of 1.15 %, which is similar to the inherent nonlinearity (1.27 %) of the GMR sensor. However, the error e_{REL} is increased from 0.4 % to 0.88 %, mainly due to the error sources of the GMR sensor.

5.5.2. Statistical Performance Parameters Estimation

The performance parameters (like SNR, σ , etc.) of the developed DIR circuits were also checked (using expressions given in Appendix A), and the results were given in Table 5.3. These quantities were estimated with the help of 250 repeated measurements. The resistance, R_x was kept as 1 k Ω for the DIR-SE circuit. The fractional resistance change of the DIR-DS and DIR-B was measured when x was fixed as 0.6 and 0.1, respectively. From Table 5.3, it can be concluded that the static parameters of the proposed DIR schemes are in an acceptable range, and the maximum resolution is obtained as 10.26 bits.

Table 5.3

Results of the Static Parameters Estimation

Parameters	DIR-SE	DIR-DS	DIR-B
	$R_x = 1 \text{ k}\Omega$	$x = 0.6$	$x = 0.1$
Signal-to-Noise Ratio (SNR) in dB	54.33	63.55	54.68
Standard Deviation (σ) in %	0.19	0.07	0.18
Resolution in bits	8.73	10.26	8.79
Repeatability Error (R_E) in %	0.15	0.26	0.16

5.5.3. Outline of Experimental Studies and Comparison with Prior-Art

The performance of the DIR circuits was thoroughly evaluated in Sections 5.4 and 5.5. A summary of the emulation results for different cases of resistive sensors is consolidated and given in Fig. 5.16. Fig. 5.16 also contains the results obtained from simulation studies of the DIR schemes. It can be seen that the parameters, e_{NL} and e_{REL} of the DIR schemes are quite low. The results from simulation and emulation environments corroborate relatively well. The additional errors present in the emulation results could include the effects of the mismatch in wire resistances as well as differences among the switch on-resistances and CTU errors. The experimental studies with commercial sensors were reported in Section 5.5.1. The results show that the parameters, e_{NL} and e_{REL} of the DIR circuits are slightly higher than the results depicted

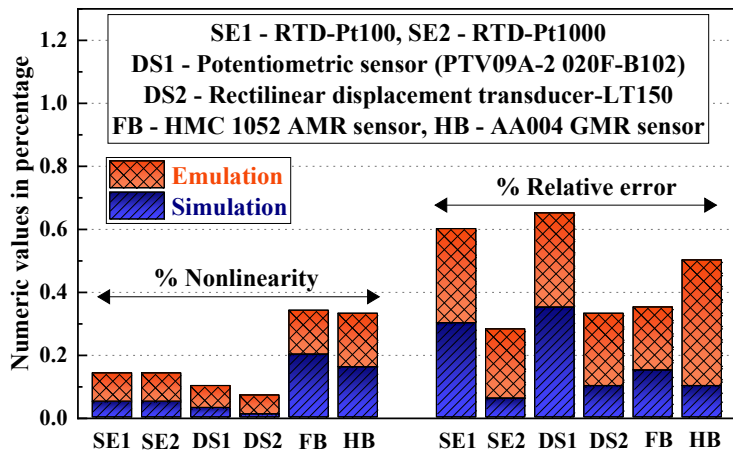


Fig. 5.16. Comparison results of the simulation and emulation studies for SE, DS, and bridge-type sensors.

in Fig. 5.16. This is mainly due to the inherent error sources of the commercial sensors. The precision-wise performance of the DIR schemes was also found to be appreciable.

The developed schemes also offer comparable or better performance, in terms of qualitative and quantitative parameters, when compared to the existing resistive sensor digitizers. The presented scheme has lesser wiring requirements compared to [85], [114], [115], [156] and possesses lower error than the two-wire schemes [60]-[62], [143]. The number of conversion cycles, and the capacity for wire resistance compensation is also similar/better when compared to many of the other schemes [60]-[62], [85], [114], [115], [143], [156]. It should be noted that the above features are realized using a simple and low-cost interfacing architecture that uses a single reference voltage, a comparator, and few switches. In addition, the cost of the DIR is not significantly high when compared to [60], [61], and [114]. The DIR circuits are independent of the threshold voltages of CTU. Thus, the developed schemes act as simple interfaces for remote measurements of three-wire resistive sensors available in various configurations.

5.6. Summary

Simple digitizing interface circuits for three-wire resistive sensors, available in SE, DS, and bridge-type configurations were designed and evaluated in this chapter. The circuits were basically configured to operate in a series of capacitive discharging processes through resistive sensor paths, such that the effect of connecting wire and switch resistances gets nullified. The charging process happens within two reference levels so that high precision measurements can be achieved. The performance of the DIR circuits was simulated and emulated and the results were compared. Results show that the developed circuits gave adequate performance parameters. Finally, the DIR circuits were interfaced with various commercial resistive sensors.

Next chapter discusses the design and implementation of a similar direct-microcontroller-based digitizing interface circuit for an industrially-relevant type of sensor (i. e., parallel RC impedance sensor).

Chapter 6

Simple and Accurate Digitizer Circuit for Parallel RC Impedance Sensors

6.1 Introduction

A digitizer based on the “charge-discharge” method for resistive sensors was evaluated in the last chapter. In this chapter, a digitizer, based on a similar method, is proffered for parallel RC impedance sensors. Such impedance sensors have utility in a number of industrial scenarios. The proposed digitizer for impedance sensors is described in this chapter.

6.2. RC Sensors and Interfacing Techniques

The parallel RC impedance sensor can be generally present as either a floating model [71], [72] or a grounded model [123], [124]. The front-end can be designed for floating impedance sensors in such a way that the output is intrinsically insensitive to parasitic elements [123]. However, due to safety reasons and/or operating limitations, the grounded model is preferable for some applications. For example, a scenario of a ground capacitive sensor is present in the level measurement of conductive liquid held in a grounded metallic container [169], [170]. Similarly, the distance/proximity measurement, using the capacitance technique, employ grounded metallic objects [116].

Various research schemes are proposed for the floating and grounded RC impedance sensors. Some of the important research works are given in Table 6.1. This table classifies the schemes based on the parameters like methodology, complexity, type of output, etc. The work proposed in [71] is based on the quadrature measurement principle and generates an analog output. The circuit is shown to be suitable for the measurement of resistance from 201 k Ω to 612 k Ω and capacitance ranging from 22 pF

Table 6.1

Literature Map and Comparison Study Between the Existing Readouts for Impedance Sensors with DFRC

Parameters	[71]	[72]	[117]	[118]	[88]	[89]	[119]	[111]	[171]	DFRC
Circuit topology	Quadrature measurement	Charge-Discharge	Bridge			Dual-slope		Relaxation oscillator		Charge-Discharge
Sensor model	Floating								Grounded	
Adaptability for R_x and C_x measurement	Yes								No	Yes
Output type	Analog	Digital	Analog			Digital				
Effect of pin/parasitic capacitance	No	Yes	No	Yes	No		Yes	No		
Complexity	High	Low	High			Moderate	High	Moderate	Low	
Conversion cycles	NA	4	NA			2	3		1 ^b	3^c
Conversion time (ms)	NA	3	NA			3000	1000	100	75	23
% e_{NL} (R_x & C_x)	2.2 & 0.6	6 ^a	8 & 6	10 ^a	5 & 0.72	NR	0.73 & 0.82	5 & 10	0.14 ^d	0.3 & 0.28
Resolution (C_x)	NR	NR	1 pF	30 fF	0.04 fF	12 fF	0.5 pF	NR		8 pF
Range of R_x (M Ω) ^f	0.2 – 0.6	1 – 10	0.33 – 3	0.33 – 1.2	0.1 – 409	0.7 – 0.9	0.05 – 0.95	1 – 10 ⁵	0.001 - 1	0.01 - 1
Range of C_x (nF) ^f	0.02 – 0.68	0.15 – 0.2	0.1 – 2	0.002 – 100	0 – 0.01	0.1 – 0.3	0.05 – 0.8	0 – 0.05	0 – 1 ^e	0.1 – 4.1
NA – Not Applicable, NR – Not Reported, a – Obtained for C_x measurement, b – Only for R_x estimation, c – Two conversion cycles can be used for calibration in C_x -mode, at the beginning of the experiment, d – Obtained for R_x measurement, e – Used to find independency from C_x , f – Range used for the developed prototype										

to 682 pF. However, the circuit is complex and requires a high analog component-count. A simple charge-discharge-based approach, for resistive and capacitive measurement, has been proposed in [72]. This scheme can be affected by the resistance and capacitance of the microcontroller pins and the accuracy levels of the microcontroller thresholds. The microcontroller delivers charging and discharging currents, which can lead to additional power consumption [145]. The work developed in [117] is also suitable for both resistance and capacitance measurements. However, the circuit requires sinusoidal excitation and generates an analog output. The circuit reported in [118] has high e_{NL} ($\approx 10\%$) for a range of 2 nF to 100 nF. The work developed in [88] employs a self-balancing technique for lossy capacitive sensors. The schemes reported in [72], [88], and [118] provide immunity against parasitic resistance for a wide-range (see Table 6.1). However, the methodology proposed in [88] requires several components, including modulator stages and analog-to-digital converters, etc. The front-end circuit in [89] is suitable for RC impedance sensors. In addition, the circuit produces a direct digital output with respect to the measurand (resistance or capacitance). However, the prototype developed in [89] consumes high power (≈ 170 mW) and requires a waveform generator which increases the complexity of the front-end. The scheme reported in [119] works based on a dual-slope mechanism. This circuit can be able to work for the resistance range of 50 k Ω to 950 k Ω and a capacitance range of 50 pF to 800 pF. A high-component-count relaxation oscillator for floating-type RC impedance sensors has also been developed in [111]. These schemes [71], [72], [88], [89], [117], and [118] consider floating-type RC sensors.

Circuits based on relaxation oscillator-based technique, especially for grounded-type sensors, are proposed in [120]-[122], [171]. The scheme in [120] uses a three-phase method with grounded capacitive sensors in the range of 100 pF to 2 μ F and nullifies the effect of offset capacitances present in the circuit. An alternate implementation of three-phase method has been achieved in [121] using a circuit that requires two reference capacitors. However, the methodologies adopted in [120] and [121] do not consider the effect of the shunt conductance of the capacitive sensor. A modified relaxation oscillator-based technique developed in [122] eliminates the

effects of shunt conductance. However, this method requires bipolar voltage and current source for its operation. In addition, the scheme in [122] does not have the capability to measure the shunt conductance.

This chapter proposes a simple and efficient digital front-end that can measure both the resistance as well as the capacitance of the grounded parallel RC impedance sensor (an industrially important sensor type). Keeping the significant issues (see Table 6.1) of the previous schemes in mind, an enhanced, but low component count, digital architecture for parallel RC impedance sensor is proposed in this work. This work does not require the use of sinusoidal voltage sweep as needed in magnitude/phase estimation schemes. This results in low complexity and less execution time. It offers many additional features when compared to the prior art as listed below. (1) Simple front-end circuitry using readily available components. Component count is lesser than [71] and [88], [89], [117], and [118], (2) Automated capability to measure the resistance and capacitance of impedance sensor, without being affected by its parasitic elements. On the other hand, techniques used in [118], [120]-[123], [171], and [173] are useful only for the measurement of either capacitance or resistance, (3) Wide range of measurements, (4) Precision direct-digitizer independent from many circuit non-idealities including the drifts in microcontroller threshold voltages and reference voltage, etc (these parameters can introduce adverse effects in traditional charge-discharge schemes [72] and [111]).

A new charge-discharge-based front-end proposed in this work enables to achieve simple circuit architecture and other salient features listed above. The working mechanism and the performance verification are detailed in the forthcoming sections.

6.3. Front-end for Interfacing Parallel RC Impedance Transducer

The proposed Digital Front-end for parallel RC sensors (DFRC) is shown in Fig. 6.1. The RC sensor is modeled using a resistor, R_x , and capacitor, C_x (see Fig. 6.1). These elements (R_x and C_x) are measured using the simple DFRC, which consists of

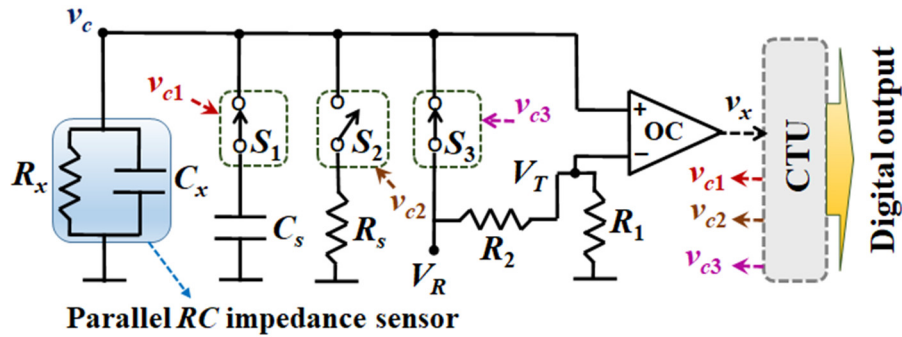


Fig. 6.1. Circuit diagram of the proposed DFRC for parallel RC sensor.

three switches (S_1 , S_2 , and S_3), a comparator, OC, a reference voltage, V_R , and a few passive components. A Control and Timing Unit (CTU) accepts the output, v_x of OC, and then controls the DFRC operation. The DFRC operates in three modes. The mode-setting is done by the CTU, with the help of the switch-control signals, v_{c1} to v_{c3} . The waveform at important nodes of the DFRC is depicted in Fig. 6.2(a) and the control signals are shown in Fig. 6.2(b). The switches will be closed-state when their control signal is high, and open, otherwise. The methodology to measure R_x and C_x is detailed in the forthcoming subsections.

6.3.1. Resistance Measurement

The DFRC measures R_x using a dual-mode (say, mode-1 and mode-2) operation. Each mode has a charging phase (phase-C) followed by a discharging phase

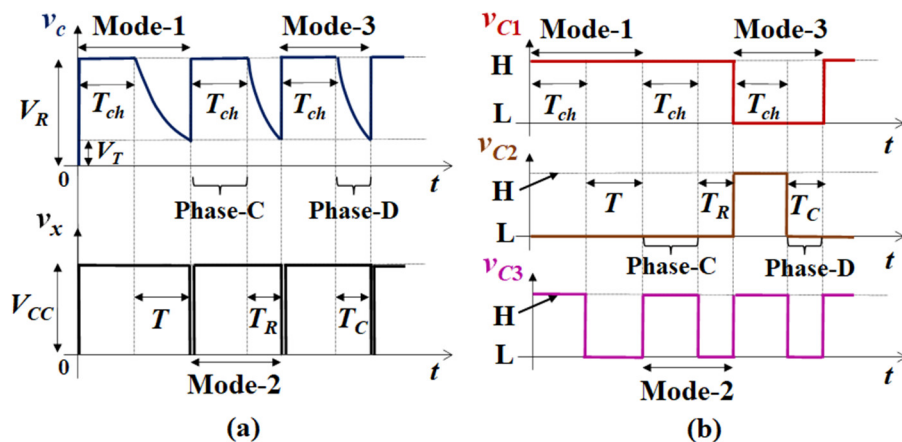


Fig. 6.2. Expected voltage waveforms (v_c and v_x) of the DFRC is shown in (a). Control signals, v_{c1} , v_{c2} , and v_{c3} are shown in (b) for the measurement of R_x and C_x of the RC sensor (H and L indicates the High and Low level of control signals).

(phase-D). The phase-C of mode-1 is initiated by setting v_{c1} and v_{c3} to logic-high and v_{c2} to logic-low for a finite time duration (say, T_{ch}). This closes the switches, S_1 and S_3 , and opens S_2 . The voltage v_c equals V_R [vide Fig. 6.2(a)] in this condition. In other words, the capacitors, C_x and C_s charge to V_R . After the duration of T_{ch} , phase-D is started. For this, v_{c3} is changed to logic low state, setting S_3 to open state. This causes the capacitors, C_x and C_s to discharge through the sensor-resistor, R_x . The discharge behavior is clearly illustrated in Fig. 6.2(a). The discharge will happen till v_c reaches V_T , where $V_T = V_R \times R_1 / (R_1 + R_2)$. At this time instant, the comparator output, v_x changes its output, from logic high to logic low. This transition in v_x is sensed by the CTU, which in turn starts the mode-2 operation. The discharge duration (say, T) can be expressed as in (6.1).

$$T = R_x (C_x + C_s) \ln (V_R / V_T) \quad (6.1)$$

In mode-2 operation, phase-C is initiated. The control strategy during phase-C of all modes is the same. Hence, v_c quickly charges toward V_R . Once the charging is over, the CTU issues the control signals for setting S_2 and S_3 to close and open states, respectively [see Fig. 6.2(b)]. In this case, the discharge will happen through the resistance path of $R_x \parallel R_s$ and it will continue till v_x sees a high-to-low transition. The duration of this discharge time (say, T_R) can be expressed as,

$$T_R = (R_x \parallel R_s) (C_x + C_s) \ln (V_R / V_T) \quad (6.2)$$

Using (6.1) and (6.2), the following expression can be written, $(T / T_R) = 1 + (R_x / R_s)$. On further simplification, equation (6.3) can be obtained.

$$R_x = F_R R_s = \left(\frac{T - T_R}{T_R} \right) R_s \quad (6.3)$$

Equation (6.3) shows that the resistance, R_x can be easily estimated using the ratiometricity-based operation of T and T_R (i. e., the function, F_R). The time measurements can be accomplished using a timer/counter module of CTU. This permits to achieve a digital indication of R_x . It can be seen that the estimated output, R_x

is independent of the sensor-capacitance C_x , reference voltage V_R , and the threshold voltage V_T . Note that the capacitor, C_s increases the conversion time. Adequate value of C_s (and hence, T and T_R) can be used to reduce the effects of Op-amp slew-rate and improve the signal-to-noise ratio. Thus, the DFRC efficiently performs the measurement of R_x using a low-component architecture, operating in a dual-mode principle.

6.3.2. Capacitance Measurement

The DFRC uses an additional mode (mode-3) to carry out C_x measurement. The control signals, v_{c1} and v_{c2} are kept at logic low (S_1 and $S_2 \rightarrow$ open) in this mode. During phase-C of mode-3, the switch, S_3 is set to closed condition ($v_{c3} \rightarrow$ logic high). This charges C_x to V_R . Then, v_{c3} is set to logic low during phase-D, enabling the discharge of C_x through the R_x path. As in the other modes, the state-transition of v_x is detected by CTU and used to end phase-D and initiate the next cycle of operation. The discharge time (say, T_C) expression can be obtained as in (6.4).

$$T_C = R_x C_x \ln(V_R / V_T) \quad (6.4)$$

Using (6.1) and (6.4), the sensor capacitance, C_x can be easily obtained as (6.5).

$$C_x = \frac{C_s}{F_C} = \left(\frac{T_C}{T - T_C} \right) C_s \quad (6.5)$$

From (6.5), it can be observed that the ratiometric time-based function F_C (like F_R) is useful to find the sensor capacitance, C_x . Equation (6.5) also implies the measurement of C_x is not affected by R_x , V_R , and V_T . Summarizing, DFRC provides a low-complexity circuit solution that can measure both R_x and C_x of a parallel RC sensor, using three operational cycles (i. e., modes). The error analysis and performance evaluation of the proposed DFRC is discussed in the next sections.

6.4. Sources of Errors and Their Effects

The proposed DFRC is immune to many circuit parameters, like parasitic elements, drifts in V_R and V_T , etc. However, some non-idealities present in the circuit can affect its performance of the circuit, as discussed next.

6.4.1. Effects of Switches

Practical switches used to implement S_1 , S_2 , and S_3 will have finite on-resistances [149]. The switch S_3 is only used for charging the capacitors, and the charging time durations are not used [see (6.3) and (6.5)] for the determination of R_x and C_x . Hence, the on-resistance of S_3 will not introduce any error in the output. Similarly, the on-resistance (say, R_{S2}) of S_2 can be modeled to be in series with the resistor, R_s . The ensuing effect can be minimized by choosing R_s to be greater than R_{S2} . The switch S_1 is connected to the capacitor, C_s . A simulation study was performed to find the effect of the on-resistance (say, R_{S1}) of S_1 . Latter was modeled using characteristics of the switch IC [149] employed for the prototype DFRC. Results showed that R_{S1} produces only a negligible output-error.

In addition, the switches, S_1 to S_3 will have input, leakage, and output stray capacitances [149]. The stray capacitances of the switch, S_1 are represented as C_{1S} (input), C_{1DS} (leakage), and C_{1D} (output) in Fig. 6.3. The capacitors associated with S_2 and S_3 can be modeled in a similar fashion. Let C_{2S} , C_{2DS} , and C_{2D} stand for the capacitors of S_2 . The symbols C_{3S} , C_{3DS} , and C_{3D} represent the capacitors of S_3 . For the sake of better viewing, the stray capacitances of S_1 are only depicted in Fig. 6.3. It can be deduced that the capacitances, C_{1S} , C_{2S} , and C_{3S} will be in parallel with the sensor capacitance, C_x , and contribute to an offset error. The methodology to nullify the offset capacitances is discussed in the next subsection. The capacitances, C_{1D} and C_{3D} do not have any effect on the output. However, C_{2D} and the leakage capacitances, C_{1DS} , C_{2DS} , and C_{3DS} can cause deviation in the output. The effect of these capacitances was estimated using simulation studies, and a maximum error of 0.2 % was observed for typical values [149] of the above parasitics. Switches with lower leakage effects [174]

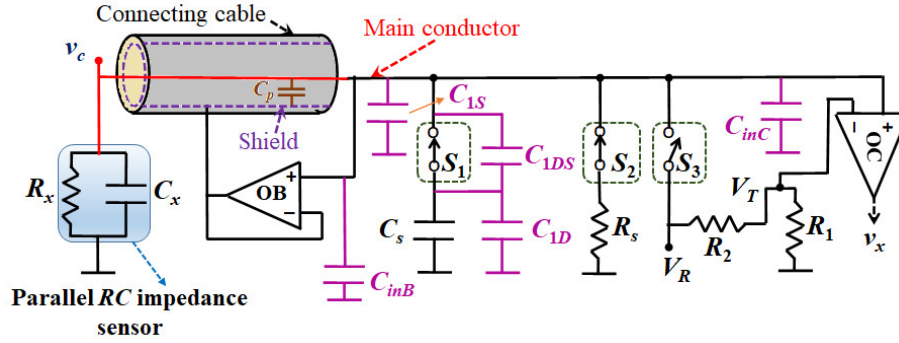


Fig. 6.3. Parasitic capacitances of DFRC are modeled and shown here. The parasitics of S_1 are represented as C_{1S} , C_{1D} , C_{1DS} . Similarly, the switches S_2 and S_3 have parasitics of C_{2S} , C_{2D} , C_{2DS} , and C_{3S} , C_{3D} , C_{3DS} , respectively. Method of active shielding is also illustrated.

could be employed to reduce this error. The effect of parasitics of other DFRC elements is discussed next.

6.4.2. Effect of Other Circuit Elements and Parasitic Capacitances of Connecting Cables

The input capacitances of the Op-amps OC and OB are modeled as C_{inC} and C_{inB} , respectively. This can be seen from Fig. 6.3. These capacitances will lead to an offset error. Therefore, the effective offset capacitance (say, C_{off}), due to circuit elements, can be written as $C_{off} = C_{inC} + C_{inB} + C_{1S} + C_{2S} + C_{3S}$. The connecting cables will also possess internal parasitic capacitances (say, C_p) between the main conductor and shield [173] (see Fig. 6.3). As a result, the total offset capacitance is $C_x + C_p + C_{off}$. It should be noted that the resistance mode operation of DFRC is independent of C_x , and hence, from C_p and C_{off} as well. The offset error in C_x -mode can be suppressed using the following methods.

6.4.2.1. Active Shielding Using Op-amp OB

This technique helps to nullify the effect of C_p . The active-shielding technique can be realized using either feedforward [123] or feedback [173] methods. As shown in Fig 6.3, the proposed DFRC employs a feedback active-shielding technique, with the help of the Op-amp OB circuit. This circuit will ensure negligible current flow through the capacitor, C_p , thus rendering it inactive.

6.4.2.2. Offset Calibration Method

This method helps to suppress the adverse effect of C_{off} . It can be applied once (beginning or end of the measurement process) or periodically. During this procedure, the sensor can be disconnected, and the following calibration can be performed.

The calibration mode consists of two conversion cycles. Each cycle comprises phase-C and phase-D. Switch positions in phase-C are the same as discussed in Section 6.3. During phase-D of the first cycle, the switches, S_1 and S_2 will be in the closed position (refer Fig. 6.3) and S_3 at open condition. The corresponding discharge time (say, T_{C1}) can be obtained as in (6.6).

$$T_{C1} = R_s (C_s + C_{off}) \ln (V_R / V_T) \quad (6.6)$$

The discharge phase of the second cycle will be done with S_1 in open condition ($v_{c1} \rightarrow$ logic low). Now, the discharge time (say, T_{C2}) becomes $T_{C2} = (R_s \times C_{off}) \ln (V_R / V_T)$. Using the new expressions of T , T_C , T_{C1} , and T_{C2} , the sensor capacitance, C_x can be obtained as (6.7).

$$C_x = \left[\frac{T_C (T_{C1} - T_{C2}) - T_{C2} (T - T_C)}{(T - T_C)(T_{C1} - T_{C2})} \right] C_s \quad (6.7)$$

Thus, we can infer that the calibration technique provides a simple method to compensate for C_{off} and render an offset-free indication of C_x .

6.4.3. Error Sources of Op-amp OB and OC

The effect of the slew-rate of Op-amp OB can also be reduced as follows: The slope of the voltage, v_c , during the discharge phase, should be kept as high as the slew-rate of the Op-amp OB. The charging phase has a large slope, however, the charge time is a fixed value. Thus, the charging time duration, T_{ch} should be selected as high enough such that the capacitor, C and (or) C_s get fully charged to V_R within T_{ch} . The developed prototype uses LF356 IC as Op-amp OB to avoid slew-rate-related errors. This Op-amp also improves the accuracy and stability of the DFRC [173]. The non-idealities like bias current and offset voltage of OB deviate the output by 0.15 % from its ideal value (i. e., $C_x = 200$ pF).

The offset voltage ($\pm \Delta V$) of OC gives a DC offset to the voltage, V_T . Thus, the offset voltage will change V_T as $V_T \pm \Delta V$. However, the output is independent of the threshold value, V_T , and thus offset voltage of OC causes a negligible error in the output.

6.4.4. CTU Errors

The output time durations, T and T_R are measured using the timer/counter modules of CTU. This module has a finite resolution (say, ΔT). This can alter the function F_R as F_R' , as given in (6.8).

$$F_R' = \frac{T - T_R + 2\Delta T}{T_R - \Delta T} \quad (6.8)$$

The worst-case error comes around 1 % when a timer module of (resolution $\approx 2 \mu\text{s}$) the ATSAM3X8E microcontroller is used for realizing the CTU. A similar approach can be used for the capacitance estimation and the ensuing maximum error can be seen as 2%. However, this error can be reduced using a timer [175] of higher resolution.

6.5. Simulation Studies of the DFRC Circuits

In this section, the performance of the proposed DFRC circuit is verified using simulation studies. For this purpose, the DFRC circuit was modeled in the LTspice simulation tool, and the following studies were performed.

6.5.1. Measurement of R_x

The proposed DFRC was modeled using the specifications of low-cost components available in LTspice software. The comparator OC was designed using LM311 IC specifications. The Op-amp OB was realized to have the specifications of LF356 IC. The switches, S_1 to S_3 were realized using MAX4053 IC characteristics. The offset capacitance, C_{off} was kept as 40 pF to mimic the capacitances of Op-amps OB and OC and switches. The reference voltage, V_R was selected as 2.5 V to mimic LM385-2.5 IC. The resistors, R_1 and R_2 were selected as 1.8 k Ω and 2.2 k Ω , respectively, to keep V_T as 1.12 V. The standard resistor, R_s was selected as 200 k Ω

and the capacitor, C_s was 10 nF. The CTU was implemented using a monostable multivibrator. It generates the control signals, v_{e1} to v_{e3} . The time duration, T_{ch} was fixed as 5 ms. The time durations, T and T_R were measured using a suitable command in LTspice software. The readings were rounded off to six decimal places (resolution $\approx 1 \mu\text{s}$) to meet the approximate timer/counter specifications of the ATSAM3X8E microcontroller.

The sensor resistance, R_x was varied from 10 k Ω to 1 M Ω with the steps of 33 k Ω , and the output (say, R_x^*) was measured in terms of resistance [using (6.3)]. The capacitance, C_x was fixed as 200 pF to comply with the specifications given in [123].

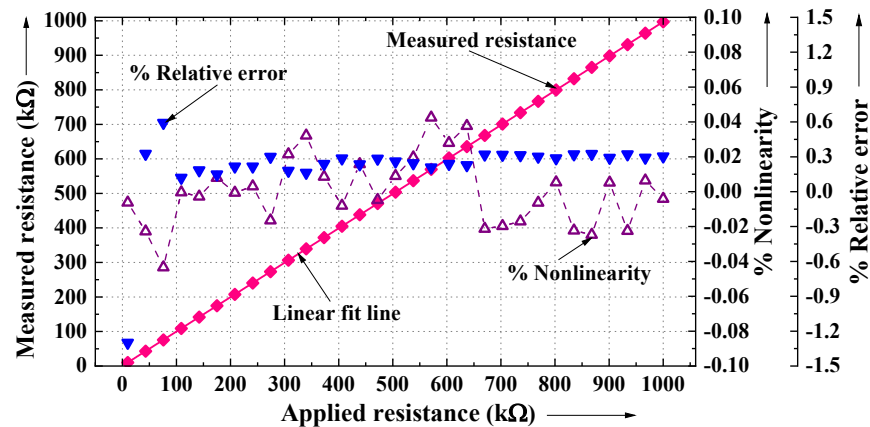


Fig. 6.4. Relationship between measured resistance and the sensor resistance of the DFRC when $C_x = 200 \text{ pF}$. The measured nonlinearity and relative error at each step of the sensor resistance are also plotted.

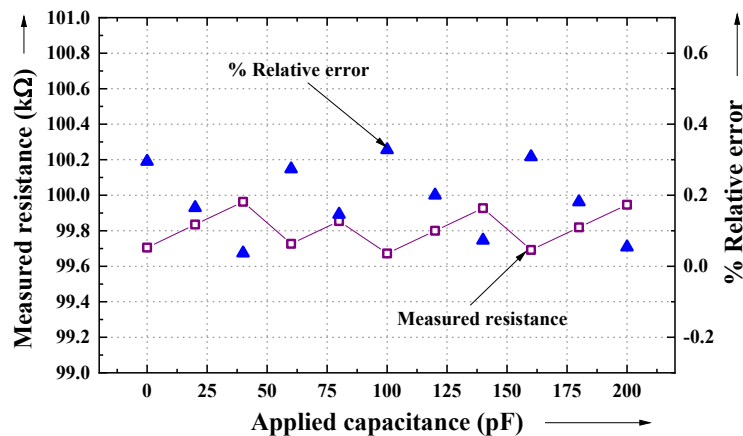


Fig. 6.5. Simulation results depicting the immunity against the variation in the capacitance, C_x during the measurement of $R_x (= 100 \text{ k}\Omega)$.

The input-output relationship is plotted in Fig. 6.4. It can be seen from Fig. 6.4 that the relationship between input and output is linear. The nonlinearity, e_{NL} at each value of R_x was estimated and it is also plotted in Fig. 6.4. The maximum e_{NL} is 0.05 %. The maximum conversion time of DFRC during the above experimentation was 20 ms. Similarly, the e_{REL} was also quantified at each step of R_x and plotted in Fig. 6.4. The maximum obtained error is 1.3 % (see Fig. 6.4).

Next, the effect of C_x during R_x measurement was also verified using simulation studies. This was done by keeping R_x as 100 k Ω and varying C_x from 0 to 200 pF in steps of 20 pF. The error, e_{REL} was measured at each step of C_x and it is

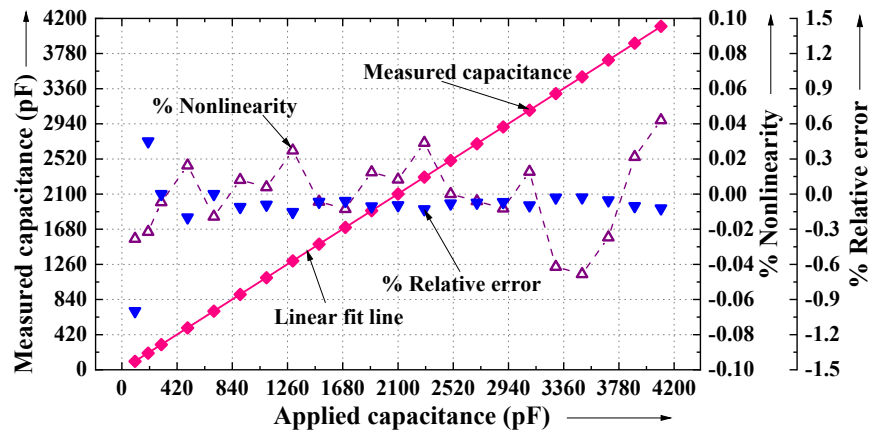


Fig. 6.6. Simulation results of the DFRC in capacitance measurement mode ($R_x = 100$ k Ω). Measured e_{NL} and e_{REL} are also plotted.

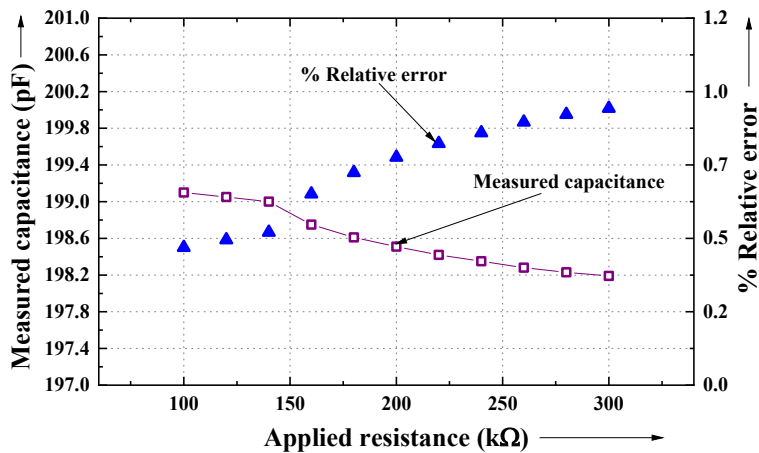


Fig. 6.7. Simulation results of DFRC, when R_x is varied from 100 k Ω to 300 k Ω and C_x is kept as 200 pF.

plotted in Fig. 6.5. It can be observed from Fig. 6.5 that the maximum e_{REL} is 0.33 %. Note that the main source of errors (shown in Fig. 6.4 and Fig. 6.5) is the resolution of the timer/counter module. The above studies validate the ability of the DFRC to generate a linear digital output with respect to R_x over a wide range. In addition, the output has a minimal effect on the variations in C_x .

6.5.2. Measurement of C_x

Similar to the measurement of R_x , the estimation of C_x was also studied by using the simulation model. In this mode, the range of sensor capacitance was selected as 100 pF to 4.1 nF, and the sensor resistance was fixed as 100 k Ω . The capacitor, C_p was selected as 80 pF to mimic 1.5 meters of coaxial cable. The offset capacitance, C_{off} was kept as 40 pF. The estimation of capacitance was done using (6.7). The measured input-output characteristics of DFRC were plotted and shown in Fig. 6.6. Fig. 6.6 shows a linear variation in output with respect to the input. The nonlinearity, e_{NL} and error, e_{REL} were also measured at each step of C_x and plotted in Fig. 6.6. From Fig. 6.6, it is observed that the maximum e_{NL} is 0.05 % and the e_{REL} is 1 %. Similarly, the maximum conversion time for C_x -mode is also found as 23 ms. This time can be reduced by choosing a lower value of T_{ch} .

Later, the errors in C_x -mode due to the variations in R_x were also measured by keeping C_x as 200 pF and varying the sensor resistance, R_x from 100 k Ω to 300 k Ω . The error, e_{REL} was calculated with respect to the true value of $C_x = 200$ pF. The measured errors are plotted in Fig. 6.7, and the maximum observed error is 1.41 % (see Fig. 6.7). The error plot can also be seen to increase with an increase in R_x . This is mainly due to the effect of the resolution of the timer, especially during the estimation of (typically low-valued) T_{c2} .

6.6. Experimentation of DFRC

The results obtained using the simulation studies were cross-verified using experimental studies. The developed DFRC model was bread-boarded. The Op-amps

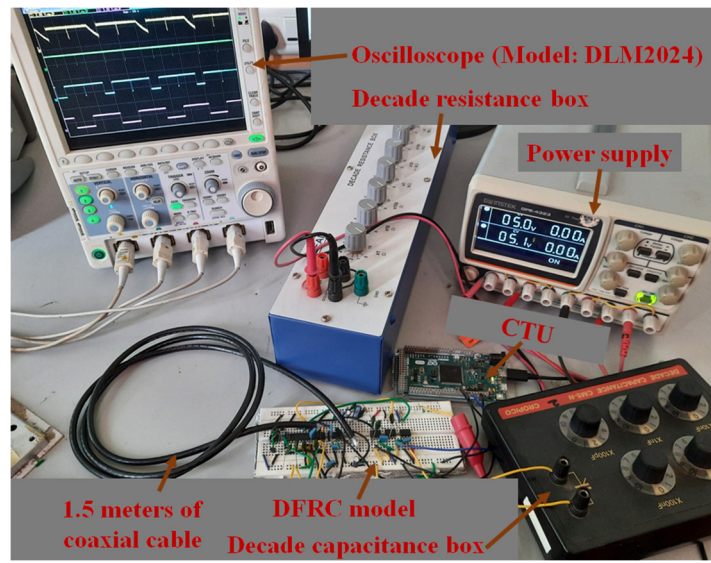


Fig. 6.8. Developed experimental setup for the resistance and capacitance measurement using DFRC circuit (C_x - mode). Note: Photograph was taken at $R_x = 100 \text{ k}\Omega$ and $C_x = 10 \text{ pF}$.

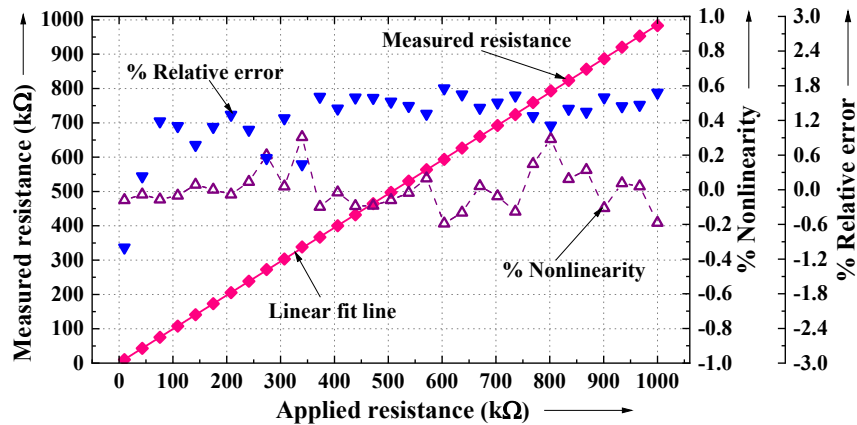


Fig. 6.9. Experimental results of the DFRC (R_x - mode) are plotted.

OC and OB were modeled using LM311 IC and LF356 IC. The switches, S_1 to S_3 were realized using MAX4053 IC, which has three internal switches. The CTU was realized using the ATSAM3X8E microcontroller, present in the Arduino Due platform. The discharge times were measured using the timer/counter module of the microcontroller. The sensor resistor, R_x and the capacitor, C_x were connected to the DFRC using 1.5 meters of coaxial cable which has $C_p \approx 80 \text{ pF}$. These elements (R_x and C_x) were varied using decade boxes, and the standard resistor, R_s was selected as $200 \text{ k}\Omega$ with 1 % tolerance. The experimental setup of the DFRC is shown in Fig. 6.8. It includes

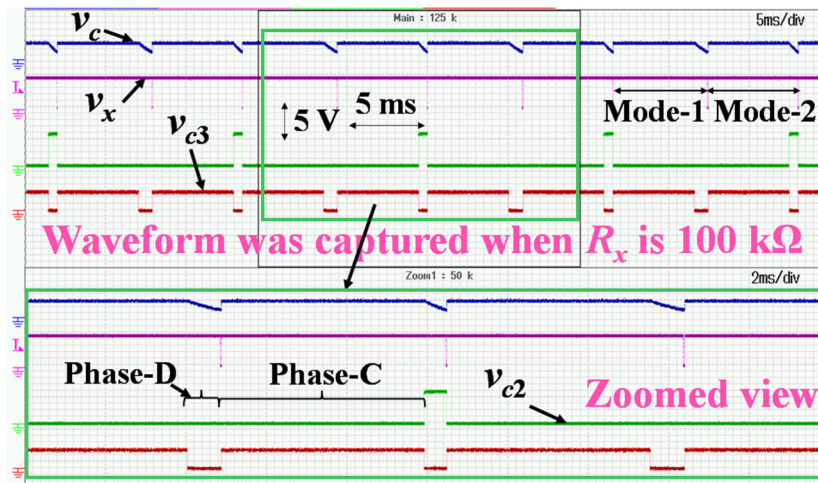


Fig. 6.10. Oscilloscope waveforms of the DFRC when the sensor resistance is 100 kΩ. Zoomed view of an important portion is also clearly shown at the bottom of the image.

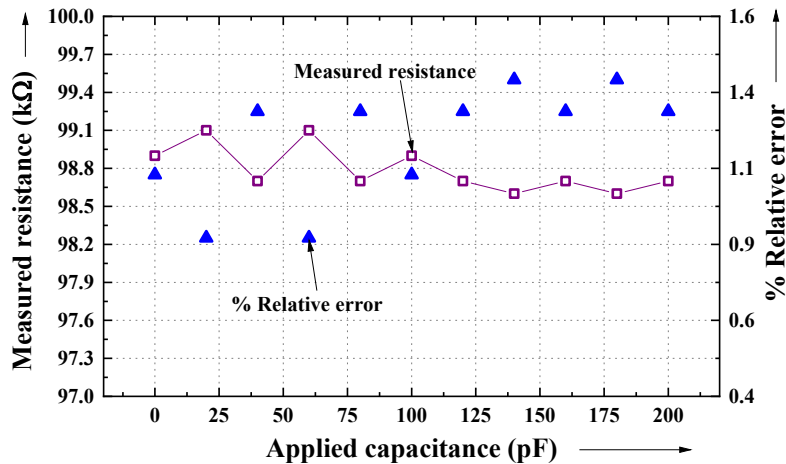


Fig. 6.11. Experimental results of DFRC (R_x - mode), when C_x is varied from 0 to 200 pF. Here R_x is kept as 100 kΩ.

the DFRC hardware, CTU, decade resistance and capacitance boxes to replicate the resistor, R_x and capacitor, C_x . The power supply (Model: GWINSTEK-4323) was used to power-up the circuit, and the oscilloscope (Model: DLM2024) was utilized to capture and verify the waveforms of DFRC. Estimation of R_x and C_x was done as detailed below.

6.6.1. Estimation of R_x

The capacitors, C_x and C_s were kept as 200 pF and 10 nF, respectively. The sensor resistance, R_x was varied using a decade resistance box from 10 kΩ to 1 MΩ.

The reference value of R_x was measured using a Keysight 5.5-digit multimeter (Model: 34450A). The output of the DFRC was noted for different values of R_x . Fig. 6.9 shows the input-output characteristics of the DFRC, obtained from this study. The nonlinearity, e_{NL} and the error, e_{REL} were also measured and plotted in Fig. 6.9. From Fig. 6.9, it can be observed that the developed DFRC can be able to render a linear digital indication of R_x for the range of 10 k Ω to 1 M Ω . The DFRC has a maximum e_{NL} of 0.3 % and the error, e_{REL} is less than 1.75 %. This error is slightly higher than the simulation results. This is mainly due to the inaccuracies in the decade resistance box used in the DFRC prototype. The oscillogram showing the node voltages v_c , v_x , v_{c2} , and v_{c3} is depicted in Fig. 6.10. This figure shows that these waveforms are matched with the theoretical predictions for R_x -mode (see Fig. 6.2). The power consumption of the circuit was found as 7 mW. This is much lower than the power consumed by the circuit proposed in [89] and other digital interfacing techniques for impedance sensors [71], and [88].

Later, the accuracy of the measurement of R_x was also verified by varying the sensor capacitance, C_x . Here, the resistor, R_x was kept as 100 k Ω , and C_x was varied from 0 to 200 pF. The error, e_{REL} was calculated for each value of C_x with respect to the reference value (i. e., $R_x = 100$ k Ω). These results are plotted in Fig. 6.11. The maximum error is 1.41 %.

6.6.2. Estimation of C_x

In this study, the capacitor, C_x was varied from 100 pF to 4.1 nF, using a decade-capacitance box (see Fig. 6.8). R_x was kept at 100 k Ω . The reference value of C_x was measured using an LCR meter (Model: GWINSTEK 6200). Note that, the sensor resistance, R_x was realized using a decade resistance box. Moreover, an oscilloscope was used for the visual inspection of the waveforms. Hence, probe capacitance and parasitic capacitance of the box will come into play and introduce an additional capacitance (say, C_{EXS}). As a result, the total offset capacitance gets modified to C_{off}' , where $C_{off}' = C_{off} + C_{EXS}$. The offset calibration technique, discussed in Section 6.4.2.2, was applied. The discharge times (T_{C1} and T_{C2}) can be found as 1.48 ms and

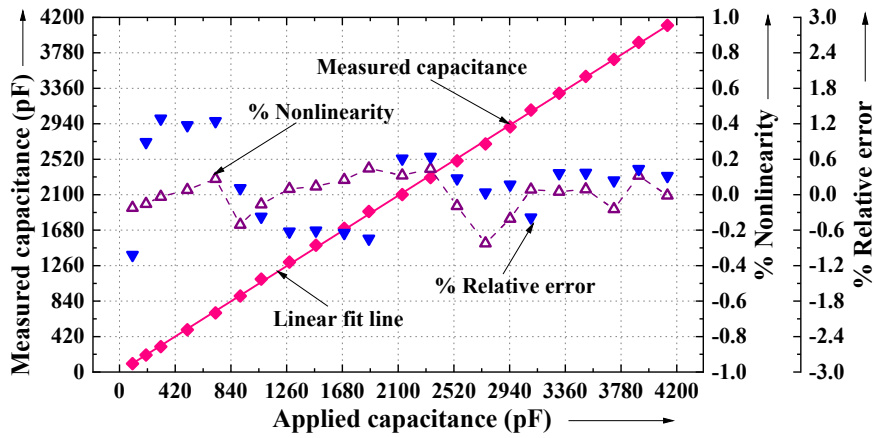


Fig. 6.12. Results of the DFRC used for the capacitance measurement.

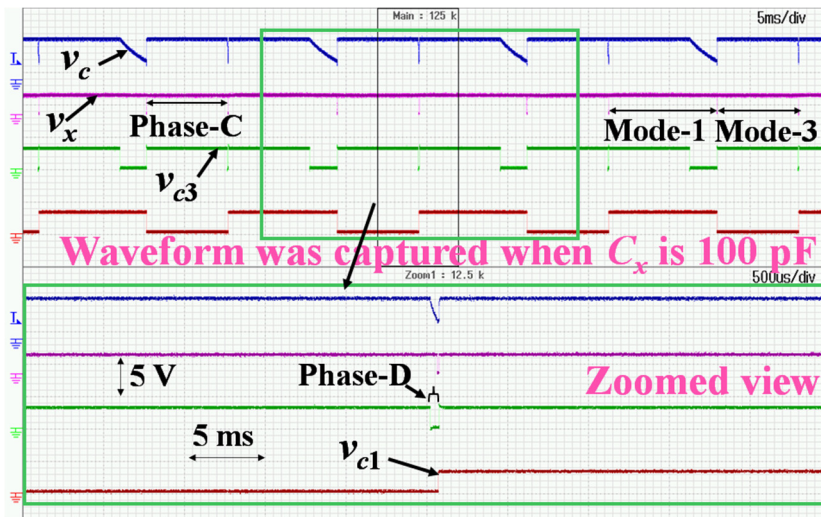


Fig. 6.13. Oscilloscope waveforms are observed from the important nodes of DFRC.

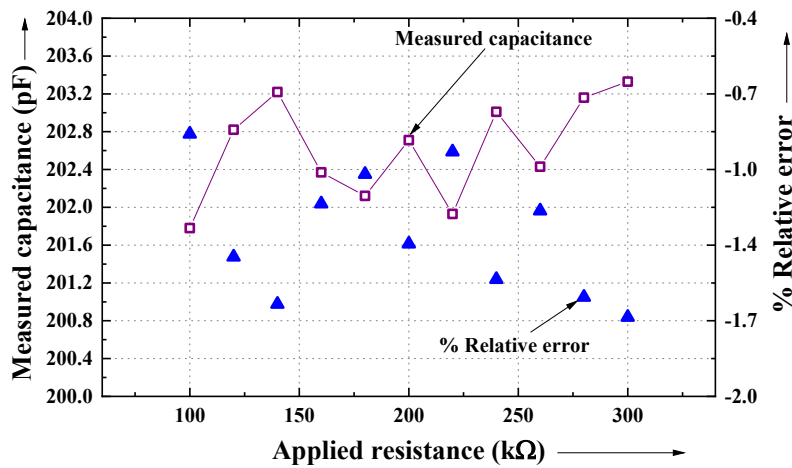


Fig. 6.14. Effect of changes in sensor resistance during the capacitance measurement of 200 pF ($= C_x$), observed on DFRC experimentation.

24 μ s. These values were used, as in (6.7), for offset-free measurement of C_x . The input versus output follows a linear relationship, as can be seen in Fig. 6.12 (data are given in Appendix B.5). From Fig. 6.12, it can be inferred that the measured e_{NL} and e_{REL} do not exceed 0.28 % and 1.3 %, respectively. The main sources of these errors are the resolution of the timer/counter module and the inaccuracies in the decade capacitance box. The oscilloscope waveforms were also captured at $C_x = 100$ pF and given in Fig. 6.13. Later, the sensor resistance, R_x was varied from 100 k Ω to 300 k Ω with a fixed C_x of 200 pF. The measured errors are shown in Fig. 6.14 and the maximum error is 1.67 %.

6.6.3. Other Performance Parameters Estimation

The performance parameters like σ , SNR, ENOB, and R_E were also found for the DFRC circuit using the expressions given in Appendix A. There were 250 consecutive measurements of R_x were used for this purpose. Here, R_x was kept as 100 k Ω and $C_x = 200$ pF. The results are given in Table 6.2. From Table 6.2, it can be inferred that the DFRC provides an SNR of 52.56 dB and R_E of 0.02 %. Similarly, the measurement of C_x (= 100 pF) was also performed using 250 samples (keeping $R_x = 100$ k Ω). The corresponding results are given in Table 6.2.

The above various experimental results show that the developed DFRC can produce a linear digital estimation of R_x and C_x , without being affected by their parasitic elements and circuit non-idealities. The main source of error of DFRC is mainly due to the timer/counter module of the CTU. It can be reduced by using high-resolution timer/counter modules [175]. The developed DFRC is useful to measure the resistance and capacitance of parallel RC impedance sensors for a wide range of the measurand.

Table 6.2

Results of the Estimation of Performance Parameters

Parameters	R_x measurement mode	C_x measurement mode
	$R_x = 100$ k Ω ; $C_x = 200$ pF	$C_x = 100$ pF; $R_x = 100$ k Ω
σ (%)	0.02	
SNR (dB)	52.56	55.79
ENOB	8.44	8.97
R_E (%)	0.02	

6.7. Summary

The developed DFRC was thoroughly analyzed and tested for performance, and the results were presented in this chapter. The DFRC, based on a low complexity charge-discharge-based circuit, is suited for resistance and capacitance measurement of parallel RC impedance sensors. In addition, the DFRC gives a direct-digital output, immune from the effects of pin-resistance and various parasitic capacitances. Further, the e_{NL} of DFRC is 0.3 % which is smaller than the existing schemes. The conversion time of the DFRC is also low. The conversion time of the DFRC can be further reduced by choosing a low value of charging time. Simulation and experimental results show that the prototype DFRC can be able to suit for wide-span measurements. The research work also proposed an offset calibration technique to reduce the effect of offset capacitances. Summarizing, the developed DFRC is an efficient linear-digital front-end circuit, suitable for various industrial applications.

The next chapter discusses the interface circuit for a special type of resistive sensor which is having a nonlinear output. Thus, it is essential to develop an interface circuit to linearize the nonlinear output of the sensor.

Chapter 7

Linearizing Circuit for Thermistor-Based Temperature Measurement System

7.1. Introduction

Interfaces reported in the previous chapters considered the availability of linear sensors. As mentioned in Chapter 1, some of the sensors (e. g., thermistor, LDR) possess nonlinear input-output relationship. This chapter focuses on the design and evaluation of linearizing digital measurement system for one of the most important nonlinear sensors (i. e., thermistor). The prior art related to thermistor signal conditioning is explained next, just followed by the design and comprehensive evaluation of the proposed digitizer for the thermistor in the forthcoming subsections.

7.2. Existing Measurement Systems for Thermistors

Linear temperature measurement systems using thermistors have been explored in [50], [87], [125]-[132], [146]. A tabular literature map of these works is given in Table 7.1. An artificial neural network-based linearizer is proposed in [125]. Here, a multilayer perception feed-forward network is used for the linearization of the thermistor-output. An astable-multivibrator in conjunction with the reciprocal transformation technique has been used in [126] to perform thermistor linearization. This scheme has been improved in [127], and the output e_{NL} is reduced to 0.8 % for temperature (say, θ) ranging from 30°C to 120°C. A Field Programmable Gate Array (FPGA) based linearization technique is proposed in [50]. This work provides excellent linearity for wide range, however, it requires many parameters of thermistors. The

This chapter is partially adapted from the post-print version of Elangovan K, B. A. Sontakke and A. Chandrika Sreekantan, "Design, Analysis, and Hardware Verification of a Linearized Thermistor-Based Temperature Measurement System," *IEEE Trans. Instrum. Meas.*, vol. 71, pp. 1-9, 2022, Art no. 2002709.

Table 7.1

Literature-Map of Linearized Thermistor-based Measurement System and Comparison Study

Ref.	Technique	Range (°C)	% e_{NL}	Remarks
[126]	555 Timer based ^S	0 to 120	1.7	Remote resistance measurement is not possible
[127]		30 to 120	0.8	
[50]	FPGA based	- 20 to 120	0.11	
[128]	μ C-based ^S	5 to 45	1	
[129]	ANN based	0 to 100	0.2	
[130]			0.8	
[131]	Analog Op-amp circuit	30 to 120	1	
[132]	Op-amp based linearizer	30 to 110	1.25	
[87]	Dual-slope digitizer	0 to 120	0.2	
[146]	ROD	0 to 120	1.4	
This work [176]	Improved ROD	0 to 120	0.44	Simple scheme providing (versatile) linearization, wide-span measurement, and lead-wire compensation (see Fig. 7.1 for other merits)

S – Simple technique, Ref. – References, μ C – Microcontroller, ANN - Artificial Neural Network, ROD - Relaxation oscillator-based digitizer

microcontroller-based scheme [128] can work with linear thermistor-based measurements for $\theta \in (5^\circ\text{C}, 45^\circ\text{C})$. The concept of an artificial neural network-based thermistor linearizer has been developed in [129], [130]. These works require complex algorithmic procedures. Table 7.1 summarizes the important performance details of these works.

The feasibility of employing Op-amp-based interface circuits for thermistor linearization has been described in [131], [132]. An inverting amplifier-based circuit has been developed for thermistors in [131], while the work in [132] has been employed

as a timing resistor of an astable multivibrator to realize linear output characteristics with temperature. The work in [131] requires a separate Analog-to-Digital Converter (ADC) for digitization. A direct digital converter employing a dual-slope method and a logarithmic amplifier, for thermistors has been demonstrated in [87]. This work possesses high linearity, however, the circuit requires bipolar reference voltage and the output depends on the switch resistances. The developed digitizer gives a high e_{NL} for wide temperature ranges (similar to some of the prior art [126], [132], [146]). Moreover, many of these schemes [50], [87], [125]-[132], [146] can render a considerable output-error due to the influence of significant lead-wire resistance, associated with remote sensors. Lead-wire resistance compensation is important where the wide-range of operations and low nominal value of thermistors are considered [172]. Lead-wire resistance will get added to the thermistor resistance and it leads to an output error especially when the resistance of the thermistor is low. This case can occur with a low nominal value of thermistors and/or at high temperature of operation. For example, the error due to lead resistance will become 1.3 % when $R_0 = 10 \text{ k}\Omega$ and $\theta \approx 105 \text{ }^\circ\text{C}$. Hence, it is essential to develop the wire resistance compensation technique for thermistors.

This chapter proposes a new Thermistor-Linearizing Digital Measurement (Th-LDM) system. The Th-LDM system not only linearizes and direct-digitizes the thermistor characteristics, but also provides an output, independent of the lead-wire resistance. A graphical overview of the scheme is illustrated in Fig. 7.1. As in Fig. 7.1,

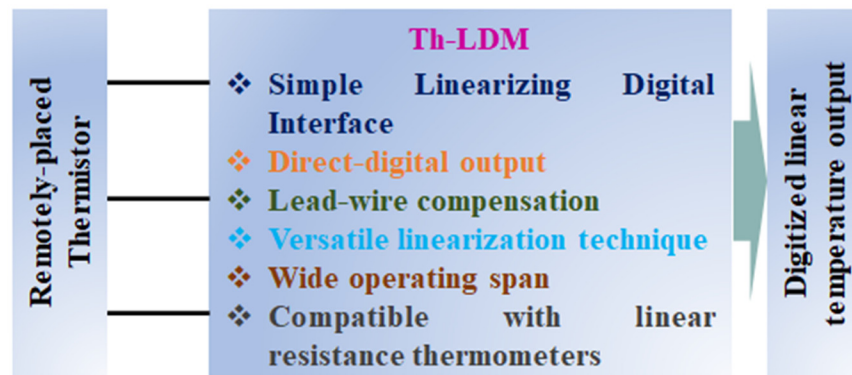


Fig. 7.1. A graphical summary of the proposed Th-LDM and its technical features.

the scheme interfaces the thermistor, using the three-wire principle, to a linearizing digitizer. The overall scheme requires lesser (connecting-) wiring infrastructure than Mueller's bridge [177] and uses a simpler and more efficient circuitry than [50], [87], [125]-[132], [146]. The novel technical contributions of this Th-LDM can be highlighted as follows:

- 1) Simple measurement system for temperature estimation using linearized thermistor
- 2) Direct-digital output
- 3) Capability to perform lead-wire compensation
- 4) Employs a novel and versatile linearization technique, which can give desired and adequate accuracy levels, with limited calibration requirements
- 5) Good performance in case of wide-span measurements
- 6) Design that ensures the low effect of circuit non-idealities
- 7) Compatibility with linear resistance thermometers as well

The working, analysis, and performance verification of the proposed system are discussed in the subsequent sections.

7.3. Linearized Thermistor-Based Digital Measurement System

The detailed circuit diagram of the Th-LDM is depicted in Fig. 7.2. The thermistor is represented using a resistor R_X . Three connecting leads (of resistances, R_{w1} to R_{w3}) are used to interface the thermistor with the linearizing digital interface. This interface works based on a relaxation oscillator principle with the help of an integrator (made using Op-amp A_1), a comparator, A_2 , and a few other components. The control-section of this interface consists of three electronic switches (S_1 to S_3) and a Timing and Logic Unit (TLU). TLU also helps to measure the ON and OFF time durations of the comparator-output (say, v_{COM}). The control signals, v_{CON1} and v_{CON2} , (issued from the TLU) help in the proper placement of the switches. The integrator-output is represented as v_{INT} , while the potential of the node, V_X equals $V_R \times R_1 / (R_1 + R_2)$, where V_R is the DC reference voltage. The Th-LDM operates in two-phases

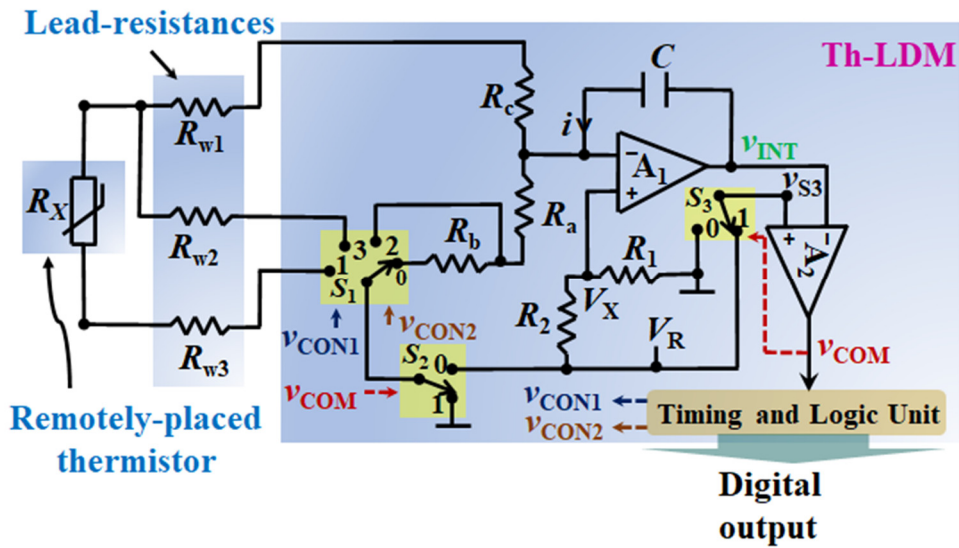


Fig. 7.2. Detailed schematic of Th-LDM for thermistor (R_X) linked with connecting wires (modeled as R_{w1} , R_{w2} , and R_{w3}).

(say, phase-1 and phase-2). Phase-1 and phase-2 denote the measurement and compensation phase, respectively. In each phase, the circuit will produce typical relaxation-oscillator waveforms at nodes v_{INT} and v_{COM} , as shown in Fig. 7.3. The ON-

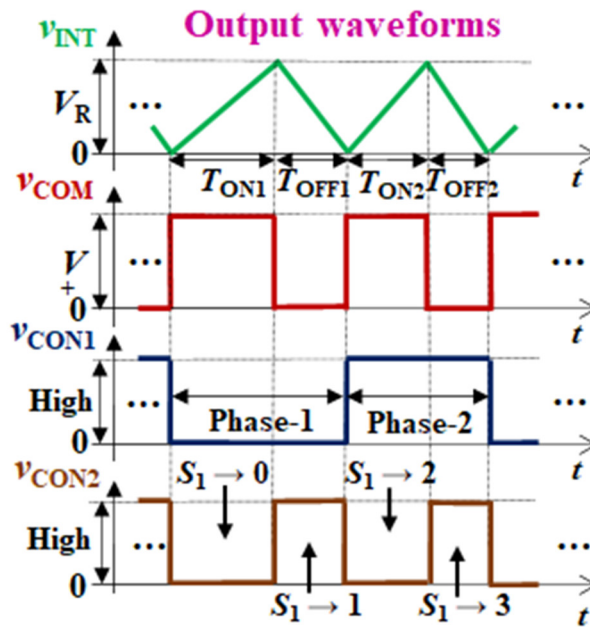


Fig. 7.3. Important node voltage (v_{INT} and v_{COM}) waveforms of Th-LDM. Control signals, v_{CON1} and v_{CON2} , are also depicted.

time and OFF-times of the signal, v_{COM} are denoted by T_{ON1} , T_{OFF1} , T_{ON2} , and T_{OFF2} [see Fig. 7.3]. The status of the control signals and the switch positions, during these time durations, are shown in Table 7.2.

A cycle of operation of the Th-LDM starts with the TLU setting v_{CON1} and v_{CON2} to logic-low. This links the switch S_1 to position-0. Let us consider that the output, v_{COM} of A_2 is at logic-high. In this condition, the switches S_2 and S_3 will be position-1 (see Table 7.2). The Th-LDM will force a current (say, i) to flow through the capacitor, C . The value of i equals V_X / R_{eq1} , where $R_{\text{eq1}} = R_a + R_b + R_{s1} + R_{s2}$. Note that R_{s1} and R_{s2} stand for the on-resistances of S_1 and S_2 , respectively. The voltage, v_{S3} equals V_R (as $S_3 \rightarrow 1$). As a result, the signal, v_{INT} will charge towards V_R , and its equation can be written as in (7.1).

$$v_{\text{INT}}(t) = \left(\frac{V_X}{R_{\text{eq1}} C} \right) t \quad (7.1)$$

This charging continues till v_{INT} becomes V_R . When v_{INT} crosses V_R , v_{COM} changes to logic-low, triggering the OFF-duration (T_{OFF1}). The ON-time duration (T_{ON1}) can be found by setting $v_{\text{INT}}(T_{\text{ON1}}) = V_R$ in (7.1). The equation of T_{ON1} can be obtained as in (7.2).

$$T_{\text{ON1}} = \frac{V_R}{V_X} R_{\text{eq1}} C \quad (7.2)$$

The low-state of v_{COM} shifts the switches S_2 and S_3 to position-0 (on setting $v_{S3} = 0$). Simultaneously, the TLU issues $v_{\text{CON1}} = \text{logic-low}$ and $v_{\text{CON2}} = \text{logic-high}$. This sets $S_1 \rightarrow 1$. Hence, the integrator will discharge towards $v_{S3} (= 0)$. The discharging current, i can be shown as $i = -(V_R - V_X) / R_{\text{eq2}}$, where $R_{\text{eq2}} = R_X + R_c + R_{w1} + R_{w3} + R_{s1} + R_{s2}$. Once v_{INT} reaches 0, v_{COM} changes to logic-high [see Fig. 7.3]. This marks the end of the OFF-time (T_{OFF1}) and the commencement of phase-2. The expression of T_{OFF1} can be derived as in (7.3).

$$T_{\text{OFF1}} = \frac{V_R}{V_R - V_X} R_{\text{eq2}} C \quad (7.3)$$

Table 7.2

Switch Positions During the Th-LDM Operation

Phase	Time durations	Control signals			Switch positions		
		v _{COM}	v _{CON1}	v _{CON2}	S ₁	S ₂	S ₃
(Measurement phase) Phase-1	T _{ON1}	High	Low	Low	0	1	
	T _{OFF1}	Low		High	1	0	
(Compensation phase) Phase-2	T _{ON2}	High	High	Low	2	1	
	T _{OFF2}	Low		High	3	0	

In phase-2, the TLU makes v_{CON1} to logic-high and v_{CON2} as logic-low. This sets S₁ → 2 and initiates the ON duration (T_{ON2}). The working of Th-LDM during phase-1 and phase-2 are similar, except for the equivalent input resistance of A₁. The equivalent resistance (say, R_{eq3}) during T_{ON2} equals R_{eq1} – R_b. Once T_{ON2} elapsed, T_{OFF2} starts, wherein the effective resistance gets altered to R_{eq4}. On solving circuit equation for R_{eq4} can be obtained as R_{eq2} – R_X (assuming equal lead resistances, R_{w1} = R_{w2} = R_{w3}). Thus, the expressions for T_{ON2} and T_{OFF2} can be obtained as in (7.4).

$$T_{ON2} = \frac{V_R}{V_X} (R_{eq1} - R_b) C \quad (7.4)$$

$$T_{OFF2} = \frac{V_R}{V_R - V_X} (R_{eq2} - R_X) C$$

Let us define a function ‘T_θ’ as in (7.5).

$$T_\theta = \frac{T_{OFF1} - T_{OFF2}}{T_{ON1} - T_{ON2}} \quad (7.5)$$

Substituting (7.2), (7.3), and (7.4) in (7.5), the function can be simplified as in (7.6).

$$T_\theta = \left(\frac{V_X}{V_R - V_X} \right) \left(\frac{R_{eq2} - R_{eq4}}{R_{eq1} - R_{eq3}} \right) = \left(\frac{R_1}{R_b R_2} \right) R_X \quad (7.6)$$

In other words, the thermistor-resistance can be obtained as R_X = T_θ (R_bR₂ / R₁). From this discussion, it can be inferred that the resistance estimated by the Th-LDM circuitry is independent of lead resistances as well as switch resistances, and other circuit elements such as C and V_R. The TLU accepts v_{COM} using one of its digital input-output ports. It listens to the state-transitions of v_{COM} and measures the time durations (T_{ON1},

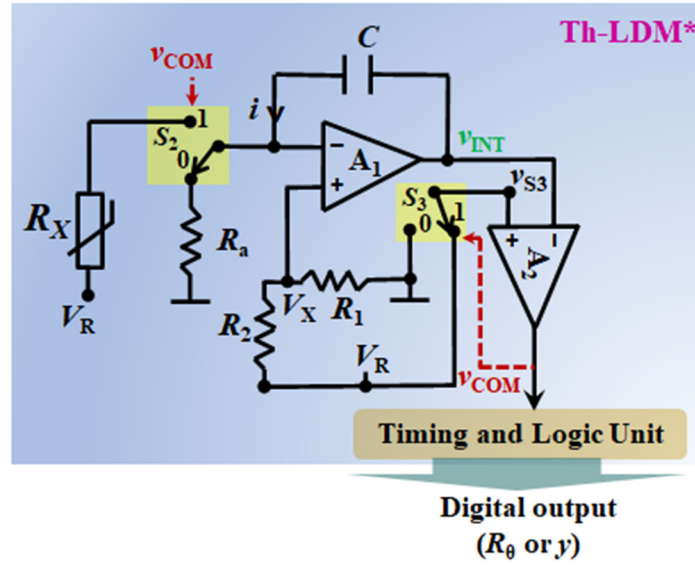


Fig. 7.4. Reduced model of Th-LDM for non-remote temperature measurement using thermistors.

T_{OFF1} , T_{ON2} , and T_{OFF2}) and then outputs T_θ and R_X . The generation of logic signals can also be done with the help of a simple digital circuit (e. g., D flip-flop and inverter). An explicit timer can be used for the measurement of time durations. Thus, Th-LDM achieves a direct-digital indication of R_X without using a separate ADC.

The Th-LDM can also be suitably modified for non-remote temperature measurement. In such a case, the switch, S_1 , connecting wires, and the resistors, R_b and R_c are not needed. Such a reduced model of Th-LDM (say, Th-LDM*) is given in Fig. 7.4. Here, the switch, S_2 can be realized using the low on-resistance switch IC. The operation of the Th-LDM* is like Th-LDM. Hence, the T_{ON} and T_{OFF} can be obtained as (7.7), where R_{s2} is the on-resistance of the switch, S_2 .

$$T_{ON} = \frac{V_R}{V_X} (R_a + R_{s2}) C \quad (7.7)$$

$$T_{OFF} = \frac{V_R}{V_R - V_X} (R_X + R_{s2}) C$$

From (7.7), the resistance, R_X can be obtained as $(T_{OFF}/T_{ON}) \times (R_2 R_a)/R_1$ when R_{s2} is 0. Thus, the non-remote case will further reduce the complexity of the circuit and power consumption. This case only requires a single conversion cycle. A linearization method is implemented in the TLU to extract θ (from R_X) and will be discussed in the next

subsection.

7.3.1. Linearization Methodology

Linearization of R_X [or T_θ in (7.6)] is carried out by using a simple mathematical function given in (7.8).

$$y = \sum_{i=1}^n \frac{R_X}{R_X + k_i} \quad (7.8)$$

Here, k_i stands for the linearization constant for the i^{th} iteration and ‘ n ’ is the number of linearizing terms. This simple function is an extended and generalized form of the approaches used in [4] (where $n = 1$) and [146] (where $n = 2$). A higher value of n requires more coefficients but will provide better linearization, even across a wide range. The optimal values of k_i and ‘ n ’ can be chosen based on the procedure, discussed next.

Let us consider that (θ_L, θ_H) represent the temperature monitoring range of Th-LDM. The computation of the constants, k_i requires the knowledge of some equally-spaced input-output points of the thermistor. Assume P represents the number of such data points. It will be shown that $P \geq (n + 2)$ for accurate computation of k_i . Consider thermistor resistances at temperatures $(\theta_L, \theta_1, \theta_2, \dots, \theta_n, \theta_H)$. In other words, $\theta_1 - \theta_L = \theta_2 - \theta_1 = \dots = (\theta_H - \theta_L) / (n + 1)$. These data points can be obtained from the experimental characterization of the thermistor.

The output, F_θ for the above points can be taken as $(y_L, y_{\theta_1}, y_{\theta_2}, \dots, y_{\theta_n}, y_H)$. To achieve linearized output, y , the linearization constants should be such that $y_{\theta_1} - y_L = y_{\theta_2} - y_{\theta_1} = \dots = y_H - y_{\theta_n}$. The constants can be found using an iterative search process such that the best-fit line joining $((y_L, y_{\theta_1}, y_{\theta_2}, \dots, y_{\theta_n}, y_H)$ exhibits the least e_{NL} with respect to θ . More insight about this technique can be gained by considering the case study discussed next.

7.3.2. Case Study for Evaluation of Linearization Method

An NTC Thermistor, NTCM-100K-B3950 (say, T-1) was considered. Initially, we assumed the number of calibration points, $P = 5$. In other words, five equally spaced points of the thermistor characteristics in the range of $\theta_L = 0\text{ }^\circ\text{C}$ to $\theta_H = 120\text{ }^\circ\text{C}$ were used. The calibration efforts are much less for this scheme when compared to the prior art [126]-[132]. The corresponding thermistor resistance values are $R_{XL} = 321.14\text{ k}\Omega$, $R_{X1} = 80.65\text{ k}\Omega$, $R_{X2} = 24.68\text{ k}\Omega$, $R_{X3} = 8.86\text{ k}\Omega$ and $R_{XH} = 3.65\text{ k}\Omega$. These values are obtained from [35]. In practice, experimental measurements can be done to obtain these thermistor resistance values at these temperature points.

Let us consider the case of $n = 3$ in (7.8). As mentioned in the previous subsection, k_1 , k_2 , and k_3 represent the linearization terms at $i = 1, 2$, and 3 , respectively. The optimal values of these terms need to be determined. The function-outputs can be assumed as $y_{\theta L}$, $y_{\theta 1}$, $y_{\theta 2}$, $y_{\theta 3}$, $y_{\theta H}$ for the afore-considered characteristic points. Then, as per the methodology considered, the following nonlinear equations should be obeyed.

$$\begin{aligned} y_{\theta L} - 2y_{\theta 1} + y_{\theta 2} &= 0 \\ y_{\theta 1} - 2y_{\theta 2} + y_{\theta 3} &= y_{\theta 2} - 2y_{\theta 3} + y_{\theta H} = 0 \end{aligned} \quad (7.9)$$

The solution of (7.9) can be simplified using the iterative procedure, and the values of k_1 , k_2 , and k_3 for best linearity can be obtained. The maximum e_{NL} of the curve joining y_{θ} 's was ascertained according to the least-squares fitting method. The values of k_1 , k_2 , and k_3 at which the curve has minimum deviation (e_{NL}) from its best fit were 6.8, 1.5, and 132. Further, the obtained coefficients were tested with the entire thermistor dataset for $\theta \in (0\text{ }^\circ\text{C}, 120\text{ }^\circ\text{C})$. Step size used was $1\text{ }^\circ\text{C}$. The function 'y' was computed for each step for the optimized coefficients. The output 'y' was observed, as expected, to follow a linear pattern with θ . The maximum e_{NL} is 0.37 %.

Next, the generic linearization approach in (7.8) was evaluated for different values of 'n' and P . The constants, k_i were evaluated for these cases, in a similar manner as described in the above paragraph. The function 'y' and its e_{NL} for the entire dataset (step size: $1\text{ }^\circ\text{C}$) was computed using the optimized constants. A plot of estimated e_{NL} for various cases (i. e., different values of n and P) is obtained and given in Fig. 7.5(a).

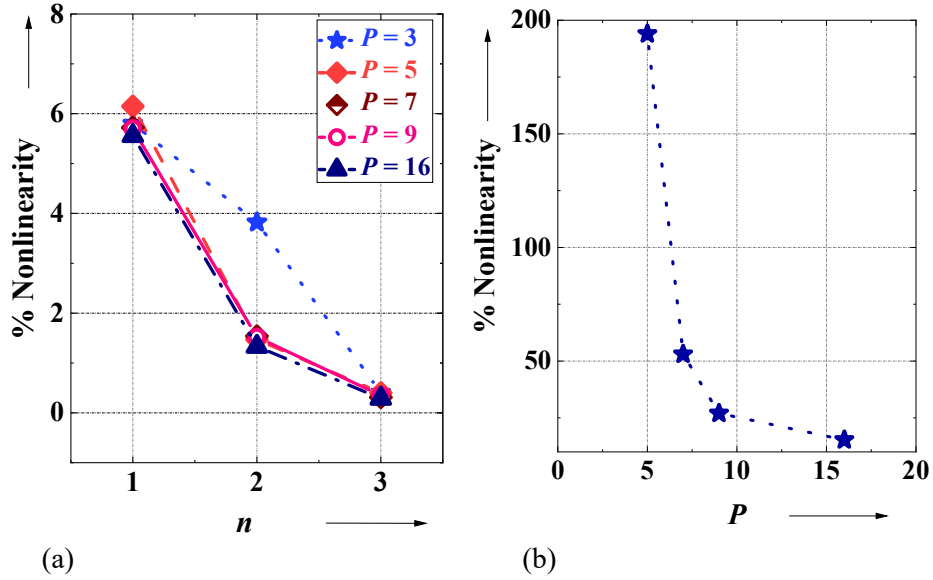


Fig. 7.5. (a) Variation of e_{NL} of Th-LDM with respect to the number of linearization terms (say, n) and number of calibration points (say, P). It can be seen that higher value of n ($= 3$) gives good output linearity, almost regardless of P . (b) Variation of e_{NL} in third-order polynomial equation with respect to P .

From Fig. 7.5(a), it can be inferred that the efficacy of this linearization approach in (7.8) increases with the value of $n \in (0, 3)$. The results (i. e., high linearity) corresponding to $n = 3$ are quite good and adequate for most thermistor-based measurement applications. The value of n also does not affect the linearity much. This shows that the proposed Th-LDM can work with limited calibration data. The technique is also versatile as the user can choose ‘ n ’ and ‘ P ’ depending on application requirements.

Further, the above results are compared with the software linearization techniques like polynomial fit and Steinhart and Hart equation [50]. Considering the polynomial fit, a third-degree polynomial is formed using 5, 7, 9, and 16 equidistant calibration points (i. e., $P = 5, 7, 9, 16$). Results are plotted in Fig. 7.5(b). The results show that e_{NL} is improved with increased P , and the obtained e_{NL} is 15.3 % with $P = 16$. The high e_{NL} is because this scheme is not able to predict optimal polynomials using a limited number of equidistant calibration points. It may require more calibration points in the high-sensitivity region. This high e_{NL} can be further reduced using a greater degree of polynomial equation, at the cost of an increase in the computational cycles

and high-level processing requirements [178]. On the other hand, the proposed Th-LDM possesses e_{NL} of 0.37 % using just five calibration points. Similarly, linearization using Steinhart and Hart equation requires the use of natural logarithmic operations, which is difficult to implement [178]. The TLU, after measuring output time-durations and R_X [using (7.6)], computes y . The constants (k_i 's) obtained from characteristics studies, can be stored in the TLU. Thus, the Th-LDM generates a digital equivalent of R_X and the linearized output, y .

7.3.3. Suitability for Linear Temperature Sensor

The proposed Th-LDM can also be used for linear RTDs. In this case, the RTD resistance can be directly evaluated using (7.6). The self-heating error can be reduced by properly selecting the resistor, R_c . Inherent compensation features (e. g., wire resistance compensation) will hold good in this case as well. Hence, the proposed scheme can act as a simple digitizer for RTD, with similar performance as in prior art [60], [144]. Related performance evaluation will be discussed in Section 7.6.4.

7.4. Effect of Error Sources

This section describes the effect of important error sources on the output of the Th-LDM.

7.4.1. Factors Affecting Equivalent Resistance (R_{eqi})

Some of the nonideal sources can affect the equivalent resistance of the Th-LDM during its dual-phase operation. For example, the wire resistances linking the thermistor to the Th-LDM circuit may not be exactly equal to each other. The mismatch (say, ΔR_w) will affect R_{eq2} and R_{eq4} and hence, the numerator of (7.6). The estimated resistance (say, R_X') will be $R_X \pm \Delta R_w$. Likewise, the on-resistance of the switches need not be the same at all positions. The mismatches between the on-resistance of S_2 will alter R_{eqi} . However, this change will get nullified due to the ratiometric operation

followed in (7.5). The mismatch (say, ΔR_{sw}) associated with the switch, S_1 can modify the estimated R_X to R_X' , given in (7.10).

$$R_X' = R_X \left(1 \pm \frac{\Delta R_{sw}}{R_b} \right) \mp \Delta R_{sw} \quad (7.10)$$

The typical values of $\Delta R_w = 0.5 \Omega$ lead to an output error of 0.05 %. Similarly, $\Delta R_{sw} = 5 \Omega$ (MAX4053 IC) can lead to an error of 0.55 %. This error can be reduced by using switches of lower ΔR_{sw} [174].

7.4.2. Non-ideal Parameters of A₁

Bias current (say, I_b) and offset voltage (say, V_{os}) of A₁ can change the time durations of Th-LDM. The modified expressions are given in (7.11).

$$\begin{aligned} T_{ON1}^* &= \frac{V_R R_{eq1}^* C}{V_y + I_b R_{eq1}^*}; & T_{ON2}^* &= \frac{V_R R_{eq3}^* C}{V_y + I_b R_{eq3}^*} \\ T_{OFF1}^* &= \frac{V_R R_{eq2}^* C}{V_z - I_b R_{eq2}^*}; & T_{OFF2}^* &= \frac{V_R R_{eq4}^* C}{V_z - I_b R_{eq4}^*} \end{aligned} \quad (7.11)$$

The expressions of R_{eq1}^* , R_{eq2}^* , R_{eq3}^* , R_{eq4}^* , V_y , and V_z are as per (7.12).

$$\begin{aligned} R_{eq1}^* &= R_{eq1}, & R_{eq2}^* &= R_{eq2}, & R_{eq3}^* &= R_{eq1} - R_b, & R_{eq4}^* &= R_{eq2} - R_X, \\ V_y &= V_X + V_{os} + I_b (R_1 || R_2) & \text{and} & & V_z &= V_R - V_y \end{aligned} \quad (7.12)$$

The resulting error in R_X estimation works out to be 0.04 % for the typical parameters (OP07 IC) of the A₁ used. This error can be minimized by using a precision Op-amp having low I_b and V_{os} [179].

7.4.3. Other Factors

The offset voltage of A₂ will not affect the timing durations of Th-LDM. Likewise, the practical resistance of S_3 will not play any significant role. The effect of the slew-rate of op-amps, as well as delays of comparator and control signal generation, can be minimized by maintaining the time durations to be in the order of milliseconds or higher. In such a case, the time resolution ($\pm \Delta T$) of the TLU can alter the time durations. The developed prototype uses the ATSAM3X8E microcontroller as TLU. It

has the ΔT of $\pm 2 \mu\text{s}$, which can lead to an error of 0.2 %. This error can be reduced by using timer units of higher resolution [175].

7.4.4. Summary of Error Sources

The preceding discussions showed the Th-LDM is affected by a few non-idealities. The combined effect of these parameters can change R_X to R_X^* , as given in (7.13).

$$R_X^* = \left[\frac{T_{\text{OFF1}}^* \pm \Delta T - T_{\text{OFF2}}^* \pm \Delta T}{T_{\text{ON1}}^* \pm \Delta T - T_{\text{ON2}}^* \pm \Delta T} \right] \left[\frac{R_b R_2}{R_1} \right] \quad (7.13)$$

The expressions of T_{ON1}^* , T_{ON2}^* , T_{OFF1}^* , and T_{OFF2}^* can be obtained from (7.11) and they can be used to estimate, R_X^* . Here, R_{eq1}^* , R_{eq2}^* , R_{eq3}^* , and R_{eq4}^* are equal to (7.14).

$$\begin{aligned} R_{\text{eq1}}^* &= R_b + R_a + R_{s10} + R_{s21}, R_{\text{eq2}}^* = R_X + R_c + R_{s11} + R_{s20} + R_{w1} + R_{w3}, \\ R_{\text{eq3}}^* &= R_a + R_{s12} + R_{s21} \text{ and } R_{\text{eq4}}^* = R_c + R_{s13} + R_{s20} + R_{w1} + R_{w2}. \end{aligned} \quad (7.14)$$

The resistances, R_{s10} , R_{s11} , R_{s12} , and R_{s13} depicts the on-resistances of S_1 at positions 0, 1, 2, and 3, respectively. Similarly, R_{s20} and R_{s21} for S_2 at positions 0 and 1. Proper selection of components and design parameters (as discussed in previous sub-sections) can keep the sensor resistance given in (7.13) close to the ideal value. This generalized expression would be used to validate the performance evaluation results in Section 7.5.2.

7.5. Performance Verification of the Th-LDM Circuits

A hardware model of the Th-LDM digitizer was first breadboarded and evaluated using a series of experiments using synthesized resistance characteristics. This study helps to ascertain the actual performance features (such as e_{NL} , e_{REL} , wide-span capability, and wire resistance compensation) of the Th-LDM. Moreover, these studies demonstrate that Th-LDM can be used to interface linear sensors as well. These experiments and the results achieved are described next.

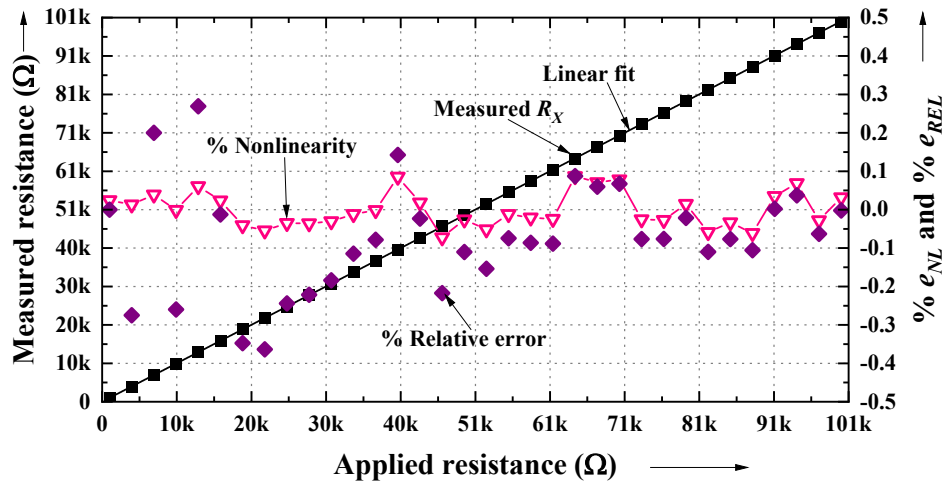


Fig. 7.6. Emulation results of the Th-LDM. Graph indicates the relation between the applied resistance (1 k Ω to 100 k Ω) and measured output resistance. Measured e_{NL} and e_{REL} are also shown.

7.5.1. Hardware Model of Th-LDM Digitizer and Emulation Studies

Low-cost commercial components were used to build the Th-LDM circuitry. The Op-amps A_1 and A_2 were modeled, respectively, using OP07 and LM311 IC. The resistors R_a , R_b , and R_c were selected as 10 k Ω , and the capacitor, C was 1 μ F to maintain the output time durations in order of milliseconds. The switches S_2 and S_3 were realized using MAX4053 IC, and S_1 was made with MAX4052 IC. The voltage, V_R was made using LM385-2.5 IC. The voltage V_X was kept as $V_R / 2$ by using $R_1 = R_2 = 1$ k Ω . The lead-wire resistances (R_{w1} to R_{w3}) were kept as 11 Ω to mimic the 30

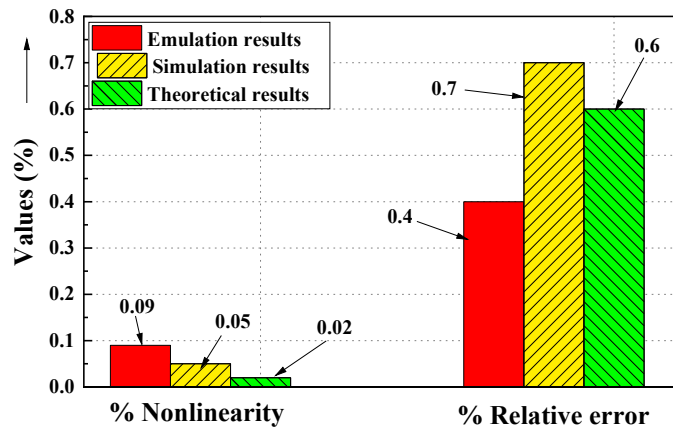


Fig. 7.7. Comparison results between emulation, simulation, and theoretical results are depicted.

standard wire gauge, 30 m copper wire. The TLU was realized using the ATSAM3X8E microcontroller present in the Arduino Due platform. A 32-bit timer/counter module of TLU with $\pm 2 \mu\text{s}$ resolution was used. The prototype developed, accepts the signal, v_{COM} using its digital port (pin-8) and generates the control signals, v_{CON1} and v_{CON2} using pin-9 and 10.

The resistance, R_X was varied from 1 k Ω to 100 k Ω using a precision decade box (from Zeal Pvt. Ltd.) with the step of 3 k Ω . This experiment will help to establish the efficacy of the Th-LDM digitizer. The relation between R_X and the measured resistance using (7.6) is linear and it is plotted in Fig. 7.6. The parameters, e_{NL} and e_{REL} were also calculated, for each step and plotted in Fig. 7.6. From Fig. 7.6, it can be observed that the Th-LDM digitizer can provide $e_{NL} < 0.09 \%$ and $e_{REL} < 0.4 \%$. These maximum values are also plotted in Fig. 7.7 for the purpose of comparison.

7.5.2. Comparison Study of Emulation Results with Simulation and Theoretical Expectations

The emulation results were also validated using simulation studies (tool: LTSpice) and theoretical evaluation [using (7.11) to (7.14)]. The components used and the range of R_X considered in the simulation have the same specifications as those in the hardware of Th-LDM. The time measurements and the control signal generation were done using a suitable code/logic in the simulation tool. The parameters, e_{NL} and

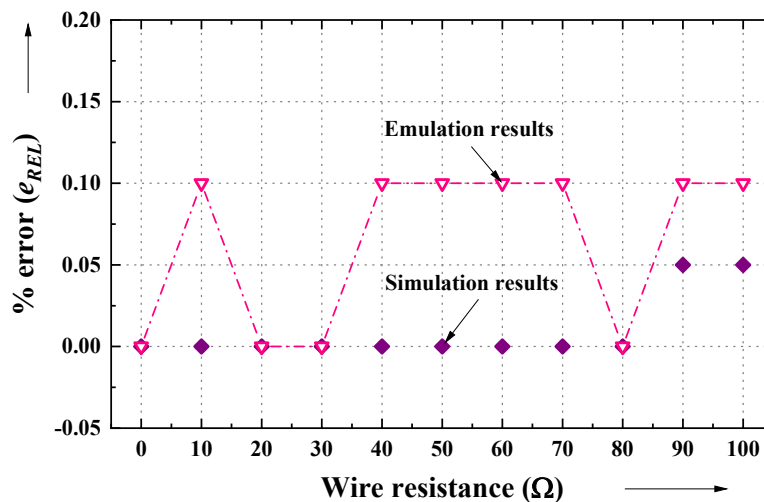


Fig. 7.8. Results showing the negligible influence of the wire impedances on the Th-LDM.

e_{REL} were found, and their maximum values are plotted and given in Fig. 7.7. The theoretical and simulation results show that the maximum e_{REL} is 0.6 % and 0.7 %, respectively. This error is slightly higher than the experimental results ($e_{REL} = 0.4 %$). This is because a worst-case mismatch (ΔR_{sw}) of 5 Ω was considered for S_1 in theoretical and simulation studies. Switch IC used in the experimental prototype may have a slightly reduced value of ΔR_{sw} .

7.5.3. Studies to Find the Effect of Wire Resistances

The Th-LDM was theoretically shown to be independent of the lead-wire resistances (vide Section 7.3). This is also verified using emulation studies. The resistor, R_X was fixed at a nominal value of 1 k Ω . Different lengths of wires (i. e., various wire resistances ranging from 0 to 100 Ω) were considered. Decade resistance boxes were used for the emulation of wire resistance. The input-output characteristics were noted for each case, using which the resulting maximum value of e_{REL} was estimated. A graph of e_{REL} versus wire resistance is shown in Fig. 7.8. Secondary verification of the above cases was also carried out in LTSpice and the corresponding e_{REL} values are also plotted in Fig. 7.8. From Fig. 7.8, it can be seen that the value of e_{REL} (emulation) is less than 0.1 %. The simulation showed that the limiting e_{REL} is 0.05 % for $R_w \in (0, 100\Omega)$. These studies clearly show that (1) the Th-LDM can be used for remotely-located sensors, and (2) the effect of R_w is minimal.

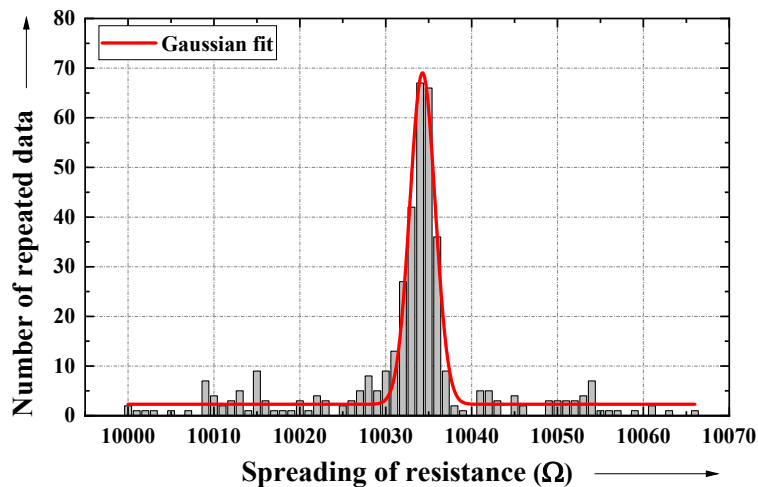


Fig. 7.9. Plot of 400 repeated measurements of Th-LDM taken when $R_X = 10$ k Ω .

Table 7.3

Precision Related Parameters

Parameters	Results
Standard deviation	0.1 %
Signal-to-noise ratio	57.87 dB
Effective number of bits	9.32 bits
Repeatability error	0.05 %

7.5.4. Additional Tests

The precision-wise performance of the developed Th-LDM was estimated. The parameters such as standard deviation (σ), SNR, ENOB, and repeatability error (R_E) were estimated using the expressions given in Appendix A. The resistance R_X was fixed as 10 k Ω , and the Th-LDM output was measured using 400 consecutive measurements. The results are plotted in Fig. 7.9. From Fig. 7.9, it can be observed that the measured resistances roughly follow a gaussian distribution. Using these measurements, the precision-related specifications were obtained as given in Table 7.3.

7.6. Experimental Studies of Complete Th-LDM System

The digitizer part of Th-LDM was thoroughly evaluated in Section 7.5. This section describes the various performance studies of the overall Th-LDM system using extensive experimentation with thermistors.

7.6.1. Experimental Studies of Th-LDM with Thermistors

The efficacy of the linearization methodology of Th-LDM was first tested. Two different thermistors (say, T-1 and T-2) [35], [56] were considered. Synthesized version of these thermistors' characteristics was emulated using decade resistances and interfaced to the Th-LDM. The wire impedances were kept as 11 Ω . The constants (k_1 to k_3) were calculated using five input-output points of the characteristics, as per the procedure given in Section 7.3. The estimated constants are given in Table 7.4. The function, y was implemented in the TLU, with the help of these deduced coefficients.

Table 7.4

Linearization Constants values Associated with Th-LDM Interfaces with Different Thermistors

Linearization constants and results	Experimental results using synthesized characteristics		Experimental results	
	T-1*	T-2#	T-1	T-2
k_1 (k Ω)	6.8	1.1	5.4	0.1
k_2 (k Ω)	1.5	0.3	0.1	0.4
k_3 (k Ω)	132	18.5	159	5.9
% e_{NL} (Theoretical)	0.4	0.37	0.12	0.4
% e_{NL} (Th-LDM + y)	0.44	0.4	0.49	0.47
Temperature range ($^{\circ}\text{C}$)	0 - 120	0 - 105	35 - 95	
Sensitivity ($^{\circ}\text{C}$)	0.02			
*T-1 - NTCM-100K-B3950, #T-2 - NTCLE413E2103H400A				

The resistance, R_X was varied, as per the thermistor, T-1 datasheet [35] for $\theta \in (0^{\circ}\text{C}, 120^{\circ}\text{C})$. The output was plotted with respect to θ and shown in Fig. 7.10. The linear nature of y can be clearly visualized from this figure. The maximum e_{NL} was obtained as 0.44 %. Similarly, the performance of Th-LDM was studied with the characteristics of the second thermistor, T-2. The obtained results are shown in Fig. 7.11. As expected, the output (y) can be seen to possess linear relation with θ , for $\theta \in (0^{\circ}\text{C}, 105^{\circ}\text{C})$ with $e_{NL} < 0.4\%$.

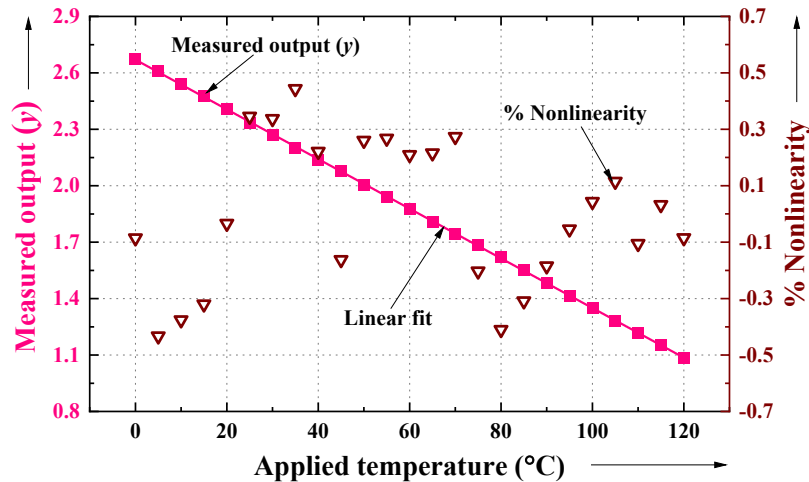


Fig. 7.10. Experimental results of Th-LDM when tested with synthesized characteristics of T-1. Linearized transfer characteristics of Th-LDM can be observed, with maximum e_{NL} less than 0.44 %.

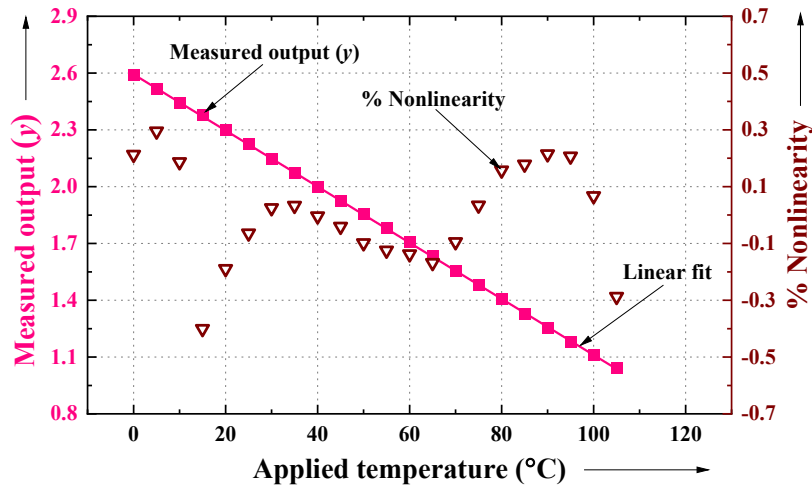


Fig. 7.11. Experimental results of Th-LDM tested with characteristics of T-2. Linearized transfer characteristics of Th-LDM can be observed, with maximum e_{NL} less than 0.4 %.

Further, using the characteristics of T-2, θ was varied in sub-degrees from 0 to 4 °C (low-temperature region) and 101 °C to 105 °C (high-temperature region) with the step size of 0.25 °C. The function, y was measured using simulation and emulation studies. The results from these studies are plotted in Fig. 7.12. The linear transfer relation and e_{NL} of the Th-LDM are noted in Fig. 7.12. It is observed that the maximum e_{NL} does not exceed 0.02 %. These results show the capability of Th-LDM to perform ‘sub-degree’ scale measurements.

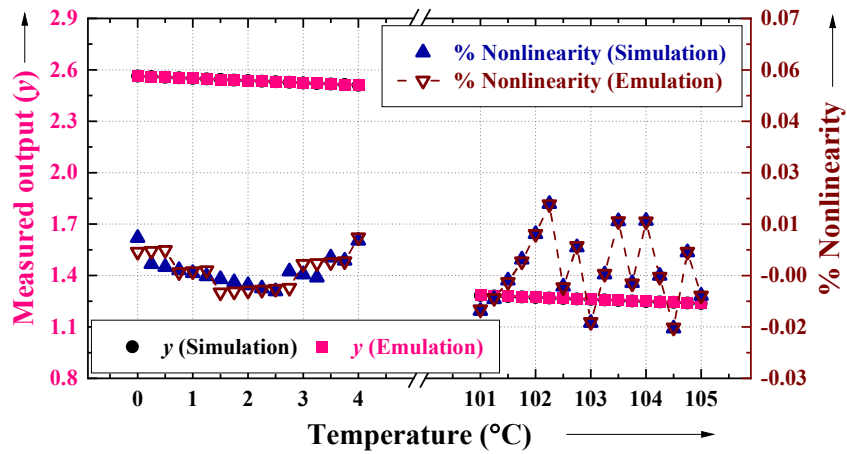


Fig. 7.12. Simulation and emulation results using T-2. Temperature is varied in sub-degrees from 0 to 4 °C and 101 °C to 105 °C.

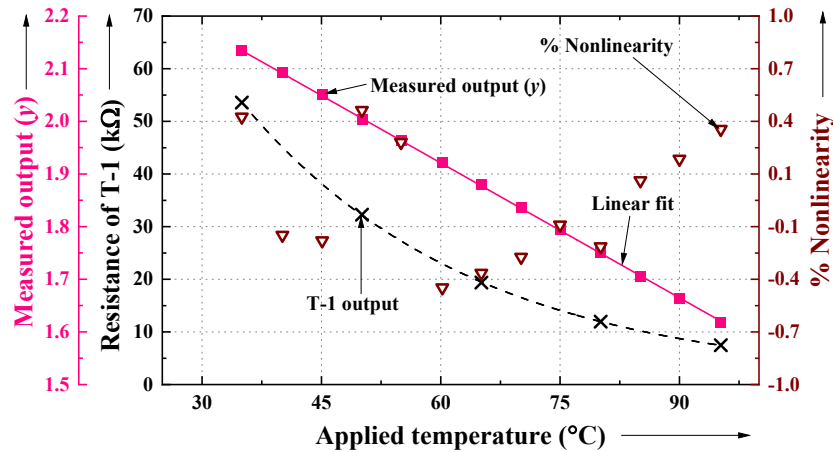


Fig. 7.14. Performance evaluation of Th-LDM with commercial sensor (T-1). Five input-output characteristics points obtained from calibration are plotted in a dashed line. Linearized transfer characteristics (bold line) of the Th-LDM are also plotted, along with experimentally obtained e_{NL} values.

The developed Th-LDM was equipped with the coefficients, derived in the previous sub-section, and interfaced with T-1 and T-2. Connecting wires were measured to have a resistance of around 1Ω . A photograph of the overall experimental setup is shown in Fig. 7.13. The input temperature (θ) was varied, and the reference temperature was observed, as per the procedure used in the calibration study. Standard equipment (power supply, oscilloscope, etc.) was used for monitoring these tests. Further, the power consumption of the Th-LDM was found as around 45 mW using the ammeter method [180]. The microcontroller was used only for the generation of control signals and time duration measurements. During these operations, the microcontroller consumes a small amount of power for running the Th-LDM. However, the total power consumed by the microcontroller unit includes the power taken by the other components in the Arduino Due unit which are not needed for the operation of Th-LDM. Hence, the power consumption of the microcontroller is not included for the above power measurement. This power consumption is also comparable with the existing circuits [60], [144]. The energy consumption of this circuit can be found using resistance-based or capacitance-based methods [180]. Further, the experimental waveforms were compared with the simulation studies at three different temperatures

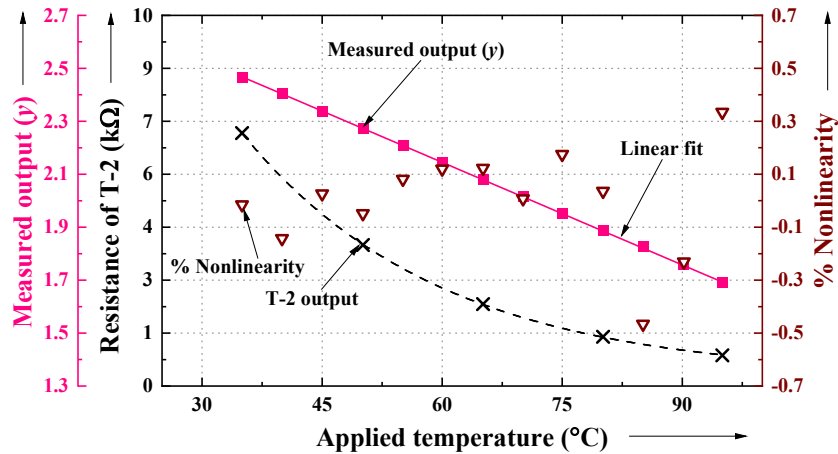


Fig. 7.15. Performance evaluation of Th-LDM with commercial sensor, T-2. Thermistor characteristics and linearized transfer characteristics (bold line) of the Th-LDM are also plotted, along with experimentally obtained e_{NL} values.

($\theta \approx 40^\circ\text{C}$, 60°C , and 80°C). The simulation and experimental waveforms can be seen to be closely matched with each other as given in Fig. 7.16.

The performance evaluation of the Th-LDM was evaluated by varying θ from 35°C to 95°C in steps of 5°C . The measured transfer characteristics of the Th-LDM + T-1 interface are plotted in Fig. 7.14. The output, y can be seen to be linear with θ . The nonlinearity error, e_{NL} is less than 0.49 %. Similar experimentation was also conducted for T-2, and the results are drawn in Fig. 7.15 (corresponding datasets are given in Appendix B.6). The nonlinearity error, e_{NL} for this case does not exceed 0.47 %. Along with the e_{NL} values, the sensitivity data are also given in Table 7.4 for T-1 and T-2. From the above studies, it is observed that the developed Th-LDM serves well to linearize the output of the thermistor and provides good sensitivity and linearity.

7.6.4 Experimental Studies using Linear Temperature Sensor

As mentioned in Section 7.3.3, the Th-LDM can also be used with linear temperature sensors. Some basic experiments of Th-LDM with RTD-Pt100 were carried out to ascertain this feature. This sensor was incorporated with the experimental setup described in Section 7.6.3 and interfaced with Th-LDM. The value of R_c was kept as $10\text{ k}\Omega$ so that the sensor current is limited to $124\ \mu\text{A}$. This helps to reduce self-heating errors. The input θ varies from 32°C to 99°C . The output, R_x [see (7.6)] was

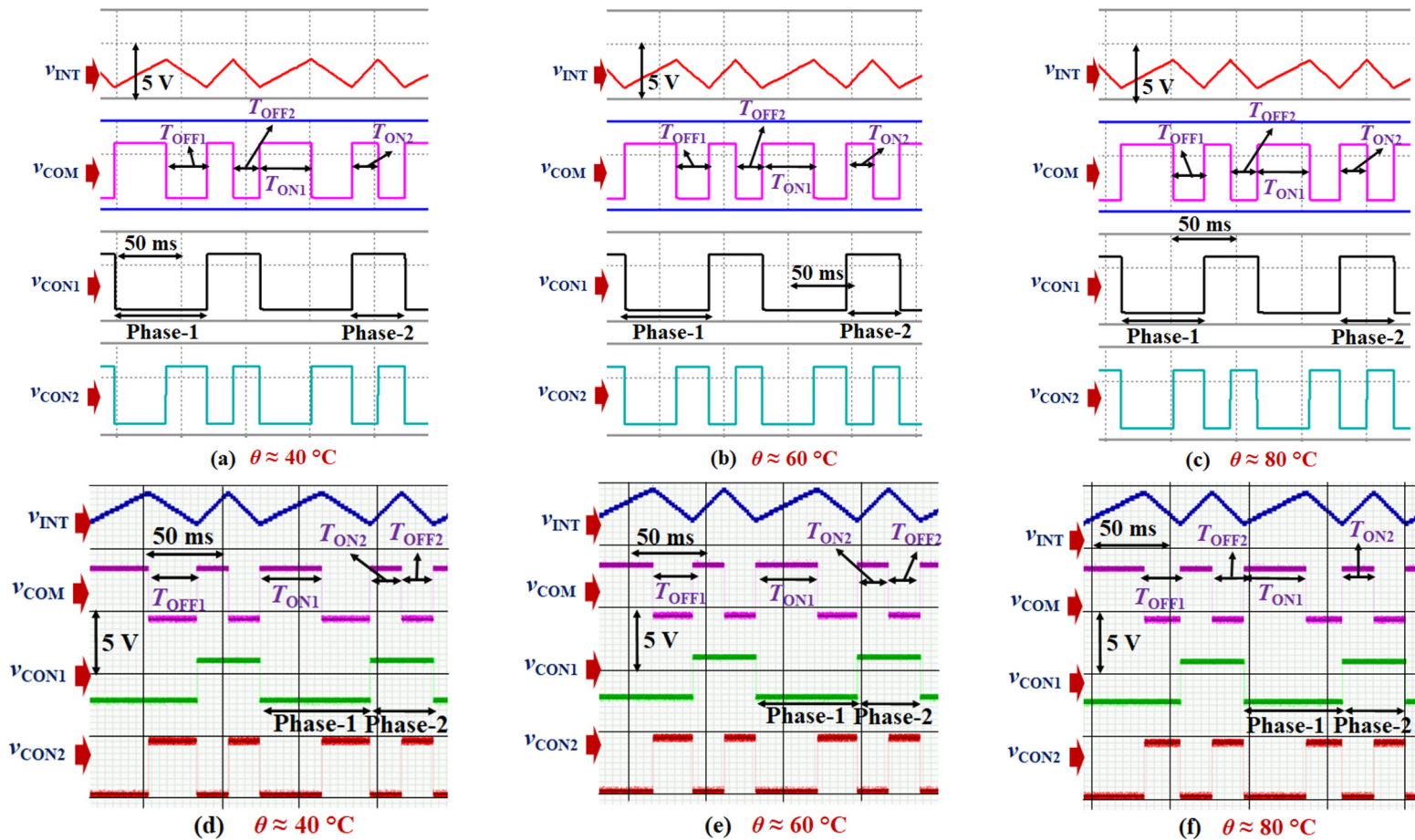


Fig. 7.16. Oscilloscope waveforms were observed during simulation and experimental studies at three different θ ($\approx 40^\circ\text{C}$, 60°C , and 80°C). (a), (b), and (c) denotes the simulation graphs while (d), (e), and (f) depicts the experimental graphs.

measured for various θ and found to be linear with θ . The maximum e_{NL} was found to be 0.53 %. It should be noted that a significant portion of this e_{NL} is contributed by the sensor itself, whose inherent e_{NL} itself turns out to be 0.59 %.

Thus, the series of experimental results, given in the previous subsections, show that Th-LDM offers a simple, but high-performing, measurement scheme for thermistor-based temperature estimation. The versatility of the scheme is also evidenced by using tests on multiple thermistors as well as linear temperature devices. The scheme also provided an innate ability to compensate for lead-wire impedances. The important specifications and features of Th-LDM are summarized in Table 7.1. From Table 7.1, it can also deduce that the developed Th-LDM offered many meritorious features (such as wide range, simple architecture, direct-digital output, generic linearization scheme, etc.) over the prior art.

7.7. Summary

The design and performance verification of a new linearized thermistor-based temperature measurement system was detailed in this chapter. The system (i. e., Th-LDM) integrated a novel relaxation oscillator-based digitizer with a simple, but effective linearization approach. The Th-LDM was extensively analyzed for error-performance and then verified using a number of experimental tests. Results established the capability of Th-LDM to provide (1) linearized digital output for thermistors, and (2) wide-span measurements with immunity to lead-wire impedances. The scheme was also found to work well with a limited amount of calibration data. The power consumption of the circuit was also comparable with the existing circuits. Finally, the superior features of Th-LDM (over prior art) make it an excellent choice for thermistor-based industrial measurement scenarios.

Better performance can be achieved using the developed prototype with the following precautions, (1) thermistors should be used in the allowable temperature range for better accuracy, (2) thermistors should be away from harmful environments to increase their lifetime, (3) thermistors need to be stored in the temperature range of

25 °C to 45 °C before opening the package and the relative humidity should be less than 75 % [181], and (4) it should ensure that removing all foreign bodies between the thermistor and the clamp contact [181].

Chapter 8

Conclusions and Future Works

The thesis described innovative digitizing interface architectures for resistive sensors and addressed a number of challenging measurement scenarios. Initially, an in-depth literature review was carried out to identify the potential (important) measurement issues related with resistive sensors. It was deduced that the properties (e. g., configuration, output nature) of resistive sensors vary from each other. In addition, industrial sensors can be available in remote locations and/or wide-span. This thesis tried to address these issues, by developing efficient accurate and versatile digitizers for resistive sensors.

The thesis first reported a dual-slope-based digitizer for constant-current excited sensors. This digitizer combined a simple preset-current source circuit (using low-cost Op-amps) with dual-slope architecture that employs a single reference voltage and possesses immunity against many non-ideal parameters. This circuit was also adapted for various resistive sensor configurations. The performance of the circuit was tested by simulation, emulation, and experimental studies with various configurations of resistive sensors. Results show that the circuit exhibited very good performance while interfacing with commercial RTD, GMR sensor as well as rectilinear displacement sensor.

In the second chapter, relaxation-oscillator-based digitizers were developed for a broad class of resistive sensors. This digitizer was designed to achieve meritorious features such as (1) simple architecture, that uses no reference voltage, (2) use of novel function, rendering output free from the capacitor and power supply drifts, and (3) negligible effect of many circuit nonidealities, etc. Detailed methodology and error analysis of the presented digitizer were performed. Later, this scheme was enhanced to adapt with wide-span resistive sensors. In addition, a novel methodology to reduce the execution time was also proposed and verified. This enhanced digitizing interface was shown to exhibit the inherent merits of the relaxation oscillator technique and render

wide-span measurements. The performance of the relaxation-oscillator-based circuits was also verified using various (i. e., simulation, emulation, and experimental) studies. The developed digitizing circuits for non-remote resistive sensors were compared with the related prior art. Results show superior/comparable performance than the existing circuits.

The thesis further focussed on the design and performance evaluation of the digitizing circuits for remotely located resistive sensors. The developed circuits employed a simple design, and those were equipped with novel compensation functions to provide a linear-digital indication of remote resistive sensors. One of the developed circuits was suitable for wide-span sensors and possesses low error. Further, the digitizer developed for bridge sensor interface, provides effective compensation for many non-ideal industrial scenarios such as remotely located sensor bridges, bridges with parasitic elements and mismatches among its elements, etc. The performance of the developed circuits was evaluated using various simulation and experimental tests. Test results demonstrate that DRR circuits served as a direct-digitizer for resistive sensors in SE, DS, and bridge configurations and they rendered all expected features.

A simplified version of the digitizer based on the direct microcontroller technique, for various types of remotely connected sensors, was detailed in chapter 5. This circuit can be easily modified to adapt with SE, DS, and bridge-based sensors. In addition, this technique is independent of various circuit nonidealities. A similar charge-discharge-based circuit was also derived for parallel RC impedance sensors. This circuit can be useful to measure both resistance as well as the capacitance of the sensor. Further, a detailed offset compensation technique was derived to nullify the offset capacitances present in the circuit. The performance of the circuit was analyzed using simulation and emulation studies. Results show that the developed simple digitizer can be useful to measure a wide range of resistance and capacitance of the sensor.

Finally, the linearizing digitizer circuit for thermistor sensors was also explored. The developed circuit requires few data points for the linearization of thermistor-output. The novel linearization approach rendered a low nonlinearity error

in the output when compared to the existing techniques. In addition, the other performance parameters were also in the comparable range. Extensive experimental studies were also performed with actual thermistors to study the efficacy of the developed system. Results show that the developed circuit can be able to linearize a wide range of resistances. The developed digitizers can be used with different types of resistive sensors to realize an efficient instrumentation system in several industrial applications.

8.1. Future Works

There are still a number of research gaps in the field of signal conditioning of resistive sensors. For example, sensors such as noncontact potentiometric sensors, low-power gas sensors, etc. have a series combination of a resistor and capacitor. Efficient digitizers are required for such sensors as well. Moreover, the performance parameters (e. g., conversion time) can be improved, especially for wide-span sensors. Novel optimization techniques need to be designed and evaluated with digitizing interfaces. The miniaturization of the developed digitizers using VLSI technology is another interesting area where research can be pursued. Further, such compact circuits can be used in various real-world applications. Summarizing, future research can be carried out on the measurement problems outlined below.

1. Design and development of the digitizing interface circuits for the sensors having a series connection of the resistor and capacitor.
2. Design and development of the digitizing interface circuits for other types of resistive sensors (e. g., low-power gas sensors, non-contact potentiometric sensors, etc.)
3. Novel digitizer circuits and optimization schemes to reduce the conversion time of the instrumentation systems with a wide operational span.

Bibliography

- [1] Q. Tong *et al.*, "A Method for Measurement of Aircraft Attitude Parameters Based on Sequence Screen-Spot Imaging," *IEEE Access*, vol. 6, pp. 41566-41577, 2018.
- [2] C. Gouldstone *et al.*, "Embedded resistive strain sensors for harsh environments," in *Proc. IEEE Aerosp. Conf.*, Big Sky, MT, USA, Aug. 2006, pp. 1–10.
- [3] Jones, Barry, "Measurement: Past, Present and Future: Part 1 Measurement History and Fundamentals" *Measurement and Control*, vol. 46, pp. 108-114, 2013.
- [4] R. P. Areny and J. G. Webster, *Sensors and Signal Conditioning*. Hoboken, NJ, USA: Wiley, 2000.
- [5] K. Hermann and P. Neubert, *Instrument Transducers*, 2nd ed. Oxford University Press, 2010.
- [6] K. Rohrmann, M. Sandner, P. Meier, and M. Prochaska, "A novel magnetoresistive wheel speed sensor with low temperature drift and high stray field immunity," in *Proc. IEEE Int. Instrum. Meas. Technol. Conf. (I2MTC)*, Houston, TX, USA, May 2018, pp. 1–6.
- [7] K. Rohrmann, M. Sandner, P. Meier, and M. Prochaska, "A novel readout technique for magnetoresistive sensors in automotive anti-lock braking systems," in *Proc. IEEE Int. Symp. Circuits Syst. (ISCAS)*, Florence, Italy, May 2018, pp. 1–5.
- [8] NASA. *Gas Sensors. Aerospace Applications*. Accessed: Jul. 5, 2019. [Online]. Available: <https://ntrs.nasa.gov/archive/nasa/casi.ntrs.nasa.gov/19990116701.pdf>.
- [9] Kenry, Joo Chuan Yeo, and Chwee Teck Lim, "Resistive microfluidic pressure sensor" U.S. Patent 10488276B2, Nov. 26, 2019.
- [10] Wolfgang Raberg, "Method for measuring a magnetic field using a magnetic field sensor device having a second magnetic field sensor between parts of a first magnetic field sensor" U. S. patent 11313923B2, April 26, 2022.
- [11] Hartmann, U. "Magnetic Multilayers and Giant Magnetoresistance—Fundamentals and Industrial Applications" Springer: Verlag/Berlin, Germany, 2000.
- [12] Examples from the Field of Industrial Sensors. Accessed: Aug. 2019. [online]. Available: <http://sensitec.com/english/applications/industry>.

- [13] Krishna, V.D., Wu, K., Perez, A.M., and Wang, J.-P., “Giant Magnetoresistance-based Biosensor for Detection of Influenza a Virus” *Front. Microbiol.* 2016.
- [14] Application Notes for Temperature sensor, *Minco*. Accessed: Apr. 5, 2022. [Online]. Available: https://www.minco.com/wp-content/uploads/temp-sensor-applications-for-aerospace-2020_DL.pdf
- [15] Application Notes for RTD sensor, *TE Connectivity*. Accessed: Mar. 5, 2022. [Online]. Available: Datasheet: <https://www.te.com/content/dam/te.com/documents/sensors/global/how-rtd-sensors-work.pdf>
- [16] Neji, Bilel & Ferko, Ndrim & Ghandour, Raymond & Karar, Abdullah S & Arbess, Houssam. “Micro-Fabricated RTD Based Sensor for Breathing Analysis and Monitoring” *Sensors*, 2021.
- [17] Application Notes for Displacement Sensor. Accessed: Apr. 1, 2022. [Online]. Available: <https://www.spaceagecontrol.com/s085a.htm>
- [18] Application Notes for Displacement Sensor, *FTE Automotive*. Accessed: Apr. 1, 2022. [Online]. Available: Datasheet: https://www.fteautomotive.com/fileadmin/user_upload/FTE_PROS.WEGSENS-GB-14_web.pdf
- [19] Mehrotra P. “Biosensors and their applications - A review” *J. Oral Biol. Craniofac Res.* vol. 6, no. 2, pp. 153-159, 2016.
- [20] Świąch, Łukasz. “Calibration of a Load Measurement System for an Unmanned Aircraft Composite Wing Based on Fibre Bragg Gratings and Electrical Strain Gauges” *Aerospace*, vol. 7, 2020.
- [21] Mavromatidis, Pavlos & Kanarachos, Andreas. “A study on wheel force measurement using strain gauge equipped wheels”, 2016.
- [22] Application Notes for Strain Gauge Sensor, *Flintec*. Accessed: Apr. 10, 2022. [Online]. Available: https://valfardochhalsa.se/wp-content/uploads/2019/01/Flintec_40_Medical_Devices_S_2012_02_22.pdf
- [23] Application Notes for Temperature Sensor, *TE Connectivity*. Accessed: may. 21, 2022. [Online]. Available: <https://www.te.com/content/dam/te.com/documents/sensors/global/sensors-in-space.pdf>

- [24] Application Notes for Temperature Sensor. Accessed: May. 11, 2022. [Online]. Available: <http://denethor.wlu.ca/pc300/projects/library/autoapp.pdf>
- [25] Application Notes for Thermistor Sensor, *TDK*. Accessed: Apr. 1, 2022. [Online]. Available: <https://www.tdk-electronics.tdk.com/download/174138/21613b18eb9896a4f09da24908d8df53/sensors-medicalapplication-pb.pdf>
- [26] Díaz-Michelena, Marina. "Small Magnetic Sensors for Space Applications" *Sensors* vol. 9, no. 4: 2271-2288, 2009.
- [27] C.P.O Treutler, "Magnetic sensors for automotive applications", *Sensors and Actuators A: Physical*, Vol. 91, Issues 1-2, pp. 2-6, 2001.
- [28] S. C. Mukhopadhyay, K. Chomsuwan, C. P. Gooneratne and S. Yamada, "A Novel Needle-Type SV-GMR Sensor for Biomedical Applications," in *IEEE Sensors J.*, vol. 7, no. 3, pp. 401-408, March 2007.
- [29] Chugh, Vinit & Kalyan, Kubera & C S, Anoop & Patra, Amit & Negi, Shubham "Analysis of a GMR-based plethysmograph transducer and its utility for real-time Blood Pressure measurement" in Proc. Annual International Conference of the IEEE Engineering in Medicine and Biology Society, 2017.
- [30] Application Notes Magnetic Sensors, *Honeywell*. Accessed: Apr. 21, 2022. [Online]. Available: https://aerospace.honeywell.com/content/dam/aerobt/en/documents/learn/products/sensors/application-notes/AN218_Vehicle_Detection_Using_AMR_Sensors.pdf
- [31] Yang, Songlin, and Jin Zhang. "Current Progress of Magnetoresistance Sensors", *Chemosensors*, vol. 9, no. 8, p. 211, 2021.
- [32] Farnell *RTD Datasheet*. Accessed: Apr. 10, 2022. [Online]. Available: <https://www.farnell.com/datasheets/2339574.pdf>
- [33] *Selection Guide for Potentiometers*. Gefran. Accessed: Aug. 10, 2019. [Online]. Available: <https://www.gefran.com/en/products/68-lt-with-shaft>.
- [34] Digikey *Strain gauge Datasheet*. Accessed: Apr. 10, 2022. [Online]. Available: <https://media.digikey.com/pdf/Data%20Sheets/MicroMeasurements%20PDFs/S5145.pdf>

- [35] Product Notes for *thermistors*, TME, accessed on July 25, 2021. [Online]. Available: <https://www.tme.eu/Document/f9d2f5e38227fc1c7d979e546ff51768/NTCM-100K-B3950.pdf>.
- [36] RS Components *LDR Sensor Datasheet*. Accessed: Apr. 30, 2022. [Online]. Available: https://components101.com/sites/default/files/component_datasheet/LDR%20Datasheet.pdf.
- [37] Application Notes for GMR Sensors, NVE Corp., [online] Available: <http://www.nve.com/Downloads/apps.pdf>.
- [38] SGS Sensortech *Gas sensor Datasheet*. Accessed: Apr. 12, 2022. [Online]. Available: <https://www.sgxsensortech.com/content/uploads/2016/07/MiCS-VZ-89TE-V1.0.pdf>
- [39] Process parameters *RTD Datasheet*. Accessed: May. 11, 2022. [Online]. Available: <https://1c0xeifhqun3vab8d33505p1-wpengine.netdna-ssl.com/wpcontent/uploads/2014/01/PPL3-P-Data-Sheet-Iss-3.pdf>
- [40] P3 America *Potentiometers Datasheet*. Accessed: Apr. 15, 2022. [Online]. Available: <https://p3america.com/content/pdf/sch22.pdf>
- [41] ALTHEN *Strain gauge Datasheet*. Accessed: Apr. 8, 2022. [Online]. Available: <https://www.althensensors.com/media/23978/yfla-series-for-very-high-strain-straingauges-en.pdf>
- [42] Indiamart *Thermistor Datasheet*. Accessed: Apr. 15, 2022. [Online]. Available: <https://pdf.indiamart.com/impdf/22450369255/MY-2644000/ntc-thermistor-10d-9.pdf>
- [43] SILONEX *LDR Datasheet*. Accessed: Apr. 5, 2022. [Online]. Available: <https://docs.rs-online.com/3fcd/0900766b8003484c.pdf>
- [44] Online Source: Accessed: June 5, 2022. [Online]. Available: <https://www.mordorintelligence.com/industry-reports/global-rtd-temperature-sensors-market-industry>.
- [45] Xiujun Li and G. C. M. Meijer, "A novel low-cost noncontact resistive potentiometric sensor for the measurement of low speeds," in *IEEE Trans. Instrum. Meas.*, vol. 47, no. 3, pp. 776-781, June 1998.
- [46] P. Kejik, S. Reymond, and R. S. Popovic, "Ultra low-power angular position sensor for high-speed portable applications," in Proc. *IEEE Sensors*, Christchurch, New Zealand, Oct. 2009, pp. 173–176.

- [47] M. Rahal and A. Demosthenous, "An ASIC front end for planar highfrequency contactless inductive position sensors," *IEEE Trans. Instrum. Meas.*, vol. 58, no. 9, pp. 3021–3030, Sep. 2009.
- [48] M. Gasulla, X. Li, G. C. M. Meijer, L. van der Ham, and J. W. Spronck, "A contactless capacitive angular-position sensor," *IEEE Sensors J.*, vol. 3, no. 5, pp. 607–614, Oct. 2003.
- [49] Yu Cong, Zhou Wang-chao, Sun Bin and Zhou Hang-xia, "Study on NTC thermistor characteristic curve fitting methods," in *Proc. Inter. Conf. on Computer Sci. and Network Tech.*, pp. 2209-2213, 2011.
- [50] K. P. S. Rana, V. Kumar, A. K. Dagar, A. Chandel and A. Kataria, "FPGA Implementation of Steinhart–Hart Equation for Accurate Thermistor Linearization," *IEEE Sensors J.*, vol. 18, no. 6, pp. 2260-2267, Mar. 2018.
- [51] SUNROM TECH. *LDR Datasheet*. Accessed: Apr. 15, 2022. [Online]. Available: <https://www.sunrom.com/get/443700>.
- [52] Application Notes for LDR. Accessed: Apr. 5, 2022. [Online]. Available: http://www.ijirset.com/upload/2020/may/97_Light.PDF.
- [53] P. Ripka and J. Michal, "Advances in Magnetic Field Sensors", *IEEE Sensors J.*, vol. 6, no. 6, pp. 1108-1116, Jun. 2010.
- [54] R.L. White, "Giant magnetoresistance: a primer", *IEEE Trans. Magn.*, vol. 28, no. 5, pp. 2482-2487, 1992.
- [55] J. Lenz and S. Edelstein, "Magnetic sensors and their applications", *IEEE Sensors J.*, vol. 6, no. 3, pp. 631-649, Jun. 2006.
- [56] R. Gupta, V. Sreenath and B. George, "A modified RDC with an auto adjustable SC source enabled auto-calibration scheme," in *Proc. IEEE Sensors Applications Symposium (SAS)*, Catania, 2016, pp. 1-6.
- [57] Product Notes for *thermistors*, Vishay Intertechnology, accessed on May 20, 2021. [Online]. Available: <https://www.vishay.com/docs/29078/ntcle413.pdf>.
- [58] Hakim, Baha & Zohir, Dibi. "A Novel Neural Network-Based Technique for Smart Gas Sensors Operating in a Dynamic Environment" *Sensors*, vol. 9, 2009.
- [59] Liu, Haotian & Zhang, Li & Li, Holden & Tan, Ooi. "Microhotplates for Metal Oxide Semiconductor Gas Sensor Applications—Towards the CMOS-MEMS Monolithic Approach" *Micromachines*, vol. 9, 2018.

- [60] P. R. Nagarajan, B. George, and V. J. Kumar, "Improved single-element resistive sensor-to-microcontroller interface," *IEEE Trans. Instrum. Meas.*, vol. 66, no. 10, pp. 2736–2744, Oct. 2017.
- [61] R. Anandanatarajan, U. Mangalanathan, and U. Gandhi, "Enhanced microcontroller interface of resistive sensors through resistance-to-time converter," *IEEE Trans. Instrum. Meas.*, vol. 69, no. 6, pp. 2698–2706, Jun. 2020.
- [62] P. Julsereewong, A. Julsereewong, A. Rerkratn, and N. Pootharaporn, "Simple resistance-to-time converter with lead-wire-resistance compensation," in *Proc. SICE Annu. Conf.*, Sep. 2011, pp. 2760–2763.
- [63] T. K. Maiti and A. Kar, "Novel remote measurement technique using resistive sensor as grounded load in an opamp based V-to-I converter," *IEEE Sensors J.*, vol. 9, no. 3, pp. 244–245, Mar. 2009.
- [64] T. Junsing, "Interface circuit for three-wire resistance temperature detector with lead wire resistance compensation," in *Proc. Res., Invention, Innov. Congr. (RI2C)*, Dec. 2019, pp. 1–4.
- [65] *Application Guide for RTD Measurement System*, Texas Instruments. Accessed: Jan. 10, 2021. [Online]. Available: <https://www.ti.com/lit/an/sbaa275/sbaa275.pdf>.
- [66] M. C. Carotta *et al.*, "Nanostructured thick-film gas sensors for atmospheric pollutant monitoring: Quantitative analysis on field tests," *Sens. Actuators B, Chem.*, vol. 76, no. 1–3, pp. 336–342, Jun. 2001.
- [67] A. Vergara *et al.*, "An RFID reader with onboard sensing capability for monitoring fruit quality," *Sens. Actuators B, Chem.*, vol. 127, no. 1, pp. 143–149, Oct. 2007.
- [68] A. Depari, A. Flammini, D. Marioli, S. Rosa, and A. Taroni, "A low-cost circuit for high-value resistive sensors varying over a wide range," *IOP Meas. Sci. Technol.*, vol. 17, no. 2, pp. 353–358, Jan. 2006.
- [69] Zhang, Q.; Guan, Z.-S., "Gas Sensors of Electric Resistance Semiconductors," *Instrum. Tech. Sens.* no. 7, pp.6–9, 2006.
- [70] T. Yang, F. Tian, J. A. Covington, F. Xu, Y. Xu, A. Jiang, J. Qian, R. Liu, Z. Wang, and Y. Huang, "Resistance-Capacitance Gas Sensor Based on Fractal Geometry," *Chemosensors*, vol. 7, no. 3, pp. 31, Jul. 2019.

- [71] A. U. Khan, T. Islam, B. George and M. Rehman, "An Efficient Interface Circuit for Lossy Capacitive Sensors," *IEEE Trans. Instrum. Meas.*, vol. 68, no. 3, pp. 829-836, Mar. 2019.
- [72] F. Reverter and Ò. Casas, "A microcontroller-based interface circuit for lossy capacitive sensors", *Meas. Sci. and Tech.*, vol. 21, no. 6, pp. 065203, 2010.
- [73] Baxter L K, *Capacitive sensors. Design and Applications* New York: IEEE Press, 1997.
- [74] Meijer G C M, *Smart Sensor Systems* Chichester, UK: Wiley, 2008.
- [75] Lensch, H., Bastuck, M., Baur, T., Schütze, A., and Sauerwald, T, "Impedance model for a high-temperature ceramic humidity sensor," *J. Sens. Sens. Syst.*, vol. 8, pp. 161–169, Apr. 2019.
- [76] Chen, Z.; Lu, C, "Humidity sensors: A review of materials and mechanisms," *Sens. Lett.* vol. 3, pp. 274–295, 2005.
- [77] Huang S M, Green R G, Plaskowski A B and Beck M S., "Conductivity effects on capacitance measurements of two-component fluids using the charge transfer method," *J. Phys. E: Sci. Instrum.* vol. 21, no. 6, pp. 539-548, 1988.
- [78] T. Sen, C. Anoop, and S. Sen, "Simple linearising front-end-circuit for giant magneto-resistance sensors," *Electron. Lett.*, vol. 54, no. 2, pp. 81–83, Jan. 2018.
- [79] N. Massari and M. Perenzoni, "A time-based technique for a resistive detector," in *Proc. IEEE Int. Symp. Circuits Syst. (ISCAS)*, Lisbon, Portugal, May 2015, pp. 361–364.
- [80] N. M. Mohan, B. George, and V. J. Kumar, "A novel dual-slope resistance-to-digital converter," *IEEE Trans. Instrum. Meas.*, vol. 59, no. 5, pp. 1013–1018, May 2010.
- [81] S. Chavan and C. S. Anoop, "A simple direct-digitizer for giant magnetoresistance based sensors," in *Proc. IEEE Int. Instrum. Meas. Technol. Conf.*, Taipei, Taiwan, May 2016, pp. 1–5.
- [82] P. Ramanathan Nagarajan, B. George, and V. J. Kumar, "An improved direct digital converter for bridge-connected resistive sensors," *IEEE Sensors J.*, vol. 16, no. 10, pp. 3679–3688, May 2016.
- [83] B. George and V. J. Kumar, "Digital differential capacitive angle transducer," in *Proc. IEEE Instrum. Meas. Technol. Conf. IMTC*, May 2007, pp. 1–6.
- [84] A. Ray and C. S. Anoop, "A direct-digitizer interface based on dual-slope technique for giant magneto-resistance sensors," in *Proc. 8th IEEE India Int. Conf. Power Electron. (IICPE)*, Jaipur, India, Dec. 2018, pp. 1–6.

- [85] P. R. Nagarajan, B. George, and V. J. Kumar, "A linearizing digitizer for wheatstone bridge based signal conditioning of resistive sensors," *IEEE Sensors J.*, vol. 17, no. 6, pp. 1696–1705, Mar. 2017.
- [86] 남제우, "An apparatus for measuring temperature with rtd and a method for measuring temperature using it" South Korea Patent KR101622435B1, May 18, 2016.
- [87] N. M. Mohan, V. J. Kumar and P. Sankaran, "Linearizing Dual-Slope Digital Converter Suitable for a Thermistor," *IEEE Trans. Instrum. Meas.*, vol. 60, no. 5, pp. 1515-1521, May 2011.
- [88] W. Q. Yang, "A self-balancing circuit to measure capacitance and loss conductance for industrial transducer applications", *IEEE Trans. Instrum. Meas.*, vol. 45, no. 6, pp. 955-958, Dec. 1996.
- [89] P. Vooka and B. George, "A Direct Digital Readout Circuit for Impedance Sensors," *IEEE Trans. Instrum. Meas.*, vol. 64, no. 4, pp. 902-912, April 2015.
- [90] E. Sifuentes, O. Casas, F. Reverter, and R. Pallàs-Areny, "Direct interface circuit to linearise resistive sensor bridges," *Sens. Actuators A, Phys.*, vol. 147, no. 1, pp. 210–215, Sep. 2008.
- [91] F. Reverter and O. Casas, "Interfacing Differential Resistive Sensors to Microcontrollers: A Direct Approach," *IEEE Trans. Instrum. Meas.*, vol. 58, no. 10, pp. 3405–3410, Oct. 2009.
- [92] O. Lopez-Lapena, E. Serrano-Finetti, and O. Casas, "Low-power direct resistive sensor-to-microcontroller interfaces," *IEEE Trans. Instrum. Meas.*, vol. 65, no. 1, pp. 222–230, Jan. 2016.
- [93] Z. Czaja, "An implementation of a compact smart resistive sensor based on a microcontroller with an internal ADC," *Metrol. Meas. Syst.*, vol. 23, no. 2, pp. 225–238, Jun. 2016.
- [94] F. Reverter, J. Jordana, M. Gasulla, and R. Pallàs-Areny, "Accuracy and resolution of direct resistive sensor-to-microcontroller interfaces," *Sens. Actuators A, Phys.*, vol. 121, no. 1, pp. 78–87, May 2005.
- [95] Martin Paul Grunthaner, Fletcher R. Rothkopf, Christopher Tenzin Mullens, Steven Porter Hotelling, and Sean Erik O'connor, "Combined force and proximity sensing" European Patent EP2546730B1, April 1, 2020.

- [96] Samiul Haque Md, Richard White, and Jani Kivioja, “An apparatus for sensing” European Patent EP2872976B1, Oct. 2, 2019.
- [97] T. Sen, A. C. Sreekantan, and S. Sen, “Linearized sigma–delta-based direct digital converter for GMR sensors,” *IEEE Trans. Instrum. Meas.*, vol. 70, 2021, Art. no. 2002010.
- [98] H. Kim, W.-S. Chung, H.-J. Kim, and S.-H. Son, “A resistance deviation-to-pulsewidth converter for resistive sensors,” *IEEE Trans. Instrum. Meas.*, vol. 58, no. 2, pp. 397–400, Feb. 2009.
- [99] Application Note for Strain Gauge Measurements. *National Instrum.* Accessed: Jun. 20, 2019. [Online]. Available: http://elektron.pol.lublin.pl/elekp/ap_notes/NI_AN078_Strain_Gauge_Meas.pdf.
- [100] Johnathan S. Coursey, Kenton C. Hasson, Gregory H. Owen, “Systems and methods for auto-calibration of resistive temperature sensors” U.S. Patent US9939336B2, Apr. 10, 2018.
- [101] N. Mohan, B. George, and V. Kumar, “Analysis of a sigma–delta resistance-to-digital converter for differential resistive sensors,” *IEEE Trans. Instrum. Meas.*, vol. 58, no. 5, pp. 1617–1622, May 2009.
- [102] V. Sreenath, K. Semeerali, and B. George, “A resistive sensor readout circuit with intrinsic insensitivity to circuit parameters and its evaluation,” *IEEE Trans. Instrum. Meas.*, vol. 66, no. 7, pp. 1719–1727, Jul. 2017.
- [103] T. Islam, L. Kumar, Z. Uddin, and A. Gangopadhyay, “Relaxation oscillator-based active bridge circuit for linearly converting resistance to frequency of resistive sensor,” *IEEE Sensors J.*, vol. 13, no. 5, pp. 1507–1513, May 2013.
- [104] K. Mochizuki and K. Watanabe, “A high-resolution, linear resistance-to-frequency converter,” *IEEE Trans. Instrum. Meas.*, vol. 45, no. 3, pp. 761–764, Jun. 1996.
- [105] S. Kaliyugavaradan, “A linear resistance-to-time converter with high resolution,” *IEEE Trans. Instrum. Meas.*, vol. 49, no. 1, pp. 151–153, Feb. 2000.
- [106] L. Areekath, B. George, and F. Reverter, “Analysis of a direct microcontroller interface for capacitively coupled resistive sensors,” *IEEE Trans. Instrum. Meas.*, vol. 70, pp. 1–10, 2021.

- [107] Z. Cai *et al.*, “A CMOS readout circuit for resistive transducers based on algorithmic resistance and power measurement,” *IEEE Sensors J.*, vol. 17, no. 23, pp. 7917–7927, Dec. 2017.
- [108] Z. Cai *et al.*, “A ratiometric readout circuit for thermal-conductivity based resistive CO₂ sensors,” *IEEE J. Solid-State Circuits*, vol. 51, no. 10, pp. 2463–2474, Oct. 2016.
- [109] M. Das, V. Sivakami, A. Pal, and B. Vasuki, “Analog-digital conditioning circuit for RTD temperature measurement,” in *Proc. 15th IEEE India Council Int. Conf. (INDICON)*, Coimbatore, India, Dec. 2018, pp. 1–5.
- [110] A. Flammini, D. Marioli, and A. Taroni, “A low-cost interface to high value resistive sensors varying over a wide range,” *IEEE Trans. Instrum. Meas.*, vol. 53, no. 4, pp. 1052–1056, Aug. 2004.
- [111] A. Depari *et al.*, “A new and fast-readout interface for resistive chemical sensors,” *IEEE Trans. Instrum. Meas.*, vol. 59, no. 5, pp. 1276–1283, May 2010.
- [112] J. A. Botín-Córdoba, Ó. Oballe-Peinado, J. A. Sánchez-Durán, and J. A. Hidalgo-López, “Quasi single point calibration method for high-speed measurements of resistive sensors,” *Micromachines*, vol. 10, no. 10, p. 664, Sep. 2019.
- [113] J. A. Hidalgo-López, J. A. Botín-Córdoba, J. A. Sánchez-Durán, and Ó. Oballe-Peinado, “Fast calibration methods for resistive sensor readout based on direct interface circuits,” *Sensors*, vol. 19, no. 18, p. 3871, Sep. 2019.
- [114] V. N. Philip, “Direct microcontroller interface based digital readout circuit for single-element resistive sensors,” in *Proc. IEEE Int. Conf. Power, Control, Signals Instrum. Eng. (ICPCSI)*, Sep. 2017, pp. 2480–2483.
- [115] V. Jain and B. George, “Self-balancing digitizer for resistive half-bridge,” in *Proc. IEEE Int. Instrum. Meas. Technol. Conf. (I2MTC)*, May 2018, pp. 1–5.
- [116] Haase W C 2004 Digital measurement circuit and system using a grounded capacitive sensor, *US Patent 6,700,392*.
- [117] S. Malik, K. Kishore, T. Islam, Z. H. Zargar and S. Akbar, "A time domain bridge-based impedance measurement technique for wide-range lossy capacitive sensors", *Sens. Actuators A Phys.*, vol. 234, pp. 248-262, Oct. 2015.

- [118] P. Mantenuto, A. De Marcellis and G. Ferri, "Novel modified de-sauty autobalancing bridge-based analog interfaces for wide-range capacitive sensor applications", *IEEE Sensors J.*, vol. 14, no. 5, pp. 1664-1672, May 2014.
- [119] V. Sreenath and B. George, "A Switched-Capacitor Circuit-Based Digitizer for Efficient Interfacing of Parallel R-C Sensors," *IEEE Sensors J.*, vol. 17, no. 7, pp. 2109-2119, 1 Apr. 2017.
- [120] Qi Jia, G. C. M. Meijer, Xiujun Li and Chao Guan, "An integrated interface for grounded capacitive sensors," in Proc. *IEEE SENSORS*, pp. 4, 2005.
- [121] A. Heidary and G. C. M. Meijer, "An integrated interface circuit with a capacitance-to-voltage converter as front-end for grounded capacitive sensors," *Meas. Sci. and Tech.*, vol. 20, pp. 015202, 2009.
- [122] X. Li and G. C. M. Meijer, "An interface circuit for grounded and leaky capacitive sensors," in Proc. *IEEE International Conf. on Industrial Tech.*, pp. 1571-1574, 2010.
- [123] F. Reverter, X. Li and G. C. M. Meijer, "A novel interface circuit for grounded capacitive sensors with feedforward-based active shielding", *Meas. Sci. Technol.*, vol. 19, no. 2, pp. 025202, 2008.
- [124] F. Reverter, X. Li and G. C. M. Meijer, "Liquid-level measurement system based on a remote grounded capacitive sensor", *Sens. Actuators A Phys.*, vol. 138, pp. 1-8, Jul. 2007.
- [125] V. Naveen Kumar and K. V. Lakshmi Narayana, "Development of thermistor signal conditioning circuit using artificial neural networks," *IET Science, Meas. & Tech.*, vol. 9, no. 8, pp. 955-961, Nov. 2015.
- [126] Z. P. Nenova and T. G. Nenov, "Linearization Circuit of the Thermistor Connection," *IEEE Trans. Instrum. Meas.*, vol. 58, no. 2, pp. 441-449, Feb. 2009.
- [127] N. Chatterjee, B. Bhattacharyya, D. Dey and S. Munshi, "A Combination of Astable Multivibrator and Microcontroller for Thermistor-Based Temperature Measurement Over Internet," *IEEE Sensors J.*, vol. 19, no. 9, pp. 3252-3259, May 2019.
- [128] F. Reverter, "A microcontroller-based interface circuit for non-linear resistive sensors," *Meas. Sci. and Tech.*, vol. 32, pp. 1-4, Sep. 2020.
- [129] V. N. Kumar, K. V. L. Narayana, A. Bhujangarao and S. Sankar, "Development of an ANN-Based Linearization Technique for the VCO Thermistor Circuit," *IEEE Sensors J.*, vol. 15, no. 2, pp. 886-894, Feb. 2015.

- [130] K. Venkata Lakshmi Narayana and V. Naveen Kumar, "Development of an Intelligent Temperature Transducer," *IEEE Sensors J.*, vol. 16, no. 12, pp. 4696-4703, June 2016.
- [131] A. R. Sarkar, D. Dey, and S. Munshi, "Linearization of NTC Thermistor Characteristic Using Op-Amp Based Inverting Amplifier," *IEEE Sensors J.*, vol. 13, no. 12, pp. 4621-4626, Dec. 2013.
- [132] S. Bandyopadhyay, A. Das, A. Mukherjee, D. Dey, B. Bhattacharyya, and S. Munshi, "A linearization scheme for thermistor-based sensing in biomedical studies," *IEEE Sensors J.*, vol. 16, no. 3, pp. 603-609, Feb. 2016.
- [133] R. L. Geiger, P. E. Allen, and Noel R. S., *VLSI Design Techniques for Analog and Digital Circuits*, McGraw-Hill Series, 2010.
- [134] K. Elangovan, S. Dutta, A. Antony, and A. C. Sreekantan, "Performance verification of a digital interface suitable for a broad class of resistive sensors," *IEEE Sensors J.*, vol. 20, no. 23, pp. 13901-13909, Dec. 2020.
- [135] J. A. Hidalgo-Lopez, J. A. Botin-Cordoba, J. A. Sanchez-Duran, J. C. Tejero-Calado, and O. Oballe-Peinado, "Improved calibration method for resistive sensors using direct interface circuits," *IEEE Trans. Instrum. Meas.*, vol. 69, no. 8, pp. 5693-5701, Aug. 2020.
- [136] J. A. Hidalgo-Lopez, J. A. Sanchez-Duran, and O. Oballe-Peinado, "Method to reduce quantization error in direct interface circuits for resistive sensors," *IEEE Sensors J.*, vol. 20, no. 23, pp. 13910-13918, Dec. 2020.
- [137] S. Kim, W. Eom, J. Choi, and J. J. Kim, "Dual-mode wide-range linear CMOS interface circuit for resistive sensors," *Electron. Lett.*, vol. 50, no. 22, pp. 1575-1577, Oct. 2014.
- [138] A. De Marcellis, G. Ferri, and P. Mantenuto, "Uncalibrated operational amplifier-based sensor interface for capacitive/resistive sensor applications," *IET Circuits, Devices Syst.*, vol. 9, no. 4, pp. 249-255, Jul. 2015.
- [139] Z. Kokolanski, C. Gavrovski, V. Dimcev, and M. Makraduli, "Simple interface for resistive sensors based on pulse width modulation," *IEEE Trans. Instrum. Meas.*, vol. 62, no. 11, pp. 2983-2992, Nov. 2013.
- [140] *Selection Guide for RTD Sensors*. Omega. Accessed: Jul. 5, 2019. [Online]. Available: https://www.omega.co.uk/temperature/pdf/SEL_GUIDE_RTD.pdf.
- [141] *Selection Guide for Potentiometer*. Vishay. Accessed: Aug. 20, 2019. [Online]. Available: <https://www.vishay.com/docs/51031/p11sp11a.pdf>.

- [142] *Atmel SAM3X Datasheet*. MICROCHIP tech. Accessed: Oct. 5, 2019. [Online]. Available: https://ww1.microchip.com/downloads/en/DeviceDoc/Atmel-11057-32-bit-Cortex-M3-Microcontroller-SAM3X-SAM3A_Datasheet.pdf.
- [143] K. Elangovan and C. S. Anoop, "Simple and efficient relaxation oscillator-based digital techniques for resistive sensors—Design and performance evaluation," *IEEE Trans. Instrum. Meas.*, vol. 69, no. 9, pp. 6070–6079, Sep. 2020.
- [144] K. Elangovan and A. C. Sreekantan, "Evaluation of new digital signal conditioning techniques for resistive sensors in some practically relevant scenarios," *IEEE Trans. Instrum. Meas.*, vol. 70, pp. 1–9, 2021.
- [145] F. Reverter, "Power consumption in direct interface circuits," *IEEE Trans. Instrum. Meas.*, vol. 62, no. 2, pp. 503–509, Feb. 2013.
- [146] K. Elangovan, B. Ashok Sontakke and C. S. Anoop, "Evaluation of a Digital Converter for Linear and Nonlinear Temperature Sensors," in *Proc. IEEE Sensors Applications Symp. (SAS)*, pp. 1-6, Mar. 2020.
- [147] Product Notes for *temperature sensors*, Texas Instruments, accessed on June 03, 2021. [Online]. Available: <https://www.ti.com/lit/ds/symlink/lm35.pdf>.
- [148] K. Elangovan and C. S. Anoop, "Analysis and performance verification of an efficient digital converter for resistive sensors," in *Proc. IEEE Annul India Conf. (INDICON)*, Coimbatore, India, 2018, pp. 1–6.
- [149] Product Notes for *TDC7200*, Texas Instruments, accessed on Sep. 03, 2022. [Online]. Available: <https://www.ti.com/lit/ds/symlink/tdc7200.pdf>.
- [150] Maxim. *MAX4053 Datasheet*. Accessed: Dec. 15, 2018. [Online]. Available: <https://datasheets.maximintegrated.com/en/ds/MAX4051-MAX4053A.pdf>.
- [151] *George Clayton and Steve Winder, Operational Amplifiers*, 5th ed. Burlington, NJ, USA: Newnes, 2003.
- [152] F. Reverter, M. Gasulla, and R. Pallas-Areny, "Analysis of power-supply interference effects on direct sensor-to-microcontroller interfaces," *IEEE Trans. Instrum. Meas.*, vol. 56, no. 1, pp. 171–177, Feb. 2007.
- [153] 贾天亮, "Electronic circuit system and power consumption reducing method thereof" Chinese Patent CN105487638A, June 29, 2018.

- [154] Reissmann. *Application Guide for RTDTENCON*, Accessed: Dec. 30, 2020. [Online]. Available: http://www.apkservice.ru/files/Pt100_Pt500_Pt1000.pdf
- [155] K. Elangovan, A. Antony and A. Chandrika Sreekantan, "Simplified Digitizing Interface-Architectures for Three-Wire Connected Resistive Sensors: Design and Comprehensive Evaluation," *IEEE Trans. Instrum. Meas.*, vol. 71, pp. 1-9, 2022, Art no. 2000309.
- [156] K. Elangovan and A. C. Sreekantan, "An efficient universal digitizer with linear transfer characteristic for resistive sensor bridges," *IEEE Trans. Instrum. Meas.*, vol. 70, pp. 1–4, 2021.
- [157] L. Xu, S. Sun, Z. Cao, and W. Yang, "Performance analysis of a digital capacitance measuring circuit," *Rev. Sci. Instrum.*, vol. 86, no. 5, May 2015, Art. no. 054703.
- [158] V. Ferrari, D. Marioli, and A. Taroni, "Oscillator-based interface for measurand-plus-temperature readout from resistive bridge sensors," *IEEE Trans. Instrum. Meas.*, vol. 49, no. 3, pp. 585–590, Jun. 2000.
- [159] S. Y. Yurish, "Universal interfacing circuit for resistive-bridge sensors," in *Proc. 1st Int. Conf. Sensor Device Technol. Appl.*, Jul. 2010, pp. 211–216.
- [160] J. Lotichius, S. Wagner, M. Kupnik, and R. Werthschützky, "Measurement uncertainty of time-based and voltage-based wheatstone bridge readout circuits," in *Proc. IEEE Sensors*, Busan, South Korea, Nov. 2015, pp. 1–4.
- [161] Vishay. *IN4007 Diode Datasheet*. Accessed: Mar. 15, 2021. [Online]. Available: <https://www.vishay.com/docs/88503/1n4001.pdf>
- [162] *On-Semiconductor Dual Transistor Datasheet*. Accessed: Apr. 5, 2021. [Online]. Available: <https://www.onsemi.com/pdf/datasheet/nst847bdp6-d.pdf>.
- [163] Texas Instruments. *Selection Guide for Cables*. Accessed: Mar. 5, 2021. [Online]. Available: <https://www.ti.com/lit/an/snla164/snla164.pdf>.
- [164] STMicroelectronics. *TSZ181 Datasheet*. Accessed: Sep. 15, 2022. [Online]. Available: <https://www.st.com/resource/en/datasheet/tsz181.pdf>.
- [165] STMicroelectronics. *TS3021 Datasheet*. Accessed: Sep. 15, 2022. [Online]. Available: <https://www.st.com/resource/en/datasheet/ts3021a.pdf>.

- [166] S. Yamamoto and O. Ozeki, "Properties of High-Frequency Conducted Noise from Automotive Electrical Accessories," *IEEE Transactions on Electromagnetic Compatibility*, vol. EMC-25, no. 1, pp. 2-7, Feb. 1983.
- [167] Mouser Electronics. *Selection Guide for Potentiometers*. Accessed: Mar. 20, 2021. [Online]. Available: <https://www.mouser.in/datasheet/2/54/ptv09-777818.pdf>.
- [168] Honeywell. *Application Notes for AMR Sensors*. Accessed: May 20, 2021. [Online]. Available: http://c1233384.r84.cf3.rackcdn.com/UK_HMP_HMC1052L_1AN.pdf.
- [169] Ross P J, "A water-level sensor using a capacitance to frequency converter," *J. Phys. E: Sci. Instrum.* vol. 16 pp. 827–828, 1983.
- [170] S. C. Bera, J. K. Ray and S. Chattopadhyay, "A low-cost noncontact capacitance-type level transducer for a conducting liquid," *IEEE Trans. Instrum. Meas.*, vol. 55, no. 3, pp. 778-786, June 2006.
- [171] K. Elangovan and C. S. Anoop, "A Digital Readout Suitable for Resistive Sensors Affected with a Parasitic Capacitance Element," in Proc. *IEEE International Instrum. Meas. Tech. Conf. (I2MTC)*, May 2021.
- [172] Murata. *Application Notes for Thermistors*. Accessed: Sep. 05, 2022. [Online]. Available: <https://www.murata.com/~media/webrenewal/support/library/catalog/products/thermistor/ntc/r44e.ashx>.
- [173] Reverter, X. Li, and G. C. Meijer, "Stability and accuracy of active shielding for grounded capacitive sensors," *Meas. Sci. and Tech.*, vol. 17, no. 11, p. 2884, 2006.
- [174] TEXAS Instrum. *TMUXHS4212 Datasheet*, accessed on Feb. 20, 2022. [Online]. Available: <https://www.ti.com/lit/ds/symlink/tmuxhs4212.pdf>.
- [175] Application Notes for *Timers*, STM, accessed on Feb. 20, 2022. [Online]. Available: <https://www.st.com/resource/en/datasheet/stm32g484ce.pdf>.
- [176] Elangovan K, B. A. Sontakke and A. Chandrika Sreekantan, "Design, Analysis, and Hardware Verification of a Linearized Thermistor-Based Temperature Measurement System," *IEEE Trans. Instrum. Meas.*, vol. 71, pp. 1-9, 2022, Art no. 2002709.
- [177] Alok Barua, *Fundamentals of Industrial Instrumentation*, John Wiley & Sons, 2013.
- [178] Application Notes for *Thermistors*, Texas, accessed on Apr. 5, 2021. [Online]. Available: <https://www.ti.com/lit/an/snoaa12/snoaa12.pdf>.

- [179] Datasheet for *Op-amps*, Analog Devices, accessed on Feb. 20, 2022. [Online]. Available: <https://www.analog.com/media/en/technical-documentation/datasheets/ltc2063-2064-2065.pdf>.
- [180] J. Rius, A. Peidro, S. Manich, and R. Rodriguez, "Power and energy consumption of CMOS circuits: Measurement methods and experimental results," in *Proc. 13th Int. Workshop PATMOS*, Turin, Italy, 2003, pp. 80–89.
- [181] Thermistor Precautions, Sensor Scientific, Inc., accessed on Sep. 20, 2022. [Online]. Available: <https://www.sensorsci.com/three-important-thermistor-precautions>.

List of Publications

IEEE Journals

1. **Elangovan K**, S. Dutta, A. Antony, and Anoop C. S., "Performance Verification of a Digital Interface Suitable for a Broad Class of Resistive Sensors," in *IEEE Sensors Journal*, vol. 20, no. 23, pp. 13901-13909, 1 Dec.1, 2020.
2. **Elangovan K** and Anoop C. S., "Simple and Efficient Relaxation-Oscillator-Based Digital Techniques for Resistive Sensors — Design and Performance Evaluation," in *IEEE Transactions on Instrumentation and Measurement*, vol. 69, no. 9, pp. 6070-6079, Sept. 2020.
3. **Elangovan K** and Anoop C. S., "Evaluation of New Digital Signal Conditioning Techniques for Resistive Sensors in Some Practically Relevant Scenarios," in *IEEE Transactions on Instrumentation and Measurement*, vol. 70, Art no. 2004709, pp. 1-9, May 2021.
4. **Elangovan K** and Anoop C. S., "An Efficient Universal Digitizer With Linear Transfer Characteristic for Resistive Sensor Bridges," in *IEEE Transactions on Instrumentation and Measurement*, vol. 70, Art no. 2004904, pp. 1-4, June 2021.
5. **Elangovan K**, A. Antony, and Anoop C. S., "Simplified Digitizing Interface-Architectures for Three-Wire Connected Resistive Sensors: Design and Comprehensive Evaluation," in *IEEE Transactions on Instrumentation and Measurement*, vol. 71, pp. 1-9, 2022, Art no. 2000309.
6. **Elangovan K**, B. A. Sontakke and Anoop C. S., "Design, Analysis, and Hardware Verification of a Linearized Thermistor-Based Temperature Measurement System," in *IEEE Transactions on Instrumentation and Measurement*, vol. 71, pp. 1-9, 2022, Art no. 2002709.

International Peer-Reviewed Conferences

1. **Elangovan K** and Anoop. C. S., "Analysis and Performance Verification of An Efficient Digital Converter for Resistive Sensors," *2018 IEEE Annual India Conf. (INDICON)*, Coimbatore, 2018.
2. **Elangovan K** and Anoop C. S., "A Digital Signal-Conditioner for Resistive Sensors and its Utility for Linearizing GMR-based Magnetometer," in *Proc. IEEE Sensors Applications Symposium (SAS)*, Kuala Lumpur, Malaysia, 2020.
3. **Elangovan K**, S. Saha, and Anoop C. S., "A Simple Digital Interface Circuit for Giant Magneto-Resistance Sensors," in *Proc. IEEE Region 10 Conference (TENCON)*, pp. 2285-2288, Oct. 2019.
4. **Elangovan K**, British Ashok Sontakke, and Anoop C. S., "Evaluation of a Digital Converter for Linear and Nonlinear Temperature Sensors," in *Proc. IEEE Sensors Applications Symposium (SAS)*, Kuala Lumpur, Malaysia, 2020.
5. **Elangovan K** and Anoop C. S., "A Self-Calibration Circuit for the Resistance Measurement of Parallel R-C sensor," in *Proc. IEEE Second International Conference on Control, Measurement, and Instrumentation (CMI)*, pp. 201-205, Jan. 2021.
6. **Elangovan K** and Anoop C. S., "A Digital Readout Suitable for Resistive Sensors Affected with a Parasitic Capacitance Element," in *Proc. IEEE International Instrumentation and Measurement Technology Conference (I2MTC)*, Glasgow, Scotland, 2021, pp. 1-5.
7. **Elangovan K** and Anoop C. S., "A Simple Digitization Scheme for Resistive Sensors and its Adaptation for Remote Measurements," in *Proc. IEEE International Instrumentation and Measurement Technology Conference*, Glasgow, Scotland, May 2021.

Appendix A

Expressions Used for the Calculation of Various Performance Parameters

Various performance parameters such as nonlinearity, relative error, signal-to-noise ratio, etc. are calculated using the following expressions.

1. Nonlinearity error (e_{NL})

$$e_{NL} = \frac{x - (S \times x^* + I)}{\text{FSS}} \times 100\%$$

Here, x^* denotes the actual resistance, and S and I represent the slope and intercept of the best fit line of x^* with respect to x . FSS denotes the full-scale span.

2. Relative error (e_{REL})

$$e_{REL} = \frac{y - y^*}{y} \times 100\%$$

Here y^* and y , respectively, are the measured and true values.

3. Full-scale error (e_{FSE})

$$e_{FSE} = \frac{y - y^*}{\text{FSS}} \times 100\%$$

4. Signal-to-noise ratio (SNR)

$$\text{Signal-to-noise ratio (in dB)} = 10 \log \left[\frac{\sum_{i=1}^n [m(i)]^2}{\sum_{i=1}^n [m(i) - m_{avg}]^2} \right]$$

Here, n is a number of consecutive measurements, m is the measurand value (either R_x or x), $m(i)$ is the measurand value at i^{th} iteration, m_{avg} represents the average value of the measurand.

5. Standard deviation (σ)

$$\text{Standard deviation (in \%)} = \left[\sqrt{\frac{\sum_{i=1}^n [m(i) - m_{avg}]^2}{n-1}} \right] \times 100\% / m$$

6. Effective number of bits (ENOB)

$$\text{Resolution in bits (ENOB)} = (\text{SNR} - 1.76) / 6.02$$

7. Repeatability error (R_E)

$$\text{Repeatability error (in \%)} = \left[\Delta_{max} / (m_u - m_l) \right] \times 100\%$$

Here, Δ_{max} is the maximum difference between the multiple measurements, m_u is the upper limit of the measurement range, m_l is the lower limit of the measurement range.

Appendix B.1

Measurement Results Related to DCR Circuit (During Experimentation with DS-type Sensor)

Measurement results of the DCR circuit when interfaced with rectilinear displacement transducer-LT-150 (Fig. 2.16), are given below.

Table B.1. Output and Error Characteristics of DCR Circuit when Tested with a Differential Resistive Sensor

DISPLACEMENT (mm)	MEASURED x	% e_{NL}
0	-0.5188	-0.0475
10	-0.3897	0.105548
20	-0.2575	-0.08138
30.2	-0.1253	0.065984
40.2	0.0054	0.024759
50.2	0.1371	-0.06503
60	0.2647	-0.10058
70.1	0.3946	0.098193

Appendix B.2

Experimental Results Related to RDR_w Circuit (During Experimentation with SE-type Sensor)

Measurement results of the developed RDR_w with a SE-type sensor (Fig. 3.19), during the emulation studies, are given below.

Table B.2. Dataset Reflecting Experimental Results of RDR_w Circuit

INPUT RESISTANCE (Ω)	MEASURED RESISTANCE (Ω)	% e_{NL}	% e_{REL}
1000	990	-0.007319	1
2000	1990	-0.007217	0.5
3000	2990	-0.007114	0.333333
4000	3990	-0.007012	0.25
5000	4990	-0.006909	0.2
6000	5990	-0.006807	0.166667
7000	6990	-0.006704	0.142857
8000	7990	-0.006602	0.125
9000	8990	-0.006499	0.111111
10000	9990	-0.006397	0.1
20000	19990	-0.005372	0.05
30000	30000	-0.005349	0
40000	39990	-0.003323	0.025
50000	50000	-0.0033	0
60000	59990	-0.001274	0.016667
70000	69990	-0.00025	0.014286
80000	80000	-0.000226	0
90000	90000	0.0007983	0
100000	100000	0.0018228	0
200000	200020	0.0100662	-0.01
300000	300020	0.0203115	-0.006667
400000	399800	0.0525789	0.05
500000	500200	0.0227842	-0.04
600000	600300	0.0230195	-0.05
700000	700300	0.0332649	-0.042857
800000	800660	0.0074742	-0.0825
900000	901000	-0.016315	-0.111111
1000000	1001620	-0.068131	-0.162

Appendix B.3

Data Related to DRR-3 Interface with the AA004 GMR Sensor

Measurement data of the DRR-3 circuit during the experimentation with the AA004 GMR sensor is given below (related to Fig. 4.23). Here, the measurement was conducted with and without the connecting wires.

Table B.3. Experimental Results of DRR-3 when Interfaced with GMR Sensor

MAGNETIC FIELD (mT)	MEASURED RESISTANCE WITH WIRE CASE (Ω)	MEASURED RESISTANCE WITHOUT WIRE CASE (Ω)	% e_{NL} FOR WITH WIRE CASE	% e_{NL} FOR WITHOUT WIRE CASE
6	4767.2	4768.1	0.7972	0.717176
8	4753.9	4753	-0.33617	0.35907
10	4735	4736.9	1.059814	0.450604
12	4720.8	4720.8	0.332946	0.542138
14	4705.7	4706.6	0.012582	-0.22064
16	4692.4	4691.5	-1.12079	-0.57875
18	4675.4	4675.4	-0.58298	-0.48722
20	4658.4	4660.2	-0.04517	-0.80036
22	4643.1	4645.1	-0.2752	-1.15847
24	4629	4628.1	-1.04723	-0.66226
26	4612.9	4612	-0.91592	-0.57072
28	4595	4594	0.028391	0.375128
30	4577.1	4577	0.972706	0.871339
32	4562.8	4561.9	0.291005	0.513232
34	4545.8	4545.7	0.828817	0.64973

Appendix B.4

Measurement Data Related to DIR Circuit During Interface with SE type Sensor

Emulation data of the proposed DIR-SE with RTD-Pt100 sensor and RTD-Pt1000 sensor-based SE sensors is given below. These data are related to Fig. 5.5.

Table B.4. Output Characteristics Obtained on Testing DIR with a SE-Type Sensor

ACTUAL RESISTANCE (Ω)	MEASURED RESISTANCE (Ω)	% e_{NL}	% e_{REL}
80	80.18	0.07321	-0.225
85	85.25	-0.0352	-0.29412
90	90.24	-0.02934	-0.26667
95	95.27	-0.08061	-0.28421
100	100.15	0.0824	-0.15
105	105.19	0.01684	-0.18095
110	110.21	-0.02015	-0.19091
115	115.21	-0.02857	-0.18261
120	120.18	0.00587	-0.15
125	125.19	-0.01684	-0.152
130	130.18	-0.01097	-0.13846
135	135.16	0.00918	-0.11852
140	140.1	0.08648	-0.07143
145	145.19	-0.05051	-0.13103
150	150.15	-0.00179	-0.1
800	799.56	-0.01505	0.055
850	849.6	-0.04582	0.04706
900	899.49	-0.05517	0.05667
950	948.68	0.03548	0.13895
1000	998.53	0.03185	0.147
1050	1048.35	0.0325	0.15714
1100	1098.1	0.04316	0.17273
1150	1148.61	-0.05476	0.12087
1200	1197.51	0.07732	0.2075
1250	1247.26	0.08797	0.2192
1300	1297.73	-0.00423	0.17462
1350	1347.95	-0.06072	0.15185
1400	1397.95	-0.08578	0.14643
1450	1447.37	-0.02799	0.18138
1500	1496.71	0.04124	0.21933

Appendix B.5

Emulation Results of the DFRC Circuit During the Measurement of Capacitance

Measurement results of the DFRC used for the capacitance measurement (data related to Fig. 6.12) are given below.

Table B.5. Output Datasets Related to DFRC Circuit (Capacitance Mode)

APPLIED CAPACITANCE (pF)	MEASURED CAPACITANCE (pF)	% e_{NL}	% e_{REL}
98	99	-0.07365	-1.02041
200	201.78	-0.05159	0.89
311	300	-0.01131	1.28617
511	501	0.02697	1.17417
724	700	0.08931	1.24309
910	901	-0.16924	0.10989
1068	1101	-0.05418	-0.37453
1281	1302	0.03296	-0.62451
1481	1501	0.04644	-0.6077
1694	1701	0.08398	-0.64935
1880	1902	0.14785	-0.74468
2131	2102	0.10883	0.61004
2344	2303	0.14637	0.63993
2544	2502	-0.06337	0.27516
2758	2702	-0.2739	0.03626
2944	2902	-0.13563	0.16984
3101	3103	0.02909	-0.38697
3314	3301	0.01703	0.3621
3514	3501	0.03051	0.36995
3727	3702	-0.08076	0.24148
3913	3904	0.10711	0.43445
4130	4105	-0.00438	0.31477

Appendix B.6

Experimental Results of Th-LDM With Thermistor (T-2) Sensor

Data related to the interface of Th-LDM with a thermistor (T-2) is given below. These data are belonging to Fig. 7.15.

Table B.6. Measurement Results of Th-LDM System

TEMPERATURE (°C)	MEASURED RESISTANCE USING CHARACTERIZATION (kΩ)	MEASURED y	% e_{NL}
35	6.825	2.4675	-0.01495
40		2.4041	-0.14274
45		2.3384	0.026089
50.1	3.805	2.2733	-0.04855
55.1		2.2079	0.081591
60		2.1445	0.119882
65.1	2.212	2.0788	0.122626
70.1		2.0153	0.007729
75		1.9509	0.174986
80.1	1.329	1.8863	0.035867
85.1		1.8258	-0.46593
90.2		1.7583	-0.23104
95	0.828	1.6921	0.334435

Biodata

Name: Elangovan K

Address: Thogamalaikottai,
Kovilur Post,
Dindigul District,
Tamilnadu – 624706.

Email: elangoece3691@gmail.com

Research interests: Digital instrumentation, Direct-digital conversion techniques, Design of analog interface circuits, Error analysis, and Compensation functions.

Academic qualifications

Doctor of Philosophy (Ph.D.) Jan 2018 – Sep 2022

Indian Institute of Space Science and Technology, Thiruvananthapuram, India.

Specialization: Efficient Digitizing Interface Circuits for Various Resistive Sensor Configurations with Considerations on Wide-span and Remote Measurements

Master of Engineering (M. E.) Sep 2014 – Apr 2016

College of Engineering, Guindy, Chennai, India.

Specialization: Control and Instrumentation Engineering

Bachelor of Engineering (B. E.) Sep 2008 – Apr 2012

University College of Engineering, Panruti, India.

Specialization: Electronics and Communication Engineering

Other Peer-reviewed Reputed IEEE International Conference Papers

1. S. K. Ambedkar, **Elangovan K**, K. B. Nandapurkar, and Anoop C. S., "Linearizing Relaxation-Oscillator Based Front-End for Magneto-Resistive Angle Sensors," in *Proc. IEEE Sensors Applications Symposium (SAS)*, pp. 1-6, Aug. 2021.
2. **Elangovan K** and Anoop C. S., "A Digital Front-End for Remotely Located Resistive Sensors," in *Proc. IEEE International Symposium on Smart Electronic Systems (iSES) (Formerly iNiS)*, pp. 7-12, Dec. 2020.
3. **Elangovan K** and Anoop C. S., "Relaxation Oscillator Based Digital Interface Circuit for Resistive Sensors," in *Proc. IEEE 17th India Council International Conference (INDICON)*, pp. 1-5, Dec. 2020.

Skills and Expertise

- Expertise in handling and operating high-precision test and measurement equipment (Gaussmeter, High-resolution digital multimeter, Mixed-signal oscilloscope)
- Programming languages: Matlab, LabVIEW, and Embedded C
- Circuit design and PCB design software: LTspice and Kicad
- Graphing and analysis software: Origin

Experience

Assistant Professor on contract

Aug 2017 – Jan 2018

Department of Electronics and Communication Engineering,

College of Engineering, Karunagappally,

Kerala – 690523.

Doctoral Committee Members

Chairman: Prof. Deepak Mishra

Professor & Head

Department of Avionics

Indian Institute of Space Science and Technology, Thiruvananthapuram

Convenor: Dr. Anoop C. S.

Associate Professor

Department of Avionics

Indian Institute of Space Science and Technology, Thiruvananthapuram

Members: Prof. N. Selvagesan

Professor

Department of Avionics

Indian Institute of Space Science and Technology, Thiruvananthapuram

Dr. Rajeevan P. P.

Associate Professor

Department of Avionics

Indian Institute of Space Science and Technology, Thiruvananthapuram

Dr. Sourin Mukhopadhyay

Assistant Professor

Department of Physics

Indian Institute of Space Science and Technology, Thiruvananthapuram